SYNTHETIC JET MICROPUMP

SYNTHETIC JET MICROPUMP

BY

SHERIF ABDOU, M.A.SC., B.SC.

A THESIS

SUBMITTED TO THE SCHOOL OF GRADUATE STUDIES

IN PARTIAL FULFILMENT OF THE REQUIREMENTS

FOR THE DEGREE

PHILOSOPHY DOCTOR

MCMASTER UNIVERSITY

© COPYRIGHT BY SHERIF ABDOU, NOVEMBER 2013

DOCTOR OF PHILOSOPHY (2013)	McMaster University
(Mechanical Engineering)	Hamilton, Ontario
MASTER OF APPLIED SCIENCE (2004)	McMaster University
(Mechanical Engineering)	Hamilton, Ontario
BACHELOR OF SCIENCE (1999)	Ain Shams University
(Mechanical Engineering)	Cairo, Egypt

TITLE	: Synthetic Jet Micropump
AUTHOR	: Sherif Abdou. M.A.Sc. (McMaster University)
SUPERVISOR	: Dr. S. Ziada
	Dr. R.N. Kleiman
NUMBER OF PAGES	: xxiii, 264

ABSTRACT

The production of a novel micropump based on the synthetic jet principle is investigated both numerically and experimentally. The proposed micropump consists of a synthetic jet actuator driven by a vibrating diaphragm issuing into an inverted T-shaped channel structure forming the inlet/outlet channels of the pump.

The software package Ansys is used to perform numerical investigations of the operation of the proposed micropump. Simulations were performed to study the effect of changing the inlet/outlet channel dimensions as well as the operating frequency, amplitude and duty cycle of the excitation signal. Inlet/outlet channel widths ranging

from 200 to 800 µm and operating amplitude and frequency of excitation of the 5 mm square membrane driving the synthetic jet actuator ranging from 20 to 60 µm and from 20 to 60 Hz respectively were investigated.

Based on the findings of the numerical simulations, a prototype design was chosen and produced. Prototype production using microfabrication techniques as well as micromachining was investigated. The final prototype was micromachined using plexiglass as the working material. An experimental setup was constructed to test the performance of the produced prototype, which allowed for measuring the produced flow rate, pressure head, actuation amplitude and frequency.

The findings of the numerical simulations verified the possibility to produce a working micropump with flow rates of up to 1.3 ml/min. Simulation results also showed the dependence of the produced flow rate on both the inlet and outlet channel widths. An increase in the inlet channel width resulted in a gain in the average flow rate through the pump while an increase in the outlet channel width results in a reduction in the flow rate. Increases in either the actuation amplitude or frequency of excitation both resulted in an improvement in the produced flow rate. Changes in the ejection duty cycle, or the ejection time relative to the suction time during an actuation cycle, were found to influence the flow rate produced by the pump. A shorter ejection time produced a higher flow rate from the pump as compared to a longer ejection time. It was also found that changes in dimensions or operating parameters affected the

fluctuations in the flow rate through the pump associated with the pulsating nature of the synthetic jet. Experimental investigations confirmed the findings of the numerical simulations in terms of the flow rate and the trends in the dependence of the flow rate on operating parameters. Values of maximum back pressure of up to 500 Pa were also reported experimentally and membrane driving powers of up to 122 μW were calculated numerically.

To my Parents and my Grand Parents

ACKNOWLEDGEMENTS

First of all, I would like to welcome into my life my lovely wife, Salma, who has been an inspiration and motivation for me. Thank you for always believing in me and supporting me throughout my thesis work. I am blessed to have you in my life.

I would like to dedicate this work to my parents and my grandparents for their continuous guidance, encouragement, backup and support. I would not be where I am today if it wasn't for them.

The author would also like to thank the following people for their contributions to this work:

Dr. S. Ziada and Dr. R. Kleiman, my supervisors, for their continuous guidance, support and their invaluable advice throughout the course of my work. Also, I would like to thank them for their patience and moral support when it was really needed.

My committee members, Dr. M. Lightstone and Dr. R. Selvaganapathy for their continued input and suggestions, patience and understanding.

Ron Lodewyks, Joe Verhaege, Mark MacKenzie, and Jim McLaren for their technical guidance and help.

Maneesh Khanna for his help and expertise with the machining of the micropump as well as the MMRI for allowing me to use their equipment.

Doris Stevanovic and Zhilin Peng for their help, guidance and training in microfabriation and clean room use as well as the CEDT team for allowing me to use their clean room and microfabrication facilities.

The students of the 4M06 project, Adam Crozier, Adrian Liu, Shailan Patel and Rickmund Von Jaeger for their contribution to the study of the effect of the nonuniform excitation signal on the performance of the micropump.

OSG tooling for providing the milling tools used for the machining of the pump.

My friends, colleagues and lab mates for their precious help, guidance, encouragement and support throughout the course of my work. Thank you all.

TABLE OF CONTENTS

ABSTRACT III

ACKNOWLEDGEMENTS VII

TABLE OF CONTENTS IX

LIST OF FIGURES XIII

LIST OF TABLES XIX

NOMENCLATURE XXI

CHAPTER 1: INTRODUCTION 1

1.1 SCOPE OF THE WORK 5

1.2 THESIS OUTLINE 6

CHAPTER 2: LITERATURE REVIEW 9

2.1 MICROFLOW CHARACTERISTICS 10

2.1.1 VOLUME VS. SURFACE FORCES 10

2.1.2 Knudson Number & the continuum assumption 11
2.2 Micropumps 13
2.2.1 Mechanical Micropumps: 15
2.2.1.1 Rotary 15
2.2.1.2 Vibrating diaphragm micropumps 18
2.2.1.2.1 Piezoelectric 19
2.2.1.2.2 Electrostatic 23
2.2.1.2.3 Electromagnetic 25
2.2.1.2.4 Thermopneumatic 25
2.2.1.2.5 Shape memory alloy 26
2.2.1.2.6 Other 27
2.2.1.2.7 Rectification Mechanism 27
2.2.1.3 Peristaltic micropumps 32
2.2.2 Non-Mechanical Micropumps 34
2.2.2.1 Electrokinetic and Magnetokinetic: 34
2.2.2.2 Phase change: 38
2.2.2.3 Other micropumps: 40
2.2.3 Concluding remarks 41
2.3 Synthetic Jets 47
2.3.1 Characteristics of Synthetic Jets 49
2.3.2 Macro-Synthetic Jets and their applications 52
2.3.3 Micro-Synthetic Jets 54
2.3.3.1 Applications of Micro-Synthetic Jets 60
2.4 Concluding Remarks 61

Chapter 3: Synthetic Jet Micropump 63

1.1. Concluding Remarks 73

Chapter 4: Numerical Simulations 75

4.1 Geometry & Dimensions 77
4.2 Meshing 78
4.3 Boundary conditions 80
4.3.1 Inlet & Outlet 80
4.3.2 Membrane 81
4.3.3 Walls & Symmetry 83

4.4 SIMULATION PARAMETERS 83
4.5 SOLVER PARAMETERS 84

CHAPTER 5: FABRICATION & EXPERIMENTAL SETUP 87

5.1 MICROFABRICATION APPROACH 88
5.1.1 LIMITATIONS 90
5.1.1.1 PHOTOLITHOGRAPHY PROBLEMS 91
5.1.1.2 ASSEMBLY PROBLEMS 92
5.1.1.3 ACTUATOR PROBLEMS 92
5.2 MICROMACHINING APPROACH 93
5.2.1 DEVICE DESIGN 93
5.2.2 MEMBRANE STRUCTURE 95
5.3 EXPERIMENTAL SETUP 97
5.3.1 LIQUID SUPPLY AND DELIVERY 98
5.3.2 MEASURING FLOW RATE 98
5.3.3 MEASURING HEAD 99
5.3.4 MEMBRANE ACTUATION 99
5.3.5 MEASURING MEMBRANE DEFLECTION 100

CHAPTER 6: RESULTS & DISCUSSION 103

6.1 BASIC PARAMETERS OF THE MICROPUMP 104
6.1.1 STROKE LENGTH: 105
6.1.2 REYNOLDS NUMBER 107
6.1.3 FORMATION CRITERION 108
6.1.4 EXCITATION AMPLITUDE CORRECTION 110
6.1.5 FLOW RATES 113
6.2 THE BASE CASE 115
6.3 EFFECT OF PUMP CHANNEL WIDTH 125
6.3.1 EFFECT OF PUMP INLET WIDTH 125
6.3.2 EFFECT OF PUMP OUTLET WIDTH 128
6.4 EFFECT OF ACTUATION PARAMETERS 129
6.4.1 EFFECT OF ACTUATION AMPLITUDE 132
6.4.2 EFFECT OF ACTUATION FREQUENCY 133
6.4.3 EFFECT OF ACTUATION EJECTION/SUCTION DUTY CYCLE 138
6.5 EXPERIMENTAL RESULTS 144

6.5.1 EFFECT OF OPERATING PARAMETERS 144
6.5.2 MICROPUMP MAXIMUM BACK PRESSURE 148
6.5.3 MICROPUMP DRIVING POWER 150
6.5.4 MICROPUMP VOLUMETRIC EFFICIENCY 153
6.6 CONCLUDING REMARKS 157

CHAPTER 7: CONCLUSION & RECOMMENDATIONS 165

7.1 RESEARCH CONTRIBUTIONS 169
7.2 RECOMMENDATIONS FOR FUTURE WORK 170

BIBLIOGRAPHY 175

APPENDIX A : NUMERICAL GRID ANALYSIS 197

A.1 GRID SIZE INDEPENDENCE 197
A.2 TIME STEP INDEPENDENCE 198
A.3 SIMULATION TIME INDEPENDENCE 199

APPENDIX B: EXPERIMENTAL RESULTS 201

APPENDIX C: UNCERTAINTY ANALYSIS 205

APPENDIX D: NUMERICAL RESULTS 209

D.1 CASE W_I=200 MM, W_O= 400 MM, A_M= 40 MM, F= 40 HZ 210
D.2 CASE W_I=400 MM, W_O= 200 MM, A_M= 40 MM, F= 40 HZ 215
D.3 CASE W_I=400 MM, W_O= 400 MM, A_M= 20 MM, F= 40 HZ 220
D.4 CASE W_I=400 MM, W_O= 400 MM, A_M= 40 MM, F= 20 HZ 225
D.5 CASE W_I=400 MM, W_O= 400 MM, A_M= 40 MM, F= 40 HZ 230
D.6 CASE W_I=400 MM, W_O= 400 MM, A_M= 40 MM, F= 60 HZ 235
D.7 CASE W_I=400 MM, W_O= 400 MM, A_M= 60 MM, F= 40 HZ 240
D.8 CASE W_I=400 MM, W_O= 800 MM, A_M= 40 MM, F= 40 HZ 245
D.9 CASE W_I=800 MM, W_O= 400 MM, A_M= 40 MM, F= 40 HZ 250
D.10 CASE W_I=400 MM, W_O= 400 MM, A_M= 40 MM, F= 40 HZ, K=0.25 255
D.11 CASE W_I=400 MM, W_O= 400 MM, A_M= 40 MM, F= 40 HZ, K=4 260

LIST OF FIGURES

Figure 2.1. Examples of rotary micropumps. (a) Rotary blade micropump. (Ahn and Allen 1995); (b) Two-gear rotary micropump. (Dewa et al. 1997; Deng et al. 1998); (c) Internal gear rotary micropump. (Weisener et al. 1996); (d) Ferrofluid rotary micropump. (Hatch et al. 2001); (e) Continuous transverse-axis rotary pump. (Sen et al. 1996; Sharatchandra et al. 1997); (f) Spiral-channel rotary micropump. (Kilani et al. 2006); (g) Disk viscous rotary micropump. (Blanchard, D. et al. 2005) 17

Figure 2.2. Schematic of a vibrating diaphragm micropump. 19

Figure 2.3. Vibrating diaphragm micropumps with passive check valves fabricated in silicon/glass. (Van Lintel et al. 1988) 20

Figure 2.4. Valveless piezoelectrically actuated micropump using temperature dependent fluid viscosity for flow rectification. (Matsumoto, S. et al. 1999) 22

Figure 2.5. (i) Electrostatically actuated micropumps (Zengerle et al. 1992); (ii) Dual-diaphragm electrostatic micropump (Cabuz et al. 2001): (a) Sectional side view, (b) Top view through chamber. 24

Figure 2.6. Example of a valved vibrating diaphragm micropump. (Singhal et al. 2004) 28

Figure 2.7. Examples of valveless flow rectification mechanisms. (Iverson and Garimella 2008) (a) A valveless micropump using Nozzle/diffuser elements. (Stemme, E. and Stemme 1993) (b) Tesla (valvular conduit) valves (Tesla 1916) 30

Figure 2.8. Sequence of operation of a peristaltic micropump. (Singhal et al. 2004) 32

Figure 2.9. Thermopneumatically actuated micropump. (Grosjean and Tai 1999) 33

Figure 2.10. Schematic of electroosmotic micropumps. (a) DC electroosmotic micropump. (b) AC electroosmotic micropump. 37

Figure 2.11. Schematic of a magnetohydrodynamic micropump. (Iverson and Garimella 2008) 38

Figure 2.12. (a) Schematic of a bubble micropump. (Jun and Kim 1996) (b) Schematic of an electrochemical micropump. (Böhm, Olthius, et al. 1999) 39

Figure 2.13. (a) Maximum flow rate per unit cross-sectional area and (b) Maximum back pressure for various micropumps reported in the literature. (Singhal et al. 2004) 43

Figure 2.14. (a) Maximum back pressure, (b) Maximum flow rate per unit platform area and (c) Maximum flow rate per unit outlet area for pumps reported in the literature (Iverson and Garimella 2008) 44

Figure 2.15. Flow rate vs typical size for: (Top left) mechanical, (Top right) non-mechanical micropumps. (Bottom) Maximum back pressure vs maximum flow rate. (Nguyen et al. 2002) (numbers indicate corresponding reference as per source) 46

Figure 2.16. Schematic diagram of a synthetic jet actuator. 48

Figure 2.17. Reynolds number vs. stokes number for the experimental data obtained by Smith and Swift (2001) for different jet widths. (Utturkar et al. 2003) 52

Figure 2.18. Synthetic microjet design: a) Hybrid membrane; b) Integrated membrane. (Coe et al. 1995) 55

Figure 2.19. Measured velocity profiles across the center row in a 4x5 microjet array at 4 mm (open symbols and exhibiting larger fluctuations) and 10 mm

(closed symbols and exhibiting less fluctuations) downstream of the jet array. (Coe et al. 1995) 56

Figure 2.20. Vorticity contours for different cases studied at t/T=0.71 (Mallinson et al. 2003): a) A = 0.5 µm, f= 0.725 kHz; b) A = 1 µm, f = 0.725 kHz; c) A = 2 µm, f = 0.725 kHz; d) A = 0.5 µm, f = 1.450 kHz; e) A = 1 µm, f = 1.450 kHz; f) A = 2 µm, f = 1.450 kHz; g) A = 0.5 µm, f = 2.900 kHz; h) A = 1 µm, f = 2.900 kHz; i) A = 2 µm, f = 2.900 kHz. 58

Figure 2.21. Comparison of peak average centerline velocity for different test cases against non-dimensional variables. (Mallinson et al. 2003) 58

Figure 3.1. Schematic layout of the synthetic microjet actuator studied (left) and the proposed synthetic microjet based pump (right). (Luo and Xia 2005) 64

Figure 3.2. Stream function contours at different intervals in a forcing cycle. (t* = t/T) (Luo and Xia 2005) 65

Figure 3.3. Velocity vector plots of the external flow field for four test cases. (Luo and Xia 2005) 66

Figure 3.4. Mass flow rate at the pump exit plane for different test cases. (Luo and Xia 2005) 67

Figure 3.5. The proposed micropump design by Dinh et al. (Dinh and Ogami 2011; Dinh et al. 2008) 69

Figure 3.6. Flow rate reported at pump outlet for the proposed micropump by Dinh et al. (2011; 2008) 70

Figure 3.7. (Left) Variation of pump flow rate vs excitation amplitude as well as maximum back pressure. (Right) Flow rate vs pressure for different amplitudes of excitation. (Dinh and Ogami 2011; Dinh et al. 2008) 71

Figure 3.8. Schematic of synthetic jet air micropump. (Choi et al. 2011) 72

Figure 3.9. Numerical model geometry and dimensional parameters (Choi et al. 2011) 73

Figure 4.1. Sample geometry used in numerical simulations. 76

Figure 4.2. Dimensioned drawing of a sample final geometry simulation test case. 78

Figure 4.3. Mesh for a sample simulation cases. 79

Figure 4.4. Boundary conditions for a sample simulation case. 80

Figure 4.5 Membrane deflection mode shape. (Colors represent amplitude of deflection from no deflection for blue to maximum deflection for red) 82

Figure 5.1. Mask used for SU-8 photoresist exposure. 89

Figure 5.2. Model of the produced prototype using the microfabriaction method. 90

Figure 5.3. Micromachined channel structure. 94

Figure 5.4. Three dimensional model cut-out of micromachined micropump design assembly. 95

Figure 5.5. Schematic of the mould used to create the membrane structure. (a) Exploded view. (b) Assembled view 96

Figure 5.6. Schematic layout of the experimental setup 98

Figure 6.1. Variation of formation criterion or flow rate with formation length for different values of excitation frequency. [Dotted lines represent values of formation criterion or flow rate corresponding to a formation criterion threshold value of 2 or 0.16 as reported in the literature for 2D and axisymmetric jets respectively]. 109

Figure 6.2. Schematic of proposed mode shapes for the circular membrane used in the experimental setup. 112

Figure 6.3. Sample flow rates from numerical simulations for the base case. 114

Figure 6.4. Location of the plane used to plot the streamlines and velocity vectors shown below. 116

Figure 6.5. Details of flow rates and flow field for the base case. 120

Figure 6.6. Effect of changing the inlet channel width W_i on the flow rates and flow field of the micropump. 126

Figure 6.7. Effect of changing the outlet channel width W_o on the flow rates and flow field of the micropump. 130

Figure 6.8. Effect of changing the amplitude of excitation A on the flow rates and flow field of the micropump. 134

Figure 6.9. Effect of changing the frequency of excitation f on the flow rates and flow field of the micropump. 136

Figure 6.10. Variation of actuator membrane centerline amplitude and jet orifice area averaged velocity with time for different values of duty cycle factor k over one excitation period. 140

Figure 6.11. Effect of changing the excitation duty cycle factor k on the flow rates and flow field of the micropump. 142

Figure 6.12. Variation of the average flow rate through the micropump with the unmodified actuation amplitude at different operating frequencies for both numerical and experimental results. 145

Figure 6.13. Variation of the average flow rate through the micropump with the formation length of the synthetic jet at different operating frequencies for both numerical and experimental results. 146

Figure 6.14. Variation of pump maximum back pressure with operating amplitude (represented by the formation length) and frequency. Inlet/Outlet channel widths were set at 400 µm for all results reported in this figure. 149

Figure 6.15. Variation of pump driving power with different geometrical and operating parameters. 152

Figure 6.16. Variation of the pump volumetric efficiency with the formation length of the synthetic jet at different operating frequencies for both numerical and experimental results. 155

Figure 6.17. Comparison of micropumps based on maximum flow rate per unit pump cross-sectional area. (Singhal et al. 2004) 160

Figure 6.18. Comparison of micropumps based on (a) Maximum flow rate per unit platform area and (b) Maximum flow rate per unit outlet area for pumps reported in the literature (Iverson and Garimella 2008) 161

Figure 6.19. Comparison of flow rate vs typical size for mechanical micropumps. (Nguyen et al. 2002) (numbers indicate corresponding reference as per source) 162

FigureB.1 Laser displacement sensor calibration curve. 202

Figure B.2 Sample laser displacement sensor output signal. 203

Figure D.1. Details of flow rates and field for the case A_m = 40 µm, f = 40 Hz, W_i = 200 µm and W_o = 400 µm. 210

Figure D.2. Details of flow rates and field for the case A_m = 40 µm, f = 40 Hz, W_i = 400 µm and W_o = 200 µm. 215

Figure D.3. Details of flow rates and field for the case A_m = 20 µm, f = 40 Hz, W_i = 400 µm and W_o = 400 µm. 220

Figure D.4. Details of flow rates and field for the case A_m = 40 µm, f = 20 Hz, W_i = 400 µm and W_o = 400 µm. 225

Figure D.5. Details of flow rates and field for the case A_m = 40 µm, f = 40 Hz, W_i = 400 µm and W_o = 400 µm. 230

Figure D.6. Details of flow rates and field for the case A_m = 40 µm, f = 60 Hz, W_i = 400 µm and W_o = 400 µm. 235

Figure D.7. Details of flow rates and field for the case A_m = 60 µm, f = 40 Hz, W_i = 400 µm and W_o = 400 µm. 240

Figure D.8. Details of flow rates and field for the case A_m = 40 µm, f = 40 Hz, W_i = 400 µm and W_o = 800 µm. 245

Figure D.9. Details of flow rates and field for the case A_m = 40 µm, f = 40 Hz, W_i = 800 µm and W_o = 400 µm. 250

Figure D.10. Details of flow rates and field for the case A_m = 40 µm, f = 40 Hz, k= 0.25, W_i = 400 µm and W_o = 200 µm. 255

Figure D.11. Details of flow rates and field for the case A_m = 40 µm, f = 40 Hz, k= 4, W_i = 400 µm and W_o = 400 µm. 260

LIST OF TABLES

Table 3.1. Location of clapboards for the different test cases. (H, D and d are as shown in Figure 3.1) (Luo and Xia 2005) 66

NOMENCLATURE

a	Synthetic jet cavity dimension in the x-direction
a_o	Cross-sectional area of the jet-producing orifice
$A(t)$	Instantaneous amplitude of excitation
A_m	Peak-to-peak amplitude of membrane deflection
b	Synthetic jet cavity dimension in the y-direction
d_o	Synthetic jet producing orifice width
f	Frequency of excitation
h_o	Synthetic jet producing orifice height
I_o	Impulse per unit orifice width
k	Actuation signal duty cycle ratio
Kn	Knudson Number

L	Characteristic length scale of the flow
L_o	Synthetic jet stroke length
$M(r,\theta)$, $M(x,y)$	Membrane deflection mode shape function
Q, Q_{ave}	Pump average flow rate
Q_{max}	Pump maximum flow rate
Q_{min}	Pump minimum flow rate
r	Radial coordinate
r_c	Cavity radius
Re	Reynolds number
Re_{I_o}	Synthetic jet Reynolds number based on impulse per unit width
Re_{U_o}	Synthetic jet Reynolds number based on average orifice outflow velocity
$Re_{\overline{U}}$	Synthetic jet Reynolds number based on average orifice velocity
S	Stokes number
St	Strouhal number
t	Time
T	Period of oscillation
T_1	Actuation cycle ejection stroke duration
T_2	Actuation cycle suction stroke duration
$u_o(t)$	Area-averaged velocity at the exit plane of the orifice
u_{o_m}	Peak to peak amplitude of area-averaged orifice velocity
U_o	Synethic jet average orifice outflow velocity
$V(t)$	Instantaneous displaced volume by the membrane
V_{disp}	Displaced volume by the pump membrane
W_i	Inlet channel width
W_o	Outlet channel width

x	x-coordinate
y	y-coordinate
z	z-coordinate
$Z(r,\theta,t), Z(x,y,t)$	Instantaneous membrane deflection
Δt	Simulation time step
η_v	Pump volumetric efficiency
θ	Angular coordinate
λ	Mean free path of molecules
μ	Working fluid viscosity
ρ	Working fluid density
τ	Time of discharge during one membrane actuation cycle
ω	Angular frequency of membrane excitation

Chapter 1

INTRODUCTION

Advancements in microelectromechanical system (MEMS) devices, especially lab-on-a-chip and DNA analysis systems, have led to the realization of microfluidic systems which incorporate networks of microchannels as well as other microfluidic components. In order to move fluids in such microchannels it was necessary to develop means to pump fluids on such small scales. The first such attempts were mainly targeted on miniaturizing macro-scale pumping methods and adapting them to small scales. As physical phenomena scale differently with diminishing length scales as well as the fact that manufacturing or fabricating such devices on small scales poses a problem, it was

realized that this approach was not the most efficient way of providing pumping methods for microfluidic devices. Hence, a lot of research has since emerged investigating the use of novel micropumping techniques to provide the necessary fluid transportation. Such pumping methods range from being mechanical, electrochemical, electromagnetic or even novel techniques that were not realized before.

Mechanical micropumps, specifically vibrating membrane ones, have received a lot of attention in research due to their ability to produce significantly higher flow rates and work against higher back pressures as well as being able to accommodate a wider range of fluids. However, most vibrating membrane micropumps, being essentially positive displacement pumps, require valves to control the flow direction. Moreover, they tend to be larger in size compared to other microfluidic pumping methods due to the necessity of having a cavity, or cavities, with one or more vibrating membranes.

In recent years the concept of synthetic jets has been introduced and has received a lot of attention in the literature. Synthetic jets are jets formed due to the successive suction and blowing through an orifice backed by a cavity, as will be discussed in in this thesis. The successive suction and blowing through the cavity orifice essentially creates a jet like flow downstream of the orifice without any mass addition. Synthetic jets are mainly governed by the size of the orifice producing the jet as well as the excitation level and frequency. Early applications of macro-scale synthetic jets utilized orifice dimensions of the order of several millimeters and numerous applications were

introduced, ranging from flow control, aerodynamic shaping, jet vectoring, to heat transfer enhancement.

In 1995 the possibility of producing micro-synthetic jets from orifices with dimensions of the order of a few hundred microns was investigated. Since then several publications have investigated the possibility of producing micro-scale synthetic jets mainly using numerical methods. Moreover, a few publications have discussed possible application of micro-synthetic jets, mainly in the areas of electronic cooling and aerodynamic shaping of bodies.

As synthetic jets transfer momentum to the fluid surrounding the orifice by sucking it into the cavity and then pushing it downstream, and because they can manipulate flows that are larger in scale than the jet producing orifice, they posses the ability to perform pumping action. It is the focus of this study to investigate the possibility of producing a working micropump by utilizing the microsynthetic jet principle. As the proposed micropump utilizes the synthetic jet itself to direct the flow from the inlet to the outlet of the micropump, it does not require any valves to perform this task during the operation of the pump. Moreover, the proposed micropump utilises a membrane that is slightly smaller than those found in comparable vibrating diaphragm micropumps.

Several methods are utilized to produce microfluidic devices, most of which are adapted from methods used to fabricate electronic devices. Those methods mostly rely on using photolithography to transfer the geometry of the device from a two-dimensional mask to a photoresist material that is then etched to reveal the device geometry. In microfluidic devices, one of the most widely used methods of fabrication is called rapid prototyping which utilises photolithography to produce a mould which is then used to pattern a polymer into the required shape. Standard micromachining methods can also be utilized to machine the required geometries but mainly are restricted by the size of the cutting tools available. Both methods of fabrication have been investigated in this study to realize a prototype of the micropump. However, in this research, the photoresist material itself was used to pattern the microchannel and synthetic jet structure while the polymer, PDMS in this case, was used to make the flexible membrane structure. A standard micromachining approach was also investigated as a means of producing the micropump by milling the micropump structure in plexiglass while utilizing PDMS moulding to produce the pump membrane.

Given the fact that microfluidic structures are quite small, hence rendering traditional measuring tools such as hotwires, or pressure transducers, …etc. unsuitable, researchers had to either rely on basic macroscale measuring techniques to measure phenomena such as pressure and flow rates or they had to design and fabricate specific measuring sensors into their devices. This poses several difficulties and makes such

methods quite complicated. In the current research, measurements are performed using basic measuring techniques to measure both the flow rate and pressure as well as the membrane vibration.

1.1 Scope of the Work

The research presented in this thesis investigates the possibility of producing a working micropump using the micro-synthetic jet principle. This is realized using both numerical as well as experimental investigations to manufacture a working prototype of the proposed micropump. The commercially available software package Ansys (including ICEM and CFX) was used to perform the numerical investigations. These simulations investigated the effect of different geometrical as well as operating parameters on the performance of the proposed micropump.

Using the findings of initial numerical investigations targeted towards traditional microfabrication methods, an initial sample device was designed and fabricated based on the geometrical parameters that produced the best performance for the pump. For this design, piezoelectric actuation was utilised as the driving mechanism. Due to fabrication as well as assembly limitations, it was decided to utilize a standard micromachining approach to produce the prototype rather than microfabrication. The design was altered accordingly and numerical investigations were carried out following the new design and actuation mechanism to investigate the operating and geometrical

parameters of the pump. Electromagnetic actuation was used for the micromachined prototype.

The resulting micromachined prototype was experimentally investigated and the results obtained were used to validate the numerical simulations which were then used to provide a deeper insight into the performance of the micropump for different geometrical and operating conditions.

1.2 Thesis Outline

This thesis consists of 7 chapters including the introduction (Chapter 1) and conclusion (Chapter 7). In chapter 2, the available literature concerning the different aspects covered in this research is discussed. This includes the literature discussing both macro- and micro- synthetic jets and their applications, micropumping methods and their performance. The proposed micropump design is introduced in Chapter 3 along with the directly related literature that addresses a similar approach to producing a working micropump. Chapter 4 introduces the numerical simulations performed and discusses the model, meshing, boundary conditions and operating parameters. The design and fabrication of the prototype is discussed in chapter 5, including both designs used for the microfabrication approach and the micromachining method. The chapter also details the experimental setup used to test the performance of the micropump prototype. The results of both the numerical and experimental investigations are

analyzed in chapter 6. The thesis concludes with chapter 7 which summarizes the findings of this thesis as well as the contributions to the state of knowledge and suggestions for future work.

Chapter 2

LITERATURE REVIEW

This chapter provides a survey of the literature related to the topics covered in this thesis starting with an introduction to micro-flow characteristics as compared to macro-flows. Following that, micropumping technologies and macro- and micro-synthetic jets will be discussed.

2.1 Microflow Characteristics

Rapid advancements in the field of microfabrication and the production of microfluidic devices did not allow for thorough analysis of the underlying physics involved with the flow of fluids in such small-scale devices. Often classical theories which have proven to be adequate to describe macro flows are used to deal with micro flows, however, they don't seem to correctly predict the behaviour of such flow systems in some cases. As a result, researchers have begun modifying the classical known theories or develop new ones to better understand the governing flow physics which describe the flow of fluids in microscale devices. (Gad-el-Hak 2002)

This section briefly touches upon the main key features that are required to better understand the behaviour of fluids on the microscale. These features are discussed in detail in several textbooks and review papers (Gad-el-Hak 2002; Nguyen and Wereley 2006; Gravesen et al. 1993; Ho and Tai 1998; Gad-el-Hak 1999).

2.1.1 Volume vs. Surface Forces

The length scale of a flow device is a fundamental measure that dictates the type of forces that control the behaviour of such device or flow. Forces mainly scale with either the volume of the body under investigation, i.e. body forces, or with its surface area, i.e. surface forces. As body forces scale with the volume, or L^3, and surface forces scale with the area, or L^2, an important parameter to govern the dominance of one set

of forces over the other is the surface to volume ratio. For example, a device with a characteristic length scale of the order of 1 m would have a surface to volume ratio of 1 m^{-1} while a device with a scale of 1 µm would have a surface to volume ratio of 10^6 m^{-1}. This huge increase in the surface to volume ratio would lend the dominance of surface forces over body forces in microflows. Surface forces that dominate in such small scales include: intermolecular forces, or Van der Waals forces, surface tension, electrostatic forces, electrokinetic and electroosmotic forces.

2.1.2 Knudson Number & the continuum assumption

Conventional fluid mechanics theory deals with fluids on the macroscale as a continuum, whereby the fluid is assumed to be continuous and its properties are defined at each point within the fluid in space and time. This approach assumes the fluid to be formed of elements that are large enough compared to the microscopic structure of the fluid but small enough with respect to the macroscopic length scale of the flow phenomena to allow the use of differential calculus to describe its behaviour.

An intuitive approach to dealing with microfluid flows is to use the same tools used for macrofluid flows such as the Navier-Stokes equations and the no-slip boundary conditions. Since these tools hold as long as the continuum assumption is valid, scaling down of the characteristic length scale of the flow raises a question to whether the continuum assumption still holds. This is more evident when dealing with gas flows, as

gases have a relatively large mean free path between its molecules. Hence, as length scales go down, fewer molecules would be present in a certain volume of fluid and the continuum assumption may no longer be valid. A measure of the relative magnitude of the mean free path of the molecules of a certain fluid to the characteristic length scale of a flow is given by the Knudson Number

$$\mathrm{Kn} = \frac{\lambda}{L} \qquad [2.1]$$

where λ is the mean free path of the molecules and L is the characteristic length scale of the flow. The Knudson number describes how far apart the fluid molecules are relative to the characteristic length scale of the flow. The Knudson number divides fluid flows into five main regimes as follows:

- For $\mathrm{Kn} \to 0$ $(\mathrm{Re} \to \infty)$ Euler equations are used to model the flow (inviscid flow) and molecular diffusion is neglected;
- For $\mathrm{Kn} < 10^{-3}$ the Navier-Stokes equations hold as well as the no-slip boundary conditions;
- For $10^{-3} < \mathrm{Kn} < 10^{-1}$ the Navier-Stokes equations hold but the no-slip boundary condition is not valid and slip occurs at the boundaries of the flow;
- For $10^{-1} < \mathrm{Kn} < 10$ is a transitional region where the continuum approach starts to fail and free molecular flow is used to describe the fluid flow;

- For $\mathrm{Kn} > 10$ the continuum assumption is no longer valid and molecular based formulation of the fluid flow is required to model the behaviour of the fluid.

It should be noted here that the Knudson number approach is valid only for gas flows. Liquids, on the other hand, are in a state of continuous collision and hence behave differently than gases. The concept of mean free path is not very beneficial in the case of liquid flows and the use of a Knudson number is not relevant. Moreover, the molecular theory for liquids is not well developed as that for gases and hence no rigorous understanding of the conditions under which liquids fail to behave as a continuum is available. A simple comparison, however, of the compactness of the molecules in the case of liquids to that of gases would suggest that liquids will tend to fail the traditional fluid mechanics approach at much smaller scales than in the case of gas flows. (Gad-el-Hak 2002; Nguyen and Wereley 2006)

2.2 Micropumps

Recent advancement in microfabrication techniques facilitated the fabrication of MEMS (MicroElectroMechanical Systems)-based microfluidic systems. These systems have a very wide range of applications including, but not limited to, cooling of electronic circuits, lab-on-a-chip applications, drug delivery, flow control, inkjet printers … etc (Gad-el-Hak 2002; Nguyen and Wereley 2006) Early investigations into MEMS devices mostly utilized macro-scale pumping methods to provide the pumping action required

for the devices through the use of externally pressurized tanks, syringe pumps, pipettes or other similar means. However, such methods negate the benefits of making MEMS devices as they make such systems cumbersome and not integrated. Hence, the necessity of finding integrated micropumping methods became evident.

The main components of any microfluidic system, as in a typical fluid flow system, are channels, pumps, valves, mixers, sensors and actuators. The need for methods to transport fluids in microchannels has become a primary concern for the success of such systems. Scaling down of macroscale pumps has proven to be inadequate, as different physical phenomena cease to be important on the small scale. Hence, the need for new pumping technologies is apparent.

A substantial amount of research has been carried out in developing micropumping techniques over the past few decades and a lot of review papers and books have been published discussing advancements in micropumping (Nguyen and Wereley 2006; Iverson and Garimella 2008; Nguyen et al. 2002; Gravesen et al. 1993; Shoji, Shuchi and Esashi 1994; Singhal et al. 2004; Woias 2005; Laser and Santiago 2004). The majority of the literature surveying micropumps classifies them according to operating principle into either mechanical, necessitating moving parts to transfer energy to the flow, or dynamic or non-mechanical, utilizing some form of direct energy transfer to the flow to increase its momentum or pressure. In the current discussion, micropumps will be categorized according to the operating principle into two main

categories as being either mechanical micropumps or non-mechanical ones. In the following sections, a brief discussion of the different types of micropumps presented in the literature will be provided with a few examples and then a concluding section will follow with a comparison summary of different pumps reported in the literature:

2.2.1 Mechanical Micropumps:

This class of micropumps comprises of devices that utilize moving parts within the device to transfer mechanical energy to the working fluid causing the pumping action. This class can be further divided into three categories; namely: Rotary (dynamic), Vibrating diaphragm or Fluid displacement micropumps as discussed below. This category of micropumps, especially those pumps within the rotary and vibrating diaphragm categories, closely resembles most commonly used macroscale pumping methods including centrifugal, gear, and positive displacement pumps.

2.2.1.1 Rotary

Rotary micropumps represent the first attempts to miniaturize macroscale pumping methods. They rely mainly on rotating geometries such as gears, vanes or blades inside a confined chamber to transport fluid from the inlet port to the outlet port. Due to the fact that they usually are quite bulky in size as well as difficult to microfabricate adding to the fact that viscous forces increase significantly with reduction in size and hence require large amounts of power to operate, this type of

micropumps did not receive a lot of attention in the literature. Below is a brief description of some examples found in the literature for rotary micropumps.

Figure 2.1 presents schematics of examples reported in the literature for this class of micropumps. Figure 2.1.a shows a micropump using a magnetically driven micromotor to drive the pump rotor (Ahn and Allen 1995). A two-gear rotary micropump is shown in Figure 2.1.b (Dewa et al. 1997; Deng et al. 1998). An internal gear micropump as shown in Figure 2.1.c consisting of two gears with the inner gear having six teeth while the outer one has seven. As the gears rotate relative to one another, the volume trapped between them changes driving the fluid from the inlet to the outlet ports. Hatch et al. (2001) utilized the motion of a plug of ferrofluid due to its interaction with a translating magnetic field, caused due to the rotation of a permanent magnet to induce the pumping action as shown in Figure 2.1.d.

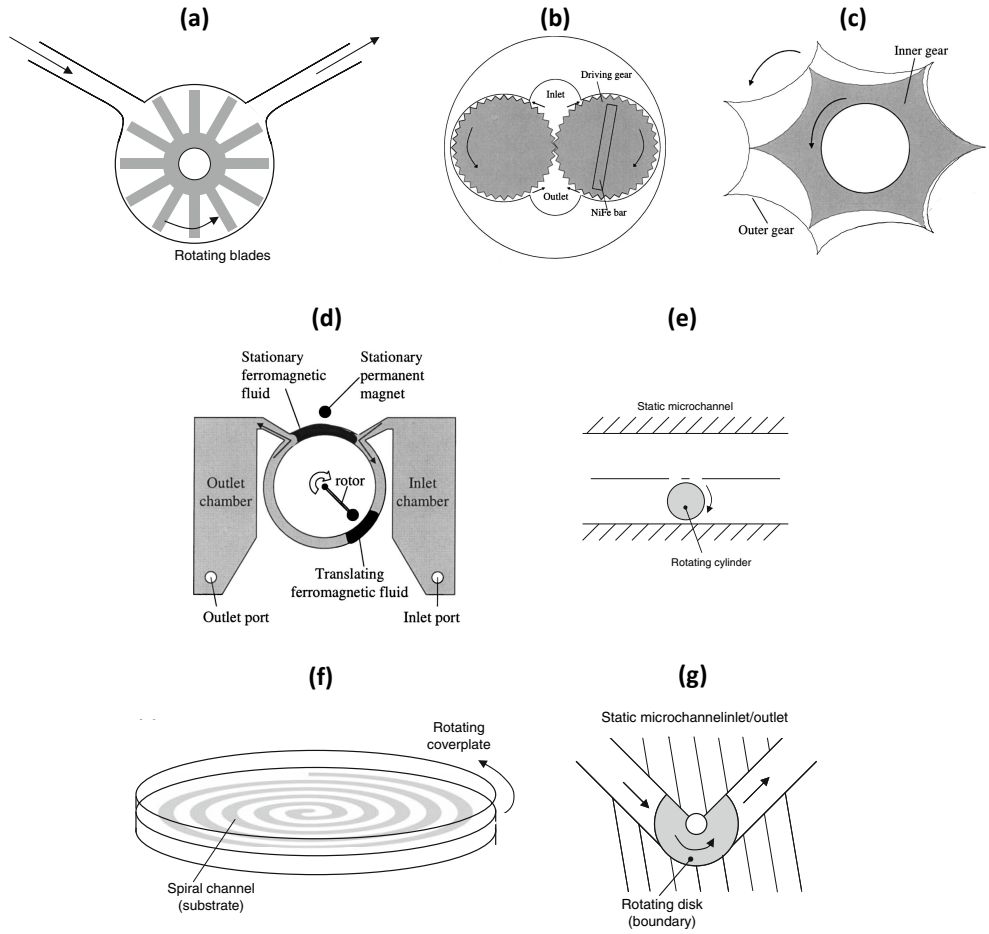

Figure 2.1. Examples of rotary micropumps. (a) Rotary blade micropump. (Ahn and Allen 1995); (b) Two-gear rotary micropump. (Dewa et al. 1997; Deng et al. 1998); (c) Internal gear rotary micropump. (Weisener et al. 1996); (d) Ferrofluid rotary micropump. (Hatch et al. 2001); (e) Continuous transverse-axis rotary pump. (Sen et al. 1996; Sharatchandra et al. 1997); (f) Spiral-channel rotary micropump. (Kilani et al. 2006); (g) Disk viscous rotary micropump. (Blanchard, D. et al. 2005)

Other types of rotary micropumps rely on viscous fluid forces to move the fluid. Figure 2.1.e shows an example of a micropump that depends on the fact that a rotating body, placed asymmetrically inside a duct, will generate a net flow through that duct (Sen et al. 1996; Sharatchandra et al. 1997). Multiple rotors and different channel

geometries were also reported in the literature (Abdelgawad et al. 2005; Da Silva et al. 2007). The rotation of the top surface of a spiral shaped channel as shown in Figure 2.1.f to induce viscous forces in the fluid causing its motion towards the outlet was also investigated numerically (Kilani et al. 2006; Al-Halhouli et al. 2007; Haik et al. 2007). Similarly, disk viscous micropumps, as shown in Figure 2.1.g generate the pumping action by using the rotation of a disk that acts as part of the pump boundary (Blanchard, D. et al. 2005).

2.2.1.2 Vibrating diaphragm micropumps

Vibrating diaphragm micropumps are positive displacement micropumps that incorporate a cavity bounded on one or more sides by a vibrating membrane as seen in Figure 2.2. On the other side, there are usually two openings, an inlet and an outlet port. The inlet and outlet ports are used as flow rectification devices to move the flow in one direction and not the other. During the suction part of the pumping cycle, the membrane moves outwards increasing the volume of the cavity and decreasing its pressure, thus allowing fluid to enter the cavity through the inlet. In the pumping part of the cycle, the membrane moves inwards decreasing the cavity volume and increasing its pressure, thus forcing the fluid inside the cavity to exit through the exit port.

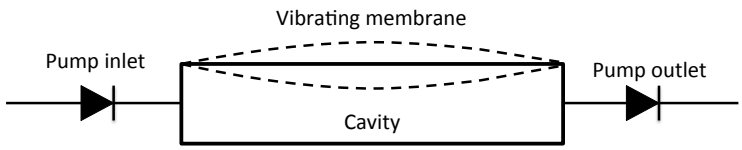

Figure 2.2. Schematic of a vibrating diaphragm micropump.

Vibrating diaphragm micropumps have received a lot of attention in the literature mainly due to their simple designs in comparison to other mechanical micropumps, their ability to accommodate a wider range of working fluids as well as their higher produced flow rates and pressures they can work against. This category of micropumps can be further categorized according to either their actuation mechanism as well as according to the mechanism of flow rectification used at the inlet and outlet ports. Several actuation mechanisms have been reported in the literature, such as piezoelectric, electrostatic, electromagnetic, pneumatic, and thermopneumatic. According to flow rectification, vibrating diaphragm micropumps can be either valved or valveless.

2.2.1.2.1 Piezoelectric

Piezoelectric materials generate internal mechanical stresses, and hence resulting strains, in the presence of an applied electric potential, and vice versa. This is probably the most widely used actuation mechanism for vibrating diaphragm micropumps. The piezoelectric material can be bonded to, deposited on or embedded in the diaphragm. An applied AC voltage drives the expansion and compression strokes due to the changing signal polarity. However, in order to achieve large displacements from

piezoelectric elements, usually bulky actuators have to be used, as usually miniaturized actuators will only be capable of producing small motions.

In 1988 Van Lintel et al (1988) presented the first piezoelectrically actuated vibrating diaphragm micropump which uses diaphragm type passive check valves as shown in Figure 2.3. Similarly, several other micropumps utilizing a similar approach have been reported with varying geometries, configurations or valve designs (Esashi et al. 1989; Carrozza et al. 1995; Koch, Harris, et al. 1998; Koch et al. 1997; Cunneen et al. 1998; Stemme, E. and Stemme 1993). Shoji et al (1990) used a similar design to produce two kinds of rippleless pumps. The first pump consists of two pumps connected in parallel and actuated with complementary periodic signals. In the second design the micropump is connected to a buffer in series which is driven complementary to the pump action, such that in the pumping mode it absorbs part of the outlet flow and pumps it out in the suction mode.

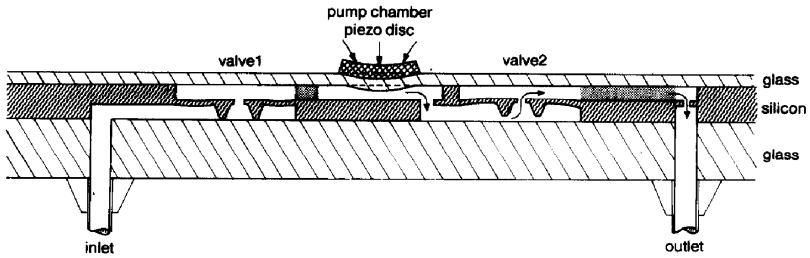

Figure 2.3. Vibrating diaphragm micropumps with passive check valves fabricated in silicon/glass. (Van Lintel et al. 1988)

Piezoelectrically actuated micropumps which utilize the pump diaphragm as a means for flow rectification were also reported in the literature. The diaphragm closes the inlet port during the pumping stroke, while both the inlet and outlet ports stay opened during the suction stroke. The pumps can accommodate both liquids and gases and are bi-directional (Stehr et al. 1996; Zengerle et al. 1995; Nguyen et al. 1998). Self-priming designs require the minimum possible dead chamber volumes and higher compression ratios in order to be able to prime the pump. Kamper et al (1998) introduce a self-priming micropump capable of pumping both liquids and gases with a very small chamber volume when the actuator is at rest. Following a similar approach Linnemann et al (1998) produced a self-priming micropump using a piezoelectric actuator glued to a thin silicon membrane.

Olsson et al (1995) produced a piezoelectrically actuated nozzle/diffuser micropump with two pumping chambers operating in parallel. Olsson et al (1996; 1997) further investigated their design by producing a miniaturized version of their pump with a 6 mm diameter pumping chamber and used it to investigate the effect of nozzle/diffuser element length on the performance of the pump. Olsson et al (1998) also produced another pump using thermoplastic replication for cheaper fabrication costs and it used a single pumping chamber. Large angle nozzle/diffuser elements were also used as the rectification mechanism. This resulted in the rectification effect being

opposite to elements with small diffuser angles (Koch, Evans, et al. 1998; Gerlach et al. 1999).

Matsumoto et al (1999) introduced a piezoelectrically actuated bidirectional valveless micropump using a rectification principle based on the temperature dependence of liquid viscosity resulting in variation in flow resistance. The pumping chamber is connected to the inlet and outlet ports through small cross-section chokes as shown in Figure 2.4. Boron-doped silicon heaters locally heat the inlet and outlet chokes. During the delivery stroke, the outlet choke is heated causing the local viscosity of the liquid at the outlet to decrease and hence more liquid goes out of the outlet than the inlet, and vice versa.

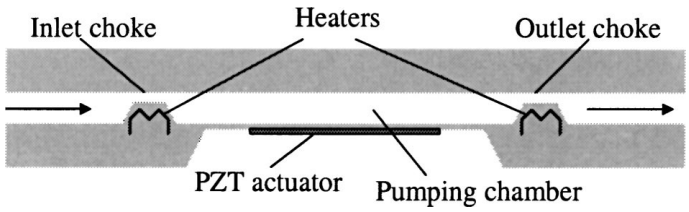

Figure 2.4. Valveless piezoelectrically actuated micropump using temperature dependent fluid viscosity for flow rectification. (Matsumoto, S. et al. 1999)

Forster et al (1995a) and Gamboa et al (2005) introduced valveless piezoelectrically actuated vibrating diaphragm micropumps using valvular conduits for flow rectification. Valvular conduits utilize different pressure drop characteristics for flow in opposite directions to cause flow rectification.

2.2.1.2.2 Electrostatic

Electrostatic actuation has received comparatively less attention in the recent micropump literature than piezoelectric actuation. Electrostatically actuated micropumps utilize the electrostatic forces generated between two electrodes of different charge to drive the diaphragm motion (Zengerle et al. 1992). When an electrical voltage is applied between an electrode and the pump diaphragm, the other electrode, electrostatic forces are generated as both electrodes act as a variable capacitor causing movement of the membrane. When the voltage is removed, the membrane returns to its original position, thus causing the pumping action as shown in Figure 2.5.i. A bidirectional micropump with a similar design was also reported that relies on the phase shift occurring between the operation of the valves and the diaphragm when the diaphragm is activated at frequencies higher than the first resonance frequency of the valves (Zengerle et al. 1995).

A dual-diaphragm bidirectional gas micropump utilizing electrostatic actuation was introduced by Cabuz et al (2001). The pumping chamber is shaped so that when the membranes are fully deflected they conform to the wall they are touching as shown in Figure 2.5.ii. Both walls and both diaphragms have insulated metal electrodes on them which are controlled and actuated separately. The pumping cycle starts with both electrodes on the inlet side. Both electrodes are moved together towards the outlet and thus expelling the fluid in the cavity out. This is followed by moving the lower

membrane towards the inlet allowing the fluid to move through the holes in the membrane to the space created between the electrodes. The upper membrane is then moved downwards and the air trapped between the electrodes moves to the space created at the top through the opening in the upper electrode and the cycle starts over again.

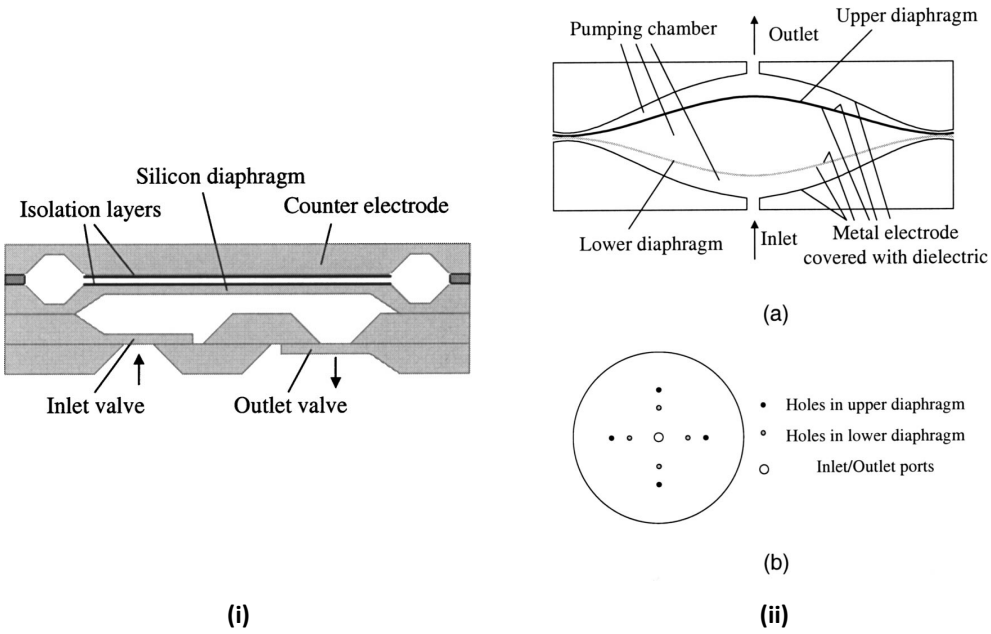

Figure 2.5. (i) Electrostatically actuated micropumps (Zengerle et al. 1992);
(ii) Dual-diaphragm electrostatic micropump (Cabuz et al. 2001):
(a) Sectional side view, (b) Top view through chamber.

Recent advancements have been considered where the counter electrode is placed on the opposite side of the pumping chamber and the voltage is applied across the liquid working fluid to take advantage of the higher relative electrical permeability of fluids as compared to the air gap utilized in the traditional method (Machauf et al.

2005). This results in higher electrostatic forces and hence higher flow rates for the same applied voltage and geometry.

2.2.1.2.3 Electromagnetic

In this method of actuation, a permanent magnet is usually embedded or attached to the vibrating diaphragm and surrounded by a coil. When an alternating current passes through the coil, the generated Lorentz forces cause the membrane to vibrate (Gong et al. 2000; Khoo and Liu 2001; Kallenbach 1999; Jiang et al. 1998). Bohm et al (1999) introduced a magnetically actuated vibrating diaphragm micropump with membrane type passive valves using a permanent magnet attached to the diaphragm and surrounded by a coil. They tested the same pump using piezoelectric actuation as well using a piezoelectric disc glued to a brass diaphragm. Although the piezoelectric version was smaller in size, easier to fabricate and had lower power consumption, the electromagnetic version used a lower actuation voltage, and a simpler design for the driver electronics.

2.2.1.2.4 Thermopneumatic

Thermopneumatically actuated vibrating diaphragm micropumps utilize the increase in the pressure of air trapped in a chamber caused by heating the air to deflect the vibrating diaphragm. When the heaters are switched off, the air contracts and its pressure decreases causing the membrane to return to its original shape and hence causing the pumping action. Thermopneumatically actuated micrpumps have an

advantage over piezoelectically actuated ones in that they do not require the alignment process that is sometimes necessary in order to fix the piezoelectric actuator to the membrane. However, they suffer from the drawback that they usually require much lower operating frequencies to allow for the cooling of the air in the pumping chamber (Van de Pol et al. 1990; Wego and Pagel 2001; Jeong and Yang 2000a; 2000b).

2.2.1.2.5 Shape memory alloy

In this class of vibrating diaphragm micropumps the shape memory effect of some alloys like TiNi is utilized in the membrane actuation. TiNi transforms from one solid phase, the low temperature martensite phase, to another solid phase, the high temperature austenite phase, when heated to a certain transformation temperature. The martensite phase has a higher ductility than the austenite phase and TiNi can undergo large deformations when in this phase. However, when heated to the transformation temperature, TiNi transforms to the austenite phase and returns to its initial undeformed shape or exerts large forces in trying to assume the initial shape if constrained. Hence, this shape memory effect can be used as an actuation mechanism for the pump membrane. As with the case of thermopneumatically actuated micropumps, this category of micropumps suffers from the necessity of using very small frequencies as they rely on the relatively slow cooling process of the shape memory alloy. Several publications have reported on the properties and behaviour of TiNi shape

memory alloy thin films. (Benard et al. 1998; Xu et al. 2001; Makino et al. 2001; 1999; Makino, Mitsuya, and Shibata 2000a; 2000b; Krulevitch et al. 1996)

2.2.1.2.6 Other

Other methods of actuation have been reported in the literature pertaining to vibrating diaphragm micropumps but have not received considerable attention in the literature. Photothermopneumatically actuated micrpumps rely on the same principles as a thermopneumatically actuated pumps but the heating process of the air is achieved by using a laser beam directed at a patch of carbon wool which absorbs the light and transforms it into heat (Mizoguchi et al. 1992). Magnetostricitve actuation depends on the change in shape of some materials under the influence of an external magnetic field (Quandt and Seemann 1995; Body et al. 1997; Quandt and Ludwig 2000).

2.2.1.2.7 Rectification Mechanism

Vibrating diaphragm micropumps require a rectification mechanism to direct the flow from the inlet to the outlet ports of the pump. This is usually achieved by either mechanical dynamic valves or through using valveless static rectification mechanisms.

Valved micropumps rely on dynamic geometry check valves which utilize deformation, deflection, or motion to perform flow rectification. They can also be divided into being either active or passive. Active valves require an external power source to achieve the rectification process. Passive ones do not require external power

sources. Vibrating diaphragms, for instance, as those discussed above for the actuation of micropumps can be also used as valves by being used to block or open the inlet/outlet ports of a pump during its operation and are usually actuated in synchronicity with the pump actuator.

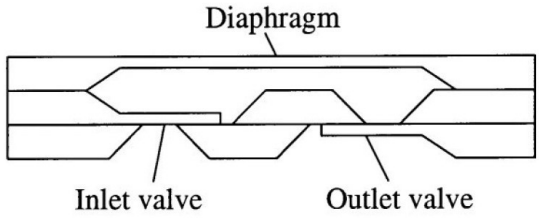

Figure 2.6. Example of a valved vibrating diaphragm micropump. (Singhal et al. 2004)

Passive check valves, especially the cantilever type such as that shown in Figure 2.6, are probably the most widely used valve mechanism. These valves use cantilevered structures designed to open or close in a certain direction depending on the differential pressure across them. Cantilever type valves can be either passive, where they are driven by the pressure difference across them and prevented from operating in the opposite direction by geometrical means, or active by using RF or piezoelectric modulation (Dissanayake et al. 2007). From the micropump designs discussed above various valve designs were utilized such as membrane type check valves (Van Lintel et al. 1988; Esashi et al. 1989; Shoji, Shuichi et al. 1990; Böhm, Olthuis, et al. 1999; Kamper et al. 1998), cantilever type check valves (Zengerle et al. 1995; 1992; Xu et al. 2001; Makino et al. 2001; Koch et al. 1997; Koch, Harris, et al. 1998; Linnemann et al. 1998),

ball valves (Carrozza et al. 1995), and a design that uses the pump membrane itself for flow rectification (Stehr et al. 1996; Nguyen et al. 1998; Cabuz et al. 2001).

All valve designs discussed here suffer from the risk of fatigue due to prolonged periods of use, adhesion due to the valves not releasing from their seats as well as from leakage especially when working with fluids that contain particles that can get stuck around the valve or its seat and hence prevent the valve from fully opening or closing. Moreover, due to their dynamic nature, their response times must be taken into consideration when designing the operating parameters, especially the frequency, of the pump. However, since they provide actual physical obstructions to the flow they are not prone to reversed flow and can withstand higher adverse pressures than other kinds of flow rectification devices.

Valveless micropumps rely on other means of directing flow than moving parts. They mainly rely on either geometrical properties of some geometries that depend on the favoured directionality of the flow due to fluid inertia and thus are passive in nature. Others rely on the addition of energy to alter the directionality of flow and as such are active. Valveless designs have the advantage of being able to accommodate fluid flows with suspended particles as they are less susceptible to blockage and clogging. Moreover, they do not have moving parts and thus do not suffer from wear or fatigue as with the case of check valves. They, on the other hand, have the drawback of reversed

flow as well as being inherently irreversible in nature where they cannot be used to perform rectification or pumping if the direction of flow is reversed.

The most commonly used configuration for passive valveless designs utilize nozzle/diffuser elements, as those shown in Figure 2.7.a. The rectification principle lies in the fact that, for small angle nozzle-diffuser elements, with half angles up to 10°, the flow rate is higher in the diffuser direction than in the nozzle direction for the same pressure drop. Nozzle/diffuser elements have gained a lot of attention in the literature in order to better understand their behaviour and performance and have been studied numerically, analytically and experimentally (Gerlach and Wurmus 1995; Olsson, Stemme, et al. 1996; Heschel et al. 1997; Gerlach 1998; Olsson et al. 2000). They have also been utilized for different designs of micropumps as presented in the previous sections (Stemme, E. and Stemme 1993; Olsson et al. 1995; Olsson, Enoksson, et al. 1996; Olsson, Larsson, et al. 1997; Olsson et al. 1998; Jiang et al. 1998; Jeong and Yang 2000a; 2000b).

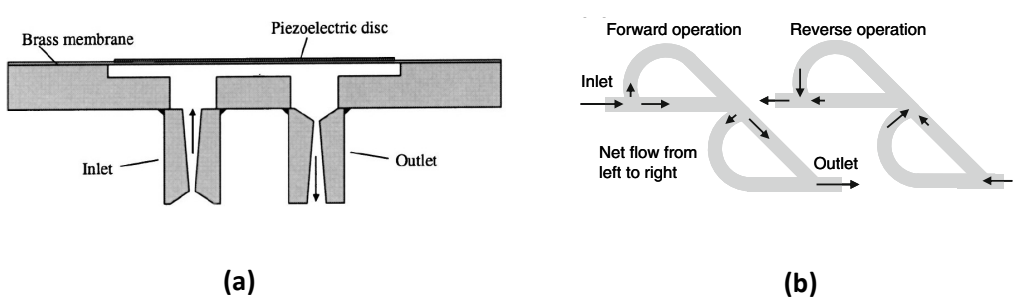

Figure 2.7. Examples of valveless flow rectification mechanisms. (Iverson and Garimella 2008) (a) A valveless micropump using Nozzle/diffuser elements. (Stemme, E. and Stemme 1993) (b) Tesla (valvular conduit) valves (Tesla 1916)

Large angle nozzle/diffuser elements were also utilized in the literature with half angles of the order of 35°. However, at these large angles the roles of the diffuser and nozzle elements are reversed with flow being favoured in the nozzle direction. This is attributed to flow separation occurring in the diffuser direction and hence a higher pressure loss coefficient. These have been utilized in the literature as discussed earlier (Gerlach et al. 1999; Koch, Evans, et al. 1998)

Other methods of valveless flow rectification has been utilized in the literature. One such example is the use of active valveless flow rectification by exploiting the temperature dependence of the local fluid viscosity resulting in the change in fluid resistance. This change is achieved by locally heating the fluid at the inlet or outlet ports depending on the actuation stroke. This method was utilized by Matsumoto et al (1999).

Other geometrical rectification mechanisms used were Tesla valves (valvular conduits) (Tesla 1916), shown in Figure 2.7.b. These valves are bifurcated channels in which, when operating in the reverse direction, flow is separated from the main flow and re-enters the main channel perpendicularly. These valves have been studied in the literature in order to optimize their performance (Gamboa et al. 2005) and have been utilized in micropump designs (Forster, Bardell, Afromowitz, Sharma, and Blanchard 1995b; Bardell et al. 1997; Jang, L. S. et al. 2000; 1999).

2.2.1.3 Peristaltic micropumps

This type of micropumps utilises the operation of a series of actuators in series to induce the pumping action using peristaltic motion. The minimum required number of actuators to be able to cause peristaltic pumping is three and most of the work cited in the literature uses three chambers with diaphragm actuators in series as can be seen in Figure 2.8 (Singhal et al. 2004; Nguyen and Huang 2001). Most peristaltic micropumps are reversible by reversing the order of actuation of the diaphragms. Given the fact that most peristaltic micropumps are essentially vibrating diaphragm ones with multiple chambers, pretty much the same actuation principles can be used to operate them.

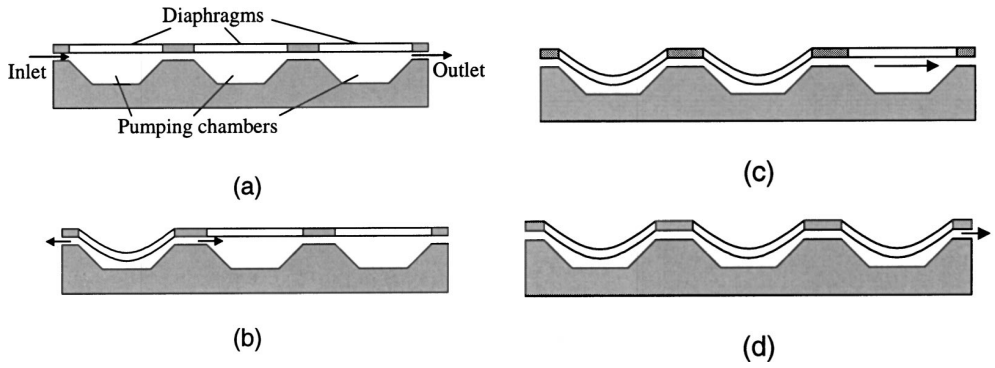

Figure 2.8. Sequence of operation of a peristaltic micropump. (Singhal et al. 2004)

One of the early works discussing micropumps in the literature was the work of Smits (1990) discussing a peristaltic micropump for insulin delivery applications. Grosjean and Tai (1999) discuss a thermopneumatically actuated peristaltic micropump. The pump uses island heaters suspended in cavities filled with a fluid and bounded on one side by the membrane and the other by a glass back plate as shown in Figure 2.9.

The pressure inside any of the cavities increases when the heater in that cavity is turned on and causes the membrane of that chamber to deflect pushing the working fluid to the next chamber.

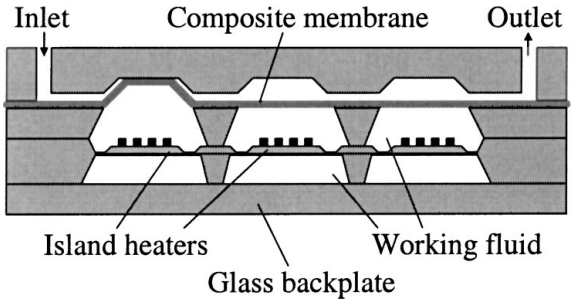

Figure 2.9. Thermopneumatically actuated micropump. (Grosjean and Tai 1999)

Cao et al (2001) demonstrated a normally closed piezoelectrically actuated peristaltic micropump used for microdosing applications. This is achieved by attaching valve closers to the membranes of the first and last pumping chambers which block the inlet and outlet valves when the membranes of those chambers are not actuated. When the membrane is actuated, it deflects and the valve closer moves away opening the corresponding port.

A photothermopneumatically actuated peristaltic micropump was investigated by Mizoguchi et al (1992). The pump uses the same principles as the pneumatically actuated micropumps with the heating of the fluid in the pneumatic chamber achieved by subjecting a piece of carbon wool (a material that absorbs light and converts it to heat) to a laser beam through an optical fibre.

2.2.2 Non-Mechanical Micropumps

This group of micropumps relies mostly on the direct transfer of energy to the fluid causing the pumping action. As such, this class of devices usually provides continuous, steady flow rates due to the constant transfer of energy. This category of micropumps can be further divided into several categories as seen in the following sections. It should be noted that most dynamic micropumps are valveless as they rely on the directionality of the applied force to determine the flow direction.

2.2.2.1 Electrokinetic and Magnetokinetic:

Electrokinetic and magnetokinetic micropumps convert either electrical or magnetic energy, respectively, directly into fluid motion. Electrokinetic pumps utilise an electric field applied to the fluid being pumped to cause ions within the fluid to move in reaction to the applied electric field while dragging the bulk of the fluid with it by momentum transfer due to viscous forces. Magnetokinetic pumps utilize Lorentz forces generated due to the pumped fluid being subjected to a magnetic field to drive the pumping action. Electrohydrodynamic micropumps rely on the interaction between electrostatic forces with ions in dielectric fluids. The main distinction between the different types of EHD micropumps is the mechanism used to introduce charged particles into the pumped fluid.

In induction-type EHD pumps a gradient in either the electrical conductivity or permittivity of the working fluid is created by either anisotropic heating of the fluid or by using layers of non-mixing fluids or with suspended particles in the fluid. When an alternating electric field is applied to electrodes on the walls of the microchannel, it induces charges in the fluid which exhibit coulomb forces. These forces cause the charges in the fluid to move and the bulk of the fluid then moves due to viscous effects. Induction-type EHD micropumps depend on the electrical properties of the fluid, such as the conductivity and permittivity. This limits the choice of fluids being able to be used in such designs, generally to non-conducting or non-ionic fluids such as alcohols and organic liquids (Woias 2005). The main advantage of induction EHD lies in part in the ability of fabricating the pump components using standard surface micromachining techniques directly in the fluid microchannels. Several examples of induction-type EHD micropumps are found in the literature (Bart et al. 1990; Fuhr, Hagedorn, Müller, Benecke, and Wagner 1992b; 1992a; Fuhr et al. 1999; Moesner and Higuchi 1995).

In injection-type EHD micropumps, free ions are injected into the bulk of the liquid due to electrochemical reactions at the electrodes. Due to the presence of the external electric field, the ions experience Coulomb forces which result in the movement of ions. The motion of the ions in turn drags the bulk of the fluid due to viscous effects. Injection-type EHD micropumps are usually used with low-conductivity fluids such as

some organic fluids and non-polar fluids. (Richter and Sandmaier 1990; Richter et al. 1991; Wong et al. 1996; Darabi and Wang 2005; Go et al. 2007)

Polarization-type EHD micropumps utilize non-homogeneous electric fields through dipolar fluids which lead to the creation of a variation in the electric field density. This results in motion of the dipoles in the fluid from regions of low electric fields, and hence higher dipole energy, to regions of high electric fields, with lower dipole energies causing the pumping action. (Darabi et al. 2001; Moghaddam and Ohadi 2005; Darabi and Wang 2005).

Electroosmotic micropumps utilize the surface charge that develops on the contact surface between a liquid and the surface of the channel. This surface charge can spontaneously develop on the surface or be artificially introduced using surface electrodes and in both cases oppositely charged ions in the fluid form a shielding layer that shields the surface charge. This layer can be manipulated using either AC or DC electric fields. DC electroosmotic micropumps have received considerable attention in the literature due to their simple construction. They can be constructed using glass or fused silica capillary tubes or channels with electrodes at both ends of the channel to provide the electrical field along the length of the channel as seen schematically in Figure 2.10.a. They face some challenges, however, as they require electrolytic solutions and usually require considerable electric fields and hence high voltages and currents, this in turn causes problems of bubble generation and electrolysis and reactions at the

electrodes. Some of these problems can be avoided by using electroosmotic pumps in series or parallel. (Zeng et al. 2001; Zheng et al. 2000; Zeng et al. 2002; Chen, Z. et al. 2005; Chen, L. et al. 2005; Kang et al. 2007; Piyasena et al. 2006; Brask et al. 2005; Broderick et al. 2005; Iverson et al. 2004)

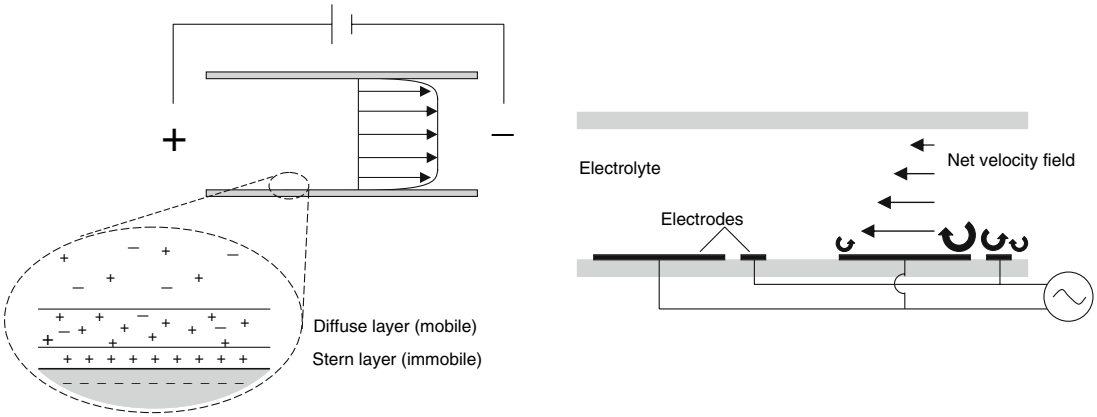

Figure 2.10. Schematic of electroosmotic micropumps. (a) DC electroosmotic micropump. (b) AC electroosmotic micropump.

AC electroosmotic micropumps have received increasing attention in the literature recently. They are capable of producing higher flow velocities for smaller operating voltages than DC electroosmotic micropumps. They rely on having electrodes on the surface of the flow channels to provide the charges to establish the electrical double layer as shown schematically in Figure 2.10.b. Most commonly, asymmetric electrodes are used to induce the electric field and cause the motion of the diffuse layer charges along the surface of the electrodes. Bidirectional operation of such micropumps is also possible. (Debesset et al. 2004; Mpholo et al. 2003; Garcia-Sanchez et al. 2006; Vijendran et al. 2006; Urbanski et al. 2006; Jie Wu 2006)

Magnetohydrodynamic micropumps rely on the Lornetz force generated when a current-carrying conductor is placed in a magnetic field. When a conducting fluid flows inside a channel with electrodes on one set of opposite channel walls and magnets on the other opposite channel walls as shown in Figure 2.11, the fluid is subjected to a force acting along the length of the channel which causes the pumping action. (Lemoff et al. 1999) Several designs have been reported in the literature using the same principle of operation. (Lemoff and Lee 2000; Heng et al. 1999; 2000; Jang, J. and Lee 2000; Duwairi and Abdullah 2007; Patel and Kassegne 2007; Homsy et al. 2007) MHD micropumps suffer from the drawback of requiring electrically conducting fluids as well as being prone to Joule heating and electrolysis.

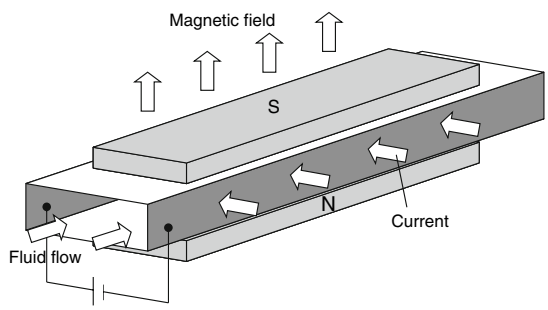

Figure 2.11. Schematic of a magnetohydrodynamic micropump.
(Iverson and Garimella 2008)

2.2.2.2 Phase change:

This class of micropumps relies on the change in the phase of the liquid being pumped to perform the pumping action. Bubble pumps utilize the successive operation of independently controlled heaters placed along the length of the flow channel as

shown in Figure 2.12.a to generate a vapour bubble in the fluid and convect it downstream causing the pumping action. This convection is due to the change in surface tension and vapour pressure gradients caused by the action of the heaters. (Jun and Kim 1996) Other actuation mechanisms for bubble pumps have been reported in the literature (Jun and Kim 1998; Ozaki 1995; Sammarco and Burns 2006; Geng et al. 2001; Tsai and Lin 2002)

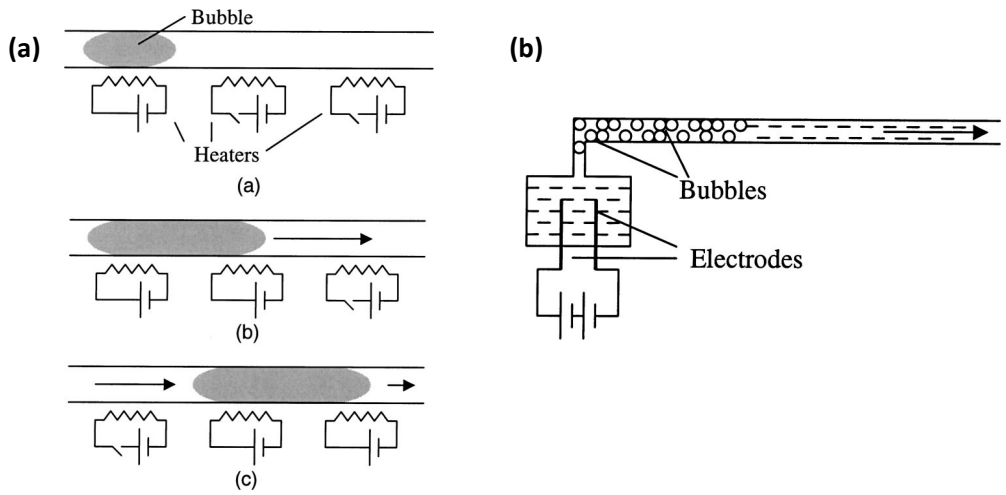

Figure 2.12. (a) Schematic of a bubble micropump. (Jun and Kim 1996) (b) Schematic of an electrochemical micropump. (Böhm, Olthius, et al. 1999)

Electrochemical micropumps are another class of phase change pumps which rely on gas bubbles generated in the pumped fluid to push the fluid in the pumped channel as shown schematically in Figure 2.12.b. (Böhm, Olthius, et al. 1999)

Both of those classes of micropumps usually require certain features in the fluids they can pump which hinder their applicability to specific scenarios. They are also not capable of producing high flow rates or heads which in turn limits their applications.

2.2.2.3 Other micropumps:

Several other mechanisms have been studied in the literature to produce pumping action in fluids. For instance, flexural plate wave pumps utilize high intensity acoustic fields generated near the surface of the channel due to flexural waves generated in piezoelectric fingers deposited on the surface to induce the pumping action in the direction of the wave. (Moroney et al. 1990; Moroney, White, and Howe 1991b; 1991a; Luginbuhl et al. 1997; 1998)

Electrowetting micropumps utilize the charges produced in the electrical double layer at the interface that is formed when a liquid metal comes in contact with an electrolyte solution. These charges that develop on the interface act as a capacitor and when an electric voltage is applied along the interface, a gradient in the surface tension occurs due to charge redistribution causing the movement of the droplet. (Yun et al. 2001; Matsumoto, H. and Colgate 1990; Lee, J. et al. 2001; Lee, J. L. J. and Kim 2000; Pollack et al. 2000)

2.2.3 Concluding remarks

Micropump scales are still quite bulky with dimensions generally in the range of tens of millimetres especially for mechanical micropumps. Moreover, most of them require flow rectification components, which constitute added complexity to their design as well as potential problems when dealing with fluids containing particulate matter. Nonetheless, vibrating diaphragm micropumps provide better performance in comparison to other methods of pumping in that they require lower power consumption, provide higher flow rates, and are able to accommodate a wider range of operating fluids.

Several excellent reviews have addressed the available literature discussing different micropump designs and principles. They also provide extensive summaries and comparisons between the different pumps reviewed (Laser and Santiago 2004; Iverson and Garimella 2008; Nguyen et al. 2002; Singhal et al. 2004). Two of such publications provide an extensive survey of the literature available up to 2008 (Singhal et al. 2004; Iverson and Garimella 2008). They provide an excellent review of not only the working principles of micropumps, but also provide a tabulated summary of the approximate sizes, flow rates, pump heads, power consumptions, operating conditions, actuation methods as well as advantages and disadvantages. They also provide a graphical comparison between those pumps reported in the tables in terms of maximum

backpressures and maximum flow rate per device area (Figure 2.13 and Figure 2.14). It has to be noted here that both figures are plotted using a logarithmic scale which shows the large variability in the performance of the reported micropumps.

The reviews delineate the fact that although micropumps are much smaller in dimensions than their macroscale counterparts, they are still bulky as compared to microfluidic devices developed recently. Moreover, the operating characteristics and limitations continue to hinder their integration into microfluidic devices.

Both reviews also discuss general guidelines for choosing which pumping method is better suited for which application and comment on possible considerations in terms of potential problems inherent in the different designs or limitations to their use. In summary, although some pumping technologies do provide superior performance to others, limitations in the working fluid or the technology used or the fabrication method or the possibility of being integrated in a microfluidic system can make them unacceptable options for certain systems which makes the comparison quite difficult.

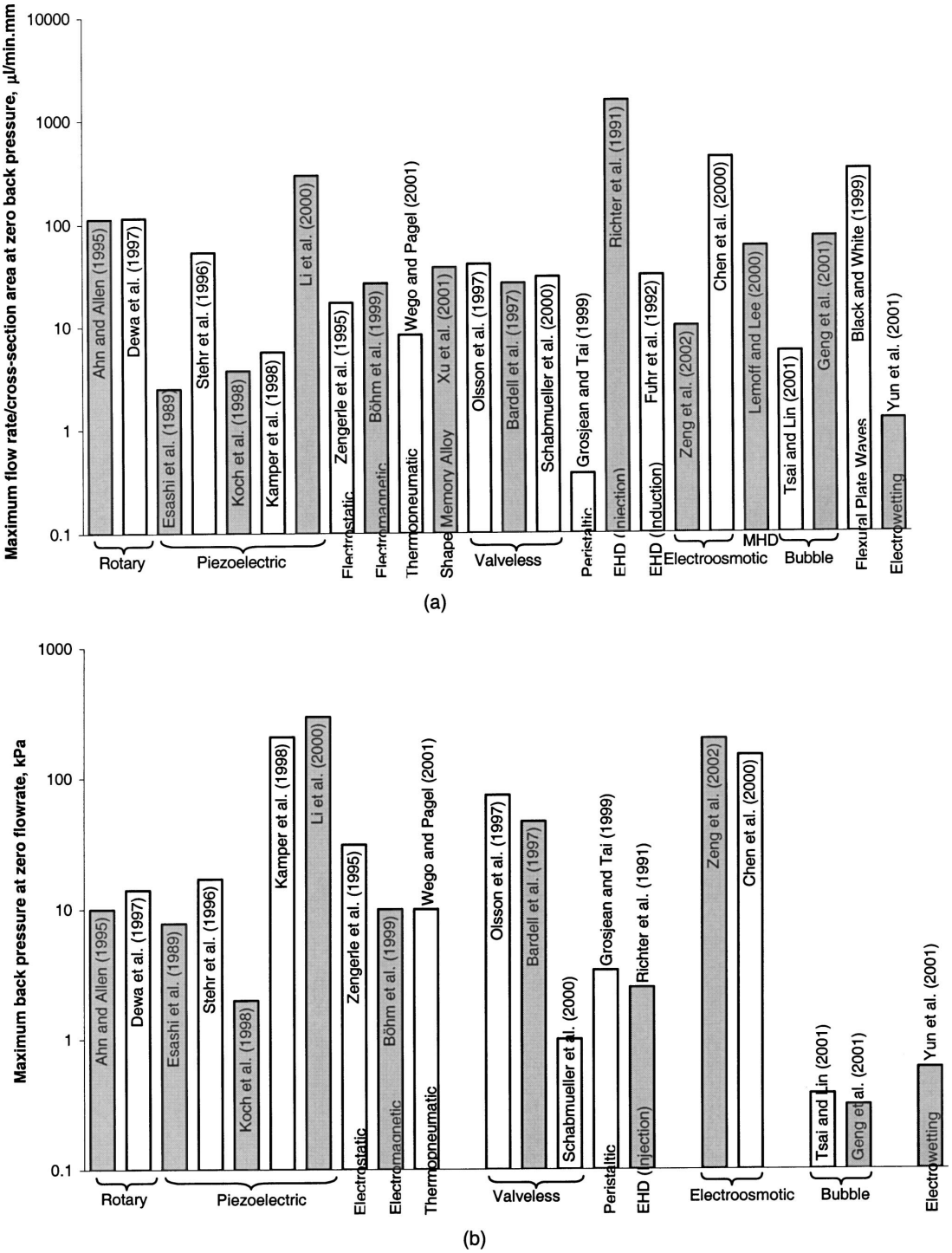

Figure 2.13. (a) Maximum flow rate per unit cross-sectional area and (b) Maximum back pressure for various micropumps reported in the literature. (Singhal et al. 2004)

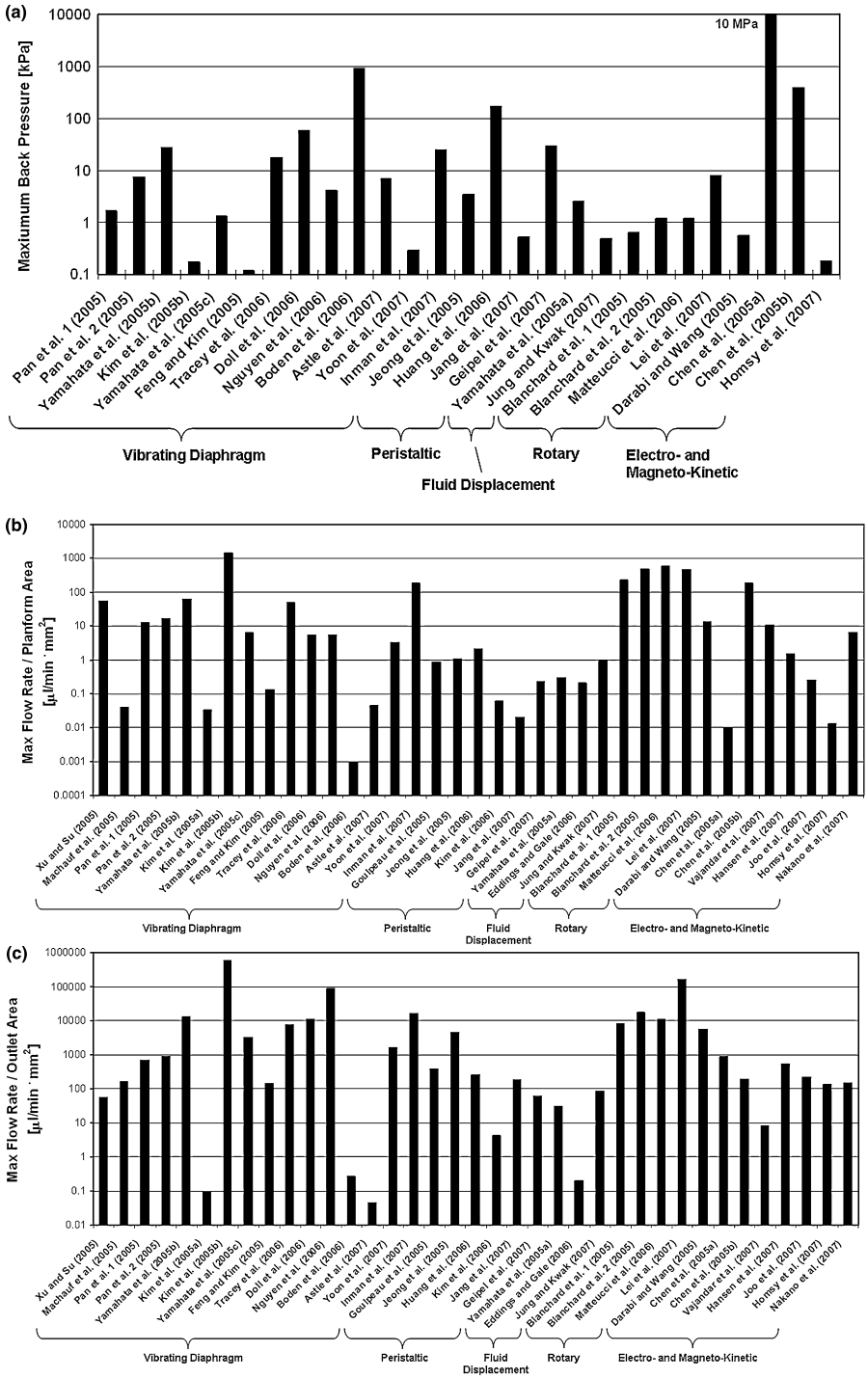

Figure 2.14. (a) Maximum back pressure, (b) Maximum flow rate per unit platform area and (c) Maximum flow rate per unit outlet area for pumps reported in the literature (Iverson and Garimella 2008)

Similar analyses and comparisons were also provided by two other extensive reviews (Laser and Santiago 2004; Nguyen et al. 2002). In addition to providing a survey of the available pumping methods and providing tabulated summaries, these two publications also try to provide graphical summaries of the performance of different pumping technologies (Figure 2.15). These two reviews also use a logarithmic scale for their plots which confirms the large variability in performance between different micropumps.

In conclusion, it can be seen, from the wide ranges of pump sizes, flow rates, backpressures, fabrication methods, and operating principles reported in the literature, that summarizing a general trend that one design principle is more superior than another is not possible. There are several factors to consider when it comes to the choice of a pumping technology such as the type of fluid being pumped, the ease of integration of the pump with the fluidic system, the application for which the fluidic system will be used … etc. The field of micropump design is yet a developing field with new ideas and technologies being implemented and improvements in fabrication methods as well as actuation mechanisms and flow rectification can improve the performance of pumps greatly, especially mechanically actuated ones.

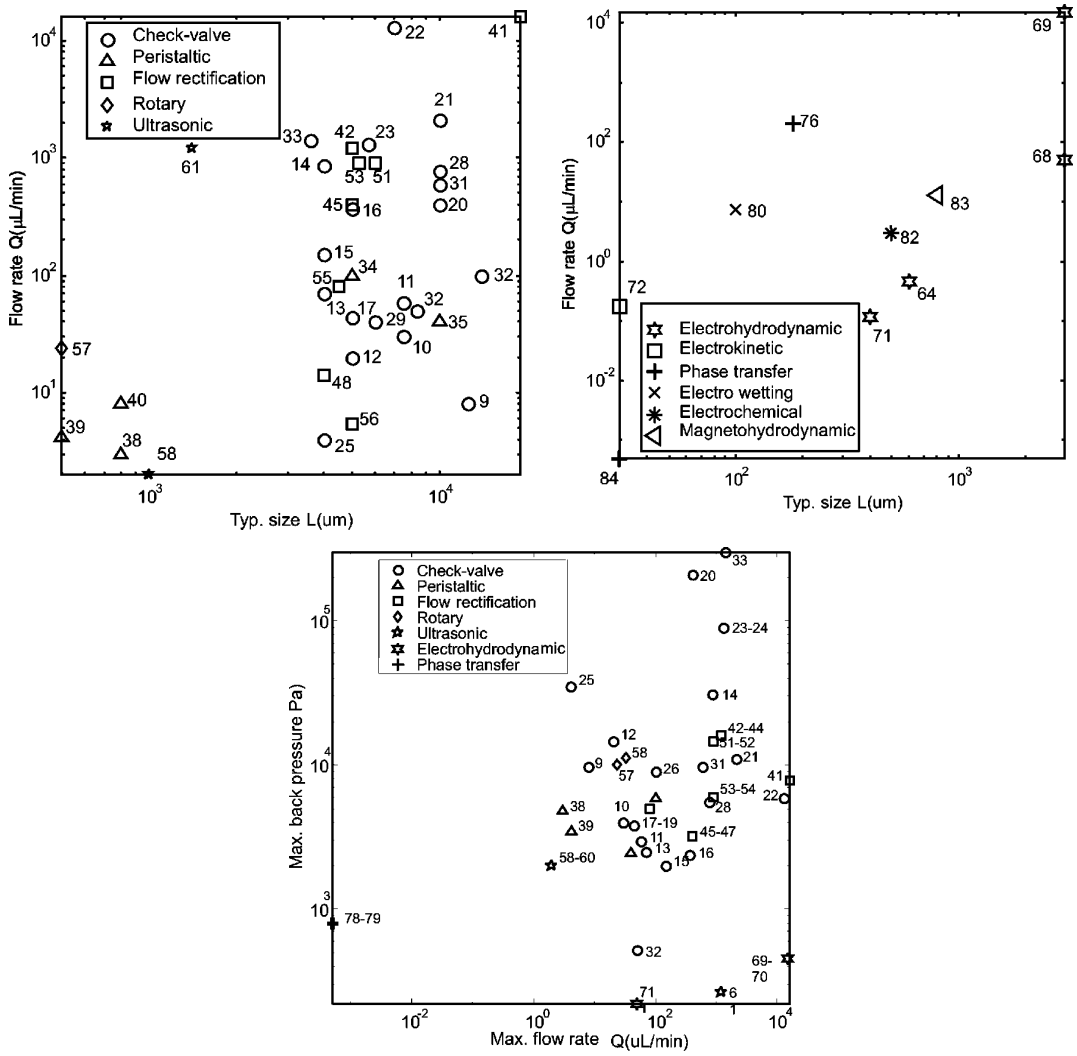

Figure 2.15. Flow rate vs typical size for: (Top left) mechanical, (Top right) non-mechanical micropumps. (Bottom) Maximum back pressure vs maximum flow rate. (Nguyen et al. 2002) (numbers indicate corresponding reference as per source)

2.3 Synthetic Jets

A Synthetic jet is a mean fluid motion created by an oscillating flow through an orifice or a slit. The fluid oscillations necessary to synthesize the jet are typically provided by intermittent suction and blowing through the jet orifice or slit. The device that produces the jet usually consists of a neck driven by a pulsating diaphragm in a cavity as shown in Figure 2.16. Flow enters and exits the cavity through the orifice. On the intake stroke, fluid is drawn into the cavity from the flow surrounding the orifice. As this fluid is driven out of the cavity, a shear layer is formed between the expelled fluid and the surrounding one. This layer of vorticity rolls up to form a vortex ring, a vortex pair in case of a 2-D slot. This vortex ring, or pair, convects downstream due to its induced velocity. By the time the diaphragm starts another intake stroke, the vortex ring has gained enough momentum and moved far enough away that it is virtually unaffected. Thus a train of vortex rings is created by the actuator. In the mean, the velocity profile appears similar to a steady jet. (Abdou 2003)

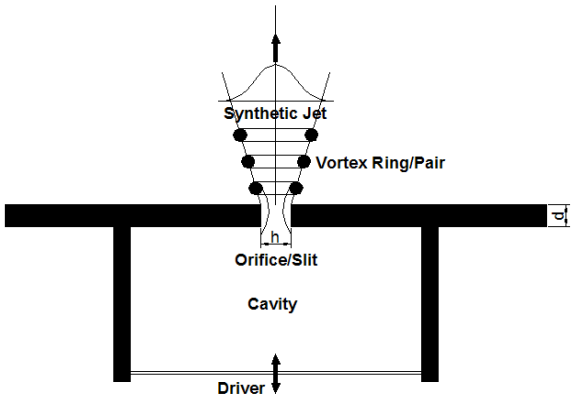

Figure 2.16. Schematic diagram of a synthetic jet actuator.

The driver, or the diaphragm, that is responsible for the production of the oscillating pressure drop across the neck necessary for the formation of the jet, can take a number of different forms including acoustic waves (Ingård and Labate 1950; Lebedeva 1980; Ziada 1995; 1999; McCormick 2000; Smith, B. L. and Swift 2001; 2003; Wolfe and Ziada 2003; Abdou and Ziada 2004; 2006), piezoelectric diaphragms (Smith, B. L. and Glezer 1997; 1998; Mallinson et al. 1999; Gilarranz and Rediniotis 2001; Utturkar et al. 2003; 2002; Gallas et al. 2002; 2003), and electromagnetically driven pistons (Rediniotis et al. 1999; Crook and Wood 2001). Since the dimensions of the synthetic jet scale with the dimensions of the orifice or slit producing the jet, it would be possible, theoretically, to produce jets over a wide range of scales including micromachined jets (Coe et al. 1995; 1994; Ho and Tai 1998).

2.3.1 Characteristics of Synthetic Jets

Since their first application in 1994 for flow manipulation, considerable research has been done to characterize synthetic jets and study their behaviour both experimentally (McCormick 2000; Smith, B. L. and Swift 2001; 2003; Smith, B. L. and Glezer 1997; 1998; 2002; Glezer and Amitay 2002) as well as numerically (Utturkar et al. 2003; 2002; Gallas et al. 2002; 2003; Rediniotis et al. 1999). Several excellent studies have been published discussing the characterization of synthetic jets covering different geometries, slit sizes, actuators and operating conditions. The work of Smith and Glezer (1998), Smith and Swift (2001; 2003), Utturkar et al. (2003; 2005), and a review paper by Glezer and Amitay (2002) provide outstanding comprehensive analysis and characterization of synthetic jets.

The work of Smith and Glezer (1998) discusses the formation and characteristics of a high aspect ratio, piezoelectrically driven, synthetic jet formed in air. Smith and Glezer introduce two primary dimensionless parameters characterizing the synthetic jet, namely: a dimensionless "stroke" length, L_o/d_o where

$$L_o = \int_0^{\tau} u_o(t)\,dt \qquad [2.2]$$

where $u_o(t)$ is the velocity at the exit plane of the orifice and $\tau = T/2$ is the half period of the cycle or the discharge time and d_o is the width or the hydraulic diameter of the orifice; and two Reynolds numbers based on either the average orifice velocity

$$\mathrm{Re}_{U_o} = \frac{\rho U_o d_o}{\mu} \qquad [2.3]$$

where $U_o = L_o/T$, or based on the impulse per unit width of the orifice

$$\mathrm{Re}_{I_o} = \frac{I_o}{\mu d_o} \qquad [2.4]$$

where

$$I_o = \rho d_o \int_0^{\tau} u_o^2(t)\,dt \qquad [2.5]$$

and ρ and μ are the density and viscosity of the fluid respectively. The studied synthetic jet ranged in stroke length, L_o/d_o, from 5.3 to 25 and the Reynolds number, Re_{U_o}, ranged from 104 to 489. They conclude that the synthetic jet is dominated in the near field by the time-periodic formation and advection of vortex pairs which ultimately transition to turbulence, slow down and lose there coherence forming an essentially two-dimensional turbulent jet in the far field of the orifice. Moreover, they state that synthetic jets are similar to conventional two-dimensional turbulent jets in that cross-stream distribution of the time-averaged jet velocity components and their corresponding rms fluctuations collapse when plotted in the usual similarity coordinates.

In more recent studies, Smith and Swift (2003; 2001) compare synthetic jets, with forcing parameters L_o/d_o and Re_{U_o} in the range of 13.5 to 80.8 and 695 to 14,700

respectively, to continuous and pulsed jets. They developed a jet formation criterion whereby a minimum stroke length (or pulsation amplitude), L_o/d_o, of $4/\sqrt{\pi}$ is required for the formation of the jet.

Utturkar et al. (2003) investigated the formation parameters of synthetic jets in search for a jet formation criterion. The study uses the same stroke length and Reynolds number based on U_o. They concluded a formation criterion, based on a simple order-of-magnitude analysis, of

$$\frac{1}{\mathrm{St}} = \frac{\mathrm{Re}}{\mathrm{S}^2} > K \qquad [2.6]$$

where S is the Stokes number, St is the Strouhal number

$$\mathrm{St} = \frac{fd_o}{U_o} = \frac{d_o}{L_o} \qquad [2.7]$$

and the constant K is approximately 2 for two dimensional synthetic jets and 0.16 for axisymmetric ones. This criterion is in good agreement with that suggested by Smith and Swift (2001; 2003) and with their own experimental results, shown in Figure 2.17. Holman et al. (2005), in 2005, revisit the subject and enhance their formation criterion formulation by introducing some corrections to their criterion to accommodate for the different geometries as well as provide a more detailed analysis of the theory.

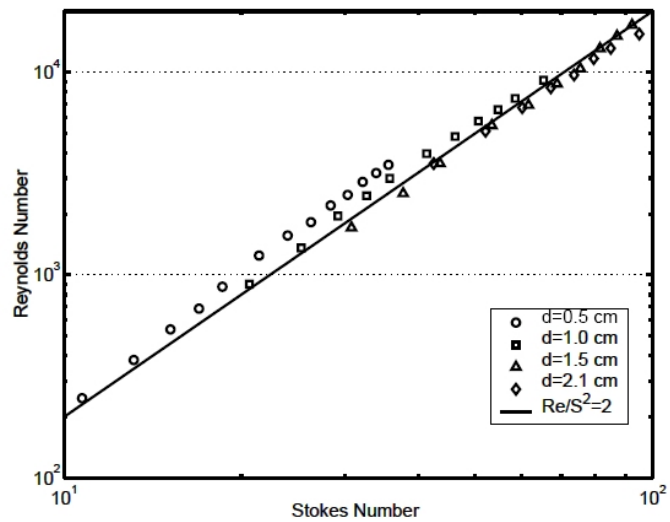

Figure 2.17. Reynolds number vs. stokes number for the experimental data obtained by Smith and Swift (2001) for different jet widths. (Utturkar et al. 2003)

Glezer and Amitay (2002) provide an excellent review of synthetic jet characteristics as well as interactions of synthetic jets with cross flow. The review covers near field characteristics as well as far field ones, and includes the most significant publications discussing the characteristics of synthetic jets.

2.3.2 Macro-Synthetic Jets and their applications

Synthetic jets possess a unique feature, that is, they are formed totally from the working fluid of the flow they are used in, and hence, require no external piping systems, making them a compact and low cost system. This feature enables the synthetic jet also to transfer linear momentum to the flow without any net mass injection. This unique property along with the fact that synthetic jets can exist in many

different scales make the applications of synthetic jet numerous, especially in the area of flow manipulation and control.

The categorization of synthetic jet research into macro- and micro- synthetic jets is quite difficult since for macro-synthetic jets the width of the orifice is sometimes less than a millimetre but the rest of the dimensions of the actuator are above the millimetre scale. On the other hand, micro-synthetic jets usually have cavity dimensions which are of the order of a few millimetres while the orifice is only a few hundred microns in width or diameter. Hence, in this thesis, the categorization will be based mainly on the orifice dimensions as well as the fabrication method used. Synthetic jets with orifice dimensions of the order of 1 mm or larger will be considered as macro-synthetic jets. Those with orifice dimensions less than a millimeter or are manufactured using fabrication techniques used for micro devices will be considered as micro-synthetic jets.

As discussed in the previous section, the characteristics of synthetic jets have been widely investigated in the literature and were mostly investigated for macro-scale jets. The applications of macro synthetic jets cover a wide range of applications including active flow control (Ziada 1999; Wolfe and Ziada 2003; Hsiao and Shyu 1991; Huang 1995; Abdou 2003), separation control (McCormick 2000; Gilarranz and Rediniotis 2001; Mittal et al. 2001), virtual aero-shaping effects (Amitay et al. 1997; Smith, D. et al. 1998), jet vectoring (Smith, B. L. and Glezer 1997; 2002), cooling (Glezer et al. 1999), and

mixing enhancement (Glezer and Amitay 2002; Davis and Glezer 1999; Glezer and Wiltse 2000).

2.3.3 Micro-Synthetic Jets

Because of the fact that the issuing synthetic jet characteristics and dimensions scale with the dimensions of the orifice through which the jet is produced, it would be possible to produce jets within a wide range of length scales (Glezer and Amitay 2002). The first reference to microfabricated synthetic jets with an orifice diameter of 150 µm was published by Coe et al. in 1994 and 1995 (Coe et al. 1994; 1995). Since then considerable attention is being given to the possibilities of integrating synthetic jets into microfluidic devices.

Coe et al. (1994; 1995) address the possibility of producing a micromachined synthetic jet, as well as an array of microjets, using standard silicon micromachining techniques. The microjets are fabricated in a single silicon wafer with cavity dimensions of the order of a 1 to 4 mm and cavity height of about 250 µm. The authors propose two different designs with integrated and hybrid membranes. Figure 2.18 shows the two proposed designs of the microjet actuator. Actuation can be realized using either electrostatic or piezoelectric means and the array can be either addressed individually or all the jets can be controlled collectively.

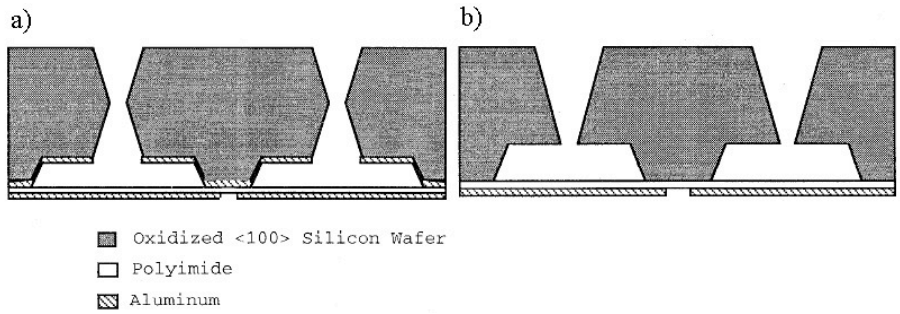

Figure 2.18. Synthetic microjet design: a) Hybrid membrane; b) Integrated membrane. (Coe et al. 1995)

Issuing jet velocity measurements using a miniature total pressure tube are provided for a 4 x 5 array as well as flow visualization images. The hotwire measurements are shown in Figure 2.19 along the four microjets of the center row at distances of 4 mm and 10 mm downstream of the jet array. The traces of the individual jets can be clearly seen for the closer data profiles, while for the ones further downstream, the jets have merged into a single larger scale jet. Although this study provides the first insight into microsynthetic jets, it lacks detailed analysis of the jet characteristics or scaling issues.

More recently, Mallinson et al. (2003) numerically study piezoelectrically actuated axisymmetric microjets with an orifice diameter of 200 µm. The cavity dimensions are of the order of 4 mm in diameter and 135 µm in height. The study compares the effect of different excitation frequencies and amplitudes on the issuing jet with Reynolds numbers reported in the range of 10 to 100. They use a laminar axisymmetric solver, modeling the membrane as a clamped circular disk using a moving mesh, and give a

brief comparison between results obtained for a macroscale version of the actuator studied earlier and those of the current microscale one.

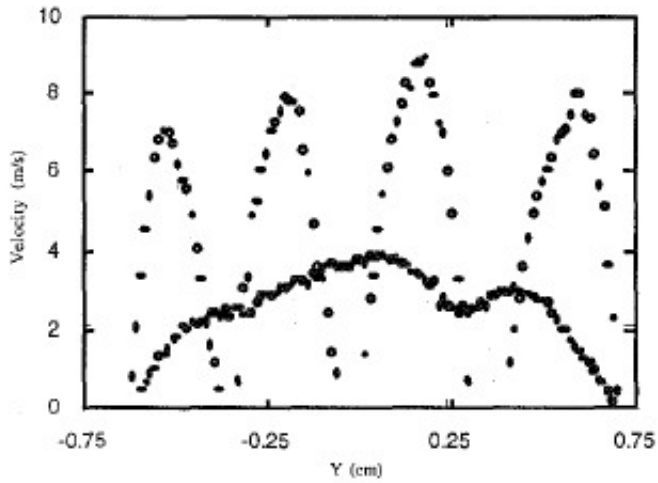

Figure 2.19. Measured velocity profiles across the center row in a 4x5 microjet array at 4 mm (open symbols and exhibiting larger fluctuations) and 10 mm (closed symbols and exhibiting less fluctuations) downstream of the jet array. (Coe et al. 1995)

Even though accurate simulations of a synthetic jet would require an unsteady, turbulent, three-dimensional solver, the authors use an unsteady, laminar, axisymmetric one and they suggest that, for the low Reynolds numbers investigated, the flow can be approximated using a laminar solver. The results presented show good agreement with other macroscale simulations for the flow in the orifice and cavity regions. The outer region shows that the expelled vortex diffuses rapidly, even in the absence of a turbulence model, and this was attributed to the increased relative magnitude of diffusion terms in the Navier-Stokes equations for such small scales.

Vorticity contours for the nine different cases studied are shown at the same instant in the forcing cycle in Figure 2.20. The nine cases show three different amplitudes and three different frequency combinations. It can be seen that by increasing the forcing amplitude and frequency, the jet is seen to get stronger and penetrates more into the external domain. The authors also perform a non-dimensional analysis using the Buckingham theorem and introduce two non-dimensional groups which they use to characterize the nine cases they studied. The plot of the peak average centerline velocity for the different test cases versus those two numbers is shown in Figure 2.21. The two non-dimensional numbers used are Ud_o/ν and Ad_of/ν, where $U$is a characteristic jet velocity, d_o is the orifice diameter, A is the forcing amplitude, f is the forcing frequency and ν is the kinematic viscosity. The first non-dimensional number is the Reynolds number based on the characteristic jet velocity and orifice diameter and the second can be viewed as the product of the Reynolds number and a Strouhal number, $\mathrm{St} = Af/U$, based on the actuating amplitude and frequency and the jet characteristic velocity. The value of this Strouhal number as obtained from the slope of the figure is $6.4\text{x}10^{-4}$. The proposed microfabricated model of the microsynthetic jet actuator is piezoelectrically actuated as opposed to the design of Coe et al.(1995) which uses electrostatic actuation.

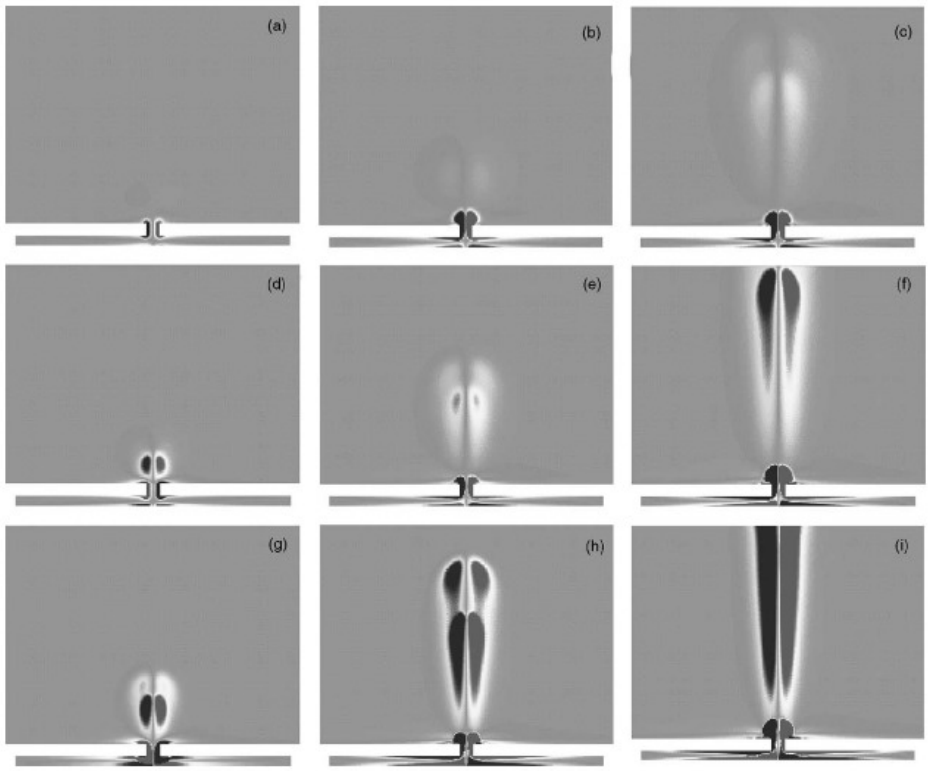

Figure 2.20. Vorticity contours for different cases studied at t/T=0.71 (Mallinson et al. 2003):
a) A = 0.5 µm, f = 0.725 kHz; b) A = 1 µm, f = 0.725 kHz; c) A = 2 µm, f = 0.725 kHz;
d) A = 0.5 µm, f = 1.450 kHz; e) A = 1 µm, f = 1.450 kHz; f) A = 2 µm, f = 1.450 kHz;
g) A = 0.5 µm, f = 2.900 kHz; h) A = 1 µm, f = 2.900 kHz; i) A = 2 µm, f = 2.900 kHz.

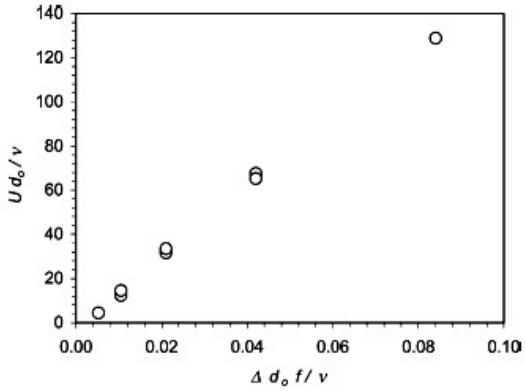

Figure 2.21. Comparison of peak average centerline velocity for different test cases against non-dimensional variables. (Mallinson et al. 2003)

Lockerby et al. (2004; 2002) provide another numerical investigation of synthetic microjets (it should be noted that this study deals with orifice dimensions of the order of 1 mm). They model the vibration of the membrane using classical thin-plate theory. However, they do not model the flow inside the cavity but rather calculate the cavity pressure using perfect gas laws. They compare their results with experimental data from another investigation with similar geometry.

In comparison to macro-synthetic jets, micro-synthetic jets have received a lot less attention as they are a much newer concept. Several numerical as well as experimental studies have been done to characterize macro-synthetic jets, as discussed earlier, while only a few have been published discussing the characteristics of micro-synthetic jets. The published literature discussing micro-synthetic jets focuses mainly on applications rather than characterization of the jets and comparison to macro-scale ones and scaling issues that might arise. Most of the published literature resorts to numerical methods to model the micro-synthetic jets rather than use experimental techniques. This is probably due to the underlying difficulty in performing comprehensive flow measurements on such small scales, where the size of the actuator is only a few millimeters and also due to the ease of performing numerical studies especially with the advancement in computational power.

2.3.3.1 Applications of Micro-Synthetic Jets

The main focus on micro-synthetic jet applications has been in the field of microprocessor and electronic circuit cooling (Mahalingam and Glezer 2002; Mahalingam et al. 2004; Kercher et al. 2003; Campbell et al. 1998), where synthetic microjets have been proven to enhance cooling of electronic chips with the added advantage of replacing cumbersome mechanical fans. Other applications of synthetic microjets, where research is currently pursued, include mixing enhancement (Wang, H. and Menon 2001; Ibrahim et al. 2002; Mautner 2004), micropropulsion (Müller, M. O. et al. 2000; Müller, M. O., Bernal, Washabaugh, Chou, and Najafi 2002; Müller, M. O., Bernal, Washabaugh, Chou, Kim, et al. 2002; Müller, M. O. et al. 2003), as well as active flow control (Lee, C. et al. 2003). Although the number of applications in which micro synthetic jets are used is increasing, there are several aspects of the already mentioned applications and other possible applications that have not been investigated yet.

Recently, Luo and Xia (2005) propose the first attempt to use synthetic microjets as a pumping device. They investigate numerically a two dimensional piezoelectrically actuated micro-synthetic jet with an orifice width of 0.5 mm using an incompressible RANS solver with a k-ε turbulence model. They then introduce the possibility of using this jet as a pumping device by introducing triangular wedges in the vicinity of the orifice in the external domain.

2.4 Concluding Remarks

Synthetic jets have been used successfully as flow control and manipulation devices on the macroscale due to their unique features. On the microscale, however, little is known about their behaviour and characteristics and the way they scale with the reduction in size. Nonetheless, the field of microsynthetic jet research is still new and a lot of research is underway in this area.

Microsynthetic jets have been increasingly used as microcooling devices for the cooling of microelectronics, as micromixers, and as microthrusters. They are proving to be successful in those applications; however, other applications for microjets are also possible. One of those applications is the use of microjets in micropumping of fluids in microchannels. With the increasing use of microfluidic devices, the need for means to transport fluids in microchannels is increasing. The main drawback of current devices lies mainly in their relatively large size and poor performance for smaller ones. Synthetic jets lend themselves as a promising actuator in this field due to their simple design, their compact size and low power consumption as well as to the possibility of seamlessly integrating them into microfluidic systems of different scales.

Chapter 3

SYNTHETIC JET MICROPUMP

Due to their simple design, simple operating principle, low power consumption, and their compactness in size, synthetic jets lend themselves to be a very promising component of microfluidic systems which can be easily integrated into such devices. Because of the fact that the issuing jet characteristics and dimensions scale with the dimensions of the orifice through which the jet is produced, it would be possible to produce jets within a wide range of length scales.

Luo and Xia (2005) propose an attempt to use synthetic microjets as a pumping device. They start by numerically studying a two dimensional piezoelectrically actuated microjet with an orifice width of 0.5 mm and a square cavity dimensions of 50x50x4 mm. The design used incorporates double membrane actuation as seen in Figure 3.1 (left). The authors use an incompressible RANS solver with a k-ε turbulence model and they start by describing the flow field of a microjet issuing in a quiescent medium, comparing their results to those obtained in another study for a similar geometry. The micropumping device is introduced by simply adding triangular wedges, or dividing clapboards, in the vicinity of the orifice in the external domain as shown in Figure 3.1 (right).

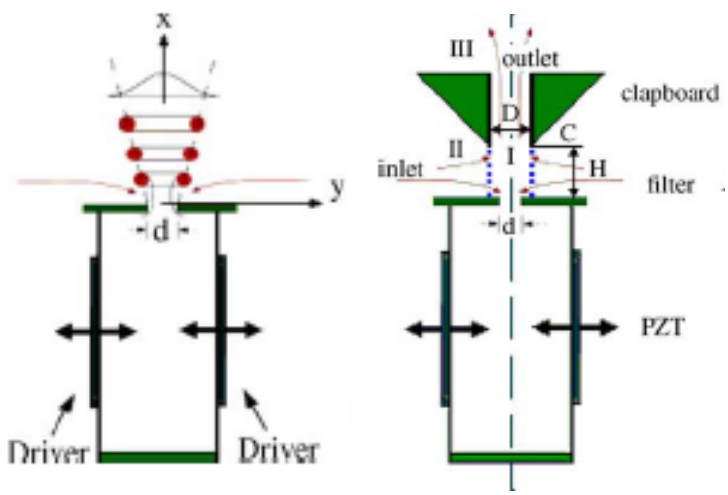

Figure 3.1. Schematic layout of the synthetic microjet actuator studied (left) and the proposed synthetic microjet based pump (right). (Luo and Xia 2005)

The authors provide a simple analysis by which they choose the optimal location for the wedges based on the stream function contours of the synthetic jet flow field,

shown in Figure 3.2. These wedges act more or less to separate the outflow from the inflow regions of the jet domain, introducing an inlet and an outlet to the micropump. The analysis provided by the authors depends on the location of the stagnation points A and B shown in Figure 3.2 which determine the extent of the effect of the suction flow and the circulation region of the external flow.

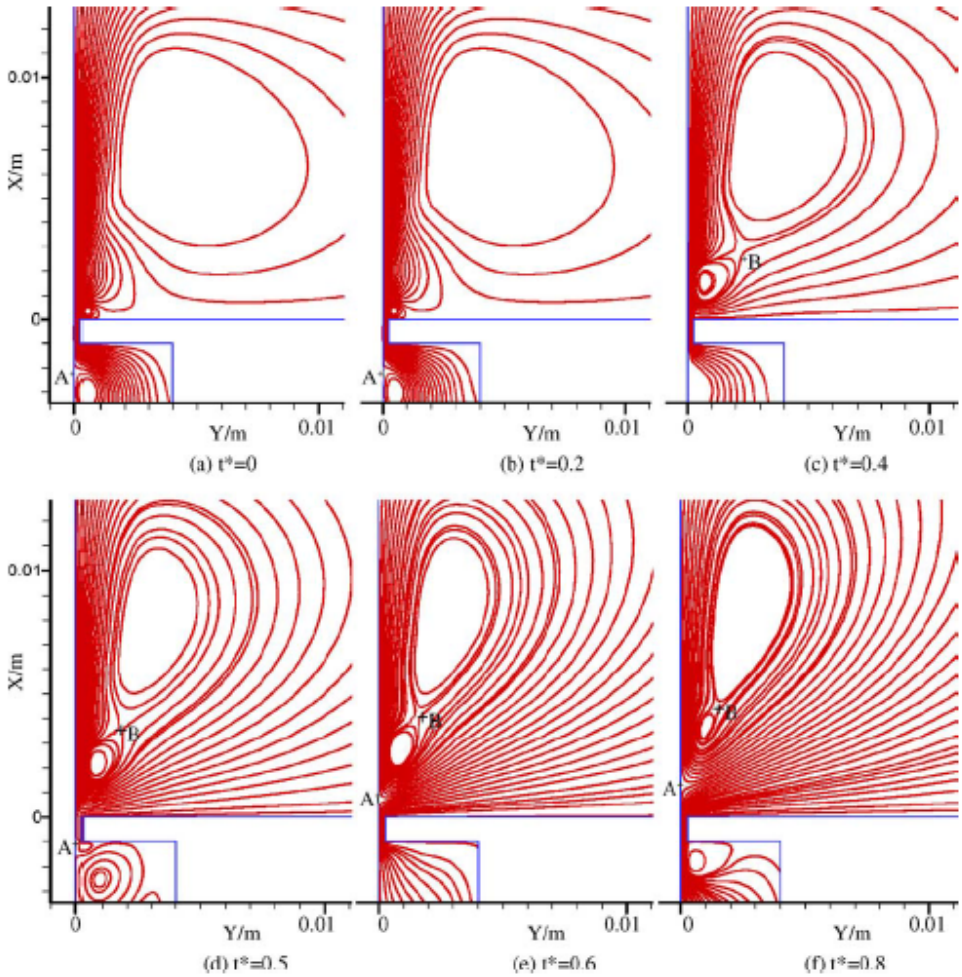

Figure 3.2. Stream function contours at different intervals in a forcing cycle. (t* = t/T) (Luo and Xia 2005)

Five different cases with different locations for the wedges were then modeled. Case 1, i.e. the case with the optimal location of the wedge as defined by the analysis, is taken as the design case for comparison with the other cases. The other "off-design" cases depict either a change in the width of the outlet region or a change in the height of the inlet region as seen in Table 3.1. Velocity vector plots of the external flow filed are shown in Figure 3.3 for four of the five test cases.

	Case 1	Case 2	Case 3	Case 4	Case 5
H/d	12	4	20	12	12
D/d	10	10	10	4	16

Table 3.1. Location of clapboards for the different test cases. (H, D and d are as shown in Figure 3.1) (Luo and Xia 2005)

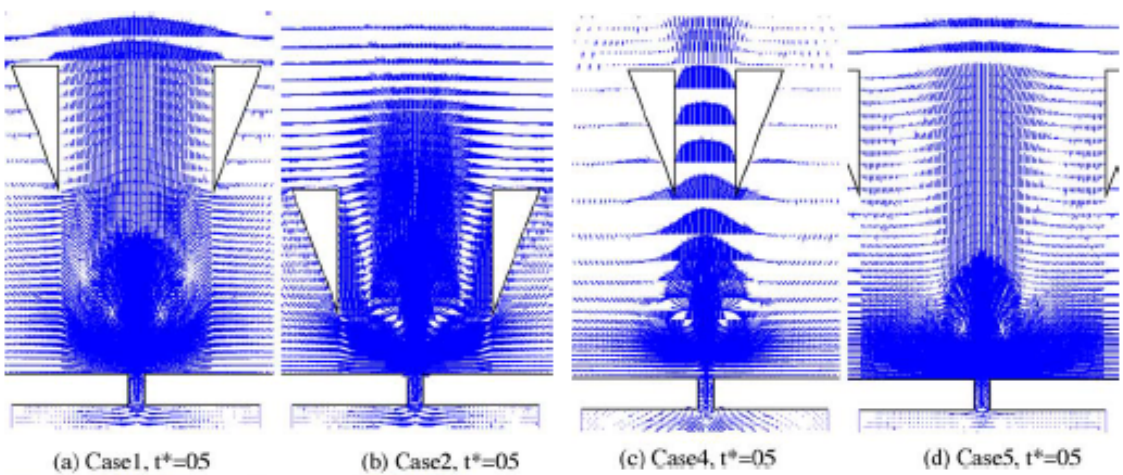

Figure 3.3. Velocity vector plots of the external flow field for four test cases. (Luo and Xia 2005)

The mass flow rate per unit length of the slit through the exit plane of the pump, i.e. the plane at the top of the clapboards, is used to compare the performance of the pump for the five different cases studied. Flow rates of up to about 3.5 g/s.m were recorded at the pump outlet. Figure 3.4 shows the variation of the outlet mass flow rate for one cycle for the different test cases. It can be seen that the design case, case 1, provides the highest average flow rate. However, it also produces the maximum variation along the cycle. Cases 3 and 4 provide the most uniform flow rates although they show a lower average flow rate. The authors also study the flow rate at the inlet plane of the pump as well as the flow rate from the actuator slit for the different test cases.

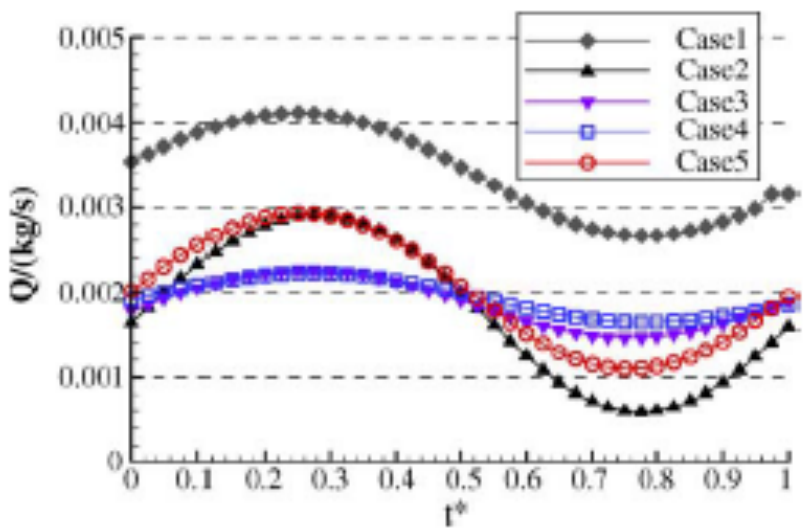

Figure 3.4. Mass flow rate at the pump exit plane for different test cases.
(Luo and Xia 2005)

This study provides a first attempt to use microjets as pumping devices and as such many issues of this new application need to be investigated. First of all, the practical applicability of the concept has not been addressed. The authors' use of the dividing clapboards does not completely separate the inlet and the outlet of the pump as flow is allowed to circulate around them. Moreover, the results only report flow rate calculations and vector plots of the flow field. In order to adequately characterize the pump, flow rates, pump efficiency as well as pressure drops and pump head characteristics need to be known which are not provided by the current study. Moreover, the effects of actuator geometry and operating conditions on the pumping characteristics need to be investigated.

Dinh et al. (2008; 2011) proposed a micropump design based on the synthetic jet principle. They only report numerical investigations of the proposed micropump with a realization of the actuation principle used and the method of fabrication. The main application they are targeting is micromixing when integrated in a microfluidic system. The design of the micropump is shown in Figure 3.5. Fluid enters through the two inlet channels on both sides of the actuator cavity and leaves through the top outlet channel. The actuation cavity is 7 mm in diameter and the whole pump is 300 µm deep in one study and 200 µm in the other. The inlet and outlet channels are 1.5 mm wide in one study and 1 mm in the other. There is no mention of the dimensions of the cavity orifice, but it is tapered with the larger diameter on the cavity side and from the design drawing

it seems the orifice average width is of the order of 0.5 mm. In a variant of the design, which has 1 mm inlet/outlet channels and 200 µm depth, an oblique ridge 70 µm high at 45° angle is introduced across the cavity orifice to improve the mixing performance of the device when two different fluids are introduced from the two inlet channels.

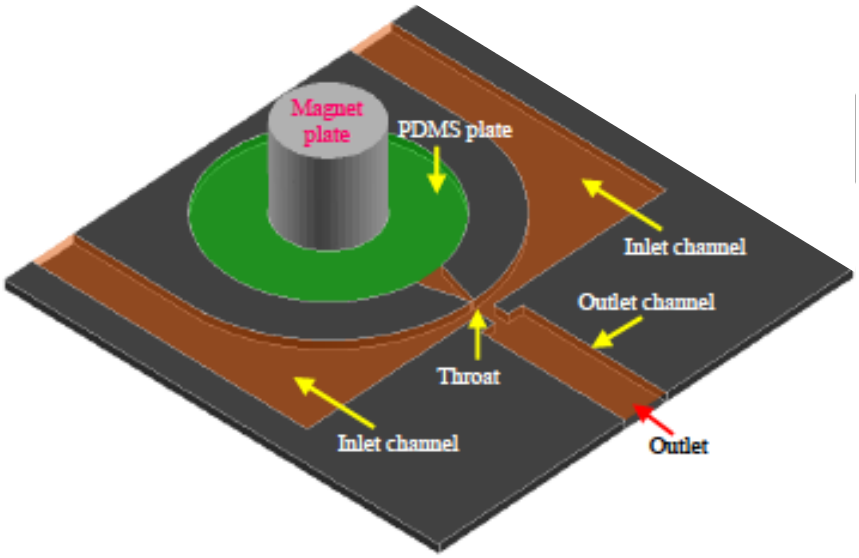

Figure 3.5. The proposed micropump design by Dinh et al.
(Dinh and Ogami 2011; Dinh et al. 2008)

Simulations are carried out using the Ansys/Fluent software package with the membrane deflection being ignored and replaced by a fluctuating velocity inlet condition the magnitude of which is obtained by differentiating the proposed displacement of the actual membrane. Water was used in the modelling of the working fluid for the simulations.

The study compares the pumping performance of the suggested micropump to another valveless vibrating diaphragm studied by Yamahata et al. (2005). The proposed actuation mechanism depends on electromagnetic actuation and the study uses an actuation frequency of 50 Hz and amplitudes of 10 to 30 µm. The flow rate at the outlet of the micropump is reported as in Figure 3.6 and show the fluctuation of the flow rate with the same frequency of excitation. While the flow rate is reversed in part of the cycle, the average is a net positive flow rate through the pump.

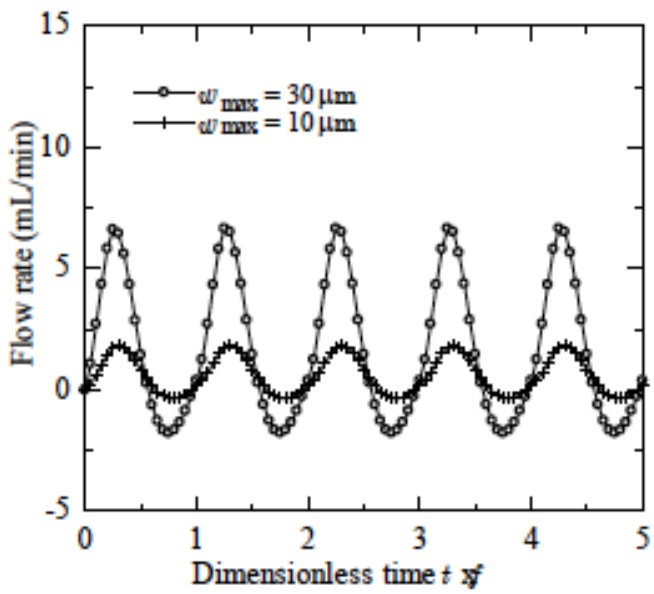

Figure 3.6. Flow rate reported at pump outlet for the proposed micropump by Dinh et al. (2011; 2008)

The reported variation of the flow rate with increasing actuation amplitude is reported as shown in Figure 3.7(Left) and shows a linear increase in flow rate with amplitude. It also shows a significant improvement in the flow rate as compared to that

of the valveless pump of Yamahata et al. The flow rate variation vs backpressure is shown in Figure 3.7(Right) and shows a linear decrease in flow rate with increasing pressure. It should be noted that even though the trend is linear among the different amplitudes, the slope is different which indicated a dependence of the trend on the amplitude of excitation.

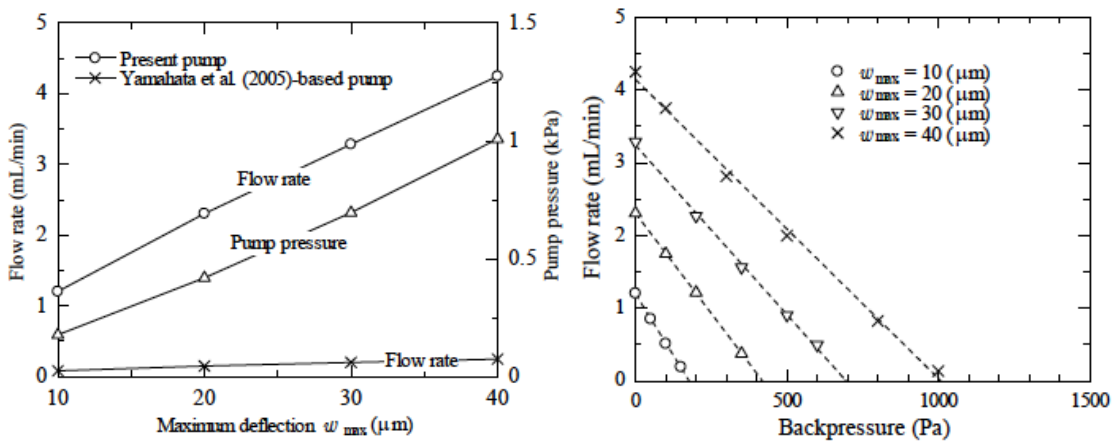

Figure 3.7. (Left) Variation of pump flow rate vs excitation amplitude as well as maximum back pressure. (Right) Flow rate vs pressure for different amplitudes of excitation. (Dinh and Ogami 2011; Dinh et al. 2008)

Choi et al. (2011) discuss the simulation and testing of a synthetic jet based air micropump. The pump is actuated piezoelectrically with a diaphragm diameter of 9 mm, an orifice depth of 1 mm, a tapered orifice with a nominal average width of 300 µm and a schematic as shown in Figure 3.8.

A commercial CFD solver was used with deforming mesh at the membrane surface was used to perform the numerical analysis. The pump is modeled with an actuation

amplitude of 200 µm using double membranes on both sides of the cavity and a frequency of 100 Hz. The effect of changing several geometrical dimensions as indicated in Table 3.2 and shown in Figure 3.9 was considered numerically. Flow rates of up to 2.8 cm^3/sec were reported. The pump was fabricated using rapid prototyping of PDMS (PolyDiMethyleSiloxane). The produced pump uses one membrane capable of producing 0.16 cm^3/sec when actuated at 30 µm and 80 Hz.

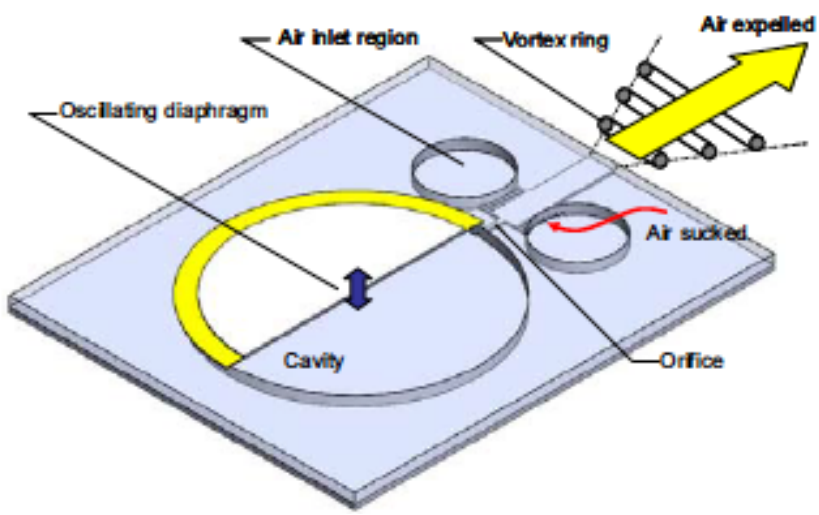

Figure 3.8. Schematic of synthetic jet air micropump. (Choi et al. 2011)

Parameters	Symbol	Dimensions (mm)
Chamber diameter	D	9 (ref. value)
Chamber height	H	1–3 (ref. value: 2)
Diffuser length	dh	1 (ref. value)
Diffuser inlet width	d_1	0.1–0.3 (ref. value: 0.2)
Diffuser outlet width	d_2	0.3–0.5 (ref. value: 0.4)
Air inlet channel width	d_3	0.6–1.4 (ref. value: 1)
Air inlet gate length	d_4	0.1–0.5 (ref. value: 0.2)
Air outlet channel width	d_5	0.4–1.4 (ref. value: 1)

Table 3.2. Numerical investigation parameters (Choi et al. 2011)

The flow rate is measured for the pump prototype by allowing the outlet flow to issue into the surrounding and measuring the air velocity at the exit and inferring the flow rate from the velocity measurement.

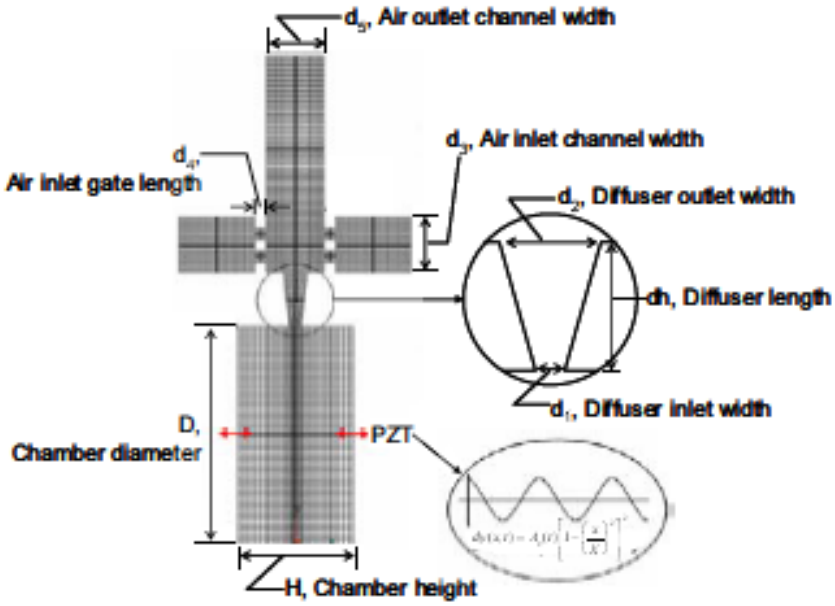

Figure 3.9. Numerical model geometry and dimensional parameters (Choi et al. 2011)

1.1. Concluding Remarks

The literature presented in this chapter represents what has been studied to date in terms of using the synthetic jet principle to induce a pumping action. With the exception of the work of Choi et al. (2011), which discusses an actual produced micropump for air pumping, all of the work reported is based solely on numerical simulations. The work of Luo and Xia (2005) only proposes a preliminary principle of

operation that does not produce an actual product even in terms of a full proposed model. The work of Dinh et al. (2011; 2008) even though it provides some initial performance reporting of the proposed micropump, their main focus is on the mixing performance of the device.

Chapter 4

NUMERICAL SIMULATIONS

Numerical investigations carried out to study the behaviour of the synthetic jet micropump will be introduced in this chapter. The studied geometry, boundary conditions, meshing, operating parameters, and solver settings will be discussed. The software package of choice for running the numerical simulations was the Ansys software package including ICEM and CFX.

The numerical simulations are based on the proposed prototype geometry and were used to optimize and study the effect of different geometrical and operational

parameters to produce a comprehensive set of results which are then used to design the physical prototype. The results of the prototype testing are then compared with those of the flow simulations.

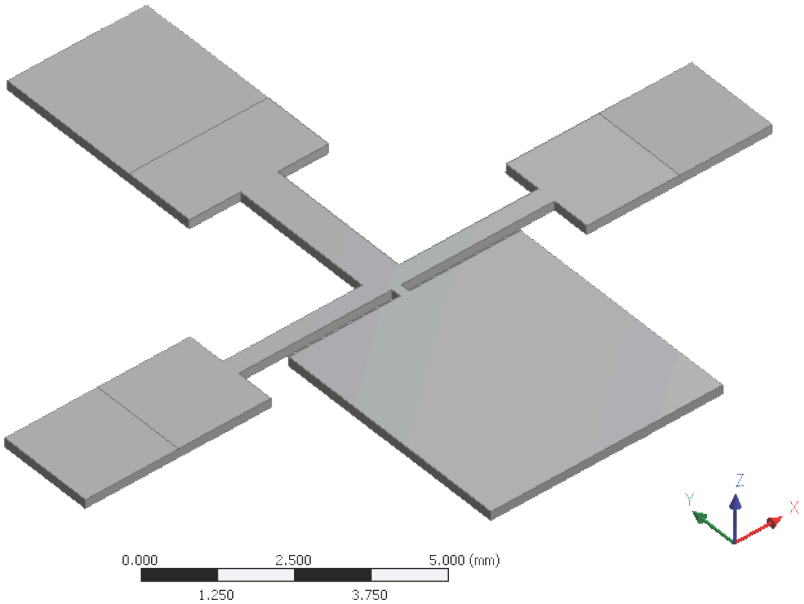

Figure 4.1. Sample geometry used in numerical simulations.

The most intuitive idea to construct the synthetic jet micropump is to simply introduce an inverted T-shaped channel structure just downstream of the orifice from which the jet is issuing. The dimensions of the created channels were chosen primarily to mimic typical dimensions of microchannels found in microfluidic devices. A square cavity was utilized with a square membrane on one side of the cavity. Figure 4.1 shows a typical geometry used for these simulations whose details will be discussed in the following sections. Geometrical as well as operating parameters were varied to investigate their effect on the operation and performance of the micropump. In the

following sections the geometry, dimensions, meshing, boundary conditions and modeling of the device will be discussed.

4.1 Geometry & Dimensions

The actual fabricated geometry of the micropump has a circular membrane with a diameter of 5 mm as will be discussed in Chapter 5. It was chosen to utilise a square cavity and membrane for numerical simulations to facilitate the use of the hexahedral meshing scheme to mesh the simulated domain. Figure 4.2 shows a top view of a sample simulation case where it can be seen that a 5 mm by 5 mm cavity was used with the cavity dimensions fixed for all test cases. A uniform device thickness or depth of 200 µm was used. The orifice from which the jet issues was also fixed in dimensions for all tested cases at a width (d_o) of 200 µm and a height (h_o) of 200 µm as seen in the figure. The two main geometrical dimensions that were varied throughout the simulations were the inlet channel width (W_i) and the outlet channel half-width (W_o).

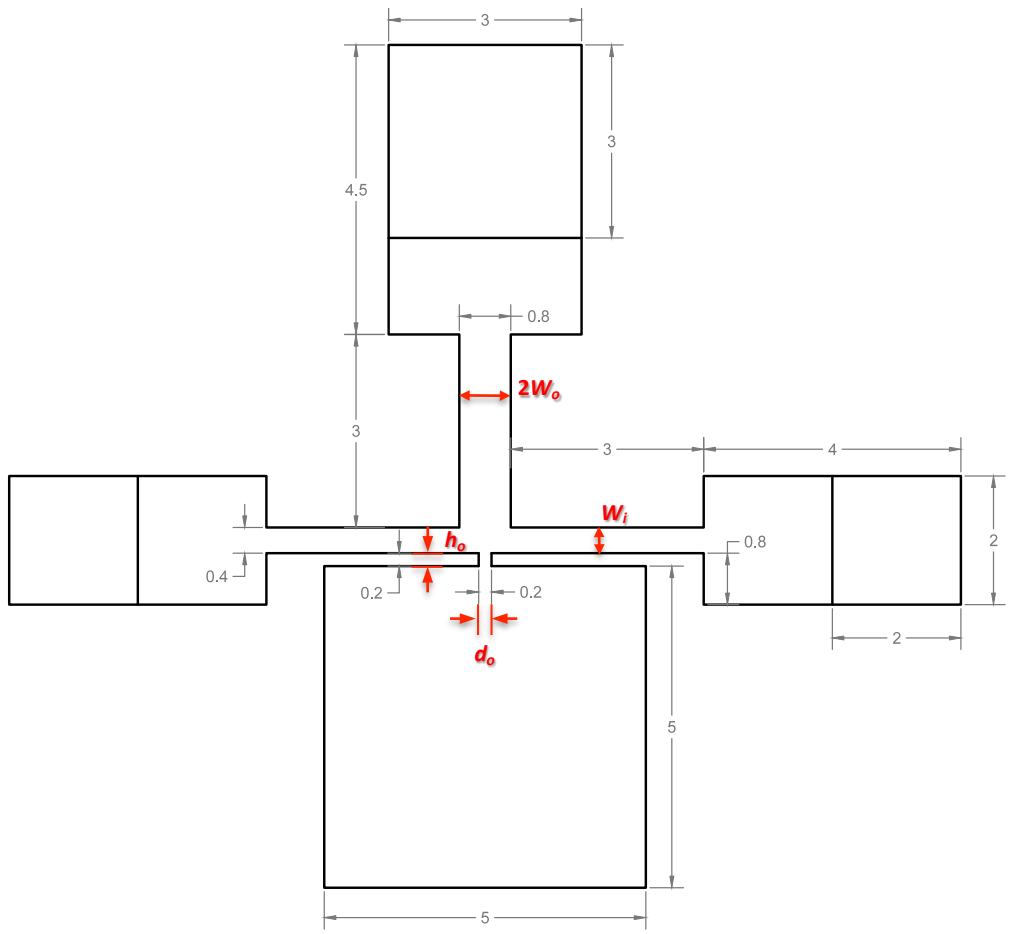

Figure 4.2. Dimensioned drawing of a sample final geometry simulation test case.
(All dimensions are in mm)

4.2 Meshing

The default meshing tool provided with the Ansys software package utilized for CFD simulations relies on tetrahedral meshing, however, since the geometry under investigation consists mainly of rectangular sections, the use of a hexahedral mesh was considered to be more appropriate. Thus the software package ICEM, which provides this functionality in Ansys, was used to construct the mesh.

A non-uniform hexahedral mesh was used with approximately 120,000 to 150,000 elements depending on the geometry under investigation with a minimum element size of 10 µm. Figure 4.3 shows a sample mesh for one of the simulated cases. The dependence of the solution on the grid size is discussed in Appendix A.

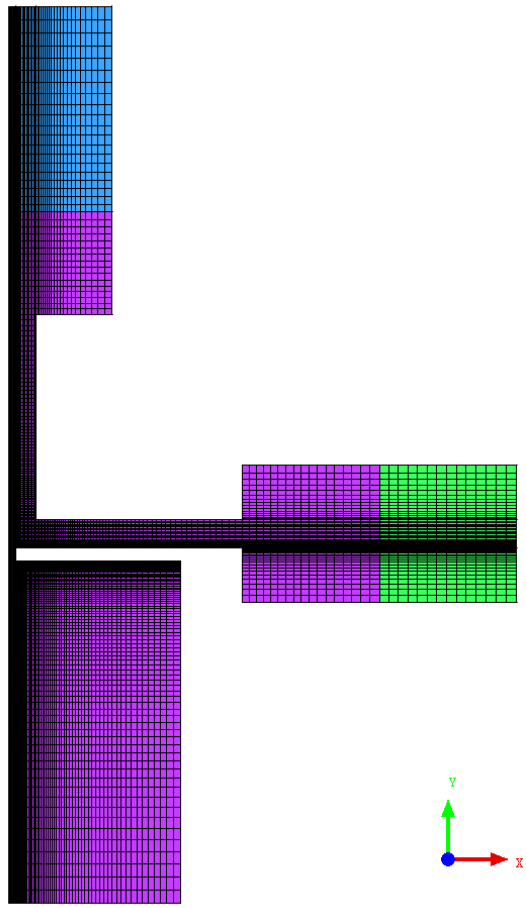

Figure 4.3. Mesh for a sample simulation cases.

4.3 Boundary conditions

Details of the boundary conditions can be summarized in Figure 4.4 and detailed as follows:

4.3.1 Inlet & Outlet

The micropump inlet and outlet boundaries are modeled in CFX as entrainment opening boundary conditions to allow for inflow and outflow from the domain with the static pressure set at 0 Pa, in order to simulate the case of zero back pressure against the pump and hence maximum flow rate. The area averaged mass flow rates through the inlet and the outlet boundaries were calculated and recorded for each time step.

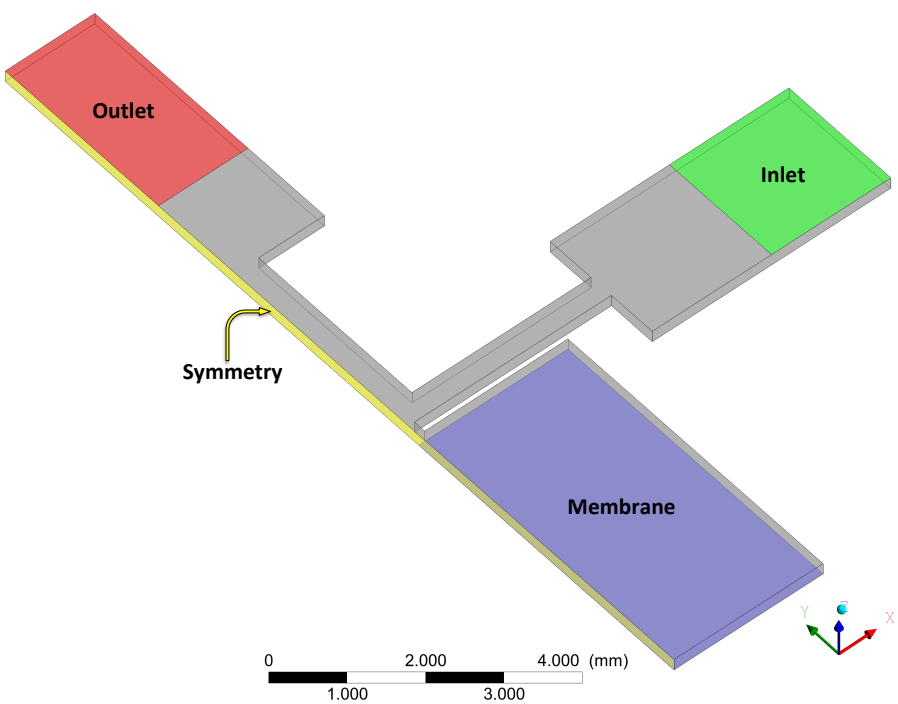

Figure 4.4. Boundary conditions for a sample simulation case.

4.3.2 Membrane

The membrane boundary was modeled as a moving wall with a prescribed displacement. Equations [4.1] and [4.2] describe the membrane wall motion in terms of a mode shape function of the in plane coordinates (x, y) and a harmonic function in time (t) which is shown in Figure 4.5.

$$Z(x,y,t) = A(t)f(x,y) \qquad [4.1]$$

where

$$f(x,y) = \sin\left(\pi \frac{\frac{a}{2}+x}{a}\right)\sin\left(\pi \frac{\left(\frac{b}{2}+h_o\right)+y}{b}\right) = \sin(\pi \frac{2.5+x}{5})\sin(\pi \frac{2.7+y}{5}) \qquad [4.2]$$

where $A(t)$ is the amplitude of the membrane at the center of the cavity as a function of time, f is the frequency of excitation, h_o is the height of the orifice, and (a, b) are the dimensions of the cavity in the x and y directions respectively. It is worth mentioning here that the origin of the coordinate system is at the centerline of the geometry at the exit plane of the orifice.

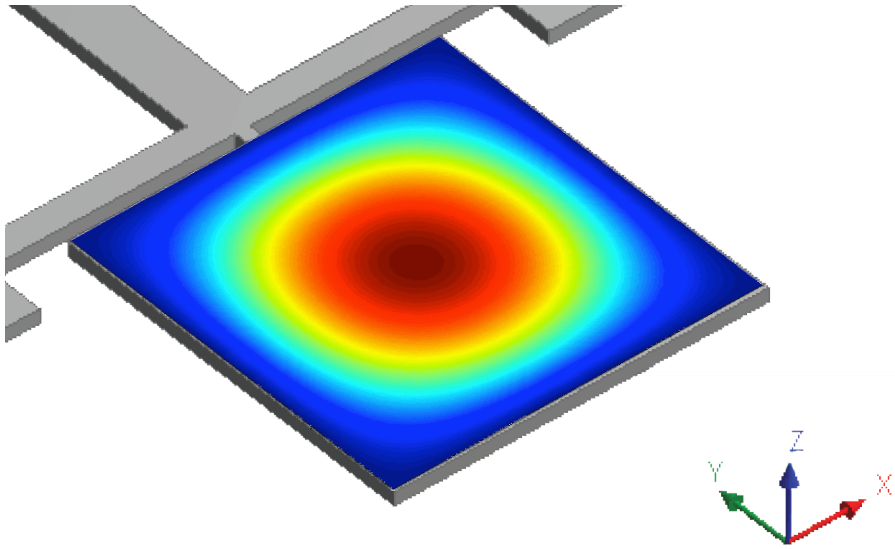

Figure 4.5 Membrane deflection mode shape.
(Colors represent amplitude of deflection from no deflection for blue to maximum deflection for red)

As will be discussed in Chapter 6, two forms of the temporal part of the membrane actuation signal function were used. The first of the two forms takes the shape of a regular sinusoidal signal in the form

$$A(t) = \frac{A_m}{2}\sin(\omega t) \qquad [4.3]$$

where A_m is the peak to peak membrane amplitude at the center of the membrane. This form was utilised to investigate the effect of the membrane amplitude and frequency on the performance of the micropump. The second form was utilised to study the effect of changing the ejection and suction duty cycles on the performance of the micropump by changing the period of the ejection and suction parts of the signal as will be discussed in details in Chapter 6. The form used in this case takes the form

$$A(t)=\begin{cases} \frac{A_m}{2}\sin\left(\omega\left(\frac{k+1}{2}\right)(t-nT)+\frac{\pi}{2}\right) & \text{for } nT \le t \le nT+\frac{T}{k+1} \\ \frac{A_m}{2}\sin\left(\omega\left(\frac{k+1}{2k}\right)(t-nT)+\frac{k-1}{k}\pi+\frac{\pi}{2}\right) & \text{for } nT+\frac{T}{k+1} \le t \le (n+1)T \end{cases} \quad [4.4]$$

where $T = 1/f$ is the overall period of excitation, n is an integer representing the cycle count, and $k = T_2/T_1$ is the duty cycle ratio defined as the ratio between the effective period of excitation of the suction part of the cycle, T_2, to that of the ejection part of the cycle, T_1. Further details of the choice of amplitude signal and the effect of the duty cycle on the micropump performance as well as a plot of the variation of the amplitude of excitation for different values of $k = T_2/T_1$ will be discussed in Chapter 6.

4.3.3 Walls & Symmetry

Due to the geometrical symmetry of the fluid domain, only one half of the total domain was simulated and one symmetry plane, along the y-z plane, was set accordingly, as shown in Figure 4.4. All the remaining boundaries were set to walls with no mesh motion settings.

4.4 Simulation parameters

The prototype that was experimentally tested utilizes electromagnetic actuation to drive the membrane motion. Hence, larger amplitudes of excitation and smaller frequencies were utilized in the simulations. Operating amplitudes were thus chosen

between 20 and 60 µm and the operating frequencies were chosen between 20 to 60 Hz. Different combinations of frequencies and amplitudes were simulated to investigate the effect of changing the operating parameters on the performance of the micropump as will be evident in Chapter 6.

The parameters that were varied through the simulations were the inlet channel width W_i (from 200 to 800 µm), the outlet channel half-width W_o (from 200 to 800 µm), the amplitude of excitation A_m (from 20 to 60 µm), and the frequency of excitation f (from 20 to 60 Hz).

The working fluid of choice was water and the default properties provided by the CFX materials properties for water were used. The fluid density used is 997 kg/m^3 and the fluid viscosity 8.89x10^{-4} Ns/m^2.

4.5 Solver Parameters

Transient laminar simulations with a high-resolution advection scheme and a second order backward Euler transient scheme were used for the simulations. Each simulation case is divided into two separate runs; the first of which is used to insure a steady solution is reached while the second utilizes the final results of the first run as a starting point to simulate one full cycle of membrane vibration after reaching steady state to collect the result set used in data analysis. In all simulation cases the time step used varies with the excitation frequency and is such that each full cycle of membrane

vibration is divided into 100 time steps, i.e. $\Delta t = T/100 = 1/100f$, where T and f are the period and frequency of excitation respectively. Each time step consists of a minimum of 2 and a maximum of 20 coefficient loops and convergence is set at an RMS residual value of 10^{-6}. The dependence of the solution on the chosen time step is discussed in Appendix A

The first run simulates 10 full cycles of membrane motion, i.e. 1000 time steps, to insure a steady solution is reached. This is achieved by monitoring the inlet and outlet flow rates as well as the velocity at the orifice exit plane. Results are recorded for this run every 10 time steps. In the second run, only one full cycle of the membrane motion is simulated, i.e. 100 time steps, using the final results for the first run as the initial values. Results in this case are recorded every time step. The dependence of the solution on the solution time is discussed in Appendix A.

Chapter 5

FABRICATION & EXPERIMENTAL SETUP

This chapter will discuss the process of making the synthetic jet micropump prototype. The chapter starts with the first attempt to use microfabrication methods utilised in the fabrication of microfluidic devices and electronic devices. The difficulties and problems faced with this kind of fabrication method will also be outlined. The chapter then discusses the use of micromachining to produce the necessary

microchannel and cavity structure required to produce the micropump. Following that, the experimental setup used to test the micropump prototype will be introduced and discussed.

5.1 Microfabrication approach

The initial approach in producing the micropump prototype was to utilize standard microfabrication techniques to produce the device through the use of photolithography in conjunction with rapid prototyping. One of the most widely used techniques in microfluidic device fabrication is the use of rapid prototyping of PDMS (Polydimethylsiloxane) as it allows for rapid production of relatively inexpensive prototypes with the flexibility of easily altering the device design. In rapid prototyping, usually a mould is created by patterning a photoresist material, usually SU-8, on a substrate, usually made of silicon, which is then used as a mould to shape the PDMS used for the device. As PDMS possesses a considerably low modulus of elasticity, even for the highest mixing ratio between elastomer to curing agent, it was evident that it might not be the optimal material to use to produce the channel and cavity geometries for this device as it might not withstand high pressures produced by the actuation of the pump.

As the use of PDMS in rapid prototyping utilizes a mould created from a photoresist to pattern the PDMS, it was suggested to try to use the photoresist material

itself as the building material of the channel structure. It was decided to use SU-8 2000 photoresist provided from MicroChem in this case to pattern the channel and cavity structure on a glass substrate. SU-8 2000 is a high contrast epoxy based negative photoresist capable of producing thick structures. The SU-8 layer thickness required in this case was the depth of the structure of 200 μm and hence SU-8 2075 was the SU-8 variant of choice capable of producing such thickness in a single coat.

In order to allow for visual access to the micropump structure, a glass substrate is used on top of which a layer of SU-8 2075 is spin coated, then prebaked. This layer of photoresist is then UV exposed using the mask shown in Figure 5.1 and then baked again before being developed to form the desired cavity and channel structure.

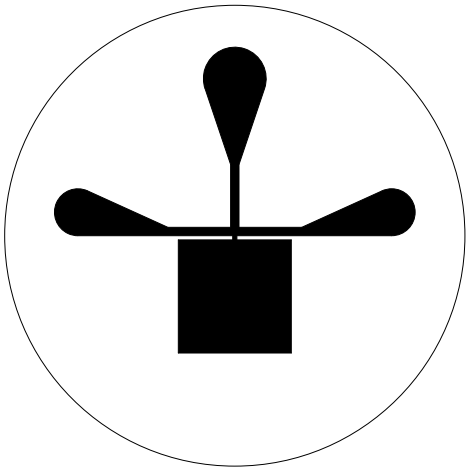

Figure 5.1. Mask used for SU-8 photoresist exposure.

The resulting prototype using this fabrication method is shown in Figure 5.2. The produced glass substrate with the channel geometry is visually aligned under a

microscope with the bottom plexiglass part containing the piezoelectric actuator and the PDMS membrane. The whole assembly is then held together using the external housing.

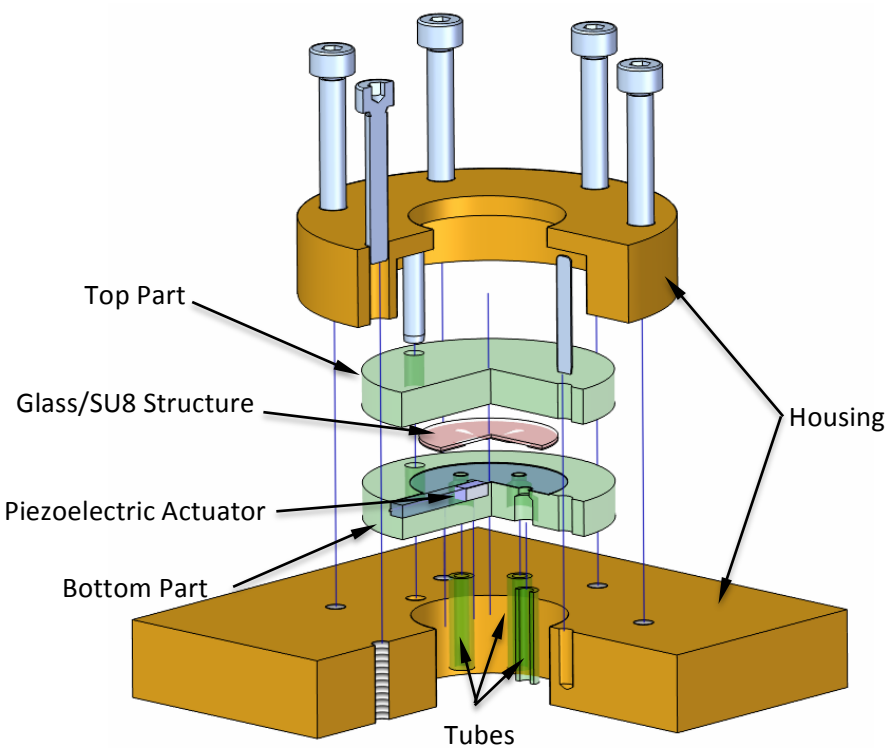

Figure 5.2. Model of the produced prototype using the microfabriaction method.

5.1.1 Limitations

Several issues arose when using photolithography to realize the device both as a result of the photolithographic process itself as well as with other parts of the device. These issues can be summarized in three main categories:

5.1.1.1 Photolithography problems

The process of creating the channel structure in SU-8 photoresist using photolithography encountered several problems that led to preferring the micromachining approach discussed later. The first of these problems was the fact that the process flow supplied by the manufacturer did not produce the desired thicknesses of the SU-8 layer and the process had to be modified in order to increase the produced thickness. The largest thickness that was produced with the photoresist was about 180 µm.

Another problem that was encountered was the fact that the produced top surface of the structure was not flat. Due to the large thickness of the SU8 layer deposited on the glass substrate, the top surface had waviness in its surface and the edges of the layer tended to be rounded and not flat. Another issue that was faced was the poor adhesion between the photoresist layer and the glass substrate, that caused a lot of the produced samples to fail completely or for parts of the layer not to adhere properly to the substrate causing leakage of liquid especially at the narrow structure around the cavity orifice. Certain procedures were investigated to improve the adhesion of SU-8 to glass but did not solve the problem completely. Produced structures also faced a few issues concerning degraded removal of the undesired photoresist while developing due to reflections of UV exposure light from the bottom glass substrate

surface. Coating the unused glass surface with an opaque coating did not significantly improve the quality of the photoresist development.

5.1.1.2 Assembly problems

During assembly of the different parts of the device together, it was realized that the unevenness of the surface of the Glass/SU8 structure caused two major problems. First of all, it was quite difficult to prevent leakage from between the top and bottom parts of the pump in most cases. This also caused some of the samples to break due to the uneven forces exerted on the thin glass substrate due to the surface unevenness.

5.1.1.3 Actuator problems

The actuator utilized for this design is a square shaped piezoelectric actuator (PI PL022.30) 2x2x2 mm in dimensions capable of producing 2.2 µm of amplitude. In this design the actuator is placed in a machined groove in the bottom part of the pump assembly where it is glued to the bottom surface of the groove before PDMS is poured on top of it to form the membrane and a sealing layer on the top surface of the bottom part, as shown in Figure 5.2, which is then allowed to cure. Although, preliminary numerical simulations showed that using such low amplitudes of excitation can still produce flow from the micropump if actuated at high frequencies of the order of 1-2 kHz, this was not possible using such setup. This could be attributed to the fact that with such small amplitudes of excitation, any defects in gluing the actuator could result in the resulting strain in the piezoactuator causing a strain in the glue layer rather than

pushing the membrane upwards. Moreover, the same behaviour could occur for the PDMS membrane which could simply be strained on its lower surface while its upper surface facing the cavity would be hardly moving.

5.2 Micromachining approach

To overcome the challenges faced with the initial prototype design discussed above, it was decided to utilise a different actuation mechanism that can warrant the ability to produce larger amplitudes of vibration while maintaining roughly the same size of cavity. Magnetic actuation was chosen for this case, whereby a magnet is embedded into the vibrating membrane and an external electro-magnet is used to provide a fluctuating magnetic field around that magnet forcing it to vibrate. Moreover, in the modified design process, a new method of manufacturing the micropump using standard micromachining processes was utilized.

5.2.1 Device design

The new device is machined into two pieces of plexiglass that are then clamped together and checked for leakage. The device is assembled visually under a microscope and the two plexiglass parts of the pump are sealed by using a thin film of polyethelene approximately 13 µm thick. A detailed drawing of the micromachined channel strucure and the device asembly are shown in Figure 5.3 and Figure 5.4.

The top part constitutes the top surface of the channels as well as the support that clamps the membrane into place above the cavity and aids in aligning the membrane with the cavity. It is machined using standard milling techniques. The bottom part is milled on a precision 3-axis vertical milling CNC machine (Matsuura FX-5G) using micromachining methods made possible by the use of a carbide end mill with a cutting edge diameter of 0.2 mm. The tool was provided by OSG tooling and has a part number of EXOCARB-HP 8544102. The tool was used to machine the channel, orifice, and cavity geometries and regular tools were used to drill the inlet and outlet ports.

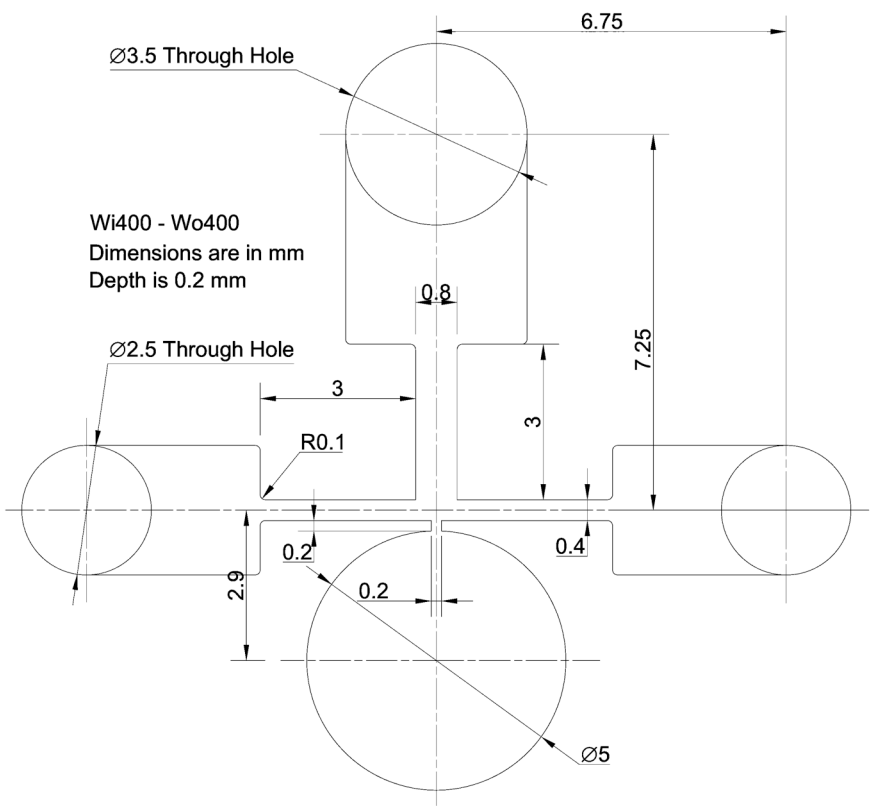

Figure 5.3. Micromachined channel structure.

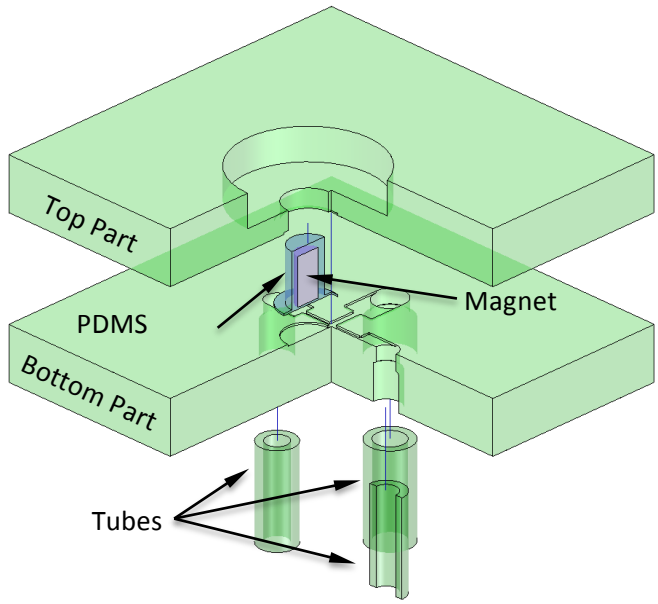

Figure 5.4. Three dimensional model cut-out of micromachined micropump design assembly.

5.2.2 Membrane structure

The membrane used for this design is made out of PDMS with an embedded magnet that is used in conjunction with an external electromagnet to actuate the micropump. Sylgard 184 PDMS with a ratio of 1:10 of curing agent to elastomer base is utilised to provide the highest stiffness possible for PDMS. Neodymium (NdFeB) magnets are embedded into the membrane structure during the curing process. A schematic model of the mould and the produced membrane structure are shown in Figure 5.5.

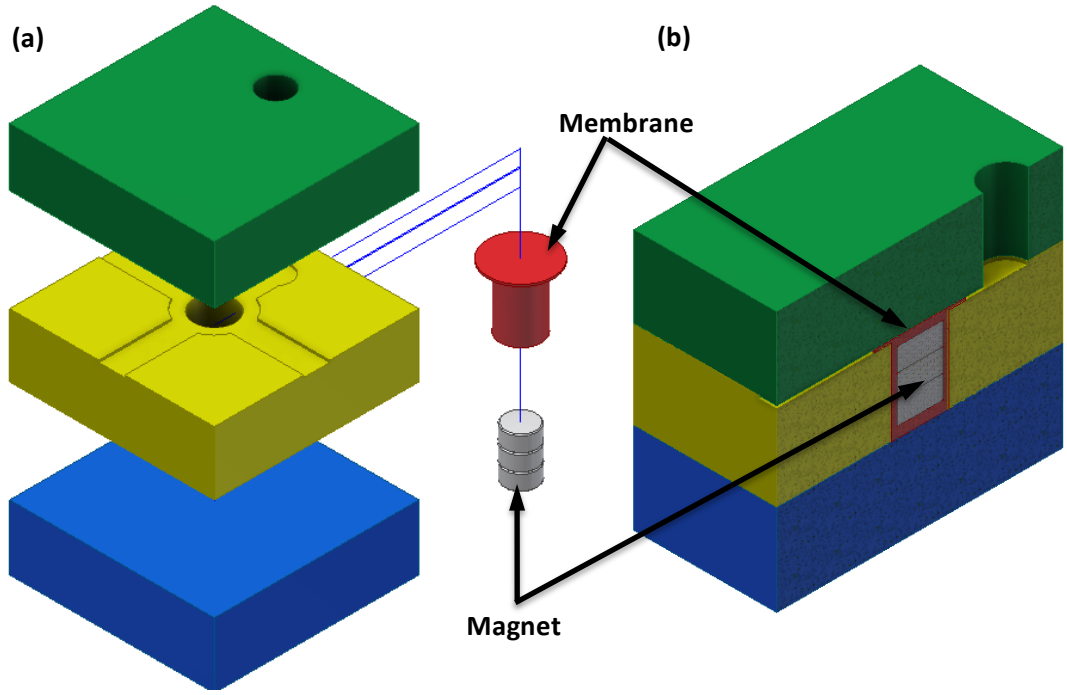

Figure 5.5. Schematic of the mould used to create the membrane structure.
(a) Exploded view. (b) Assembled view

The three parts of the mould are clamped together during the curing process. The magnet is initially suspended in the liquid PDMS until it is cured. To insure the magnet remains aligned, two magnets are attached to the top and bottom surfaces of the mould and aligned with the magnetic field of the embedded magnet to insure the magnet stays suspended approximately at the desired position. The side branched channels on each side of the mould ensure that any excess liquid can drain to the sides and also helps reduce any shrinkage during the curing process by providing excess liquid PDMS especially from the riser on one of the sides. After the curing process is completed, the membrane structure is released from the mould and excess parts of PDMS are removed.

5.3 Experimental Setup

In order to perform experimental investigations of fluid flows in microdevices and to characterize their performance, measurement of flow related properties, such as the flow velocity and pressure, are required. This is not a straight forward task as with macroscale flows due to the very small scale of the devices as well as the difference in behaviour of the physical property used by the sensor to perform the measurement as discussed above. Hence, traditional flow measuring techniques need to be modified or new measuring methods must be introduced to enable such flow measurements. Such a task is not an easy or straightforward one and this is one of the main reasons why the majority of microfluidic research utilizes numerical simulations rather than experimental measurements to characterize the performance of microdevices.

For the research undertaken in this thesis, the main focus is on measuring the performance of the micropump in terms of flow rate and pressure head across the pump. Hence, the main parameters that need to be measured are the operating variables in terms of amplitude and frequency of excitation, as well as the flow rate produced by the pump and the static pressure difference between the pump inlet and outlet. A schematic layout of the experimental setup is shown in Figure 5.6. The following sections will detail the different components of the setup as well as the measurements performed.

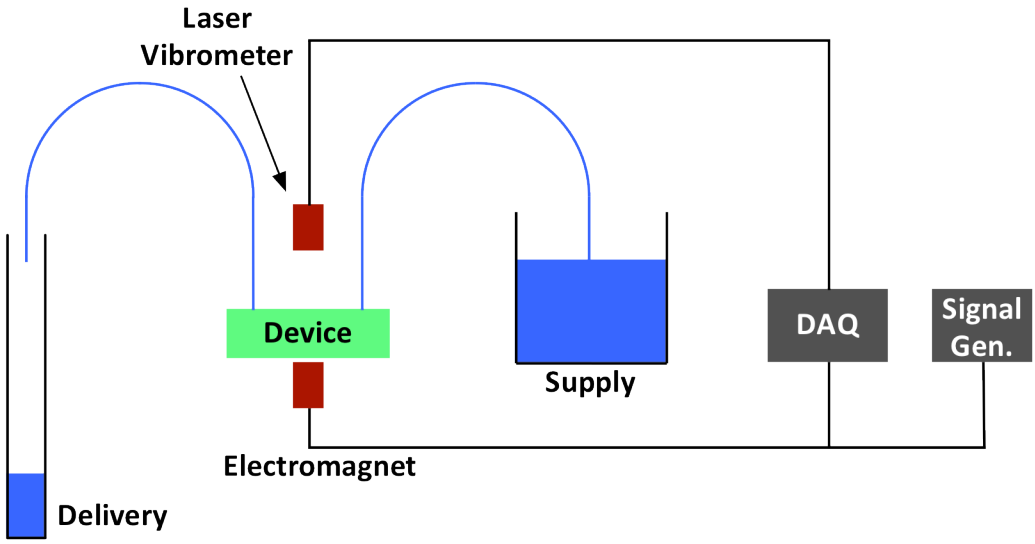

Figure 5.6. Schematic layout of the experimental setup

5.3.1 Liquid supply and delivery

The inlet and outlet ports of the micropump are connected to tubes that transport the fluid to and from the outlet and inlet reservoirs. Tygon R-3603 tubes are used with inner/outer diameters of 2.38 mm (3/32”)/3.97 mm (5/32”) for the inlet tubes and 3.175 mm (1/8”)/4.763 mm (3/16”) for the outlet tubes to maintain approximately an equal total flow cross sectional area. All three tubes are the same length of approximately 150 mm.

5.3.2 Measuring flow rate

Since detailed measurements of flow velocity or flow rate inside the micropump channels is quite difficult given the small size of the device, relying on basic global measurements was necessary. As such, the flow rate is measured by noting the time it

takes to collect prescribed volumes of fluid from the outlet of the micropump. The time taken to collect 1, 2, 3, 4 and 5 ml of fluid is recorded for each set of operating settings and then the flow rate is calculated for each. The calculated values of flow rate are then analyzed to obtain the average value as well as the standard deviation in the measurements.

5.3.3 Measuring head

The tubes connected to the inlet of the micropump are submerged into the source reservoir and the outlet tube tip location is adjusted to control the static head value relative to the liquid level in the supply reservoir. For the maximum flow rate measurements it was positioned at the same level as the surface of the liquid in the inlet reservoir resulting in no head. For the measurements of the maximum backpressure, the outlet tube was positioned vertically and the maximum elevation the liquid rises to in the outlet tube was recorded to calculate the maximum head that can be generated by the pump.

5.3.4 Membrane actuation

In order to provide the vibrating motion of the membrane, a variable magnetic field is required in order to induce the vibrating motion of the embedded magnet in the membrane. An electromagnet consisting of a coil wound around an iron core and connected to a signal generator and amplifier is used to provide the required magnetic

field. The electromagnet actuator is supplied with a sinusoidal input at the specified frequency and the voltage supplied to the actuator is adjusted until the desired amplitude of excitation is obtained.

The gap between the electromagnet and the membrane structure is adjusted visually and minimized as much as possible to provide the strongest possible magnetic forces. Since there is no control in the test setup over the gap between the electromagnet and the membrane structure as a way to measure the electromagnetic force acting on the embedded magnet in the membrane, it was not possible to evaluate the power required to run the micropump using the current setup.

5.3.5 Measuring membrane deflection

The vibrating membrane motion was monitored using a laser displacement sensor. A Keyence LK-G82 CCD laser displacement sensor was used and calibrated to measure the displacement of the membrane by utilizing the reflection of the laser beam off of the surface of the magnet embedded in the membrane. Although the sensor can readily measure the displacement of objects directly, a calibration was required in this case to ensure proper measurement of the motion of the membrane. This is due to the fact that reflections or refractions off of the surface of the plexiglass top cover of the pump or the PDMS membrane surface can cause errors in the measurements.

A static calibration of the laser sensor was performed by using a micrometer attached to the bottom side of the membrane structure. A calibration coefficient of 0.7 was used based on the calibration data. Details of the laser displacement censor calibration and sample experimental measurements can be found in Appendix B.

Chapter 6

RESULTS & DISCUSSION

In this chapter the results of both the numerical simulations and the experiments will be presented. The main objective of this study is to investigate the possibility of producing a working micropump using the synthetic jet principle and then study the performance of such micropump under different actuation conditions as well as investigate the effect of different geometrical factors on the performance of the pump. The first part of the chapter will discuss some general findings and considerations which will be utilized for presenting results in later sections. The chapter then introduces the

results of the numerical simulations and the effect of varying the actuation parameters as well as the geometry of the inlet and outlet channels. This will be followed by the results of the experimentation carried out on a prototype of the micropump. The experiments focus mainly on the effect of actuation parameters on the performance of the pump in order to validate the findings of the numerical simulations. The chapter then concludes with a discussion of the findings of both the numerical simulations and the prototype testing.

6.1 Basic parameters of the micropump

Some general terminologies, ideas and concepts that will be utilised in presenting and discussing the results are introduced in this section. These include the general definitions of the average, maximum and minimum flow rates reported for the numerical simulation results, the normalization of the membrane amplitudes between the numerical and experimental studies to be able to compare the two sets of results, as well as a discussion of the formation parameters and criteria of the synthetic jet actuator. We will start with the parameters which characterize the synthetic jet and thereafter focus our attention on those controlling the overall performance of the micropump.

6.1.1 Stroke Length:

The dimensionless stroke length (L_o/d_o) represents the length of slug of fluid pushed out of the cavity during the expulsion stroke of the actuation cycle and is defined as:

$$L_o = \int_0^{\tau} u_o(t)\,dt \qquad [6.1]$$

where $u_o(t)$ is the area-averaged velocity over the orifice cross-section at the exit plane of the orifice, $\tau = T/2$ is the time of discharge during one cycle of the membrane motion, and d_o is the orifice width.

In the current study, the stroke length is determined from the numerical simulations by calculating the area-averaged velocity at the exit plane of the orifice ($u_o(t)$) at each time step during one full actuation cycle and integrating these values over the expulsion part of the actuation cycle.

For the experimental measurements, the stroke length is determined by assuming the deflection mode shape of the membrane and using continuity to infer an expression for the average velocity at the orifice exit as follows: Starting by the expression for the membrane deflection

$$Z(r,\theta,t) = \frac{A_m}{2}\sin(\omega t)M(r,\theta) \qquad [6.2]$$

where $Z(r,\theta,t)$ is the magnitude of deflection of each point on the membrane, defined in polar coordinates (r,θ) as the membrane is circular in shape, at any time t, A_m is the recorded peak to peak amplitude of the membrane, $\omega = 2\pi f$ is the frequency of the excitation signal and $M(r,\theta)$ is the function representing the mode shape of the membrane deflection. By integrating the deflection $Z(r,\theta,t)$ with respect to the spatial coordinates, an expression for the instantaneous volume displaced by the membrane can be obtained as

$$V(t) = \frac{A_m}{2}\sin(\omega t)\int_0^{2\pi}\int_0^{r_c} M(r,\theta) r\, dr\, d\theta = \frac{A_m F}{2}\sin(\omega t) \qquad [6.3]$$

where $V(t)$ is the instantaneous displaced volume by the membrane, r_c is the radius of the cavity and

$$F = \int_0^{2\pi}\int_0^{r_c} M(r,\theta) r\, dr\, d\theta \qquad [6.4]$$

Since continuity necessitates that the volume displaced by the membrane is equal to the volume moving through the orifice, then

$$a_o u_o(t) = \frac{dV(t)}{dt} = \frac{A_m \omega F}{2}\cos(\omega t) \qquad [6.5]$$

where a_o is the cross-sectional area of the orifice and $u_o(t)$ is the area averaged velocity at the orifice. Thus $u_o(t)$, L_o become

$$u_o(t) = \frac{A_m \omega F}{2a_o}\cos(\omega t) \qquad [6.6]$$

$$L_o = \int_{-\tau/4}^{\tau/4} u_o(t)\,dt = \frac{A_m F}{a_o} \qquad [6.7]$$

Based on the construction of the actuator membrane, $M(r,\theta)$ can be determined or estimated and hence the value of the formation length for the experimental results can be determined. This will be further discussed in Section 6.1.4 below. In this study, the values of the dimensionless stroke length, L_o/d_o, tested were up to about 75.

6.1.2 Reynolds Number

Two Reynolds numbers can be used to identify synthetic jets: A Reynolds number based on the average orifice outflow velocity and the orifice width

$$\mathrm{Re}_{U_o} = \frac{\rho U_o d_o}{\mu} \qquad [6.8]$$

where the average orifice outward velocity U_o is given by

$$U_o = \frac{L_o}{T} \qquad [6.9]$$

and μ, ρ and T are the fluid viscosity, density and period of oscillation of the driver respectively. The other Reynolds number is based on the impulse per unit width and the orifice width

$$\mathrm{Re}_{I_o} = \frac{I_o}{\mu d_o} \qquad [6.10]$$

where the impulse per unit orifice width I_o can be given as

$$I_o = \rho d_o \int_0^{\tau} u_o^2(t)\,dt \qquad [6.11]$$

For the current study, the values of the Reynolds number based on the average orifice outflow velocity, Re_{U_o}, ranged from about 5 to 120, while values of the Reynolds number based on the impulse per unit orifice width, Re_{I_o}, ranged from about 75 to 23,000.

6.1.3 Formation Criterion

According to the work of Utturkar et al (2003) and Holman et al (2005), the proposed formation criterion for a synthetic jet is that

$$\frac{1}{St} = \frac{\bar{U}}{\omega d_o} = \frac{2U_o}{\omega d_o} = \frac{\mathrm{Re}_{\bar{U}}}{S^2} = \frac{2\,\mathrm{Re}_{U_o}}{S^2} > K \qquad [6.12]$$

where $Re_{\bar{U}}$ is the Reynolds number based on the average orifice outflow velocity

$$\mathrm{Re}_{\bar{U}} = \frac{\rho \bar{U} d_o}{\mu} \qquad [6.13]$$

and

$$\bar{U} = \frac{2}{T}\int_0^{\tau} u_o(t)\,dt = 2U_o \qquad [6.14]$$

is the average orifice velocity, $S = \sqrt{\frac{\omega d_o^2}{\nu}}$ is the Stokes number, $\omega = 2\pi f$ where f is the frequency of excitation of the vibrating membrane, and $St = \frac{\bar{U}}{\omega d_o}$ is the Strouhal number

based on the average orifice outflow velocity. The value of K in Equation [6.14] is approximately 2 for two-dimensional synthetic jets and 0.16 for axisymmetric ones.

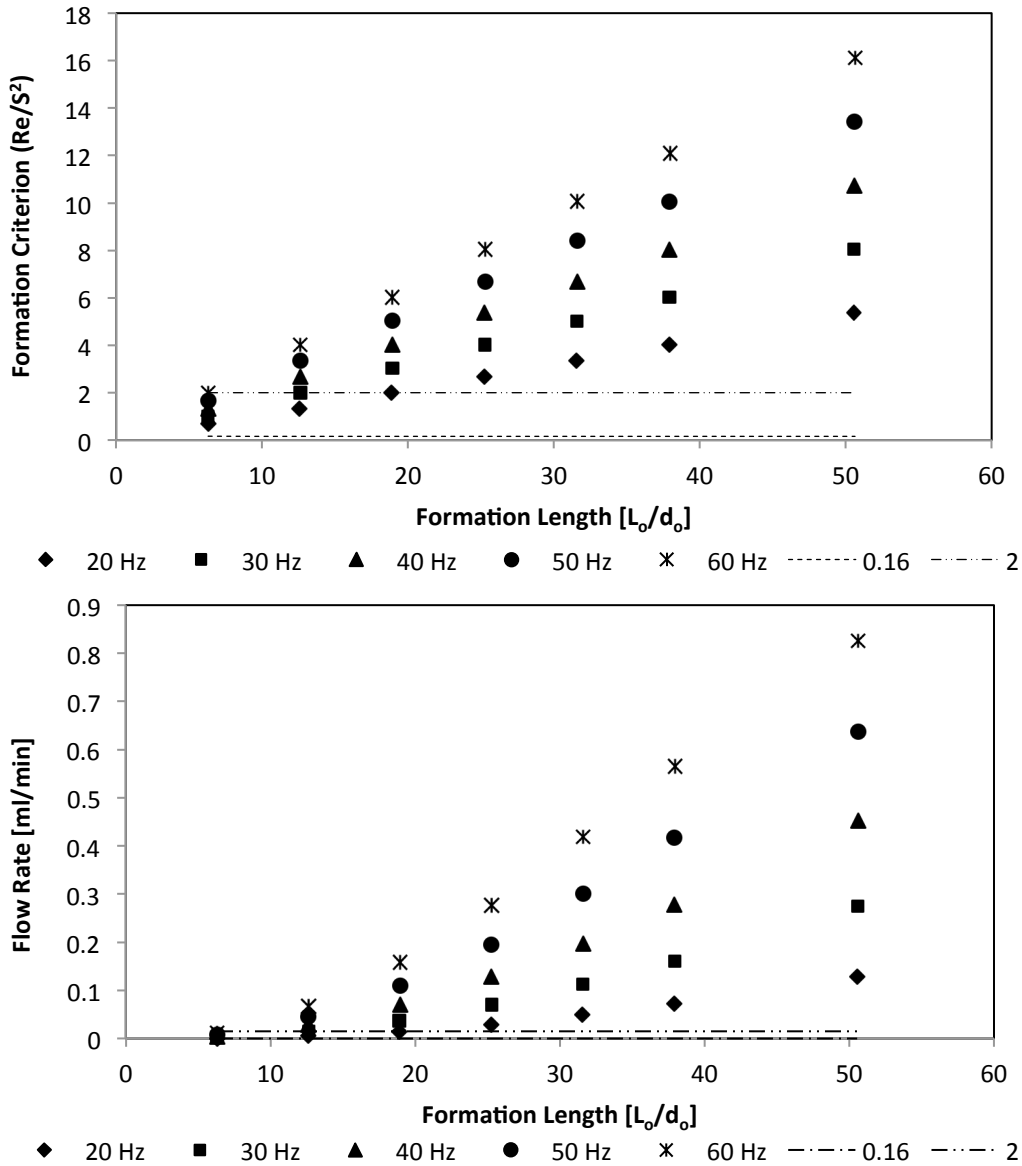

Figure 6.1. Variation of formation criterion or flow rate with formation length for different values of excitation frequency.
[Dotted lines represent values of formation criterion or flow rate corresponding to a formation criterion threshold value of 2 or 0.16 as reported in the literature for 2D and axisymmetric jets respectively].

Based on the above parameters, Figure 6.1 shows values of the formation criterion and flow rates plotted for test cases based on the numerical simulation results for different amplitudes and frequencies of excitation. It can be seen from the figure that in fact for very low excitation amplitudes and frequencies, where reported flow rates are very low or close to zero, the corresponding value of the jet formation criterion is in the range of 2 as reported in the literature.

6.1.4 Excitation amplitude correction

When comparing the results of the numerical simulations with those of the prototype testing, it has to be noted that the cavities have different shapes and the membranes have different mode shapes of excitation. Hence, in order to be able to compare the variation of the flow rate for different excitation amplitudes between different test sets, a common or equivalent amplitude of excitation has to be used.

In the case of the numerical simulations there is one square membrane on one side of the cavity 5 mm on a side. The membrane was modeled as a moving flexible wall whose motion is described as

$$Z(x,y,t) = \frac{A_m}{2}\sin(\omega t)M(x,y) \qquad [6.15]$$

where

$$M(x,y) = \sin(\pi\frac{2.5+x}{5})\sin(\pi\frac{2.7+y}{5}) \qquad [6.16]$$

and x, y are the coordinates in the plane of the membrane with the center point of the membrane at $x = 0$ mm, $y = -2.7$ mm from the origin , A_m is the peak to peak amplitude of excitation, $\omega = 2\pi f$ is the frequency of excitation and t is time.

The instantaneous displaced volume can then be obtained as

$$V(t) = \int_{-5.2}^{-0.2} \int_{-2.5}^{2.5} Z(x,y,t)\,dx\,dy = \frac{A_m F}{2}\sin(\omega t) = \frac{10^{-4}}{\pi^2}\frac{A}{2}\sin(\omega t) \qquad [6.17]$$

The actual membrane used in the experiments is circular in shape with a diameter of 5 mm and is clamped around the edges. Similar to the numerical simulation vibration amplitude, the membrane vibration can be represented as

$$Z(r,\theta,t) = \frac{A_m}{2}\sin(\omega t) M(r,\theta) \qquad [6.18]$$

As the amplitude measurements in the case of the experimental setup depend on a single point measurement at the center of the cavity, it is not possible to obtain the actual mode shape of the membrane excitation, $M(r, \theta)$. An approximation can be utilized based on the expected shape that the membrane vibration. A sketch of the membrane structure, shown in Figure 6.2, lends to the following possibilities to approximate the vibration of the membrane:

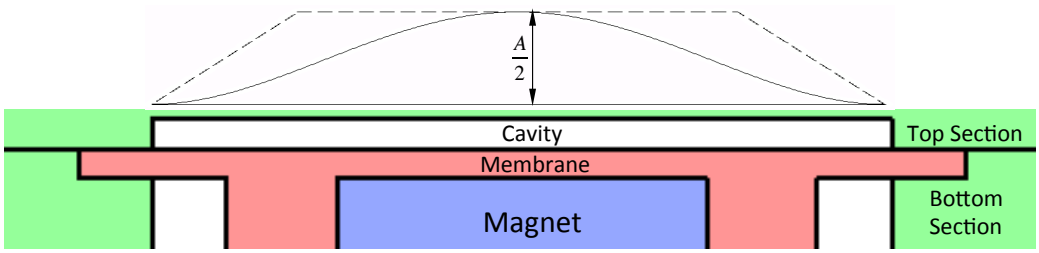

Figure 6.2. Schematic of proposed mode shapes for the circular membrane used in the experimental setup.

- The mode shape of a vibrating circular disc clamped on the edges (ignoring the effect of the magnet at the center part of the disc)

$$M(r,\theta) = J_0\left(\frac{\lambda r}{2.5}\right) - \frac{J_0(\lambda)}{I_0(\lambda)} I_0\left(\frac{\lambda r}{2.5}\right) \qquad [6.19]$$

and J_0, I_0 are Bessel functions and modified Bessel functions of the first kind respectively and $\lambda^2 = 10.22$. This can be integrated numerically using Matlab to obtain the displaced volume per cycle.

The displaced volume in this case can be found to be

$$V(t) = \frac{A_m F}{2} \sin(\omega t) \qquad [6.20]$$

where F is obtained numerically using Matlab to integrate the membrane mode shape.

- Assuming a flat motion of the part of the membrane top surface opposite to the magnet embedded in the membrane structure. In this case, the displaced volume is

$$V(t) = \frac{A_m F}{2}\sin(\omega t) = \frac{1.225\times10^{-5}\pi}{3}\frac{A_m}{2}\sin(\omega t) \qquad [6.21]$$

It can be seen from the above discussion that although the provided maximum displacement at the centerline of the vibrating membrane, A_m, is the same in all cases, the resulting displaced volume is different from one case to the other. This has led to the necessity of finding a common representation of the actuation amplitude. Since the formation length represents a non-dimensional representation of the strength of the synthetic jet and takes into account the displaced volume of the cavity, as it is directly proportional to the velocity at the orifice, it was chosen as a representation of the amplitude of excitation when comparing numerical results to experimental ones. Moreover, it was found that the use of the mode shape of a clamped circular disc for the vibrating membrane in the experimental part provides the closest match between the results of the numerical and experimental results, thus it was chosen to be the method of representing the mode shape of deflection of the membrane and hence in calculating the formation length and the Reynolds number.

6.1.5 Flow rates

Due to the pulsating nature of the synthetic jet occurring during an actuation cycle, the flow rates at both the pump inlet and outlet are not uniform but are periodic. As such, the net flow rate of the pump always refers to the time averaged flow rate at

either the inlet or the outlet. A sample time plot of the flow rate at the inlet and outlet of the pump for a given geometry and actuation is shown in Figure 6.3.

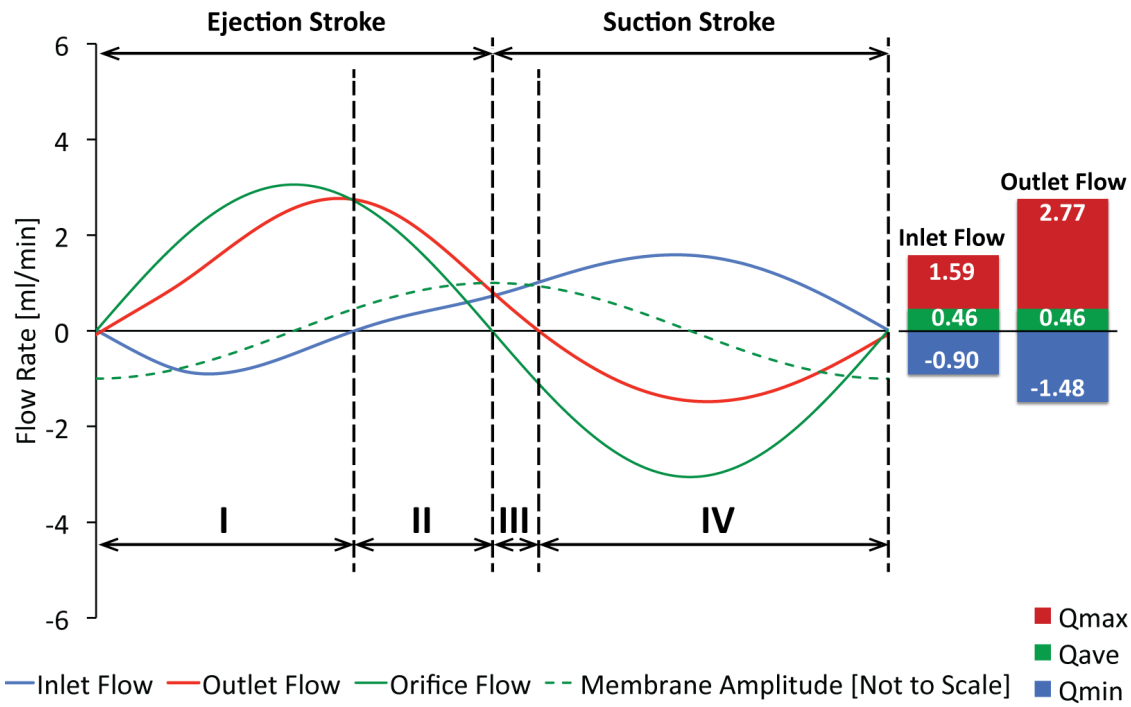

Figure 6.3. Sample flow rates from numerical simulations for the base case. A_m = 40 µm, f = 40 Hz, W_i = 400 µm and W_o = 400 µm. [A positive flow rate indicates flow in the forward direction (from inlet to outlet) and a negative flow rate indicates reversed flow. For the orifice flow, positive indicates flow out of the cavity and negative indicates flow into the cavity].

Figure 6.3 shows one full actuation cycle for a sample case, which will be referred to thereafter as the base case, with an amplitude of excitation A_m = 40 µm, frequency of excitation f = 40 Hz, inlet channel width W_i = 400 µm and outlet channel width W_o = 400 µm. This case, with this given combination of the geometrical and actuation parameters, will be considered the basis for comparison with other cases as discussed in the following sections.

The cycle starts at the beginning of the expulsion stroke of the membrane, where the membrane is at its lowest, or outermost, position and the volume of the cavity is at its maximum. It can be seen that during the expulsion stroke, the flow through the cavity is outwards, while during the suction stroke of the membrane, it's inwards. The flow at the outlet and inlet of the pump is also seen to be periodic with the same frequency as the excitation. Both flows have parts during the cycle where the flow is reversed. However, the net time averaged flow rate generated by the pump, Q, is positive. The right part of the figure shows the maximum, minimum and average values of flow rate reported at the inlet and outlet of the pump and shows that although the average flow rate is only 0.46 ml/min, the instantaneous flow rate fluctuates as high as 2.8 ml/min and as low as -1.5 ml/min at the outlet and as high as 1.6 ml/min and as low as -0.9 ml/min at the inlet for this specific case shown. Additional details of the flow for the base case are discussed in the following section.

6.2 The base case

As mentioned in the previous section, the reference, or base case, which is to be used as the basis of comparison to study the effect of different parameters on the performance of the pump has an amplitude of excitation A_m = 40 µm, frequency of excitation f = 40 Hz, inlet channel width W_i = 400 µm and an outlet channel half width

W_o = 400 µm. In order to better understand the behaviour of the pump, the flow features during the operation of the base case are discussed in more details.

Figure 6.5 [(i) to (v)] shows streamlines, velocity vectors, velocity profiles in the outlet channel and velocity profiles in the inlet channel for nine instances of time during one actuation cycle starting at the beginning of the expulsion stroke. The plane used to visualize the velocity vectors and streamlines is located at the mid-height of the device as shown in Figure 6.4. Velocity profiles are provided along lines at three different locations at the middle of the channel and both ends of the channel on the same plane. As the membrane moves upwards, expelling liquid from the cavity, a jet can be seen to form (instance [B] in Figure 6.5) with the characteristic vortex pair of synthetic jets appearing just downstream of the orifice. As the cycle progresses, the vortex pair convects downstream and enters the outlet channel as shown in instance [C] in Figure 6.5. During the suction stroke (instances [E] through [I] in Figure 6.5) fluid is drawn from both the inlet and the outlet to enter the cavity as shown in the figure.

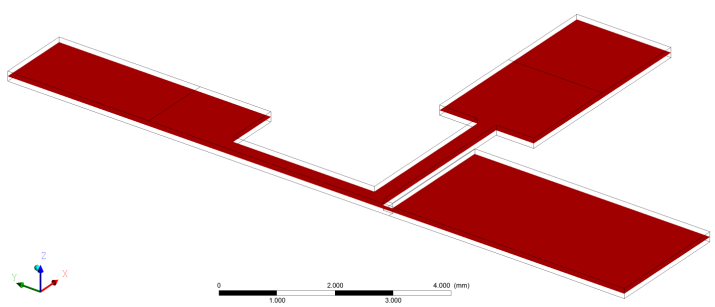

Figure 6.4. Location of the plane used to plot the streamlines and velocity vectors shown below.

The cycle can be divided into four main parts based on the behaviour of the membrane (whether in suction or ejection) and the behaviour of the flow at both the inlet and the outlet. The ejection stroke can be divided into two main parts, indicated by “I” and “II” on Figure 6.5 (i), while the suction stroke can be divided into two other parts “III” and “IV”. Part “I” is characterized by fluid flowing outward from both the inlet and outlet channels, while in part “II” the inlet flow reverses direction while the outlet flow continues to flow outwards. The same behaviour extends to part “III” during the suction stroke. In part “IV” the outlet flow reverses direction and both the inlet and outlet channels supply fluid into the pump domain.

Initially in Part “I”, between time periods [A] and [B] in Figure 6.5, the fluid being ejected from the orifice due to the increased pressure in the cavity does not exhibit a preferred direction and causes an outward flow from both the inlet and outlet channels of the micropump, as indicated by the positive value of flow rate at the outlet and negative value at the inlet. As the flow progresses past point [B] the vortex pair, characteristic of synthetic jets, forms at the orifice exit area and starts convecting into the outlet channel. As the vortex pair convects into the outlet channel, the reversed flow caused by the circulation around the vortex cores, which is initially directed towards the inlet channel and contributes to the outward flow from the inlet, starts being entrained into the vortex circulation, as indicated by the arrows in instance [C] in

Figure 6.5 (ii) and (iii), and the flow rate at the inlet starts decreasing until ultimately reaches zero at the end of stage “I”.

This is more evident by looking at the outlet channel velocity profiles at Y=0.4 mm at [B] in Figure 6.5 (iv) as well as the inlet channel velocity profiles at X=0.4 mm at [B] in Figure 6.5 (v). The outlet channel profile shows that the major part of the flow is directed towards the outlet of the channel with reversed flow at the outer edges of the channel which are then directed towards the inlet channel towards the pump inlet as indicated by the increased flow velocity at the inlet channel top side.

By the time stage “II” starts, the vortex pair has fully entered the outlet channel and convects downstream the channel (evident by the presence of a negligible reversed flow region by the time stage [D] is reached in Figure 6.5 (iv) at Y=0.4 mm). As the flow issuing from the orifice is decreasing as well during that stage, the convection of the vortex pair slows down causing a reduction in the flow rate at the outlet as well as causing fluid to be entrained from the inlet channel due to the convection of the vortex pair as indicated by the increasing positive inlet flow rate in the inlet channel during stage “II”. This entrainment stage extends a little beyond the end of the ejection stroke, and into stage “III”.

In stage “III”, the membrane starts reversing direction causing suction of fluid into the jet cavity. During that stage the inlet flow is the main contributor to the fluid sucked

into the cavity, as the flow in the outlet channel is still directed outwards due to the convection of the vortex pair. By the end of stage “III”, it can be seen that the outlet flow as well reverses direction and the fluid being sucked into the cavity is being supplied through both the inlet and outlet channels.

Stage “IV” is mainly characterized by fluid being directed into the jet cavity by both the inlet and outlet channel flows and by the end of that stage both inlet and outlet channel flows start reversing direction again with the initiation of a new actuation cycle.

In conclusion, the results presented for the base case, suggest that the net positive flow produced by the pump is produced in part by the effect of delivering fluid into the outlet channel in the expulsion stroke while drawing fluid mainly from the inlet channels during the suction stroke as well as the effect of the entrainment of fluid from the inlet to the outlet caused by the convection of the vortex pair in the outlet channel. This behaviour can be observed for the other cases presented in the following sections as well and shown in the details of all the cases presented as found in Appendix D.

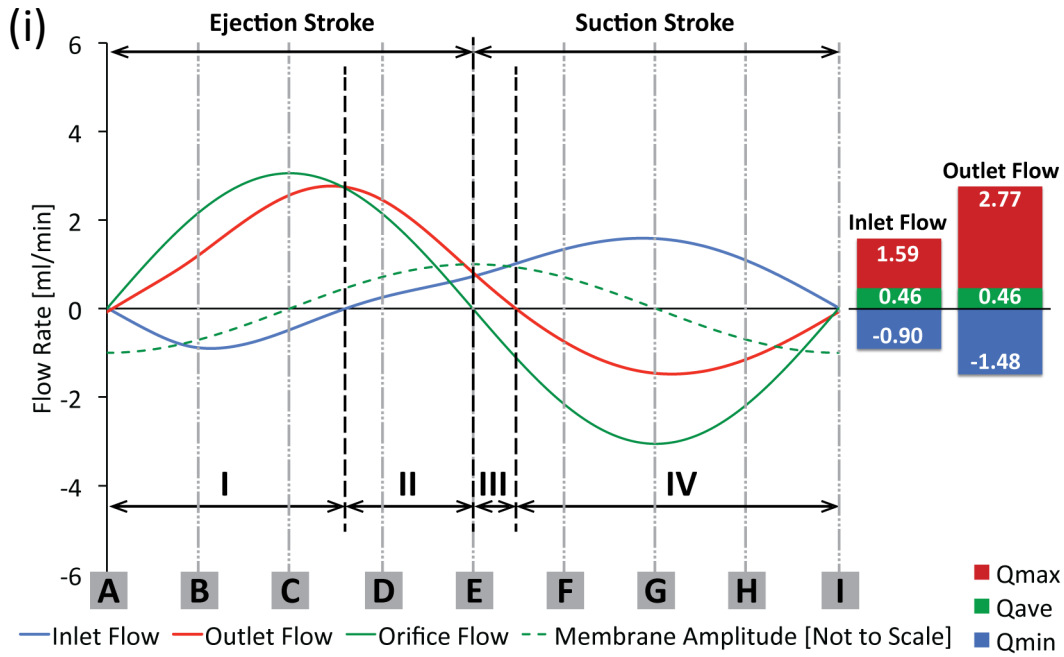

Figure 6.5. Details of flow rates and flow field for the base case.
(i) [above] Cycle flow rates [A positive flow rate indicates flow in the forward direction (from inlet to outlet). For orifice flow, positive indicates flow out of the cavity].
Letters on the figure indicate instances along the actuation cycle where details of the flow field are shown in parts ii to v of the figure as follows:
[A] t/T=0.000, [B] t/T=0.125, [C] t/T=0.250,
[D] t/T=0.375, [E] t/T=0.500, [F] t/T=0.625,
[G] t/T=0.750, [H] t/T=0.875, [I] t/T=1.000.
(ii) [Page 121] Streamlines coloured by the velocity magnitude at the mid-height plane of the micropump.
(iii) [Page 122] Velocity vectors coloured by the velocity magnitude at the mid-height plane of the micropump.
(iv) [Page 123] Velocity profiles at three different locations along the length of the outlet channel at the mid-height plane of the micropump.
(v) [Page 124] Velocity profiles at three different locations along the length of the inlet channel at the mid-height plane of the micropump.

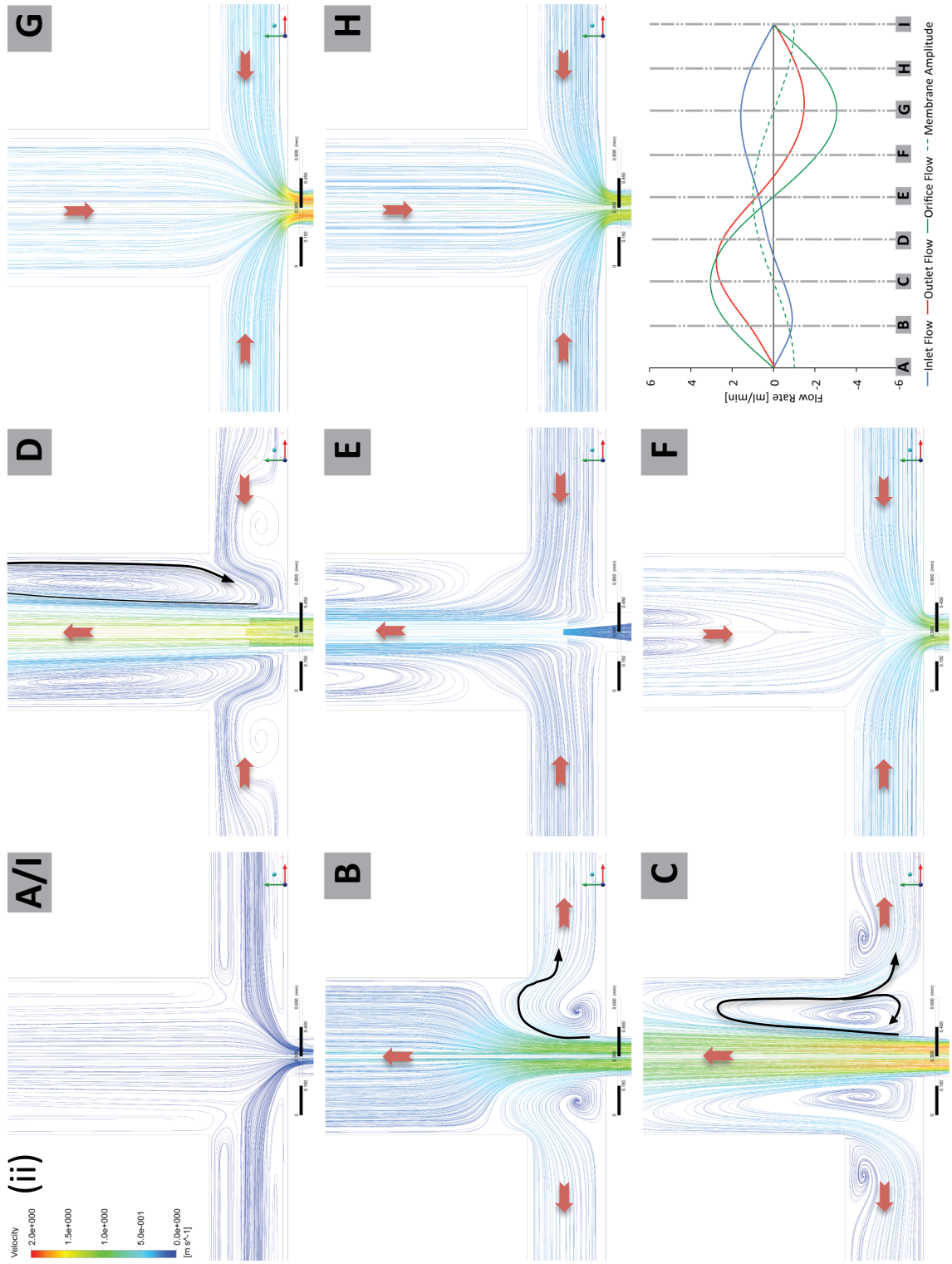

Figure 6.5 Continued.

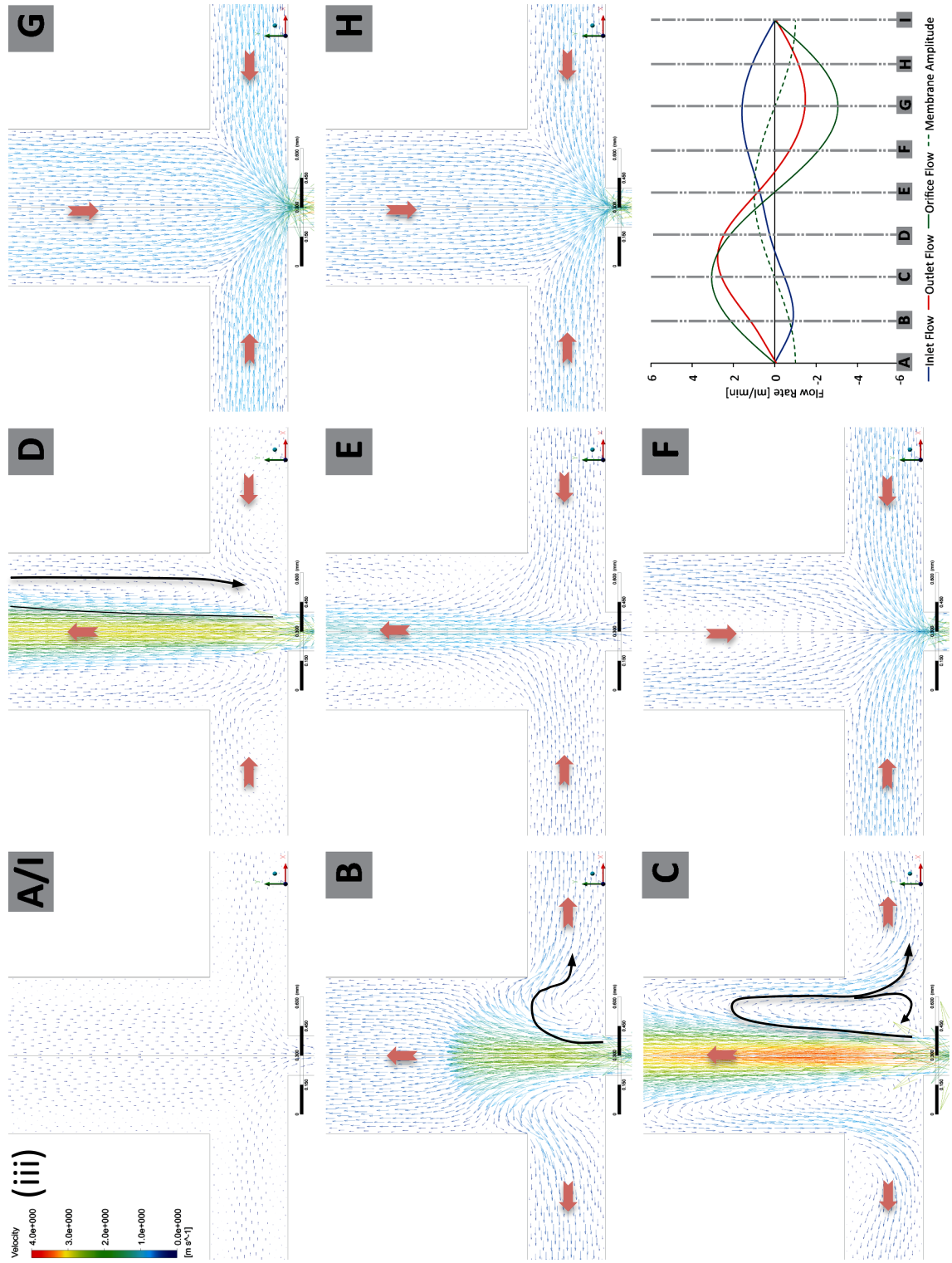

Figure 6.5 Continued.

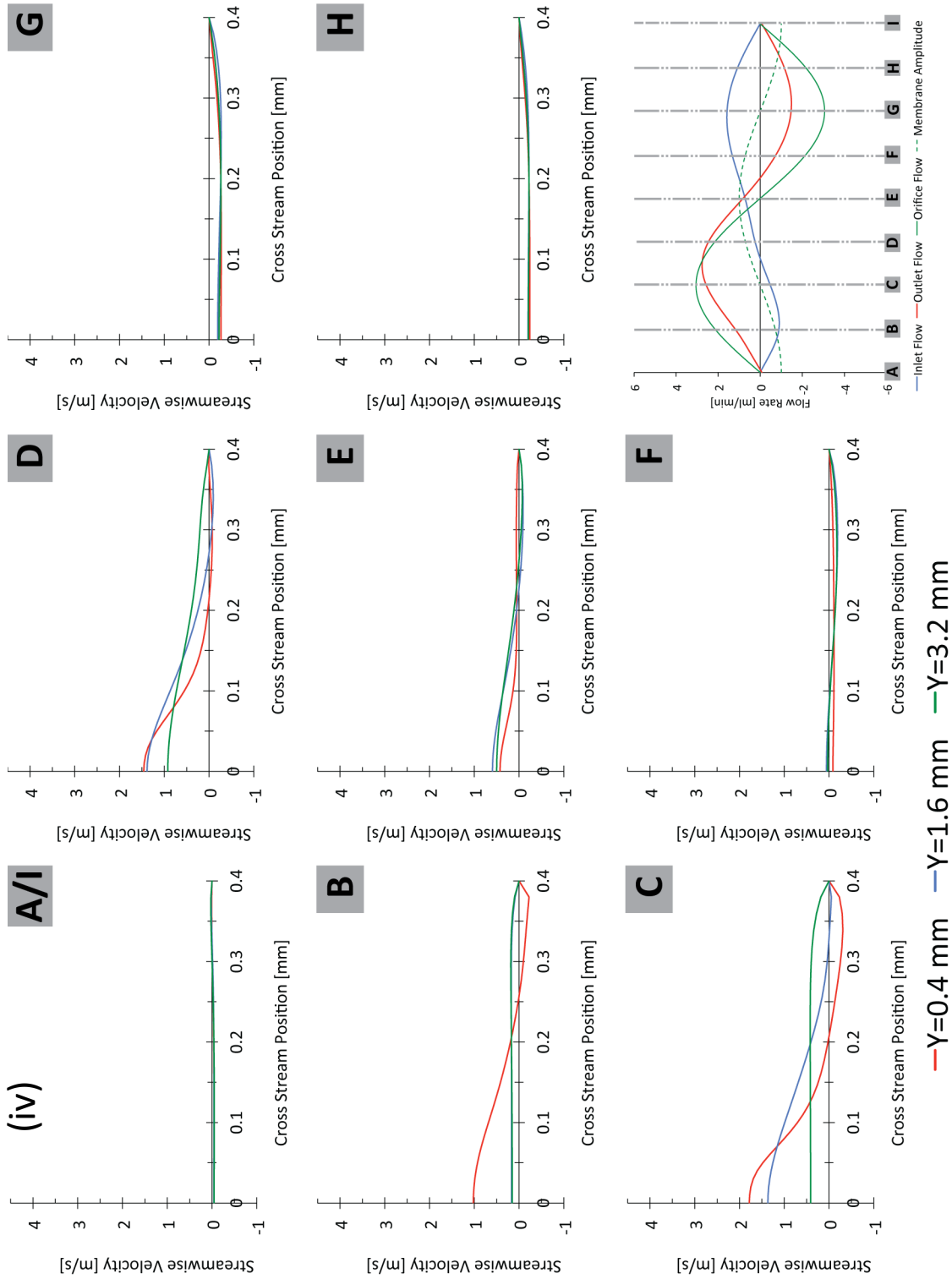

Figure 6.5 Continued.

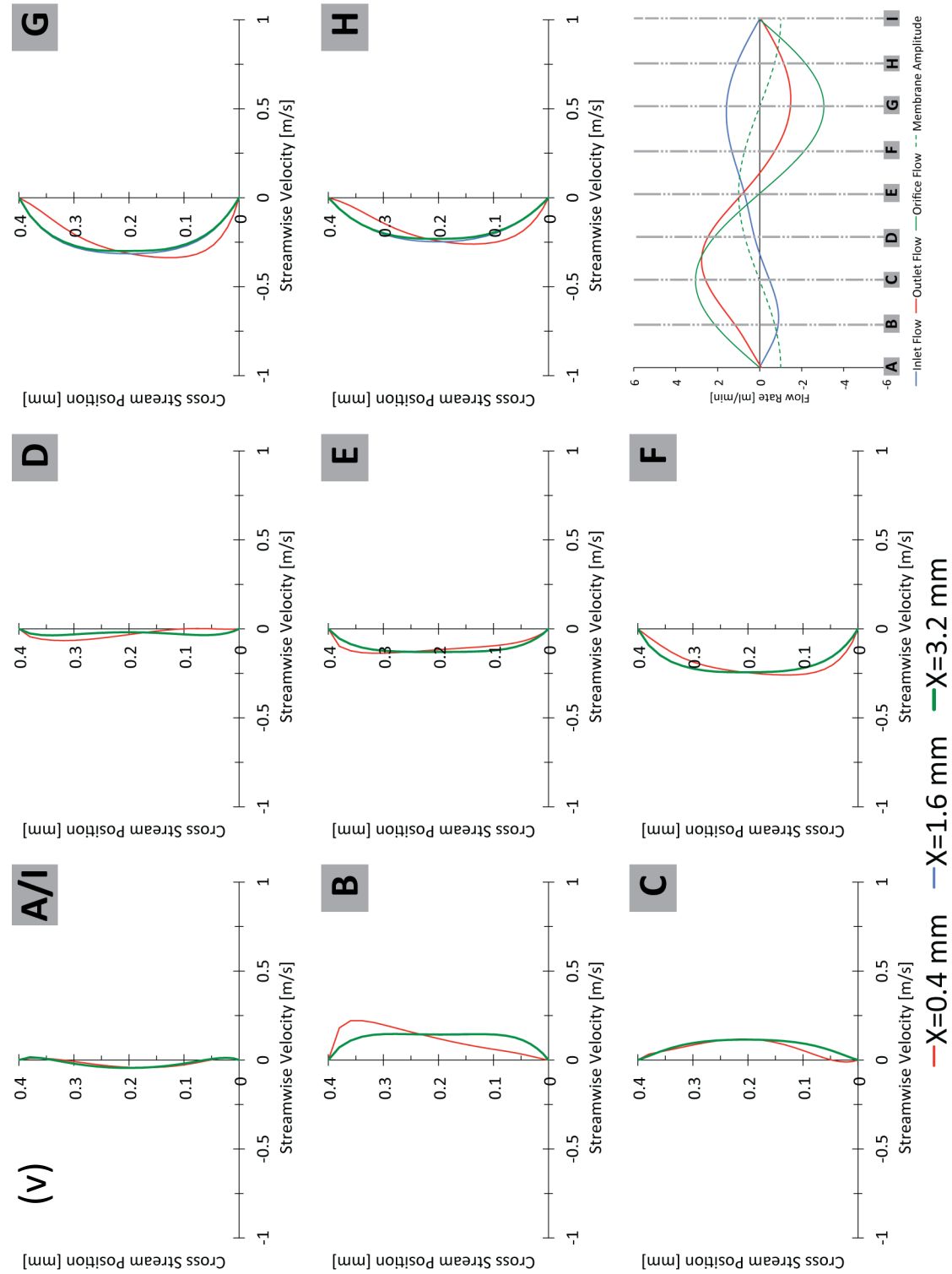

Figure 6.5 Continued.

6.3 Effect of pump channel width

In the next two sections, the effect of changing the width of the inlet and the outlet channels on the flow through the micropump will be investigated. In addition to the base case presented in the previous section, two other cases will be presented for each of the inlet and outlet channels. A width smaller and another larger than that used in the base case will be investigated and compared to the base case. Thus, in total, the effect of three different inlet widths will be discussed in section 6.3.1 and the effect of three different outlet widths will be discussed in section 6.3.2.

6.3.1 Effect of pump inlet width

The effect of changing the width of the inlet channel W_i on the inlet and outlet flow rate as well as the flow around the exit area of the orifice is shown in Figure 6.6. Three different cases are studied; the base case with W_i=400 µm, and two cases with W_i=200 µm and W_i=800 µm. It is evident from Figure 6.6 (i) that as the width of the inlet channel increases the average flow rate through the pump increases as well, from 0.24 ml/min to 0.46 ml/min to 0.62 ml/min. Moreover, it can be seen that the fluctuations in the outlet flow rate also decrease with the increase in the inlet channel width, while the fluctuations in the inlet flow rate increase. The change in the fluctuations of the flow rate can be attributed to the fact that as the inlet channel width increases the flow

(i)

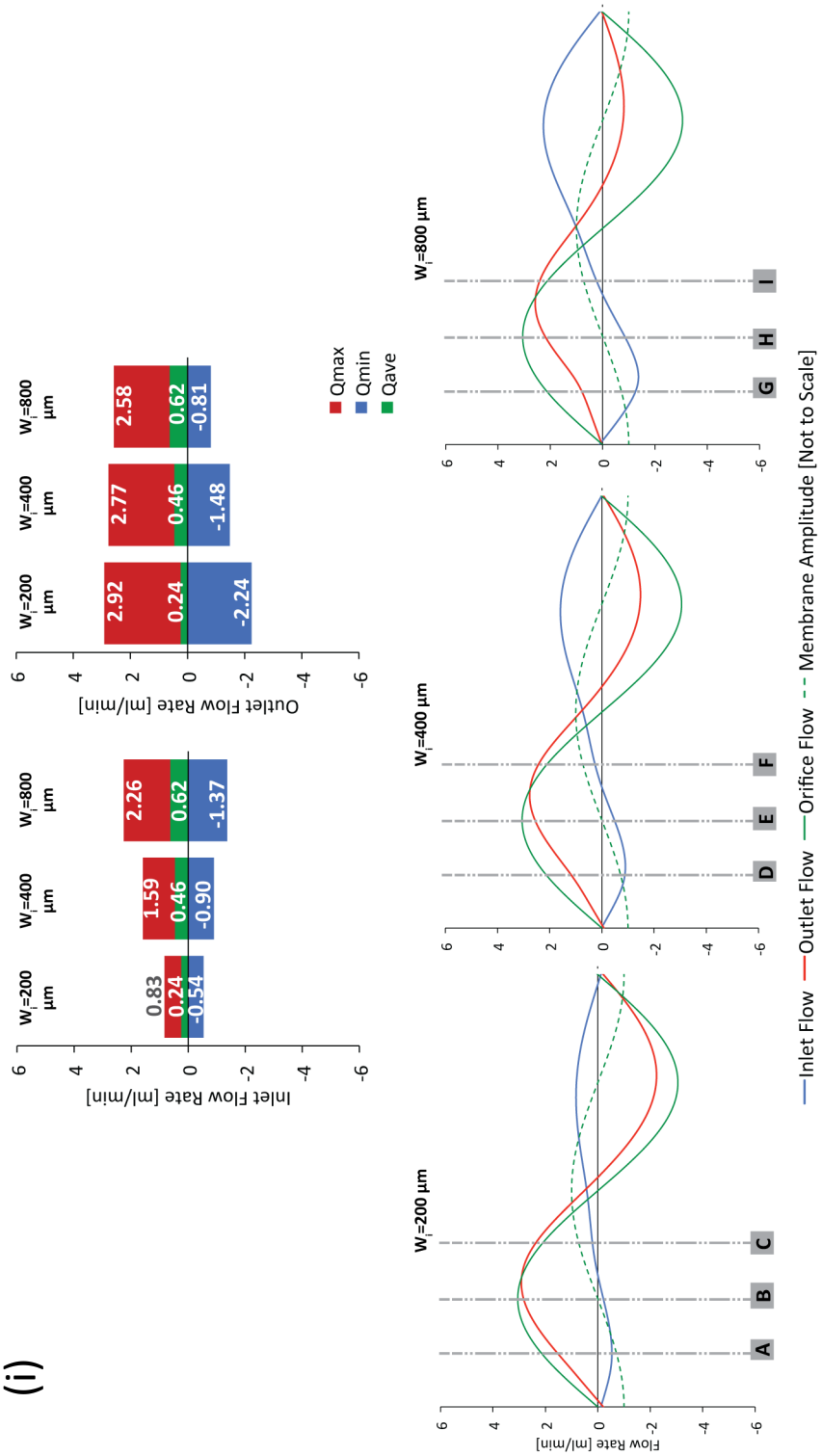

Figure 6.6. Effect of changing the inlet channel width W_i on the flow rates and flow field of the micropump.
(i) [above] Comparison of pump flow rates. [A positive flow rate indicates flow in the forward direction (from inlet to outlet). For orifice flow, positive indicates flow out of the cavity]. Letters on the figure indicate instances along the actuation cycle where details of the flow field are shown in parts ii of the figure as follows:
[A], [D], [G] t/T =0.125, [B], [E], [H] t/T=0.25, [C], [F], [I] t/T=0.375.
(ii) [Page 127] Streamlines coloured by the velocity magnitude at the mid-height plane of the micropump.

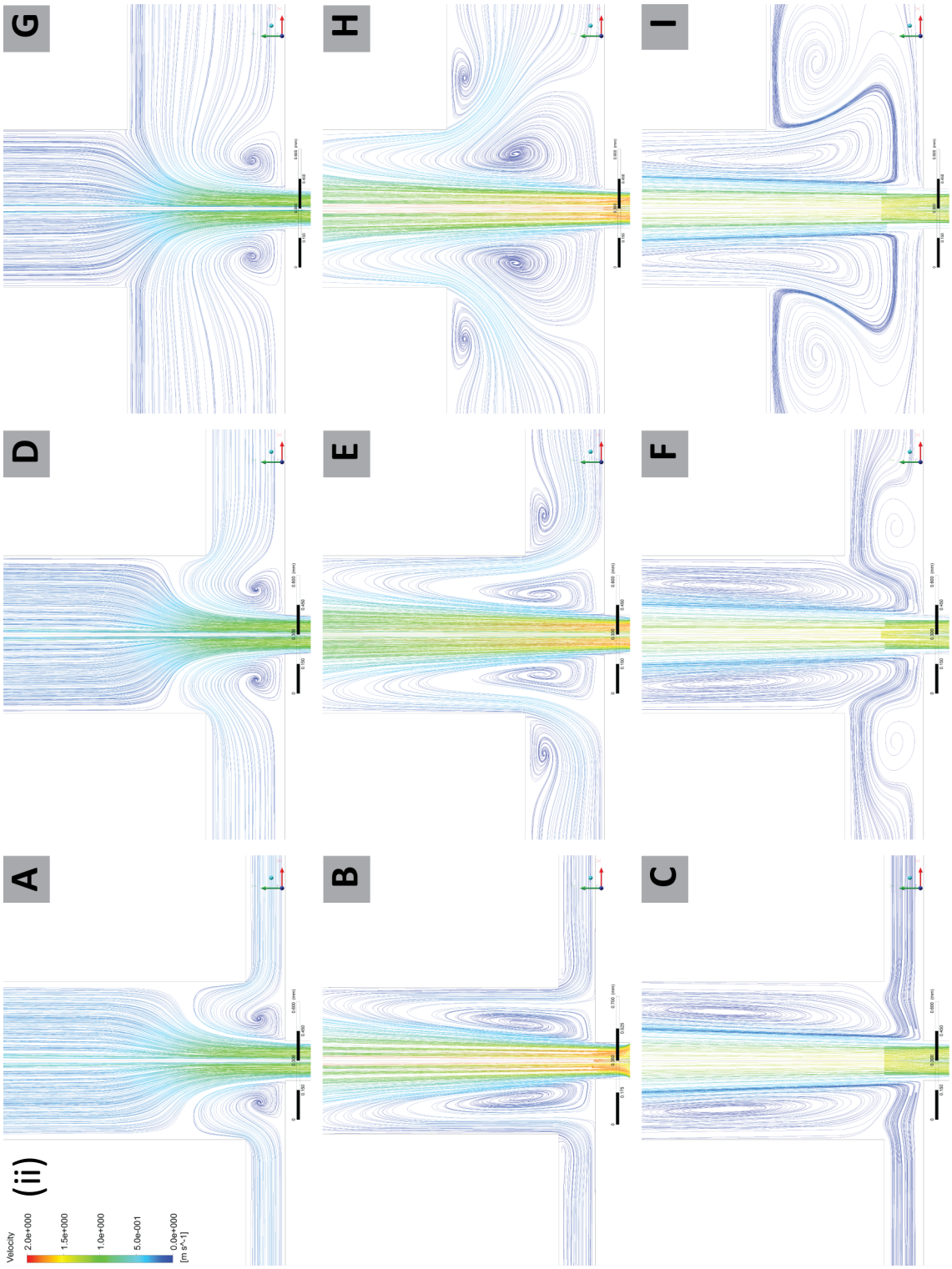

Figure 6.6 Continued.

resistance in the channel is reduced and thus during the suction stroke a bigger portion of the fluid is sucked into the cavity from the inlet channel rather than from outlet one. It is also worth mentioning that the same behaviour, as discussed in Section 6.2, with regards to the three regions of flow during the expulsion stroke can be seen in all three cases shown.

6.3.2 Effect of pump outlet width

Figure 6.7 shows the effect of changing the width of the outlet channel on the flow through the micropump. Similar to the previous section, three cases are investigated; the base case with W_o=400 µm, and two cases with W_o=200 µm and W_o=800 µm. It can be seen from the top part of the figure that increasing the outlet channel width causes a reduction in the average flow rate through the micropump, from 0.5 ml/min to 0.46 ml/min to 0.28 ml/min, with an increase in the fluctuation of the flow rate at the outlet and a decrease in the fluctuations at the inlet. This can similarly be attributed to the fact that as the width of the outlet channel increases, the flow resistance through that channel is reduced. This causes more fluid to be drawn from the outlet channel during the suction stroke than for a smaller outlet channel width.

It can also be seen that the change in flow rate between a width of 200 µm and 400 µm is much smaller than from 400 µm to 800 µm. This can be attributed to the fact that for the smallest width, the width of the outlet channel seems to be smaller than the

size of the formed vortex pair and this seems to hinder the convection of the vortex pair down the outlet channel. This apparently reduces the chance of the convection of the vortex pair down the outlet channel in entraining fluid from the inlet as can be seen by the delayed point where the inlet flow switches from negative to positive.

Similar to the discussion in Section 6.2, with regards to the three regions of flow during the expulsion stroke, it can be seen that the same behaviour exists in all three cases studied here as well.

6.4 Effect of actuation parameters

The actual pump prototype tested in this study is actuated using electromagnetic forces generated in a coil. These forces act on a permanent rare earth magnet embedded in the pump membrane. Both the amplitude of the voltage supplied to the magnet and the frequency of excitation are controlled. The resulting amplitude of excitation at the membrane centerline and frequency are monitored using a laser vibrometer. In the numerical simulations, the amplitude of excitation and the excitation frequency are both manipulated to study the effect of the operating parameters on the pump performance.

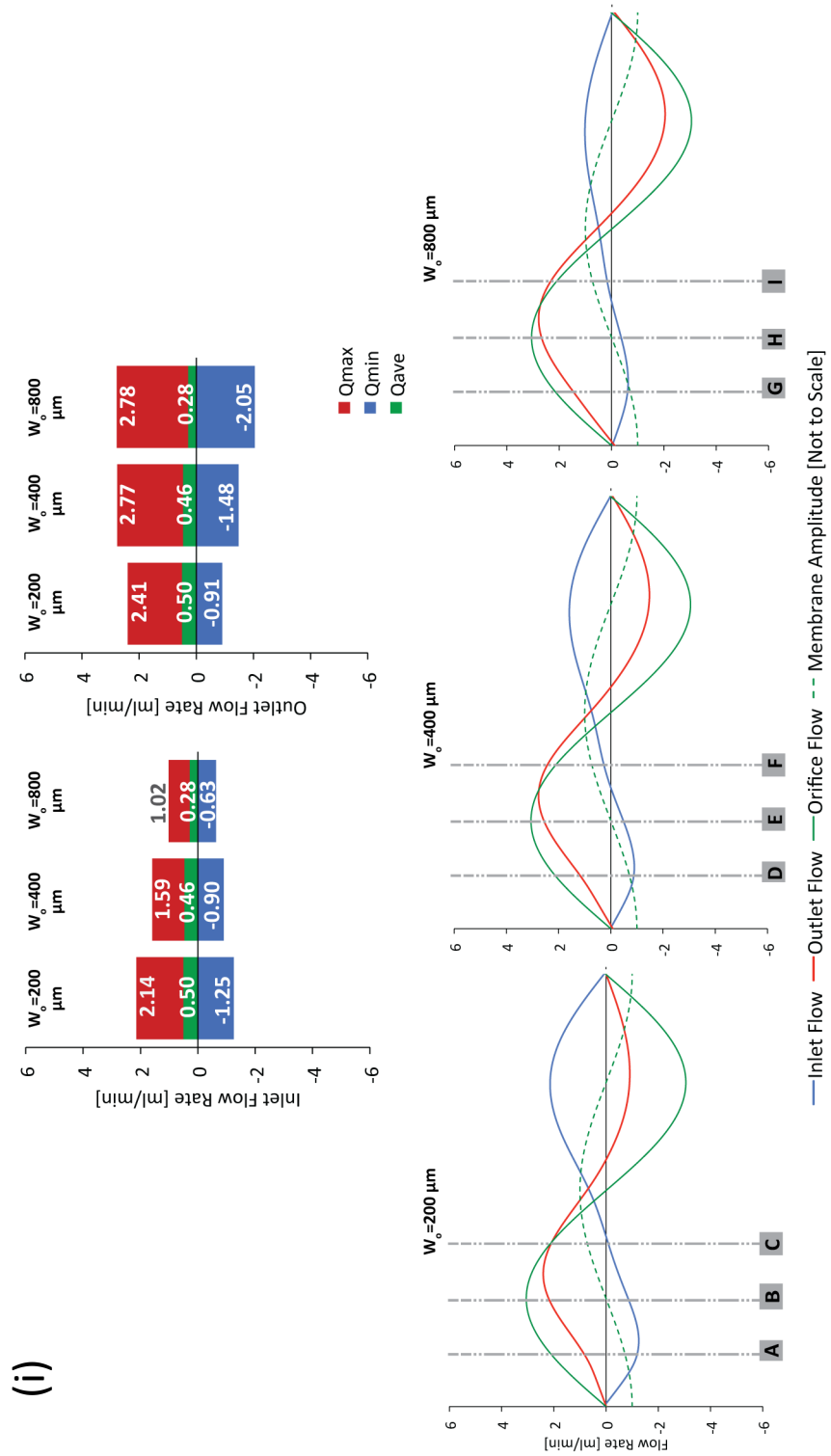

Figure 6.7. Effect of changing the outlet channel width W_o on the flow rates and flow field of the micropump.
(i) [above] Comparison of pump flow rates. [A positive flow rate indicates flow in the forward direction (from inlet to outlet). For orifice flow, positive indicates flow out of the cavity]. Letters on the figure indicate instances along the actuation cycle where details of the flow field are shown in parts ii of the figure as follows:
[A], [D], [G] t/T =0.125, [B], [E], [H] t/T=0.25, [C], [F], [I] t/T=0.375.
(ii) [Page 131] Streamlines coloured by the velocity magnitude at the mid-height plane of the micropump.

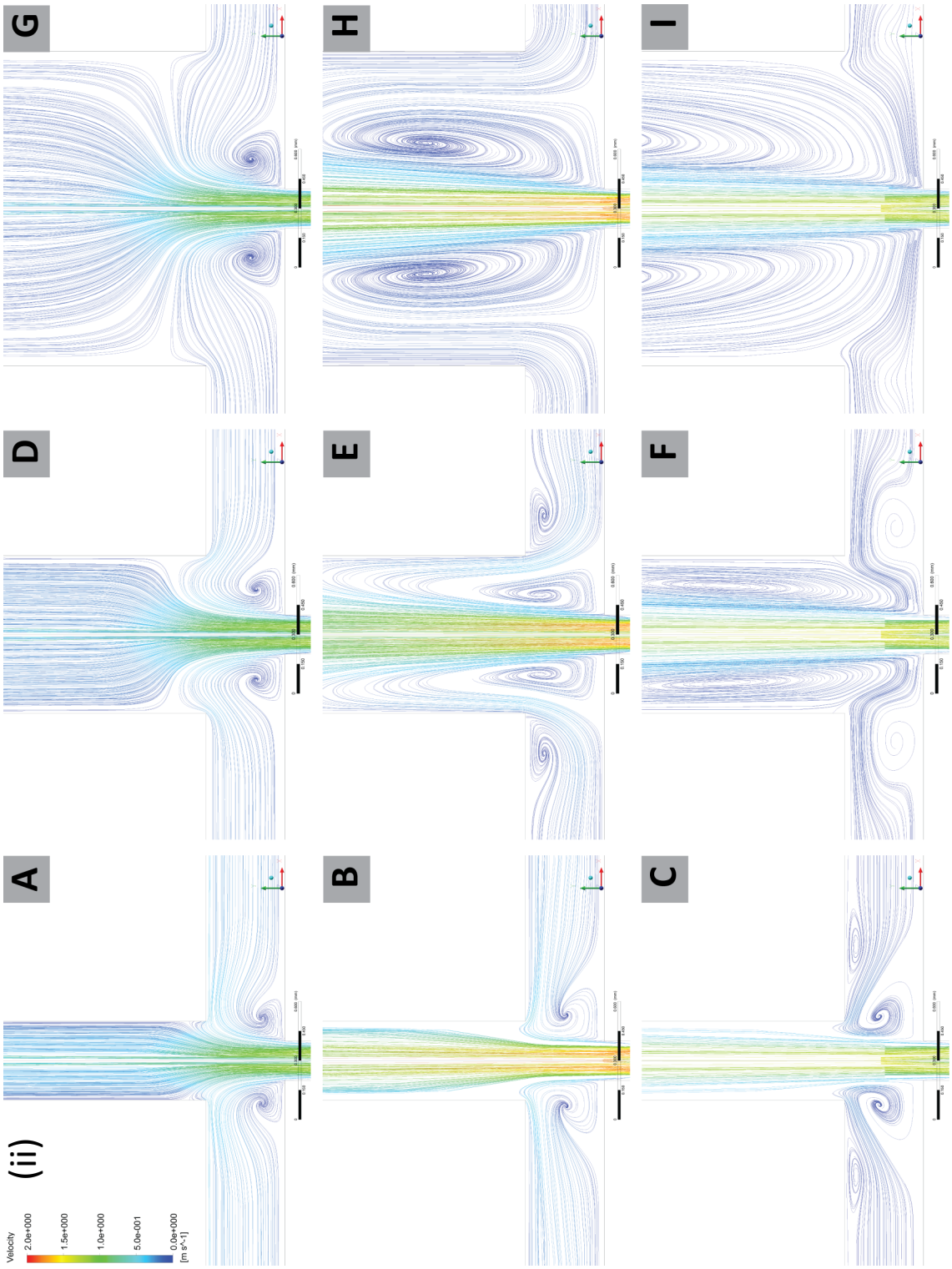

Figure 6.7 Continued.

6.4.1 Effect of actuation amplitude

As the amplitude of excitation of the actuation signal increases, the resultant net flow rate through the pump increases as well as the fluctuations in both the inlet and outlet flow rates. This is evident by comparing the three different cases with three different amplitudes as shown in Figure 6.8. The figure compares the base case with A_m=40 µm (shown in the middle) with cases having A_m=20 µm (shown on the left) and A_m=60 µm (shown on the right). The figure shows that the increase in both the average flow rate, from 0.13 ml/min to 0.46 ml/min to 0. 8 ml/min, and the fluctuations in both the inlet and outlet channel flow appears to be linear with the excitation amplitude. The streamline plots also suggest a more linear progression of the locations of the vortex pairs across the cycle from one case to the other. Recalling the discussion in Section 6.1.1, the formation length of the synthetic jet is dependent on the amplitude of excitation, it can be concluded that as the amplitude of excitation is increased, a stronger synthetic jet is formed; thus an increased flow rate for the pump is observed.

Similar to the discussion in Section 6.2, with regards to the three regions of flow during the expulsion stroke, it can be seen that the same behaviour exists in all three cases studied here as well. It is worth noting here that for the case of A_m=60 µm, the end of region “I” occurs at time location [H], where the streamlines for that instance are shown in Figure 6.8. It can be seen from the figure that at this instance in time the

streamlines at the exit plane (the one closest to the orifice) of the inlet channel are nearly vertical with essentially no flow through the inlet channel while all the reversed flow from the vortex pair simply becomes entrained once more with the issuing jet from the orifice. This supports the suggestion that after this point in time, the convection of the vortex pair upstream the outlet channel causes this entrainment of flow to the issuing jet to be supplied from the inlet channel causing the positive inlet flow in region “II”.

6.4.2 Effect of actuation frequency

Similar to the discussions above, three different cases are presented in Figure 6.9 to show the effect of changing the excitation frequency on the flow through the pump. The three frequencies studied are 20 Hz, 40 Hz (the base case) and 60 Hz. It can be seen from the figure that an increase in the operating frequency causes an increase in the average flow rate through the pump, from 0.13 ml/min to 0.46 ml/min to 0. 84 ml/min, as well as an increase in the fluctuations in both the inlet and outlet flows. The behaviour of the fluid does not seem to be altered significantly except for increased velocity amplitudes for higher frequencies. This behaviour can be attributed to the fact that the formation length for all cases is typically the same as it depends only on the actuation amplitude. However, given the increased frequency of excitation, the time

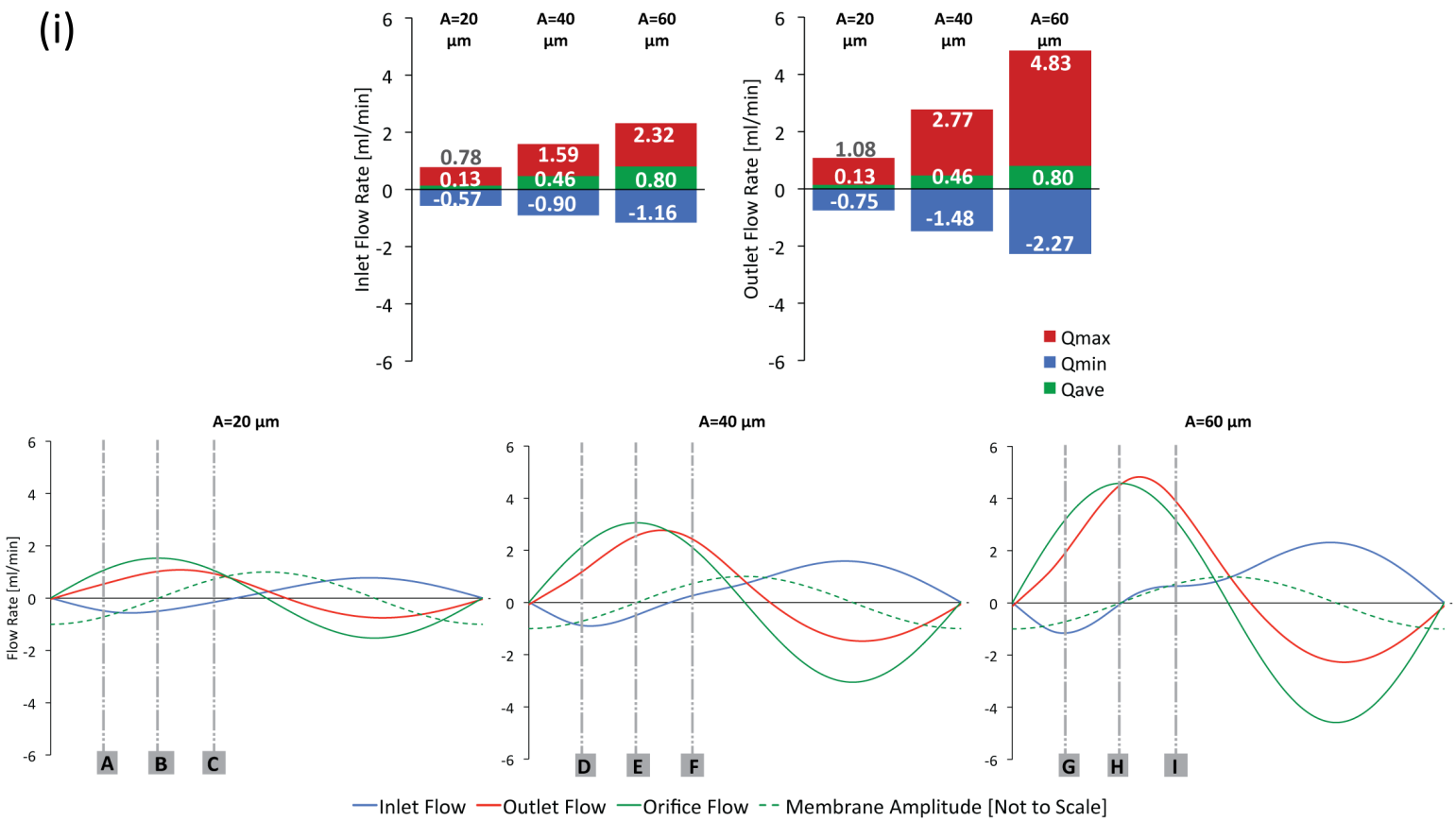

Figure 6.8. Effect of changing the amplitude of excitation A on the flow rates and flow field of the micropump.
(i) [above] Comparison of pump flow rates. [A positive flow rate indicates flow in the forward direction (from inlet to outlet). For orifice flow, positive indicates flow out of the cavity]. Letters on the figure indicate instances along the actuation cycle where details of the flow field are shown in parts ii of the figure as follows:
[A], [D], [G] t/T =0.125, [B], [E], [H] t/T=0.25, [C], [F], [I] t/T=0.375.
(ii) [Page 135] Streamlines coloured by the velocity magnitude at the mid-height plane of the micropump.

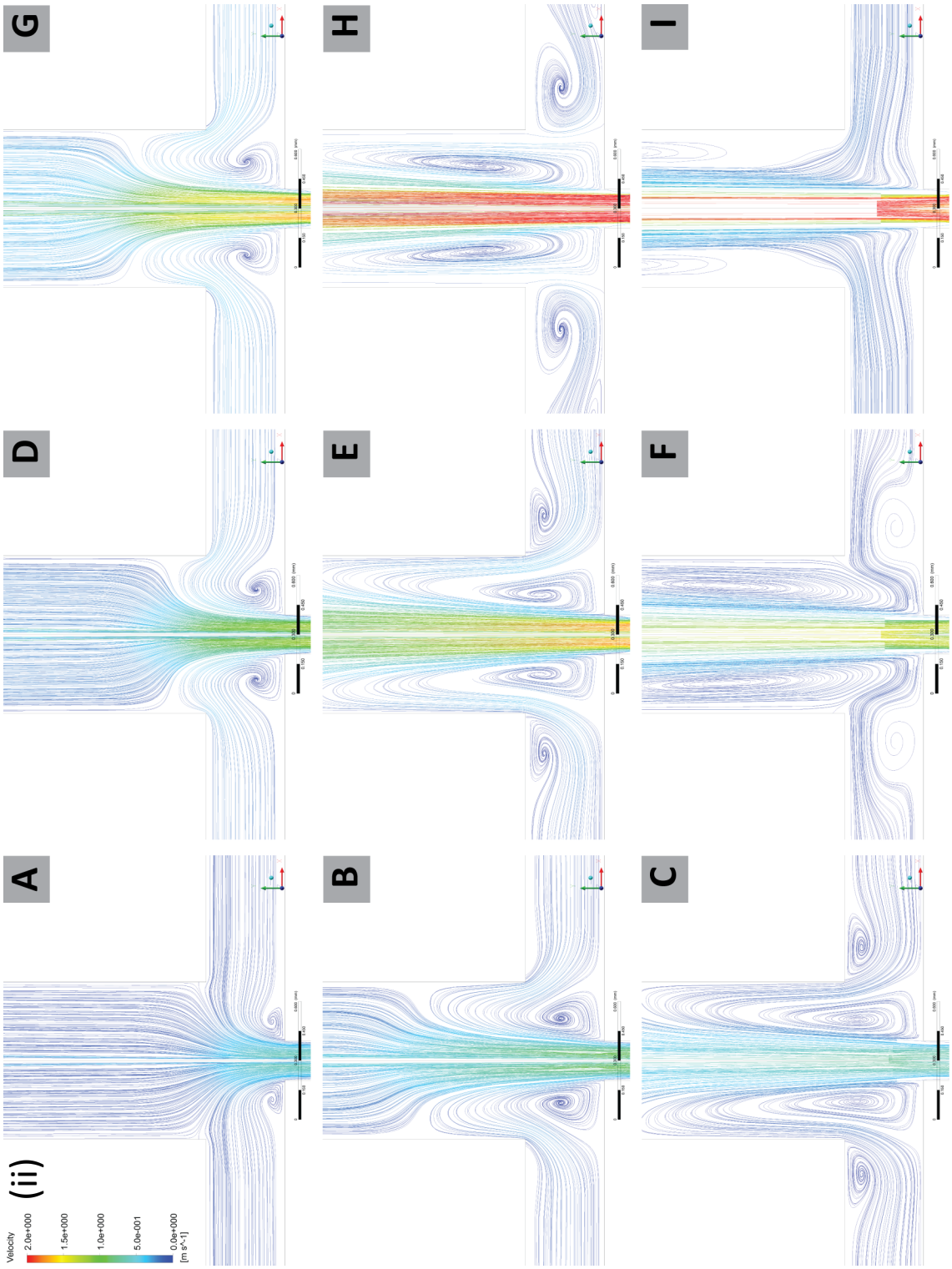

Figure 6.8 Continued.

(i)

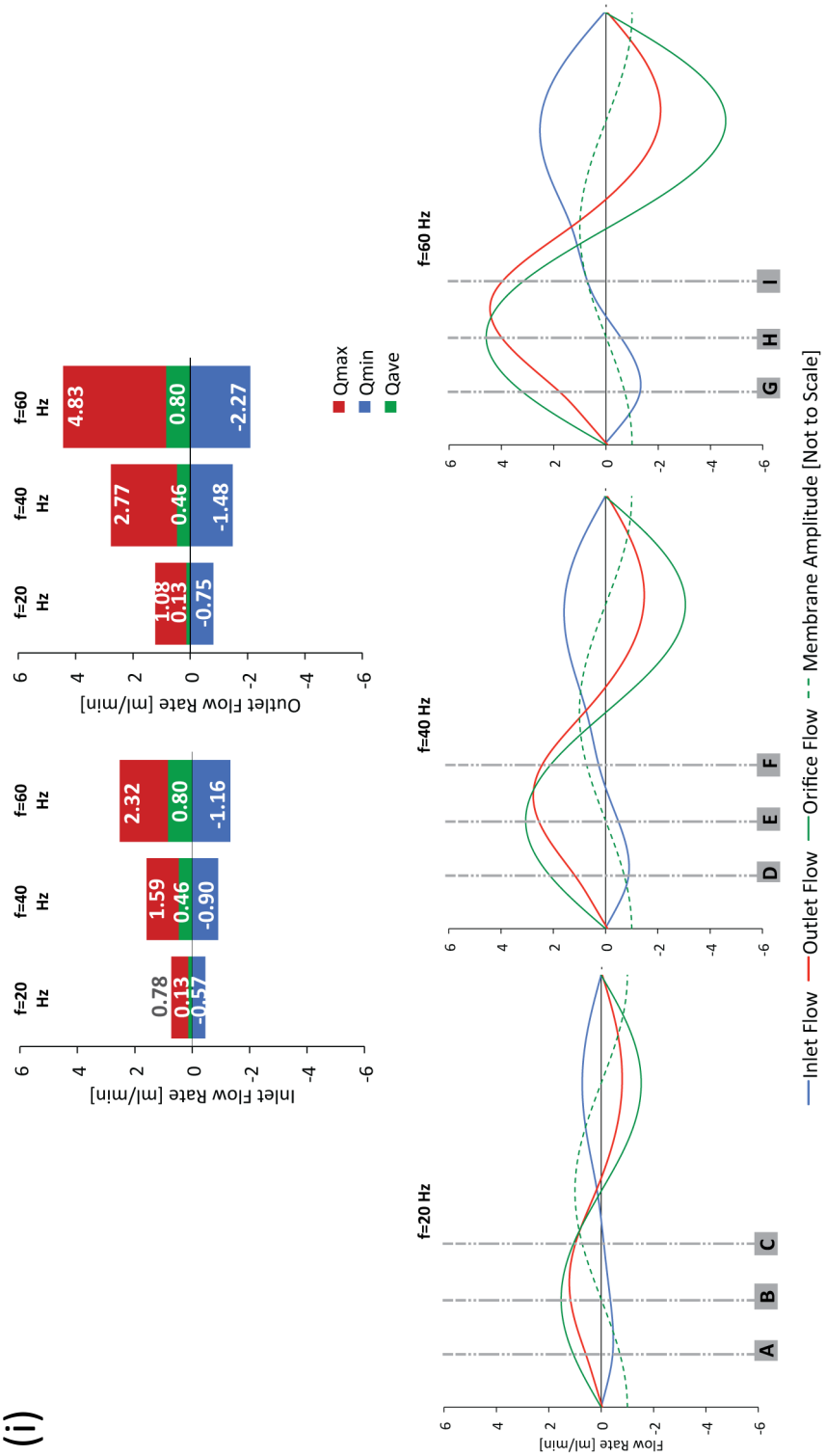

Figure 6.9. Effect of changing the frequency of excitation f on the flow rates and flow field of the micropump. (i) [above] Comparison of pump flow rates. [A positive flow rate indicates flow in the forward direction (from inlet to outlet). For orifice flow, positive indicates flow out of the cavity]. Letters on the figure indicate instances along the actuation cycle where details of the flow field are shown in parts ii of the figure as follows: [A], [D], [G] t/T =0.125, [B], [E], [H] t/T=0.25, [C], [F], [I] t/T=0.375.
(ii) [Page 137] Streamlines coloured by the velocity magnitude at the mid-height plane of the micropump.

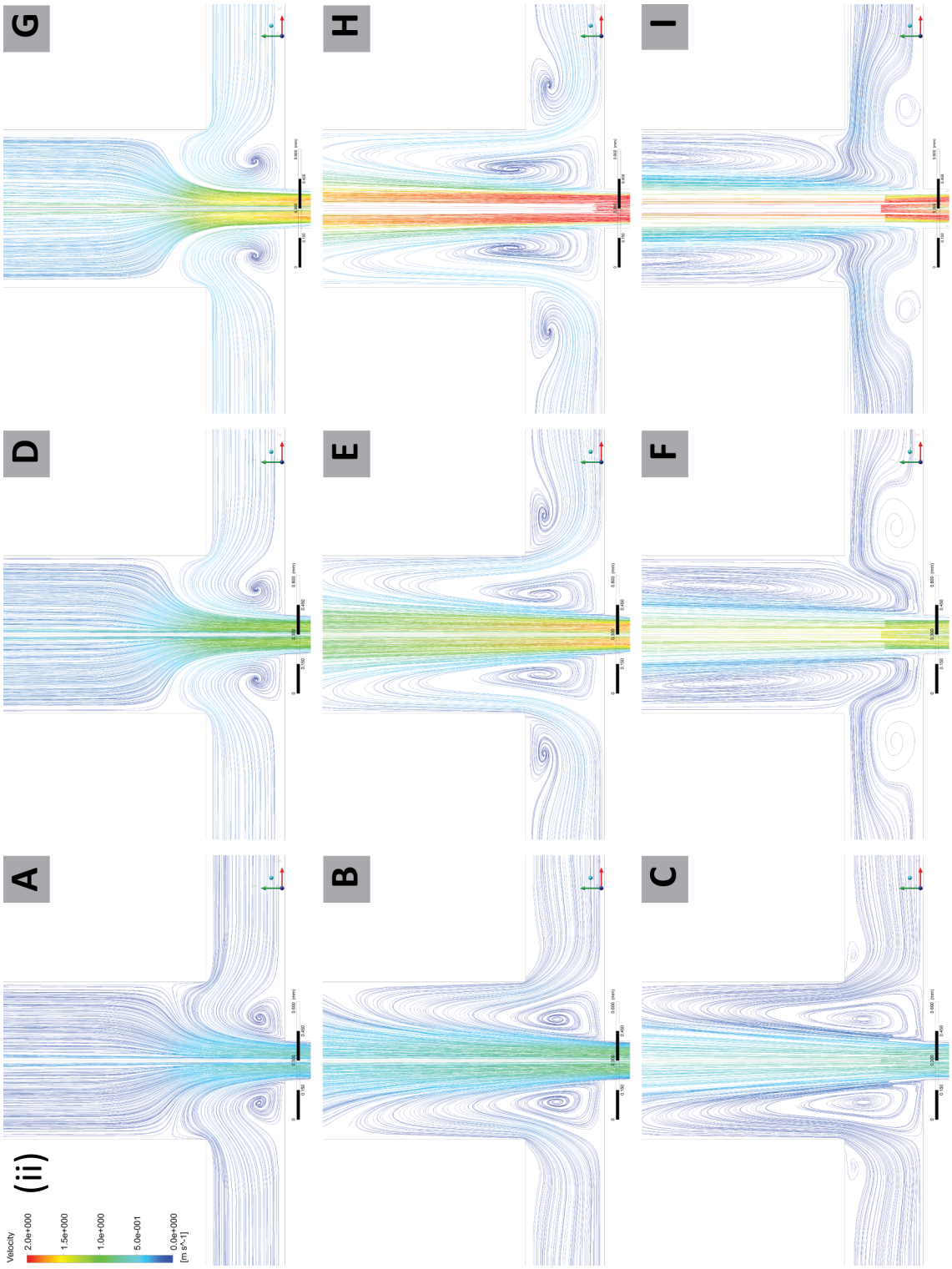

Figure 6.9 Continued.

allowed for the fluid to enter and exit the cavity reduces, thus requiring higher velocities through the orifice. Moreover, given the increased number of actuation cycles in a given time period, the pumped volume in a given time period increases as well.

6.4.3 Effect of actuation ejection/suction duty cycle

In the previous discussion the actuation signal that was utilized was a sinusoidal one with a constant frequency and amplitude. Zhang and Wang (2007) and later Feng et al. (2010) proposed the use of a modulated actuation signal to enhance the synthetic jet formation process. The synthetic jet formation is mainly governed by two main factors: the self-induced convection velocity of the formed vortex pair during the ejection part of the actuation cycle, as well as the average suction velocity during the suction part of the actuation cycle. If the self-induced velocity of the vortex pair is larger than the suction velocity, this will insure that the vortex pair is not significantly affected by the suction stroke and is not ingested back into the jet-forming cavity. Thus, if the time duration of the suction stroke is increased in comparison to that of the ejection stroke while maintaining the same mass-flux, it would be possible to produce a stronger synthetic jet. This can be achieved by changing the relative duration of the ejection and suction strokes or in other words the ejection and suction duty cycles. Following the same approach, the membrane actuation signal was modified to obtain an orifice velocity in the form

$$u_o(t)=\begin{cases} \frac{u_{o_m}}{2}\sin\left(\omega\left(\frac{k+1}{2}\right)(t-nT)\right) & \text{for } nT \le t \le nT+\frac{T}{k+1} \\ \frac{u_{o_m}}{2}\sin\left(\omega\left(\frac{k+1}{2k}\right)(t-nT)+\frac{k-1}{k}\pi\right) & \text{for } nT+\frac{T}{k+1} \le t \le (n+1)T \end{cases} \quad [6.22]$$

where $u_o(t)$ is the instantaneous special average velocity at the orifice exit, $u_{o_m}$is the peak to peak amplitude of $u_o(t)$ and has the same magnitude as that used in the uniform sinusoidal excitation cases, $\omega = 2\pi f$ is the overall frequency of excitation, $k = T_2/T_1$ is the duty cycle factor defined as the ratio of the time duration of the suction stroke to that of the ejection stroke, T is the overall period of the excitation signal and n is an integer representing the cycle count. Using continuity the amplitude of excitation of the membrane can be obtained as

$$Z(x,y,t)=A(t)M(x,y) \quad [6.23]$$

$$A(t)=\begin{cases} \frac{A_m}{2}\sin\left(\omega\left(\frac{k+1}{2}\right)(t-nT)+\frac{\pi}{2}\right) & \text{for } nT \le t \le nT+\frac{T}{k+1} \\ \frac{A_m}{2}\sin\left(\omega\left(\frac{k+1}{2k}\right)(t-nT)+\frac{k-1}{k}\pi+\frac{\pi}{2}\right) & \text{for } nT+\frac{T}{k+1} \le t \le (n+1)T \end{cases} \quad [6.24]$$

where $A_m$is the peak to peak amplitude at the membrane centerline, and $M(x,y)$ is the membrane mode shape as discussed in Chapter 4. It should be noted that choosing the orifice velocity in this form results in the formation length of the produced synthetic jet L_o and the corresponding Reynolds number $Re_{U_o}$to remain at the same value regardless

of the value of k. The variation of the orifice velocity and the membrane centerline amplitude with different values of k is shown in Figure 6.10.

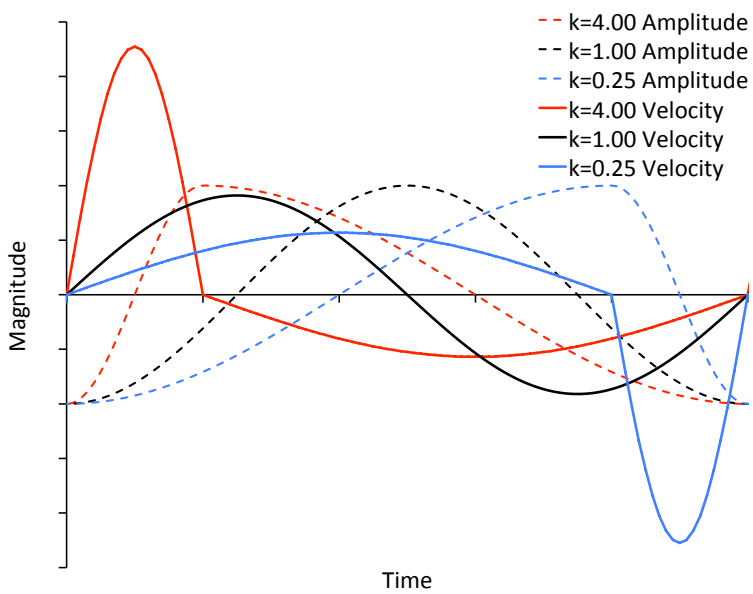

Figure 6.10. Variation of actuator membrane centerline amplitude and jet orifice area averaged velocity with time for different values of duty cycle factor $\boldsymbol{k}$ over one excitation period.

Using this amplitude of excitation, three simulation cases were performed to study the effect of changing the value of k on the performance of the micropump. For all three cases, the nominal frequency and amplitude of excitation were set at 40 Hz and 40 µm. Values of k of 0.25, 1 (the base case) and 4 were used in the simulations. Figure 6.11 shows the effect of the value of the duty cycle factor on the flow rate and flow field of the micropump for the three cases. It can clearly be seen that for a k value of 4 the average flow rate through the pump increases to 0.72 ml/min as compared to

0.46 ml/min for the base case. Similarly, a value of k of 0.25 results in a reduction in the flow rate to 0.31 ml/min.

It is interesting to note that the change in the duty cycle factor not only alters the average flow rate through the pump but also the fluctuations in the inlet and outlet flow rates. It can be seen that for higher values of k, the contribution of the outlet flow to the suction part of the cycle is reduced while that of the inlet flow is increased and vice versa for lower values of k. Moreover, the streamlines indicate that even though the formation length is the same for all cases, the higher k value case shows a vortex pair that has propagated further through the outlet channel than the base case and the opposite for the lower k value case, a behaviour similar to that of increasing the amplitude of excitation.

(i)

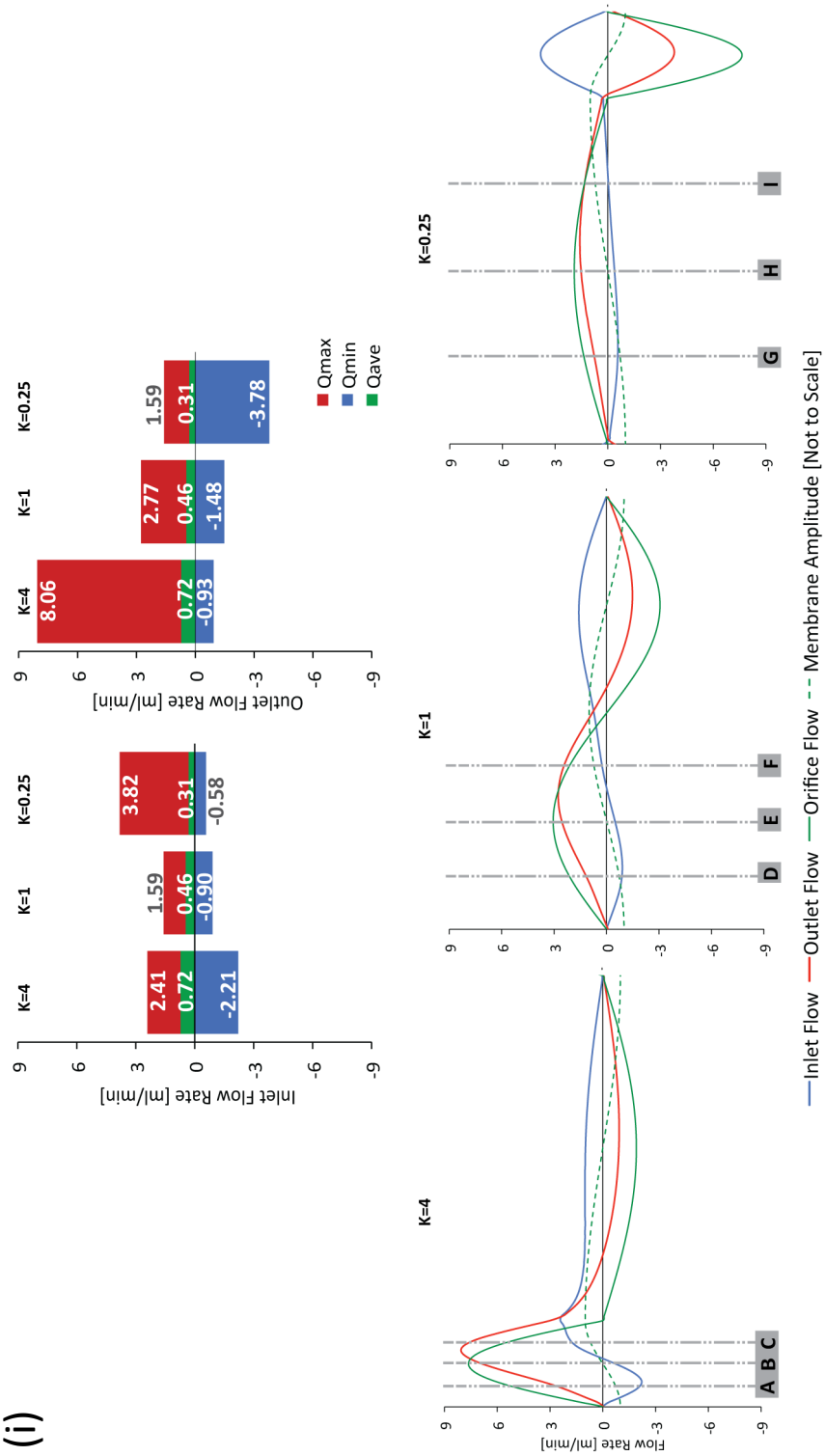

Figure 6.11. Effect of changing the excitation duty cycle factor k on the flow rates and flow field of the micropump. (i) [above] Comparison of pump flow rates. [A positive flow rate indicates flow in the forward direction (from inlet to outlet). For orifice flow, positive indicates flow out of the cavity]. Letters on the figure indicate instances along the actuation cycle where details of the flow field are shown in parts ii of the figure as follows: [A], [D], [G] t/T =0.125, [B], [E], [H] t/T=0.25, [C], [F], [I] t/T=0.375. (ii) [Page 143] Streamlines coloured by the velocity magnitude at the mid-height plane of the micropump.

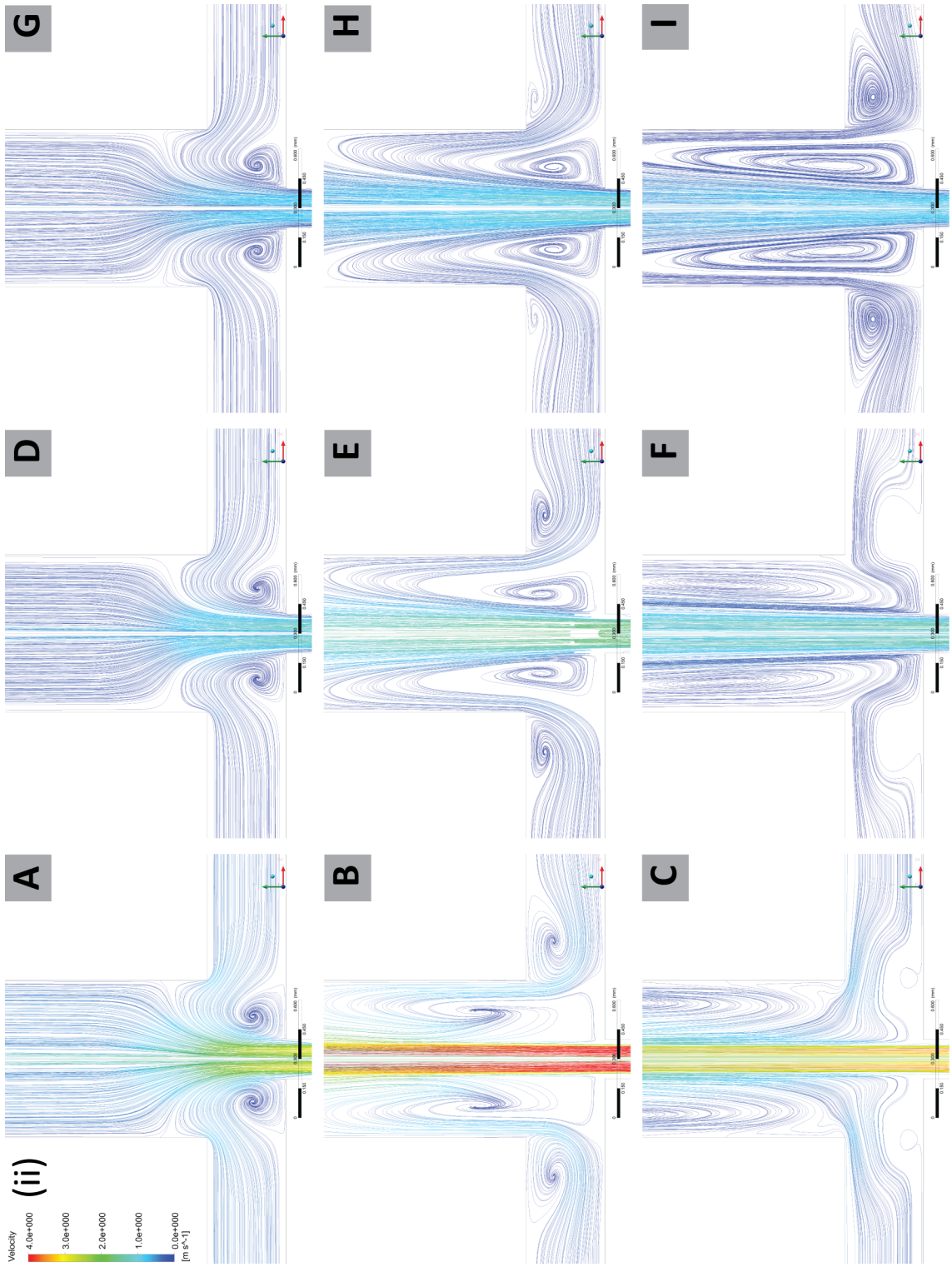

Figure 6.11 Continued.

6.5 Experimental Results

In the previous sections, the effect of varying different geometric and operating parameters on the flow rate through the pump as well as the flow during one actuation cycle has been investigated. In the following section, the effect of varying the operational parameters on the performance of the base case design of the micropump will be discussed based on both numerical as well as experimental results.

6.5.1 Effect of operating parameters

The operating conditions have been varied over a range of amplitudes and frequencies ranging from 20 Hz to 60 Hz for the frequency and from 10 µm to 60 µm for the amplitude. For the experimental results, very low frequencies and amplitudes were not attainable since the pump flow rate at these conditions is extremely low and requires extended periods of operation of the micropump which made it impractical to obtain meaningful results.

As discussed in Section 6.1.4, the representation of the results in terms of the actuation amplitude would not be an accurate comparison as the displaced volume in the numerical simulations is different than that for the experimental one for the same amplitude of excitation. This will be seen very obviously from the following discussion.

In Figure 6.12 the average flow rate through the micropump is plotted against the value of the unmodified excitation amplitude of the pump membrane. It can be seen from the figure that although both experimental and numerical simulations exhibit similar trends in terms of how the flow rate varies with frequency and amplitude, the difference between the values of the flow rate for the numerical simulations and the experimental ones seems to be substantial.

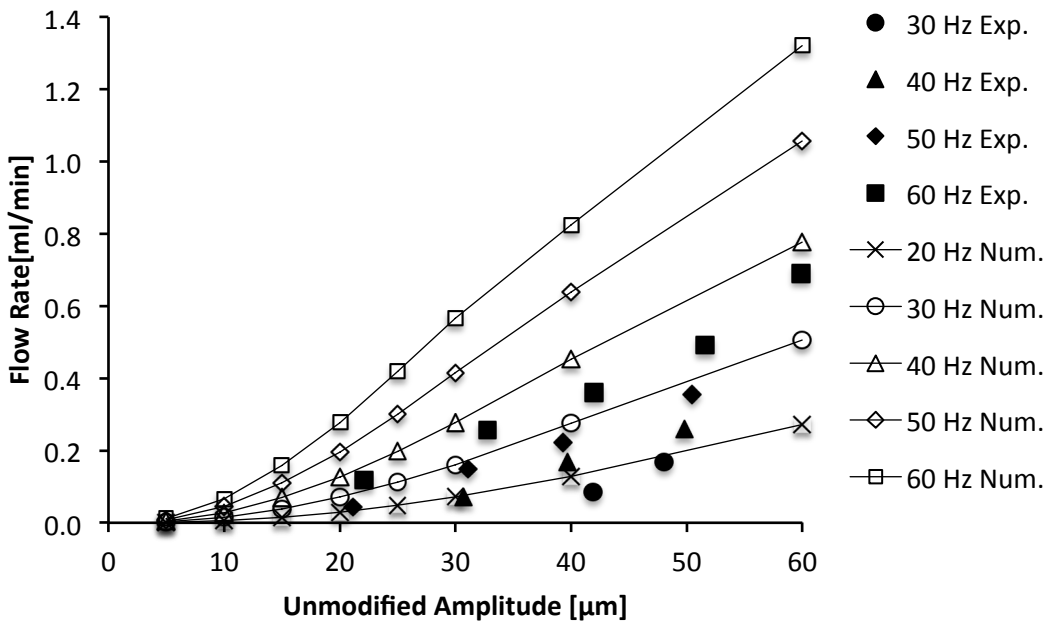

Figure 6.12. Variation of the average flow rate through the micropump with the unmodified actuation amplitude at different operating frequencies for both numerical and experimental results.

Taking into account the differences in the displaced volume at corresponding values of excitation amplitude between experimental and numerical cases as discussed in section 6.1.4, the same flow rate data is plotted against the formation length of the

synthetic jet in Figure 6.13, with the formation length calculated for the experimental results based on the mode shape of a clamped circular disc. It can be seen from the figure that the data collapses much better with smaller differences between both the numerical and the experimental results.

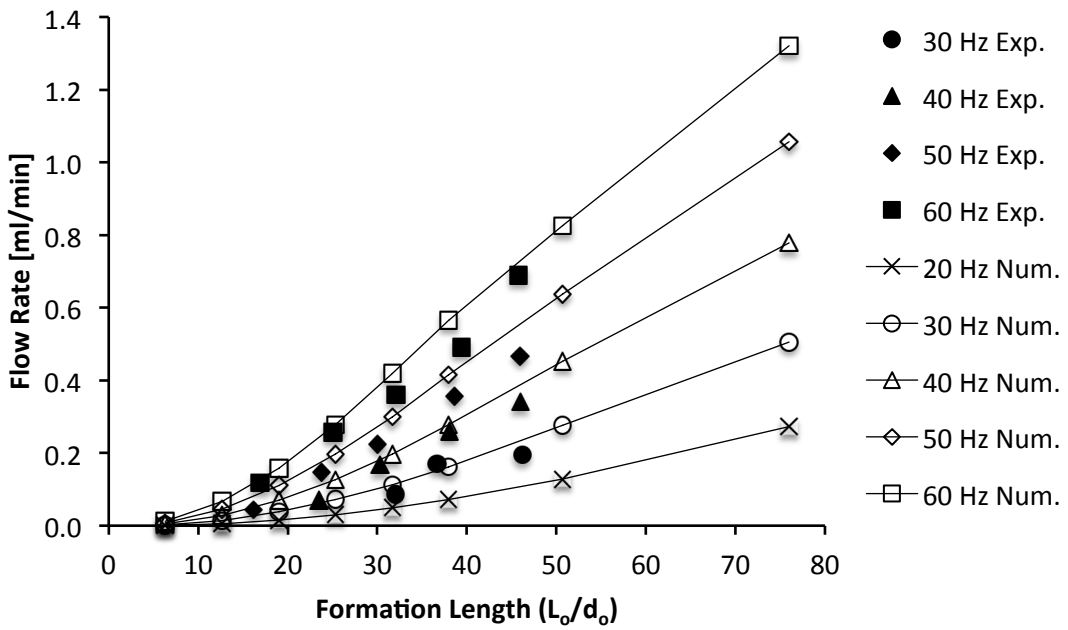

Figure 6.13. Variation of the average flow rate through the micropump with the formation length of the synthetic jet at different operating frequencies for both numerical and experimental results.

Flow rates of up to 1.32 ml/min were recorded for the numerical simulations at an amplitude of 60 µm (a formation length of 76) and a frequency of 60 Hz. For the experimental results, a maximum flow rate of about 0.69 ml/min was recorded for an amplitude of 60 µm (a formation length of 46) and a frequency of 60 Hz.

It can be seen from Figure 6.13 that the flow rate increases with an increase in either the amplitude of excitation or the frequency or both. There seems to be a rather linear trend of increase in the flow rate with the frequency at a given amplitude as indicated by the rather equally spaced trend lines at different frequencies. The excitation amplitude, however, seems to produce a slightly nonlinear effect on the flow rate especially at lower amplitudes.

It can also be seen that the data suggests the existence of an amplitude below which the flow rate is negligible or almost non-existent in both experimental as well as numerical results. This finding is in agreement with the formation criterion which has been discussed at the beginning of the chapter. For very low excitation parameters, the plug of fluid being ejected from the cavity during the ejection stroke either does not convect down stream far enough when the suction stroke begins so it is sucked back into the cavity rather than fluid from the surrounding area, or if the excitation is low enough, the plug of fluid fails to be ejected out of the orifice and in essence just keeps pulsating across the orifice from one actuation cycle to the next.

From the reported results for both numerical and experimental data, there exists differences in reported values for the same excitation parameters which are within 15% to 20%. The experimental data tends to be always lower than the numerical ones as well as the differences seem to be higher for higher amplitudes and frequencies. These discrepancies can be postulated to be caused by several factors. One factor can be due

to assembly problems or inaccuracies in producing the prototype. For example, in the tested prototype, the alignment of the membrane with pump cavity depended to a great extent on visual alignment under a microscope and with such small dimensions, small misalignment errors can quite easily happen. Another factor that could have contributed to the differences is in machining inaccuracies in the production process especially the surface finish of the produced channel which could have an effect on the flow in the pump due to the surface roughness of the walls, especially that in the simulations the walls were taken as smooth. Losses in the connecting tubes could also contribute to the difference between the flow rates. Although care was taken to use connecting tubes that are much larger in size compared to the pump channels in order to minimize the effect of friction losses in them, they would still contribute to a reduction in flow rate due to frictional as well as entry and exit losses in the tubes.

6.5.2 Micropump maximum back pressure

By modifying the outlet tube carrying the fluid out of the micrpump to be vertical in position, the maximum back, or delivery, pressure the pump can work against can be recorded by observing the level the fluid rises to in the tube. This method was utilized to record the maximum back pressure for different operating amplitudes and frequencies experimentally. The micropump inlet and outlet channel widths in this case were both 400 µm.

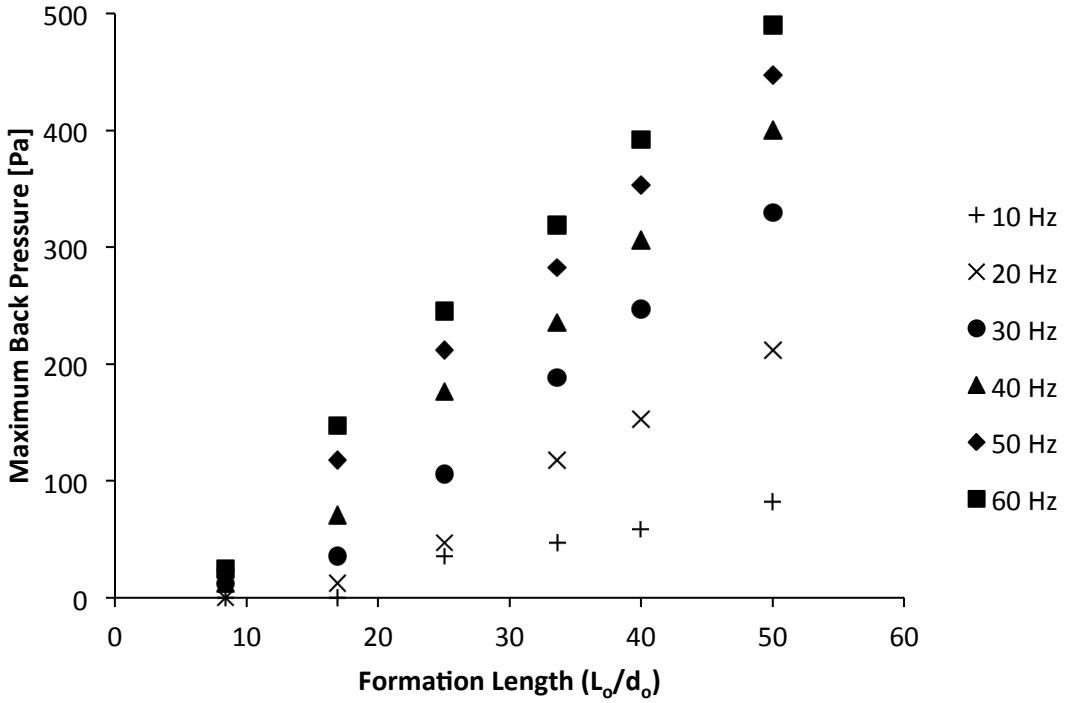

Figure 6.14. Variation of pump maximum back pressure with operating amplitude (represented by the formation length) and frequency. Inlet/Outlet channel widths were set at 400 µm for all results reported in this figure.

Obtaining the values of the maximum back pressure using the numerical simulations would not be a straight forward procedure as the pump back pressure would have to be increased gradually until the flow reverses in direction and then the value where the flow is zero would be interpolated. Hence, it was decided to rely on the experimental measurements to record the pump maximum back pressure.

It can be seen from Figure 6.14 that the pump was able to provide a maximum back pressure of about 500 Pa at an operating frequency of 60 Hz and a dimensionless formation length of about 50. It can also be seen that increasing either the amplitude or frequency of excitation resulted in an increase in the maximum back pressure.

6.5.3 Micropump driving power

Since the current micropump prototype was driven by magnetic actuation and the gap between the magnet embedded in the pump membrane and the driving electromagnet was adjusted visually, measuring the input power to the electromagnet would not have been an actual representation of the power required to drive the micropump. This is due to the fact that the magnetic driving force would vary significantly depending on this gap and the driving voltage was always adjusted so that the same amplitude of excitation was always observed irrespective of the driving voltage or current.

In this section, however, the power required to drive the microump was obtained from the numerical simulations. The force on the surface of the membrane was multiplied by the membrane displacement and integrated over the whole surface of the membrane at each time step to obtain the driving energy, which is then integrated over one driving cycle and multiplied by the driving frequency to obtain the net power required to drive the pump. It has to be noted that the values of the driving power

obtained are for the cases corresponding to zero back pressure acting on the micropump.

Figure 6.15 shows the variation of the driving power with various geometrical and operating parameters of the micropump. It can be seen that values of up to 122 µW are needed to drive the micropump. Increasing the inlet or the outlet channel width results in a slight reduction in the driving power. This is due to the reduced flow resistance in the inlet/outlet channels because of the increased channel size. On the other hand, increasing either the driving amplitude or frequency results in significant increases in the driving power of the micropump. This is due to the increased power required to drive the flow at higher flow velocities in the channels at higher amplitudes and frequencies of excitation.

Modifying the ejection cycle duty factor results in an increase in the driving power whether the value is increased or decreased. This is due to the fact that for values of k other than 1, the power required to drive the flow during the shorter stroke are higher due to the higher flow velocities and reduced stroke time. For values of k higher than 1, the power required to push the fluid out of the cavity in the ejection stroke would increase due to the shorter ejection stroke, while for values of k less than 1, the power required to pull the fluid into the cavity in the suction stroke would increase. It can also be seen that the increase in driving power for a k value higher than one is slightly lower than that for the k value lower than 1 corresponding to the same change in stroke

duration. This is due to the flow behaviour being different during the ejection or suction strokes as can be seen in Figure 6.11.

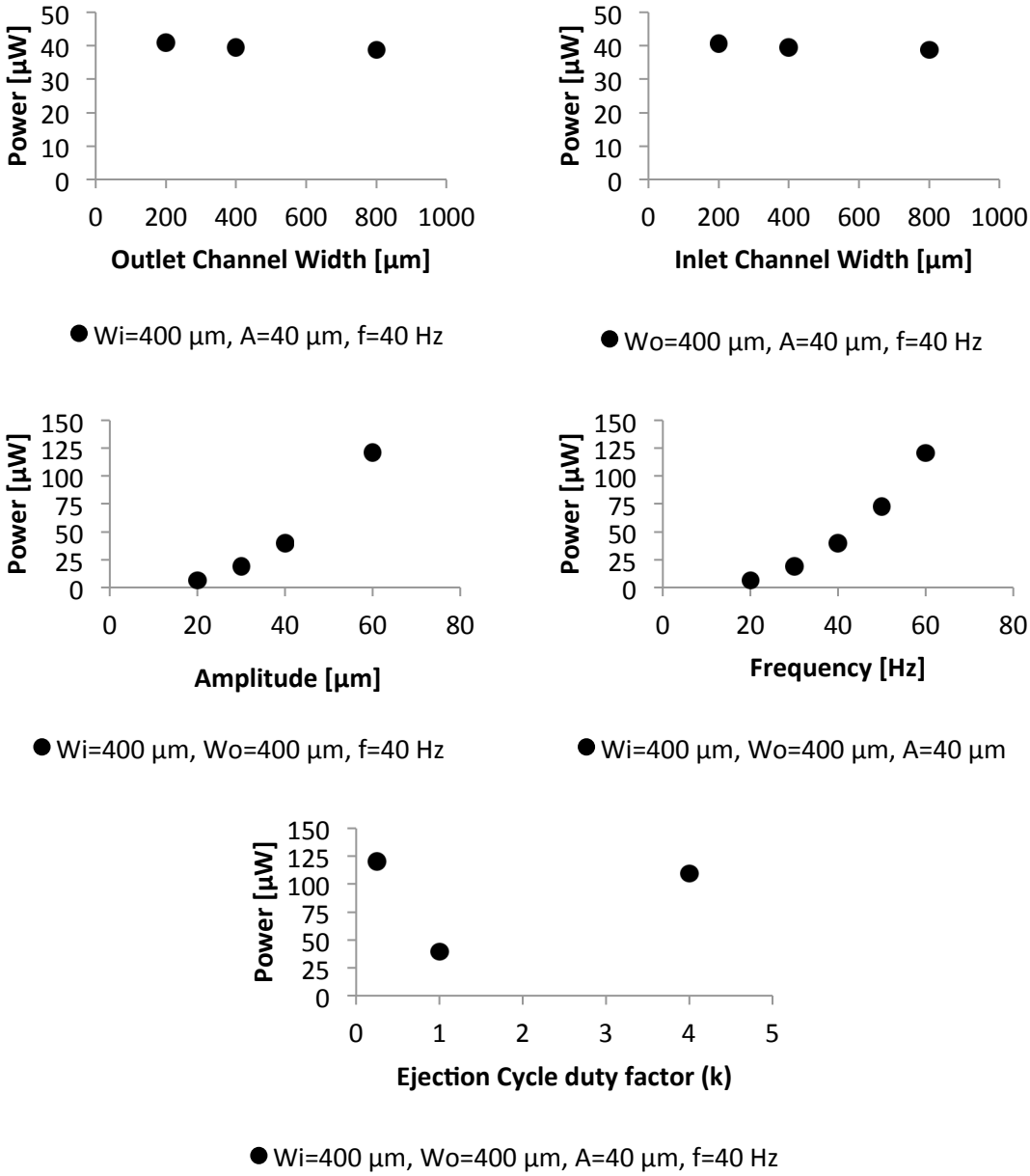

Figure 6.15. Variation of pump driving power with different geometrical and operating parameters.

6.5.4 Micropump volumetric efficiency

One of the basic parameters to evaluate the performance of a micropump is the efficiency. Due to the limitations in the test facility used to run the experiments and given the actuation mechanism of the micropump, it was not possible to measure the overall efficiency of the pump in terms of the output flow rate, or output flow power vs the input electrical power. As the electromagnetic forces between the actuating coil and embedded magnet in the membrane would vary significantly with the separation gap between them, it would have been necessary to accurately control this gap in order to be able to utilize the input electrical signal as a measure of the input power. However, since this gap was not setup to be accurately controlled in the current setup and we relied mainly on obtaining the desired actuation amplitude no matter what the input power was, we could not calculate an overall efficiency for the pump.

In an attempt to characterize a pumping efficiency for the synthetic jet micropump, it was decided to rely on the volumetric efficiency rather than the overall efficiency. The suggested efficiency would make it easier to evaluate the performance of the pump regardless of the actuation mechanism used to generate the jet. The volumetric efficiency represents the fraction of the displaced volume per unit time that the pump is capable of delivering at the outlet of the pump.

The volumetric efficiency in this case can be represented as

$$\eta_v = \frac{Q}{V_{disp} f} \qquad [6.25]$$

where Q is the net average flow rate through the pump, f is the operating frequency, and V_{disp} is the displaced volume per actuation cycle and can be calculated from the mode shape of the membrane and the amplitude of excitation as discussed earlier in the chapter as

$$V_{dsip} = V(t)_{\max} - V(t)_{\min} \qquad [6.26]$$

Figure 6.16 shows values of the volumetric efficiency plotted against the normalized formation length for different operating frequencies for both numerical and experimental data. It should be noted here that for the numerical results two additional simulation points were added for the frequencies 20 Hz, 40 Hz, and 60 Hz to verify the saturation trend shown to exist in the data. For the experimental results, it was not possible to operate the pump at such high amplitudes of excitation due to limitations of the current experimental setup and hence it was not possible to establish if the same trend would exist for the experimental data.

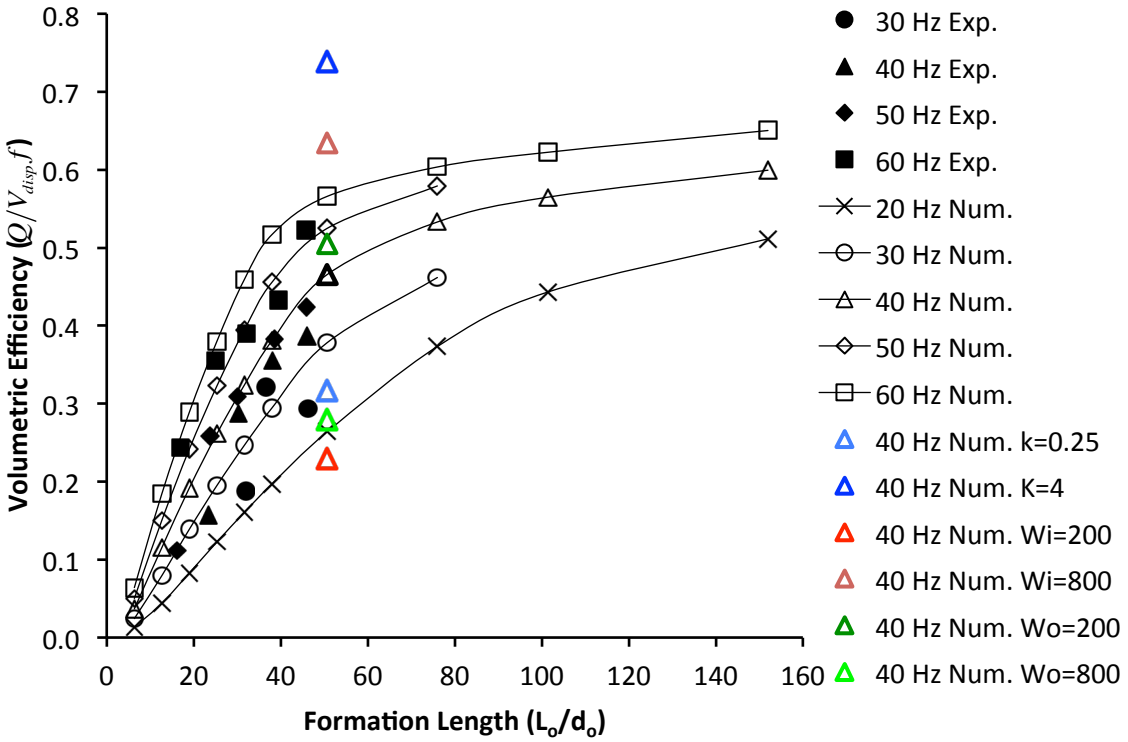

Figure 6.16. Variation of the pump volumetric efficiency with the formation length of the synthetic jet at different operating frequencies for both numerical and experimental results.

It can be seen from the figure that the efficiency increases with increasing amplitude and frequency of excitation. Moreover, the data suggests a saturation trend in the frequency for higher amplitudes of excitation, or formation lengths. At low amplitudes, the efficiency improves significantly with increasing amplitude till a normalized formation length of about 40 where the rate of increase begins to drop. This suggests that operating the micropump within the range of normalized formation length of about 40 to 60 and frequencies of about 40 to 60 Hz would be an optimal range of

operation as the pumping efficiency is about 0.5 for that range while further increase in amplitude or frequency would not cause a significant increase in the pumping efficiency.

Figure 6.16 also shows values of the volumetric efficiency for numerical simulations cases with different inlet/outlet channel widths and operating signal k values that have been discussed in the previous sections. Those cases are plotted with coloured hollow triangular markers on the figure (the same marker shape as that of the 40 Hz Numerical case). All those cases have an amplitude of excitation of 40 µm and a frequency of 40 Hz and hence they all share the same value of formation length L_o/d_o of 50.7. The marker for the corresponding base case point on the figure with a value of frequency of 40 Hz has been made darker to ease comparison. It can be seen that the dimensions of the inlet/outlet channel as well as the actuation signal k value both can have a significant effect on the efficiency of the pump. For instance the efficiency can be improved to about 74% by simply using a nonuniform actuation signal with k =4. Improvements can also be achieved by using an inlet width of 800 µm and an outlet width of 200 µm. These findings are essentially the cause of the value of the frequency and the displaced volume of the pump remaining constant while the value of the flow rate through the pump is changed.

It was mentioned in section 6.2 above that the flow cycle can be divided into four main parts with two of them, namely II and III in Figure 6.5, exhibiting flow entrainment from the inlet to the outlet. By examining Figure 6.6, Figure 6.7, Figure 6.8, Figure 6.9,

and Figure 6.11, it can be seen that the duration of that region as well as the amount of flow being entrained changes. The amount of flow being entrained in one cycle in that region is essentially the area under the inlet flow curve for region II added to the area under the outlet flow curve in region III. It can be seen that a larger entrained flow generates a higher average flow rate through the pump and a higher efficiency as well. This suggests that this entrainment effect is a significant contributor to the performance of the micropump.

6.6 Concluding Remarks

In this chapter, the results of both numerical simulations and experimental studies performed on the synthetic jet micropump have been presented and compared. The results showed a fair agreement between the numerical and experimental results for the range of operating conditions tested. The trends observed for changing the amplitude and frequency of excitation were similar between numerical and experimental results which indicate that the numerical simulations closely represent what is physically happening in the actual pump. Flow rates of more than 1 ml/min were reported for operating frequencies up to 60 Hz and normalized formation lengths of up to 75.

Details of the behaviour of the pump during the pumping cycle were introduced based on the numerical simulation results which indicated that although average flow

rates of the order of 1 ml/min were reported, the flow through the pump was periodic with fluctuations in flow rate of up to 4 ml/min were observed.

The effects of changing the inlet and outlet channel widths on the flow through the pump were investigated and indicated a favourable effect when increasing the inlet channel width while an adverse effect on the flow rate was observed when increasing the outlet channel width. The change in inlet and outlet channel width also had an effect on the level of fluctuations in the inlet and outlet flow rates with an increase in the inlet channel width causing a reduction in the fluctuations of the flow rate at the pump outlet.

Operating conditions, in terms of amplitude and frequency, also play a significant role in the performance of the pump. Higher amplitudes and frequencies cause better average flow rates through the pump, while also increasing fluctuations in the flow rates. Utilizing a nonuniform excitation signal, by altering the actuation signal duty cycle factor, also changed the behaviour of the micropump; improving the pump flow rate for values of k>1.

Measurements of the maximum back pressure produced by the micropump showed that a maximum back pressure of about 500 Pa can be obtained using an excitation signal at 60 Hz with a formation length of about 50. The power required to drive the pump membrane was calculated from the numerical simulations and showed

that it would require a power of up to 122 µW to drive the membrane. These values of power requirement were calculated based on the cases with zero back pressure imposed on the outlet of the micropump.

When evaluating the pumping efficiency of the micropump, the volumetric efficiency was used which represents the ratio between the actual average flow rate through the pump to the total displaced volume by the pump per unit time. Pumping efficiency was found to reach a saturation value at higher amplitudes and frequencies of excitation. It was also found that the geometry of the inlet/outlet channels as well as the actuation signal duty cycle factor affected the pumping efficiency of the micropump. An efficiency value of about 74% was achievable by using a duty cycle factor of 4 with nominal inlet/outlet channels of 400 µm width, actuation amplitude of 40 µm and frequency of 40 Hz.

In Chapter 2, several review papers have been discussed summarizing the literature available concerning micropumping technologies and summary graphs were presented to compare the flow rates produced by such micropumps in terms of flow rate/pump area. In order to compare the performance of the studied micropump to those reported in the literature, the current pump will be compared to those plots reported in Chapter 2. In the work of Singhal et al. (2004), the pump area is taken as the largest pump cross-sectional area perpendicular to the main flow direction. In the current study the cavity cross-section is taken as the pump cross-sectional area. In terms

of flow rate, the maximum flow rate reported for the numerical simulations and that for the experimental results were both plotted as seen in Figure 6.17.

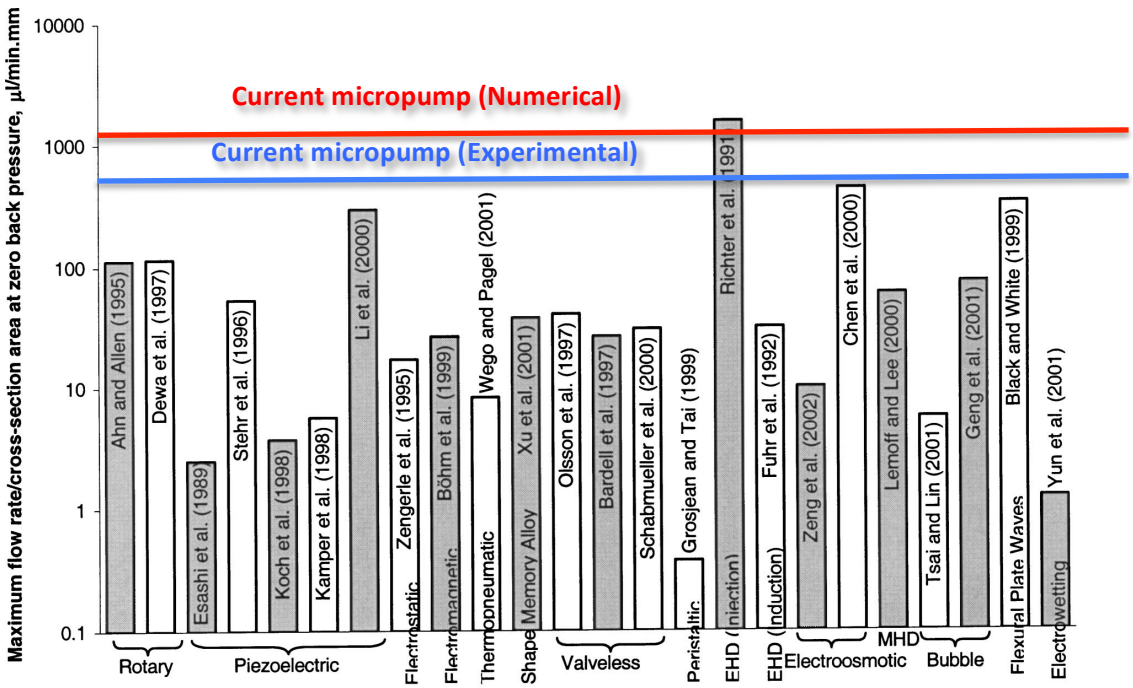

Figure 6.17. Comparison of micropumps based on maximum flow rate per unit pump cross-sectional area. (Singhal et al. 2004)

In the work of Iverson and Garimella (2008), the pump area was taken as the largest area of any cross section of the pump, hence for the current study the area of the cavity was taken as the pump area. Similarly, both maximum flow rates for the numerical and experimental results are plotted for comparison as seen in Figure 6.18.(a). In the same study the flow rate per pump outlet cross-sectional area was also compared as shown in Figure 6.18.(b).

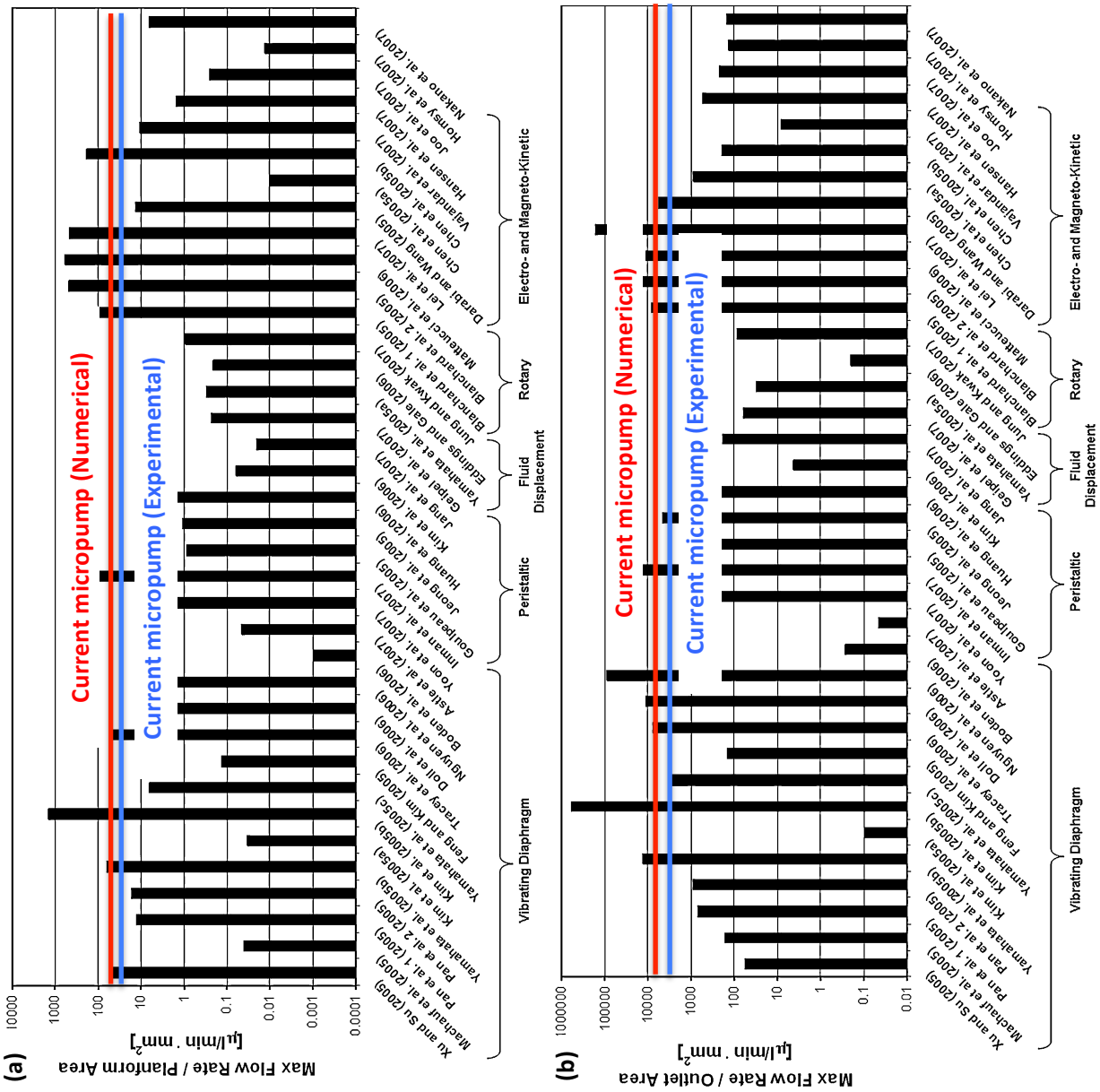

Figure 6.18. Comparison of micropumps based on (a) Maximum flow rate per unit platform area and (b) Maximum flow rate per unit outlet area for pumps reported in the literature (Iverson and Garimella 2008)

Nguyen et al (2002) also provide a graphical comparison of mechanical micropumps where they compare the pump flow rate vs typical pump size represented by the diameter of the pump diaphragm. Similar to the two previous comparisons both the results based on the numerical and experimental results are plotted on the figure as show in Figure 6.19.

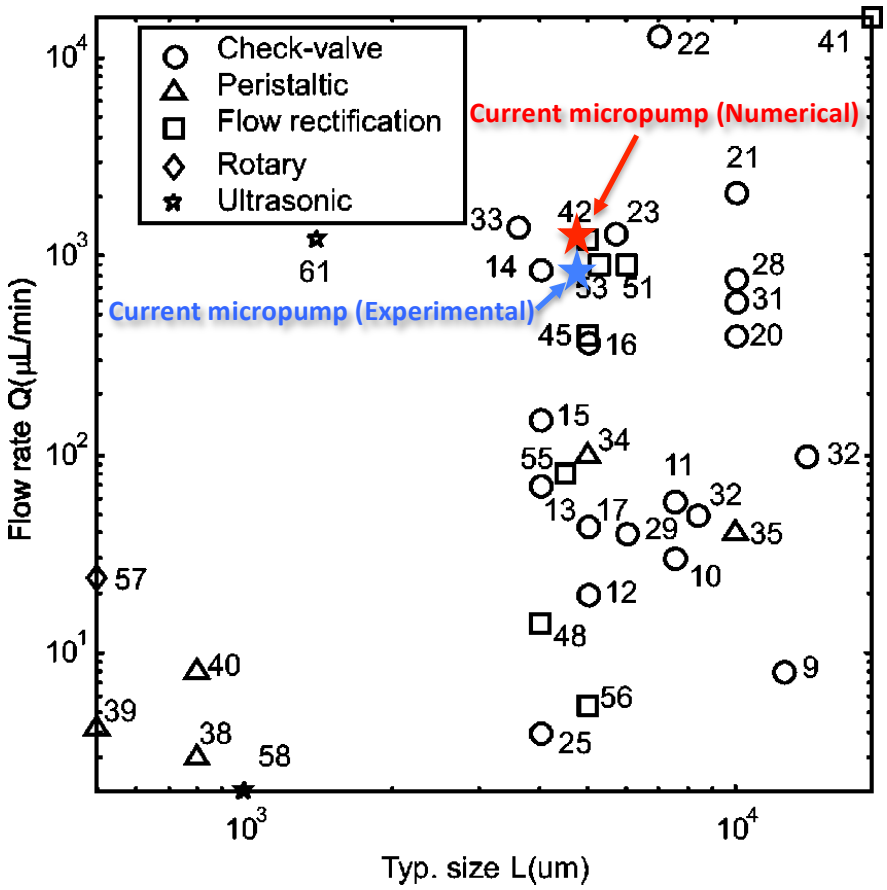

Figure 6.19. Comparison of flow rate vs typical size for mechanical micropumps. (Nguyen et al. 2002) (numbers indicate corresponding reference as per source)

It can be seen from the comparisons that the current pump under investigation provides similar performance in comparison with the better performing micropumps reported in the literature. For older pump technologies as reported by Singhal et al (2004) the pump provides a much superior performance in terms of flow rate as compared to the pump size. As pumping technologies improve, more recent pumps reported in the literature provide more comparable performance to the pump under investigation, however the current pump still provides a more superior performance over a significant number of different pumps and pumping technologies reported in the literature.

In addition to the performance benefits, the current micropump design offers a small number of component elements, namely the cavity, orifice and moving diaphragm, as well as a relatively smaller diaphragm size as compared to other vibrating diaphragm micropumps reported in the literature. It also offers a simple design with no mechanical valves and the minimum number of moving components.

The current micropump also offers a higher potential for scalability and adaptability to fabrication methods or materials used as well as operating fluids. This is attributed to the fact that the performance of the synthetic jet actuator depends mainly on the size of its orifice and the displaced volume by the membrane and hence the size of the membrane and its actuation amplitude can be altered to adapt to the actuation mechanism being used. Since the synthetic jet actuator of the pump integrates into the

piping structure it is to perform the pumping action for, several actuators can be attached at different locations and their performance can be changed by simply changing the relative actuation amplitudes and frequencies of the different actuators used.

Chapter 7

CONCLUSION & RECOMMENDATIONS

In this thesis, the utilization of the synthetic jet actuator principle to produce a working micropump has been investigated both numerically and experimentally. For the numerical investigation part, the commercial software package Ansys/CFX was utilized to perform finite volume simulations of the fluid domain for the proposed micropump to solve the set of momentum and continuity equations to predict the flow

through the micropump. The effect of changing the operating parameters of the actuator in terms of actuating amplitude, frequency, and actuation duty cycle were studied as well as the effect of the inlet/outlet channel dimensions. Based on the results of the numerical simulations a sample design was chosen to produce a prototype of the micropump for experimental testing. Experimental investigations were carried out to validate the results of the numerical simulations and measure the performance of the micropump under different operating amplitudes and frequencies.

The proposed micropump consists of a synthetic jet actuator comprising of a 5 mm diameter cavity driven by an orifice 0.2 mm wide and 0.2 mm long. An inverted T-Shaped channel structure was placed at the exit of the synthetic jet actuator cavity, with branches 3 mm long, to form the inlet/outlet channels with the inlet being the two side branches and the outlet being the stem of the inverted T. For the numerical simulations the domain was discretized using a non-uniform grid with approximately 150000 nodes. The actual prototype was fabricated using a combination of standard micromachining and rapid prototyping using PDMS to produce the pump membrane. The pump was actuated using electromagnetic actuation with a permanent rare earth magnet embedded in the PDMS membrane and an external coil through which an alternating current was passed.

Actuation amplitudes in the range of 20 to 60 µm, frequencies between 20 and 60 Hz, and actuation signal duty cycle factor values of 0.25 to 4 were tested with

inlet/outlet channel dimensions between 200 and 800 µm. Based on the results of the numerical simulations, it was found that the micropump can deliver a fluctuating flow rate due to the pulsations of the synthetic jet with an average flow rate of up to 1.3 ml/min. It was also found that the flow rate through the pump was directly proportional to the amplitude of excitation, the frequency of excitation, and the actuation signal duty cycle factor with the increase of one parameter causing a net increase in the flow rate. The inlet/outlet channel dimensions were also found to affect the resulting average flow rate through the pump as well as the fluctuations in the instantaneous flow rate through the pump. An increase in the inlet channel width resulted in a gain in the average flow rate through the pump while decreasing the fluctuations in the flow rate at the outlet at the expense of increasing those fluctuations in the inlet flow rate. An increase in the outlet channel width results in the opposite effect; causing a reduction in the average flow rate through the pump while increasing the fluctuations in the flow rate at the outlet at the expense of decreasing those fluctuations at the inlet.

A modified excitation signal was also utilized to actuate the micropump which resulted in an improved pumping performance in comparison to the base case. The signal is modified by changing the ratio between the suction stroke duration to that of the ejection stroke while maintaining the same mass flux. This change in the actuation signal resulted in an enhancement in the flow rate of the micropump by increasing the duration of the suction stroke while reducing that of the ejection stroke.

The experimental results confirmed the trends that were seen from the numerical simulations with small differences in the values of the flow rates reported which could be attributed to several factors such as losses in the actual pump that were not taken into consideration in the numerical simulations such as entrance and exit losses through the variations in channel cross-sections as well as surface roughness effects … etc.

The maximum back pressure the pump can operate against was also measured experimentally and values of up to 500 Pa were reported at the higher values of operating amplitude and frequency. The power required to drive the pump membrane was also calculated from the numerical simulation results and it was found that up to 122 µW were required to drive the pump membrane. The effect of different geometrical and operating parameters on the value of the driving power were also examined and discussed.

A volumetric efficiency value for the pump was proposed as the ratio of the actual flow rate through the pump to the volume displaced by the membrane per unit time (i.e. the product of the displaced volume of the membrane and the actuation frequency). It was found that the value of the volumetric efficiency depended not only on the actuating signal frequency and amplitude but also on the inlet/outlet channel size as well as the actuation signal duty cycle factor. The numerical simulation results showed that the volumetric efficiency reaches a saturation value for higher values of actuation amplitude which the experimental results could not verify as it was not

possible to achieve such high values of excitation amplitude with the current experimental setup. The pump efficiency values recorded were up to about 74% for the case with a nonuniform excitation signal with a duty cycle ratio value of 4.

7.1 Research contributions

This work provides a fundamental understanding of the mechanism of operation of a novel micropump based on the synthetic jet actuator principle. It also provides an insight into the effect of different geometrical and operating parameters on the performance of the micropump. The main contributions of this work are:

1. The findings of this thesis show that it is possible to produce a working micropump that depends on the synthetic jet principle.
2. Characterization of the synthetic jet actuator in terms of reported formation criteria reported in the literature.
3. The effect of different operating and geometrical parameters on the performance of the micropump was clarified including:
   a. Operating amplitude of the membrane oscillations.
   b. Operating frequency of the membrane oscillations.
   c. Modulation of the operating signal suction/ejection stroke duration ratio.
   d. Pump inlet channel width.
   e. Pump outlet channel width.

4. A physical understanding of the mechanism by which the pumping action is performed in the micropump was also introduced along with details of the flow field in the vicinity of the jet-producing orifice.
5. The effect of different geometrical as well as operational parameters on the driving power required to drive the pump membrane was also examined and discussed.
6. Introduction of a pump volumetric efficiency figure to relate the resultant flow rate to the volume displaced by the actuating membrane.
7. A fabrication method that combines micromachining with rapid prototyping using PDMS was devised to produce the pump prototype.

7.2 Recommendations for future work

This research provides a fundamental understanding of the principle of operation of a micropump based on the synthetic jet principle and the effect of the operating amplitude and frequency of the actuator as well as the widths of the inlet and outlet channels were studied. A fabrication technique for producing a working prototype of micropump was also investigated and utilized to produce a prototype of the micropump which was tested to validate the results of the numerical simulations. Even though, the parameters studied in this thesis provide a general guideline to aid in the design of micropumps based on the synthetic jet principle, several other parameters can further

be studied to improve the state of knowledge of the optimal design of such micropump to obtain the best possible performance. The following provides several recommendations for further parameters that can be studied to further optimize the pump design.

The current research utilizes an electromagnetic actuation mechanism with sinusoidal actuation signal to drive the pump membrane and the effect of changing its amplitude and frequency was studied. Such actuation mechanism requires low frequencies and high amplitudes to operate. Preliminary simulations that were carried out showed that it is possible to obtain a working micropump utilizing much higher frequencies and smaller amplitudes which could lend the use of alternate actuation mechanisms for the pump such as piezoelectric actuation.

Valveless vibrating diaphragm micropumps in the literature utilize nozzle/diffuser elements to replace mechanical valves and provide flow rectification. The effect of manipulating the dimensions and shape of the inlet/outlet channels of the proposed micropump to provide nozzle/diffuser type channels can also be investigated as a means to improve the directionality of the flow from inlet to outlet and thus improve the performance of the pump.

In the current study the geometry and dimensions of the jet producing orifice were fixed at 0.2 mm for the width and 0.2 mm for the length. The effect of changing

the width or length of the orifice can also be studied to examine if these parameters have an effect on the pump performance especially the ratio between the orifice width and the outlet channel width. Utilizing a deeper orifice could change the behavior of the issuing jet and hence affect the pump performance. Moreover, the use of a varying width orifice whether as a nozzle or a diffuser can also be investigated. The shape of the edge of the orifice either on the cavity or exit sides as well can be an affecting parameter whether it has sharp, round or tapered edges.

Since the flow rate through the pump is inherently unsteady due to the pulsating nature of the synthetic jet actuator, the use of several actuators whether in series or in parallel can also be investigated as a means of reducing the fluctuations in the net resultant flow rate.

In the current study, the effect of using a nonuniform excitation signal was also investigated by modifying the relative duration of the ejection/delivery strokes to the total period of excitation. It was found that this resulted in a significant improvement in the performance of the pump. It was suggested that one of the factors that contributed to this improvement was the increase in the entrained flow rate from inlet to outlet during part of the actuation cycle. Further modification to the actuation cycle to enhance that entrainment effect could yield further improvement to the pump performance.

The current prototype was fabricated using a combination of micromachining/rapid prototyping using PDMS. Even though photolithography was investigated in this study as well but was not successful as a means of fabrication due to both limitations in the available photolithographic process or due to assembly problems, the use of other methods of fabrication can also be investigated to produce a pump that is more easily integrated into any microfluidic system with varying production techniques. The use of 3D printing for instance can provide a fast and cost effective way of producing such micropump.

BIBLIOGRAPHY

Abdelgawad, M.; Hassan, I.; Esmail, N. and Phutthavong, P., (2005), "Numerical Investigation of Multistage Viscous Micropump Configurations," *Journal of fluids Engineering*, Vol. 127 (4): 734–742. doi:10.1115/1.1949639.

Abdou, S., (2003), "Synthetic Jet Actuator for Active Flow Control." MASc Thesis, McMaster University.

Abdou, S. and Ziada, S., (2004), "Spanwise Characteristics of High Aspect Ratio Synthetic Jets," *10th AIAA/CEAS Aeroacoustics Conference [AIAA Paper 2004-2855]*. doi:10.2514/6.2004-2855.

Abdou, S. and Ziada, S., (2006), "Spanwise Characteristics of High-Aspect-Ratio Synthetic Jets," *AIAA Journal*, Vol. 44 (7): 1516–1523. doi:10.2514/1.12462.

Ahn, C.H. and Allen, M.G., (1995), "Fluid Micropumps Based on Rotary Magnetic Actuators," *Proceedings of 1995 IEEE Micro Electro Mechanical Systems Workshop (MEMS'95), Amsterdam, Netherlands*: 408–412. doi:10.1109/MEMSYS.1995.472590.

Al-Halhouli, A.T.; Al-Salaymeh, A.; Kilani, M.I. and Büttgenbach, S., (2007), "Numerical Investigation of the Effect of Spiral Curvature on the Flow Field in a Spiral Channel Viscous Micropump," *Microfluidics and Nanofluidics*, Vol. 3 (5): 537–546. doi:10.1007/s10404-006-0144-1.

Amitay, M.; Honohan, A.; Trautman, M.; Glezer, A.; Amitay, M.; Honohan, A.; Trautman, M. and Glezer, A., (1997), "Modification of the Aerodynamic Characteristics of Bluff Bodies Using Fluidic Actuators," *28th Fluid Dynamics Conference, 4th AIAA Shear Flow Control Conference, [AIAA Paper 1997-2004]*. doi:10.2514/6.1997-2004.

Bardell, R.L.; Sharma, N.R.; Forster, F.K.; Afromowitz, M.A. and Penney, R.J., (1997), "Designing High-Performance Micro-Pumps Based on No-Moving-Parts Valves," *Proceedings of 1997 ASME Int. Mechanical Engineering Congress and Exposition*.

Bart, S.F.; Tavrow, L.S.; Mehregany, M. and Lang, J.H., (1990), "Microfabricated Electrohydrodynamic Pumps," *Sensors and Actuators A: Physical*, Vol. 21 (1-3): 193–197. doi:10.1016/0924-4247(90)85037-5.

Benard, W.L.; Kahn, H.; Heuer, A.H. and Huff, M.A., (1998), "Thin-Film Shape-Memory Alloy Actuated Micropumps," *Journal of Microelectromechanical Systems*, Vol. 7 (2): 245–251. doi:10.1109/84.679390.

Blanchard, D.; Ligrani, P. and Gale, B., (2005), "Single-Disk and Double-Disk Viscous Micropumps," *Sensors and Actuators A: Physical*, Vol. 122 (1): 149–158. doi:10.1016/j.sna.2005.03.072.

Body, C.; Reyne, G.; Meunier, G.; Quandt, E. and Seemann, K., (1997), "Application of Magnetostrictive Thin Films for Microdevices," *IEEE Transactions on Magnetics*, Vol. 33 (2): 2163–2166.

Böhm, S.; Olthius, W. and Bergveld, P., (1999), "An Electrochemically Actuated Micropump for Use in a Push-Pull Microdialysis Based in-Vivo Monitoring System," *Proceedings of the Transducer 1999*, Vol. 99: 880–881.

Böhm, S.; Olthuis, W. and Bergveld, P., (1999), "A Plastic Micropump Constructed with Conventional Techniques and Materials," *Sensors and Actuators A: Physical*, Vol. 77 (3): 223–228.

Brask, A.; Goranović, G.; Jensen, M.J. and Bruus, H., (2005), "A Novel Electro-Osmotic Pump Design for Nonconducting Liquids: Theoretical Analysis of Flow Rate–Pressure Characteristics and Stability," *Journal of Micromechanics and Microengineering*, Vol. 15 (4): 883–891. doi:10.1088/0960-1317/15/4/029.

Broderick, S.L.; Webb, B.W. and Maynes, D., (2005), "Thermally Developing Electro-Osmotic Convection in Microchannels with Finite Debye-Layer Thickness," *Numerical Heat Transfer, Part A: Applications*, Vol. 48 (10): 941–964. doi:10.1080/10407780500283309.

Cabuz, C.; Herb, W.R.; Cabuz, E.I. and Lu, S.T., (2001), "The Dual Diaphragm Pump," *The 14th IEEE International Conference on MicroElectroMechanical Systems, 2001. (MEMS 2001)*: 519–522. doi:10.1109/MEMSYS.2001.906593.

Campbell, J.S., Jr; Black, W.Z.; Glezer, A. and Hartley, J.G., (1998), "Thermal Management of a Laptop Computer with Synthetic Air Microjets," *The Sixth Intersociety Conference on Thermal and Thermomechanical Phenomena in Electronic Systems, 1998 (ITHERM '98)*: 43–50. doi:10.1109/ITHERM.1998.689518.

Cao, L.; Mantell, S. and Polla, D., (2001), "Design and Simulation of an Implantable Medical Drug Delivery System Using Microelectromechanical Systems Technology," *Sensors and Actuators A: Physical*, Vol. 94 (1-2): 117–125.

Carrozza, M.C.; Croce, N.; Magnani, B. and Dario, P., (1995), "A Piezoelectric-Driven Stereolithography-Fabricated Micropump," *Journal of Micromechanics and Microengineering*, Vol. 5 (2): 177.

Chen, L.; Wang, H.; Ma, J.; Wang, C. and Guan, Y., (2005), "Fabrication and Characterization of a Multi-Stage Electroosmotic Pump for Liquid Delivery," *Sensors and Actuators B: Chemical*, Vol. 104: 117–123.

Chen, Z.; Wang, P. and Chang, H.-C., (2005), "An Electro-Osmotic Micro-Pump Based on Monolithic Silica for Micro-Flow Analyses and Electro-Sprays," *Analytical and Bioanalytical Chemistry*, Vol. 382 (3): 817–824. doi:10.1007/s00216-005-3130-7.

Choi, J.P.; Kim, K.S.; Seo, Y.H. and Kim, B.H., (2011), "Design and Fabrication of Synthetic Air-Jet Micropump," *International Journal of Precision Engineering and Manufacturing*, Vol. 12 (2): 355–360. doi:10.1007/s12541-011-0046-3.

Coe, D.J.; Allen, M.G.; Smith, B.L. and Glezer, A., (1995), "Addressable Micromachined Jet Arrays," *The 8th International Conference on Solid-State Sensors and Actuators and Eurosensors IX (Transducers '95)*, Vol. 2: 329–332. doi:10.1109/SENSOR.1995.721813.

Coe, D.J.; Allen, M.G.; Trautman, M.A. and Glezer, A., (1994), "Micromachined Jets for Manipulation of Macro Flows," *Solid-state sensor and actuator workshop, 1994*: 13–16.

Crook, A. and Wood, N., (2001), "Measurements and Visualizations of Synthetic Jets," *39th Aerospace Sciences Meeting and Exhibit [AIAA Paper 2001-0145]*. doi:doi:10.2514/6.2001-145.

Cunneen, J.; Lin, Y.-C.; Caraffini, S.; Boyd, J.G.; Hesketh, P.J.; Lunte, S.M. and Wilson, G.S., (1998), "A Positive Displacement Micropump for Microdialysis," *Mechatronics*, Vol. 8 (5): 561–583.

Da Silva, A.K.; Kobayashi, M.H. and Coimbra, C.F.M., (2007), "Optimal Theoretical Design of 2-D Microscale Viscous Pumps for Maximum Mass Flow Rate and Minimum Power Consumption," *International Journal of Heat and Fluid Flow*, Vol. 28 (3): 526–536. doi:10.1016/j.ijheatfluidflow.2006.07.005.

Darabi, J. and Wang, H., (2005), "Development of an Electrohydrodynamic Injection Micropump and Its Potential Application in Pumping Fluids in Cryogenic Cooling Systems," *Microelectromechanical Systems*, Vol. 14 (4): 747–755.

Darabi, J.; Ohadi, M.M. and DeVoe, D., (2001), "An Electrohydrodynamic Polarization Micropump for Electronic Cooling," *Journal of Microelectromechanical Systems*, Vol. 10 (1): 98–106. doi:10.1109/84.911097.

Davis, S.A. and Glezer, A., (1999), "Mixing Control of Fuel Jets Using Synthetic Jet Technology: Velocity Field Measurements," *37th Aerospace Sciences Meeting & Exhibit [AIAA Paper 1999-0447]*, (0447).

Debesset, S.; Hayden, C.J.; Dalton, C.; Eijkel, J.C.T. and Manz, A., (2004), "An AC Electroosmotic Micropump for Circular Chromatographic Applications.," *Lab on a chip*, Vol. 4 (4): 396–400. doi:10.1039/b314123c.

Deng, K.; Dewa, A.S.; Ritter, D.C.; Bonham, C. and Guckel, H., (1998), "Characterization of Gear Pumps Fabricated by LIGA," *Microsystem Technologies*, Vol. 4 (4): 163–167. doi:10.1007/s005420050122.

Dewa, A.S.; Deng, K.; Ritter, D.C.; Bonham, C.; Guckel, H. and Massood-Ansari, S., (1997), "Development of LIGA-Fabricated, Self-Priming, in-Line Gear Pumps," *International Solid State Sensors and Actuators Conference (Transducers '97)*, Vol. 2: 757–760. doi:10.1109/SENSOR.1997.635210.

Dinh, T.X. and Ogami, Y., (2011), "An Integrated Pumping and Mixing Device," *Journal of Fluid Science and Technology*, Vol. 6 (6): 949–961. doi:10.1299/jfst.6.949.

Dinh, T.X.; Dau, V.T.; Ogami, Y. and Sugiyama, S., (2008), "Numerical Design and Performance of a Valveless Micropump," *Transactions of the IRE Professional Group on Audio*: 323–326. doi:10.1109/ATC.2008.4760587.

Dissanayake, D.W.; Tikka, A.C.; Al-Sarawi, S.F. and Abbott, D., (2007), "A Radio Frequency Controlled Microvalve for Biomedical Applications," *Proceedings of SPIE—The international society for optical engineering*, Vol. 6413: 64130D. doi:10.1117/12.695743.

Duwairi, H. and Abdullah, M., (2007), "Thermal and Flow Analysis of a Magneto-Hydrodynamic Micropump," *Microsystem Technologies*, Vol. 13: 33–39.

Esashi, M.; Shoji, S. and Nakano, A., (1989), "Normally Closed Microvalve and Mircopump Fabricated on a Silicon Wafer," *Sensors and Actuators*, Vol. 20 (1-2): 163–169. doi:10.1016/0250-6874(89)87114-8.

Feng, L.H.; Wang, J.J. and Pan, C., (2010), "Effect of Novel Synthetic Jet on Wake Vortex Shedding Modes of a Circular Cylinder," *Journal of fluids and structures*, Vol. 26 (6): 900–917. doi:10.1016/j.jfluidstructs.2010.05.003.

Forster, F.K.; Bardell, R.L.; Afromowitz, M.A.; Sharma, N.R. and Blanchard, A., (1995a), "Design, Fabrication and Testing of Fixed-Valve Micro-Pumps," *Proceedings of the ASME Fluids Engineering Division*: 39–44.

Forster, F.K.; Bardell, R.L.; Afromowitz, M.A.; Sharma, N.R. and Blanchard, A., (1995b), "Design, Fabrication and Testing of Fixed-Valve Micro-Pumps," *ASME Fluids Engineering Division*: 39–44.

Fuhr, G.; Hagedorn, R.; Müller, T.; Benecke, W. and Wagner, B., (1992a), "Pumping of Water Solutions in Microfabricated Electrohydrodynamic Systems," *Proceedings IEEE Micro Electro Mechanical Systems '92*: 25–30. doi:10.1109/MEMSYS.1992.187685.

Fuhr, G.; Hagedorn, R.; Müller, T.; Benecke, W. and Wagner, B., (1992b), "Microfabricated Electrohydrodynamic (EHD) Pumps for Liquids of Higher Conductivity," *Journal of Microelectromechanical Systems*, Vol. 1 (3): 141–146. doi:10.1109/84.186393.

Fuhr, G.; Schnelle, T. and Wagner, B., (1999), "Travelling Wave-Driven Microfabricated Electrohydrodynamic Pumps for Liquids," *Journal of Micromechanics and Microengineering*, Vol. 4 (4): 217–226. doi:10.1088/0960-1317/4/4/007.

Gad-el-Hak, M., (1999), "The Fluid Mechanics of Microdevices - the Freeman Scholar Lecture," *Journal of fluids Engineering*, Vol. 121 (5).

Gad-el-Hak, M., (2002), *The MEMS Handbook*. CRC Press.

Gallas, Q.; Mathew, J.; Anurag, K.; Holman, R.; Nishida, T.; Carroll, B.; Sheplak, M. and Cattafesta, L., (2002), "Lumped Element Modeling of Piezoelectric-Driven Synthetic Jet Actuators," *AIAA 40th Aerospace Sciences Meeting & Exhibit [AIAA Paper 2002-0125]*.

Gallas, Q.; Wang, G.; Papila, M.; Sheplak, M. and Cattafesta, L., (2003), "Optimization of Synthetic Jet Actuators," *41st Aerospace Sciences Meeting & Exhibit [AIAA Paper 2003-0635]*. doi:10.2514/6.2003-635.

Gamboa, A.R.; Morris, C.J. and Forster, F.K., (2005), "Improvements in Fixed-Valve Micropump Performance Through Shape Optimization of Valves," *Journal of fluids Engineering*, Vol. 127 (2): 339. doi:10.1115/1.1891151.

Garcia-Sanchez, P.; Ramos, A.; Green, N.G. and Morgan, H., (2006), "Experiments on AC Electrokinetic Pumping of Liquids Using Arrays of Microelectrodes," *IEEE Transactions on Dielectrics and Electrical Insulation*, Vol. 13 (3): 670–677. doi:10.1109/TDEI.2006.1657983.

Geng, X.; Yuan, H.; Oguz, H.N. and Prosperetti, A., (2001), "Bubble-Based Micropump for Electrically Conducting Liquids," *Journal of Micromechanics and Microengineering*, Vol. 11 (3): 270–276. doi:10.1088/0960-1317/11/3/317.

Gerlach, T., (1998), "Microdiffusers as Dynamic Passive Valves for Micropump Applications," *Sensors and Actuators A: Physical*, Vol. 69 (2): 181–191. doi:10.1016/S0924-4247(98)00056-9.

Gerlach, T. and Wurmus, H., (1995), "Working Principle and Performance of the Dynamic Micropump," *Sensors and Actuators A: Physical*, Vol. 50 (1-2): 135–140. doi:10.1016/0924-4247(96)80097-5.

Gerlach, T.; Schuenemann, M. and Wurmus, H., (1999), "A New Micropump Principle of the Reciprocating Type Using Pyramidic Micro Flowchannels as Passive Valves," *Journal of Micromechanics and Microengineering*, Vol. 5 (2): 199–201. doi:10.1088/0960-1317/5/2/039.

Gilarranz, J. and Rediniotis, O., (2001), "Compact, High-Power Synthetic Jet Actuators for Flow Separation Control," *39th Aerospace Sciences Meeting and Exhibit [AIAA Paper 2001-737]*. doi:10.2514/6.2001-737.

Glezer, A. and Amitay, M., (2002), "Synthetic Jets," *Annual Review of Fluid Mechanics*, Vol. 34 (3): 503–529. doi:10.1146/annurev.fluid.34.090501.094913.

Glezer, A. and Wiltse, J.W., (2000), "Synthetic Jet Actuators for Mixing Applications." US Patent 6,056,204.

Glezer, A.; Allen, M.G.; Coe, D.J.; Smith, B.L.; Trautman, M.A. and Wiltse, J.W., (1999), "Synthetic Jet Actuator and Applications Thereof." US Patent 5,894,990.

Go, D.B.; Garimella, S.V.; Fisher, T.S. and Mongia, R.K., (2007), "Ionic Winds for Locally Enhanced Cooling," *Journal of Applied Physics*, Vol. 102 (5): 053302–053302–8. doi:10.1063/1.2776164.

Gong, Q.; Zhou, Z.; Yang, Y. and Wang, X., (2000), "Design, Optimization and Simulation on Microelectromagnetic Pump," *Sensors and Actuators A: Physical*, Vol. 83 (1-3): 200–207. doi:10.1016/s0924-4247(99)00384-2.

Gravesen, P.; Branebjerg, J. and Jensen, O.S., (1993), "Microfluidics - a Review," *Journal of Micromechanics and Microengineering*, Vol. 3: 168–182. doi:10.1088/0960-1317/3/4/002.

Grosjean, C. and Tai, Y.-C., (1999), "A Thermopneumatic Peristaltic Micropump," *Proceedings of the 10th International Conference on Solid-State Sensors and Actuators*, Vol. 99: 1776–1779.

Haik, Y.; Kilani, M.; Hendrix, J.; Rifai, O.A. and Galambos, P., (2007), "Flow Field Analysis in a Spiral Viscous Micropump," *Microfluidics and Nanofluidics*, Vol. 3 (5): 527–535. doi:10.1007/s10404-006-0143-2.

Hatch, A.; Kamholz, A.E.; Holman, G.; Yager, P. and Böhringer, K.F., (2001), "A Ferrofluidic Magnetic Micropump," *Microelectromechanical Systems, Journal of*, Vol. 10 (2): 215–221. doi:10.1109/84.925748.

Heng, K.-H.; Huang, L.; Wang, W. and Murphy, M.C., (1999), "Development of a Diffuser/Nozzle-Type Micropump Based on Magnetohydrodynamic (MHD) Principle," *Proceedings SPIE, Microfluidic Devices and Systems II*, Vol. 3877: 66–73. doi:10.1117/12.359355.

Heng, K.-H.; Wang, W.; Murphy, M.C. and Lian, K., (2000), "UV-LIGA Microfabrication and Test of an Ac-Type Micropump Based on the Magnetohydrodynamic (MHD)

Principle," *Proceedings SPIE, Microfluidic Devices and Systems III*, Vol. 4177: 161–171. doi:10.1117/12.395655.

Heschel, M.; Mullenborn, M. and Bouwstra, S., (1997), "Fabrication and Characterization of Truly 3-D Diffuser/Nozzle Microstructures in Silicon," *Microelectromechanical Systems, Journal of*, Vol. 6 (1): 41–47. doi:10.1109/84.557529.

Ho, C.-M. and Tai, Y.-C., (1998), "Micro-Electro-Mechanical-Systems (MEMS) and Fluid Flows," *Annual Review of Fluid Mechanics*, Vol. 30 (1): 579–612.

Holman, R., (2005), "Formation Criterion for Synthetic Jets," *AIAA Journal*, Vol. 43 (10). doi:10.2514/1.12033.

Homsy, A.; Linder, V.; Lucklum, F. and De Rooij, N.F., (2007), "Magnetohydrodynamic Pumping in Nuclear Magnetic Resonance Environments," *Sensors and Actuators B: Chemical*, Vol. 123: 636–646. doi:10.1016/j.snb.2006.09.026.

Hsiao, F.B. and Shyu, J.Y., (1991), "Influence of Internal Acoustic Excitation Upon Flow Passing a Circular Cylinder," *Journal of fluids and structures*, Vol. 5: 427–442. doi:10.1016/0889-9746(91)90429-S.

Huang, X.Y., (1995), "Suppression of Vortex Shedding From a Circular Cylinder by Internal Acoustic Excitation," *Journal of fluids and structures*, Vol. 9 (5): 563–570.

Ibrahim, M.K.; Kunimura, R. and Nakamura, Y., (2002), "Mixing Enhancement of Compressible Jets by Using Unsteady Microjets as Actuators," *AIAA Journal*, Vol. 40 (4): 681–688. doi:10.2514/2.1700.

Ingård, U. and Labate, S., (1950), "Acoustic Circulation Effects and the Nonlinear Impedance of Orifices," *The Journal of the Acoustical Society of America*, Vol. 22: 211.

Iverson, B.D. and Garimella, S.V., (2008), "Recent Advances in Microscale Pumping Technologies: a Review and Evaluation," *Microfluidics and Nanofluidics*, Vol. 5 (2): 145–174. doi:10.1007/s10404-008-0266-8.

Iverson, B.D.; Maynes, D. and Webb, B.W., (2004), "Thermally Developing Electroosmotic Convection in Rectangular Microchannels with Vanishing Debye-Layer Thickness," *Journal of Thermophysics and Heat Transfer*, Vol. 18 (4): 486–493. doi:10.2514/1.3769.

Jang, J. and Lee, S.S., (2000), "Theoretical and Experimental Study of MHD (Magnetohydrodynamic) Micropump," *Sensors and Actuators A: Physical*, Vol. 80 (1): 84–89. doi:10.1016/S0924-4247(99)00302-7.

Jang, L.S.; Morris, C.J.; Sharma, N.R.; Bardell, R.L. and Forster, F.K., (1999), "Transport of Particle-Laden Fluids Through Fixed-Valve Micropumps," In, 503–509.

Jang, L.S.; Sharma, N.R. and Forster, F.K., (2000), "The Effect of Particles on Performance of Flxed-Valve Mlcropumps," *4th International Symposium on Micro Total Analysis Systems*: 283–286.

Jeong, O.C. and Yang, S.S., (2000a), "Fabrication of a Thermopneumatic Microactuator with a Corrugated P+ Silicon Diaphragm," *Sensors and Actuators A: Physical*, Vol. 80 (1): 62–67. doi:10.1016/S0924-4247(99)00300-3.

Jeong, O.C. and Yang, S.S., (2000b), "Fabrication and Test of a Thermopneumatic Micropump with a Corrugated P+ Diaphragm," *Sensors and Actuators A: Physical*, Vol. 83 (1-3): 249–255. doi:10.1016/S0924-4247(99)00392-1.

Jiang, X.N.; Zhou, Z.Y.; Huang, X.Y.; Li, Y.; Yang, Y. and Liu, C.Y., (1998), "Micronozzle/Diffuser Flow and Its Application in Micro Valveless Pumps," *Sensors and Actuators A: Physical*, Vol. 70 (1-2): 81–87. doi:10.1016/S0924-4247(98)00115-0.

Jie Wu, (2006), "Biased AC Electro-Osmosis for on-Chip Bioparticle Processing," *IEEE Transactions On Nanotechnology*, Vol. 5 (2): 84–89. doi:10.1109/TNANO.2006.869645.

Jun, T.K. and Kim, C.-J., (1996), "Microscale Pumping Using Traversing Vapor Bubbles in Microchannels," *1996 Solid-State Sensor and Actuator Workshop*: 144–147.

Jun, T.K. and Kim, C.-J., (1998), "Valveless Pumping Using Traversing Vapor Bubbles in Microchannels," *Journal of Applied Physics*, Vol. 83 (11): 5658–5664. doi:10.1063/1.367419.

Kallenbach, E., (1999), "New Polarized Electromagnetic Actuators as Integrated Mechatronic Components Ð Design and Application," *Mechatronics*, Vol. 9: 769–784.

Kamper, K.-P.; Dopper, J.; Ehrfeld, W. and Oberbeck, S., (1998), "A Self-Filling Low-Cost Membrane Micropump," *Proceedings of the Eleventh Annual International Workshop on MicroElectroMechanical Systems (MEMS '98)*: 432–437. doi:10.1109/MEMSYS.1998.659796.

Kang, Y.; Tan, S.C.; Yang, C. and Huang, X., (2007), "Electrokinetic Pumping Using Packed Microcapillary," *Sensors and Actuators A: Physical*, Vol. 133: 375–382.

Kercher, D.S.; Lee, J.-B.; Brand, O.; Allen, M.G. and Glezer, A., (2003), "Microjet Cooling Devices for Thermal Management of Electronics," *IEEE Transactions on Components and Packaging Technologies*, Vol. 26 (2): 359–366. doi:10.1109/TCAPT.2003.815116.

Khoo, M. and Liu, C., (2001), "Micro Magnetic Silicone Elastomer Membrane Actuator," *Sensors and Actuators A: Physical*, Vol. 89 (3): 259–266.

Kilani, M.I.; Al-Salaymeh, A. and Al-Halhouli, A.T., (2006), "Effect of Channel Aspect Ratio on the Flow Performance of a Spiral-Channel Viscous Micropump," *Journal of fluids Engineering*, Vol. 128 (3): 618. doi:10.1115/1.2175169.

Kline, J.S. and McClintock, F.A., (1953), "Describing Uncertainties in Single-Sample Experiments," *Mechanical engineering*, Vol. 75 (1): 3–8.

Koch, M.; Evans, A.G.R. and Brunnschweiler, A., (1998), "The Dynamic Micropump Driven with a Screen Printed PZT Actuator," *Journal of Micromechanics and Microengineering*, Vol. 8 (2): 119. doi:10.1088/0960-1317/8/2/019.

Koch, M.; Harris, N.; Evans, A.G.R.; White, N.M. and Brunnschweiler, A., (1998), "A Novel Micromachined Pump Based on Thick-Film Piezoelectric Actuation," *Sensors and Actuators A: Physical*, Vol. 70 (1-2): 98–103.

Koch, M.; Harris, N.; Maas, R.; Evans, A.G.R.; White, N.M. and Brunnschweiler, A., (1997), "A Novel Micropump Design with Thick-Film Piezoelectric Actuation," *Measurement Science and Technology*, Vol. 8: 49.

Krulevitch, P.; Lee, A.P.; Ramsey, P.B.; Trevino, J.C.; Hamilton, J. and Northrup, M.A., (1996), "Thin Film Shape Memory Alloy Microactuators," *Microelectromechanical Systems, Journal of*, Vol. 5 (4): 270–282.

Laser, D. and Santiago, J.G., (2004), "A Review of Micropumps," *Journal of Micromechanics and Microengineering*, Vol. 14: R35–R64.

Lebedeva, I.V., (1980), "Experimental Study of Acoustic Streaming in the Vicinity of Orifices," *Soviet Physics Acoustics*, Vol. 26: 331.

Lee, C.; Hong, G.; Ha, Q.P. and Mallinson, S.G., (2003), "A Piezoelectrically Actuated Micro Synthetic Jet for Active Flow Control," *Sensors and Actuators A: Physical*, Vol. 108 (1-3): 168–174. doi:10.1016/S0924-4247(03)00267-X.

Lee, J.; Moon, H.; Fowler, J.; Kim, C.-J.K.C.-J. and Schoellhammer, T., (2001), "Addressable Micro Liquid Handling by Electric Control of Surface Tension," *Proceedings of the IEEE International Conference on MicroElectroMechanical Systems*: 499–502. doi:10.1109/MEMSYS.2001.906588.

Lee, J.L.J. and Kim, C.-J.K.C.-J., (2000), "Surface-Tension-Driven Microactuation Based on Continuous Electrowetting," *Journal of Microelectromechanical Systems*, Vol. 9 (2): 171–180. doi:10.1109/84.846697.

Lemoff, A.V. and Lee, A.P., (2000), "An AC Magnetohydrodynamic Micropump," *Sensors and Actuators B: Chemical*, Vol. 63 (3): 178–185. doi:10.1016/S0925-4005(00)00355-5.

Lemoff, A.V.; Lee, A.P.; Miles, R.R. and McConaghy, C.F., (1999), "An AC Magnetohydrodynamic Micropump: Towards a True Integrated Microfluidic

System," *10th International Conference on Solid-State Sensors and Actuators (Transducers '99)*.

Linnemann, R.; Woias, P.; Senfft, C.D. and Ditterich, J.A., (1998), "A Self-Priming and Bubble-Tolerant Piezoelectric Silicon Micropump for Liquids and Gases," *Proceedings of the Eleventh Annual International Workshop on MicroElectroMechanical Systems (MEMS '98)*: 532–537.

Lockerby, D.A. and Carpenter, P.W., (2004), "Modeling and Design of Microjet Actuators," *AIAA Journal*, Vol. 42 (2): 220–227. doi:10.2514/1.9091.

Lockerby, D.A.; Carpenter, P.W. and Davies, C., (2002), "Numerical Simulation of the Interaction of Microactuators and Boundary Layers," *AIAA Journal*, Vol. 40 (1): 67–73. doi:10.2514/2.1615.

Luginbuhl, P.; Collins, S.D.; Racine, G.-A.; Grétillat, M.-A.; De Rooij, N.F.; Brooks, K.G. and Setter, N., (1997), "Microfabricated Lamb Wave Device Based on PZT Sol-Gel Thin Film for Mechanical Transport of Solid Particles and Liquids," *Journal of Microelectromechanical Systems*, Vol. 6 (4): 337–346. doi:10.1109/84.650131.

Luginbuhl, P.; Collins, S.D.; Racine, G.-A.; Grétillat, M.-A.; De Rooij, N.F.; Brooks, K.G. and Setter, N., (1998), "Ultrasonic Flexural Lamb-Wave Actuators Based on PZT Thin Film," *Sensors and Actuators A: Physical*, Vol. 64 (1): 41–49.

Luo, Z.-B. and Xia, Z.-X., (2005), "A Novel Valve-Less Synthetic-Jet-Based Micro-Pump," *Sensors and Actuators A: Physical*, Vol. 122 (1): 131–140. doi:10.1016/j.sna.2005.03.062.

Machauf, A.; Nemirovsky, Y. and Dinnar, U., (2005), "A Membrane Micropump Electrostatically Actuated Across the Working Fluid," *Journal of Micromechanics and Microengineering*, Vol. 15 (12): 2309–2316. doi:10.1088/0960-1317/15/12/013.

Mahalingam, R. and Glezer, A., (2002), "Air Cooled Heat Sinks Integrated with Synthetic Jets," *The Eighth Inter Society Conference on Thermal and Thermomechanical Phenomena in Electronic Systems (ITHERM 2002)*: 285–291.

Mahalingam, R.; Rumigny, N. and Glezer, A., (2004), "Thermal Management Using Synthetic Jet Ejectors," *IEEE Transactions on Components and Packaging Technologies*, Vol. 27 (3): 439–444. doi:10.1109/TCAPT.2004.831757.

Makino, E.; Mitsuya, T. and Shibata, T., (2000a), "Dynamic Actuation Properties of TiNi Shape Memory Diaphragm," *Sensors and Actuators A: Physical*, Vol. 79 (2): 128–135.

Makino, E.; Mitsuya, T. and Shibata, T., (2000b), "Micromachining of TiNi Shape Memory Thin Film for Fabrication of Micropump," *Sensors and Actuators A: Physical*, Vol. 79 (3): 251–259.

Makino, E.; Mitsuya, T. and Shibata, T., (2001), "Fabrication of TiNi Shape Memory Micropump," *Sensors and Actuators A: Physical*, Vol. 88 (3): 256–262.

Makino, E.; Shibata, T. and Kato, K., (1999), "Dynamic Thermo-Mechanical Properties of Evaporated TiNi Shape Memory Thin Film," *Sensors and Actuators A: Physical*, Vol. 78 (2-3): 163–167.

Mallinson, S.G.; Kwok, C.Y. and Reizes, J.A., (2003), "Numerical Simulation of Micro-Fabricated Zero Mass-Flux Jet Actuators," *Sensors and Actuators A: Physical*, Vol. 105 (3): 229–236. doi:10.1016/S0924-4247(03)00204-8.

Mallinson, S.G.; Reizes, J.A.; Hong, G. and Buttini, M., (1999), "Synthetic Jet Actuators for Flow Control," *Proceedings of SPIE*, Vol. 3891: 146.

Matsumoto, H. and Colgate, J.E., (1990), "Preliminary Investigation of Micropumping Based on Electrical Control of Interfacial Tension," *Micro Electro Mechanical Systems, 1990. Proceedings, An Investigation of Micro Structures, Sensors, Actuators, Machines and Robots. IEEE*: 105–110. doi:10.1109/MEMSYS.1990.110258.

Matsumoto, S.; Klein, A. and Maeda, R., (1999), "Development of Bi-Directional Valve-Less Micropump for Liquid," *Proceedings of the Twelfth IEEE International Conference on MicroElectroMechanical Systems (MEMS '99)*: 141–146. doi:10.1109/MEMSYS.1999.746791.

Mautner, T., (2004), "Application of the Synthetic Jet Concept to Low Reynolds Number Biosensor Microfluidic Flows for Enhanced Mixing: a Numerical Study Using the Lattice Boltzmann Method.," *Biosensors & bioelectronics*, Vol. 19 (11): 1409–1419. doi:10.1016/j.bios.2003.12.023.

McCormick, D., (2000), "Boundary Layer Separation Control with Directed Synthetic Jets," *38th Aerospace Sciences Meeting and Exhibit [AIAA Paper 2000-0519]*. doi:10.2514/6.2000-519.

Mittal, R.; Rampunggoon, P. and Udaykumar, H.S., (2001), "Interaction of a Synthetic Jet with a Flat Plate Boundary Layer," *31st AIAA Fluid Dynamics Conference and Exhibit [AIAA Paper 2001-2773]*. doi:10.2514/6.2001-2773.

Mizoguchi, H.; Ando, M.; Mizuno, T.; Takagi, T. and Nakajima, N., (1992), "Design and Fabrication of Light Driven Micropump," *Micro Electro Mechanical Systems, 1992, MEMS '92, Proceedings. An Investigation of Micro Structures, Sensors, Actuators, Machines and Robot. IEEE*: 31–36. doi:10.1109/MEMSYS.1992.187686.

Moesner, F.M. and Higuchi, T., (1995), "Devices for Particle Handling by an AC Electric Field," *IEEE Micro Electro Mechanical Systems. 1995*: 66–71. doi:10.1109/MEMSYS.1995.472552.

Moghaddam, S. and Ohadi, M.M., (2005), "Effect of Electrode Geometry on Performance of an EHD Thin-Film Evaporator," *Journal of Microelectromechanical Systems*, Vol. 14 (5): 978–986. doi:10.1109/JMEMS.2005.851812.

Moroney, R.M.; White, R.M. and Howe, R.T., (1990), "Fluid Motion Produced by Ultrasonic Lamb Waves," *Ultrasonics Symposium, 1990 Proceedings, IEEE*: 355–358. doi:10.1109/ULTSYM.1990.171385.

Moroney, R.M.; White, R.M. and Howe, R.T., (1991a), "Ultrasonically Induced Microtransport," *IEEE Micro Electro Mechanical Systems*: 277–282. doi:10.1109/MEMSYS.1991.114810.

Moroney, R.M.; White, R.M. and Howe, R.T., (1991b), "Microtransport Induced by Ultrasonic Lamb Waves," *Applied Physics Letters*, Vol. 59 (7): 774–776. doi:10.1063/1.105339.

Mpholo, M.; Smith, C.G. and Brown, A.B.D., (2003), "Low Voltage Plug Flow Pumping Using Anisotropic Electrode Arrays," *Sensors and Actuators B: Chemical*, Vol. 92 (3): 262–268. doi:10.1016/S0925-4005(03)00289-2.

Müller, M.O.; Bernal, L.P.; Moran, R.P.; Washabaugh, P.D.; Parviz, B.A.; Chou, T.-K.A.; Zhang, C. and Najafi, K., (2000), "Thrust Performance of Micromachined Synthetic Jets," *Fluids 2000 [AIAA Paper 2000-2404]*.

Müller, M.O.; Bernal, L.P.; Washabaugh, P.D.; Chou, T.-K.A. and Najafi, K., (2002), "Flow Field and Performance of High Frequency Micromachined Synthetic Jets," *AIAA 40th Aerospace Sciences Meeting & Exhibit [AIAA Paper 2002-0974]*. doi:10.2514/6.2002-974.

Müller, M.O.; Bernal, L.P.; Washabaugh, P.D.; Chou, T.-K.A.; Kim, H.S. and Najafi, K., (2002), "Acoustically Generated Micromachined Jet Arrays for Micropropulsion Applications," *Proceedings of the ASME International Mechanical Engineering Congress and Exposition (IMECE '02)*.

Müller, M.O.; Bernal, L.P.; Washabaugh, P.D.; Kim, H.S. and Najafi, K., (2003), "Resonance Effects of Electrostatically Actuated Acoustic Jets," *AIAA 41st Aerospace Schiences Meeting and Exhibit [AIAA Paper 2003-1272]*. doi:doi:10.2514/6.2003-1272.

Nguyen, N.-T. and Wereley, S.T., (2006), *Fundamentals and Applications of Microfluidics*. Second Edition. Artech House Publishers.

Nguyen, N.-T.; Huang, X. and Chuan, T.K., (2002), "MEMS-Micropumps: a Review," *Journal of Fluids Engineering (Transactions of the ASME)*, Vol. 124 (2): 384–392. doi:10.1115/1.1459075.

Nguyen, N.-T.; Schubert, S.; Richter, S. and Dötzel, W., (1998), "Hybrid-Assembled Micro Dosing System Using Silicon-Based Micropump/Valve and Mass Flow Sensor," *Sensors and Actuators A: Physical*, Vol. 69 (1): 85–91.

Nguyen, N.T. and Huang, X., (2001), "Miniature Valveless Pumps Based on Printed Circuit Board Technique," *Sensors and Actuators A: Physical*, Vol. 88 (2): 104–111.

Olsson, A.; Enoksson, P.; Stemme, G. and Stemme, E., (1996), "A Valve-Less Planar Pump Isotropically Etched in Silicon," *Journal of Micromechanics and Microengineering*, Vol. 6: 87.

Olsson, A.; Enoksson, P.; Stemme, G. and Stemme, E., (1997), "Micromachined Flat-Walled Valveless Diffuser Pumps," *Microelectromechanical Systems, Journal of*, Vol. 6 (2): 161–166. doi:10.1109/84.585794.

Olsson, A.; Larsson, O.; Holm, J.; Lundbladh, L.; Ohman, O. and Stemme, G., (1997), "Valve-Less Diffuser Micropumps Fabricated Using Thermoplastic Replication," *10th Annual International Workshop on MicroElectroMechanical Systems (MEMS '97), Proceedings, IEEE*: 305–310. doi:10.1109/MEMSYS.1997.581836.

Olsson, A.; Larsson, O.; Holm, J.; Lundbladh, L.; Ohman, O. and Stemme, G., (1998), "Valve-Less Diffuser Micropumps Fabricated Using Thermoplastic Replication," *Sensors and Actuators A: Physical*, Vol. 64 (1): 63–68.

Olsson, A.; Stemme, G. and Stemme, E., (1995), "A Valve-Less Planar Fluid Pump with Two Pump Chambers," *Sensors and Actuators A: Physical*, Vol. 47 (1-3): 549–556.

Olsson, A.; Stemme, G. and Stemme, E., (1996), "Diffuser-Element Design Investigation for Valve-Less Pumps," *Sensors and Actuators A: Physical*, Vol. 57 (2): 137–143. doi:10.1016/S0924-4247(97)80104-5.

Olsson, A.; Stemme, G. and Stemme, E., (2000), "Numerical and Experimental Studies of Flat-Walled Diffuser Elements for Valve-Less Micropumps," *Sensors and Actuators A: Physical*, Vol. 84 (1-2): 165–175. doi:10.1016/S0924-4247(99)00320-9.

Ozaki, K., (1995), "Pumping Mechanism Using Periodic Phase Changes of a Fluid," *Micro Electro Mechanical Systems, 1995, MEMS '95, Proceedings. IEEE*. doi:10.1109/MEMSYS.1995.472558.

Patel, V. and Kassegne, S.K., (2007), "Electroosmosis and Thermal Effects in Magnetohydrodynamic (MHD) Micropumps Using 3D MHD Equations," *Sensors and Actuators B: Chemical*, Vol. 122: 42–52.

Piyasena, M.E.; Lopez, G.P. and Petsev, D.N., (2006), "An Electrokinetic Cell Model for Analysis and Optimization of Electroosmotic Microfluidic Pumps," *Sensors and Actuators B: Chemical*, Vol. 113: 461–467.

Pollack, M.G.; Fair, R.B. and Shenderov, A.D., (2000), "Electrowetting-Based Actuation of Liquid Droplets for Microfluidic Applications," *Applied Physics Letters*, Vol. 77 (11): 1725–1726. doi:10.1063/1.1308534.

Quandt, E. and Ludwig, A., (2000), "Magnetostrictive Actuation in Microsystems," *Sensors and Actuators A: Physical*, Vol. 81 (1-3): 275–280.

Quandt, E. and Seemann, K., (1995), "Fabrication and Simulation of Magnetostrictive Thin-Film Actuators," *Sensors and Actuators A: Physical*, Vol. 50 (1): 105–109.

Rediniotis, O.K.; Ko, J.; Yue, X. and Kurdila, A., (1999), "Synthetic Jets, Their Reduced Order Modeling and Applications to Flow Control," *AIAA 37th Aerospace Sciences Meeting & Exhibit [AIAA Paper 99-1000]*.

Richter, A. and Sandmaier, H., (1990), "An Electrohydrodynamic Micropump," *Micro Electro Mechanical Systems, An Investigation of Micro Structures, Sensors, Actuators, Machines and Robots.*: 99–104. doi:10.1109/MEMSYS.1990.110257.

Richter, A.; Plettner, A. and Hofmann, K.A., (1991), "A Micromachined Electrohydrodynamic (EHD) Pump," *Sensors and Actuators A: Physical*, Vol. 29: 159–168.

Sammarco, T.S. and Burns, M.A., (2006), "Thermocapillary Pumping of Discrete Drops in Microfabricated Analysis Devices," *AIChE Journal*, Vol. 45 (2): 350–366. doi:10.1002/aic.690450215.

Sen, M.; Wajerski, D. and Gad-el-Hak, M., (1996), "A Novel Pump for MEMS Applications," *Journal of fluids Engineering*, Vol. 118 (3): 624–627.

Sharatchandra, M.C.; Sen, M. and Gad-el-Hak, M., (1997), "Navier-Stokes Simulations of a Novel Viscous Pump," *Journal of fluids Engineering*, Vol. 119: 372.

Shoji, Shuchi and Esashi, M., (1994), "Microflow Devices and Systems," *Journal of Micromechanics and Microengineering*, Vol. 4: 151–171.

Shoji, Shuichi; Nakagawa, S. and Esashi, M., (1990), "Micropump and Sample-Injector for Integrated Chemical Analyzing Systems," *Sensors and Actuators A: Physical*, Vol. 21 (1-3): 189–192. doi:10.1016/0924-4247(90)85036-4.

Singhal, V.; Garimella, S.V. and Raman, A., (2004), "Microscale Pumping Technologies for Microchannel Cooling Systems," *Applied Mechanics Reviews*, Vol. 57 (3): 191–221.

Smith, B.L. and Glezer, A., (1997), "Vectoring and Small-Scale Motions Effected in Free Shear Flows Using Synthetic Jet Actuators," *AIAA 35th Aerospace Sciences Meeting and Exhibit [AIAA Paper 97-0213]*. doi:10.2514/6.1997-213.

Smith, B.L. and Glezer, A., (1998), "The Formation and Evolution of Synthetic Jets," *Physics of fluids*, Vol. 10 (9): 2281–2297.

Smith, B.L. and Glezer, A., (2002), "Jet Vectoring Using Synthetic Jets," *Journal of Fluid Mechanics*, Vol. 458. doi:10.1017/S0022112001007406.

Smith, B.L. and Swift, G.W., (2001), "Synthetic Jets at Large Reynolds Number and Comparison to Continuous Jets," *31st AIAA Fluid Dynamics Conference and Exhibit [AIAA Paper 2001-3030]*. doi:10.2514/6.2001-3030.

Smith, B.L. and Swift, G.W., (2003), "A Comparison Between Synthetic Jets and Continuous Jets," *Experiments in fluids*, Vol. 34 (4): 467–472.

Smith, D.; Amitay, M.; Kibens, V.; Parekh, D. and Glezer, A., (1998), "Modification of Lifting Body Aerodynamics Using Synthetic Jet Actuators," *36th AIAA Aerospace Sciences Meeting and Exhibit [AIAA Paper 98-0209]*. doi:doi:10.2514/6.1998-209.

Smits, J.G., (1990), "Piezoelectric Micropump with Three Valves Working Peristaltically," *Sensors and Actuators A: Physical*, Vol. 21 (1-3): 203–206.

Stehr, M.; Messner, S.; Sandmaier, H. and Zengerle, R., (1996), "The VAMP — a New Device for Handling Liquids or Gases," *Sensors and Actuators A: Physical*, Vol. 57 (2): 153–157. doi:10.1016/S0924-4247(97)80106-9.

Stemme, E. and Stemme, G., (1993), "A Valveless Diffuser/Nozzle-Based Fluid Pump," *Sensors and Actuators A: Physical*, Vol. 39 (2): 159–167.

Tesla, N., (1916), "Valvular Conduit." US Patent 1,329,559.

Tsai, J.H. and Lin, L., (2002), "A Thermal-Bubble-Actuated Micronozzle-Diffuser Pump," *Microelectromechanical Systems, Journal of*, Vol. 11 (6): 665–671. doi:10.1109/JMEMS.2002.802909.

Urbanski, J.P.; Thorsen, T.; Levitan, J.A. and Bazant, M.Z., (2006), "Fast AC Electro-Osmotic Micropumps with Nonplanar Electrodes," *Applied Physics Letters*, Vol. 89 (14): 143508–143508–3. doi:10.1063/1.2358823.

Utturkar, Y.; Holman, R.; Mittal, R.; Carroll, B.; Sheplak, M. and Cattafesta, L., (2003), "A Jet Formation Criterion for Synthetic Jet Actuators," *AIAA 41st Aerospace Schiences Meeting and Exhibit [AIAA Paper 2003-0636]*. doi:10.2514/6.2003-636.

Utturkar, Y.; Mittal, R.; Rampunggoon, P. and Cattafesta, L., (2002), "Sensitivity of Synthetic Jets to the Design of the Jet Cavity," *AIAA 40th Aerospace Sciences Meeting & Exhibit [AIAA Paper 2002-0124]*. doi:10.2514/6.2002-124.

Van de Pol, F.C.M.; Van Lintel, H.T.G.; Elwenspoek, M. and Fluitman, J.H.J., (1990), "A Thermopneumatic Micropump Based on Micro-Engineering Techniques," *Sensors and Actuators A: Physical*, Vol. 21 (1-3): 198–202. doi:10.1016/0924-4247(90)85038-6.

Van Lintel, H.; Van de Pol, F.C.M. and Bouwstra, S., (1988), "A Piezoelectric Micropump Based on Micromachining of Silicon," *Sensors and Actuators*, Vol. 15 (2): 153–167.

Vijendran, S.; Smith, C.G. and Mpholo, M.I., (2006), "Multi-Directional Electrokinetic Pumping for Efficient Transport and Mixing in Biochip Applications," *Proceedings of SPIE 6112, Microfluidics, BioMEMS, and Medical Microsystems IV*: 61120H. doi:10.1117/12.646084.

Wang, H. and Menon, S., (2001), "Fuel-Air Mixing Enhancement by Synthetic Microjets," *AIAA Journal*, Vol. 39 (12): 2308–2319. doi:10.2514/2.1236.

Wego, A. and Pagel, L., (2001), "A Self-Filling Micropump Based on PCB Technology," *Sensors and Actuators A: Physical*, Vol. 88 (3): 220–226. doi:10.1016/S0924-4247(00)00519-7.

Weisener, T.; Voegele, G.; Widmann, M.; Bark, C.; Schraft, R.D.; Bertholds, A. and Braunschweiler, A., (1996), "Development and Fabrication of a Rotary Micropump and Its Industrial and Medical Applications," *Proc. SPIE 2882, Micromachined Devices and Components II*: 218–225. doi:10.1117/12.250707.

Woias, P., (2005), "Micropumps--Past, Progress and Future Prospects," *Sensors and Actuators B: Chemical*, Vol. 105 (1): 28–38.

Wolfe, D. and Ziada, S., (2003), "Feedback Control of Vortex Shedding From Two Tandem Cylinders," *Journal of fluids and structures*, Vol. 17 (4): 579–592. doi:10.1016/S0889-9746(02)00147-0.

Wong, C.C.; Adkins, D.R. and Chu, D., (1996), "Development of a Micropump for Microelectronic Cooling," *1996 International Mechanical Engineering Congress and Exhibition*.

Xu, D.; Wang, L.; Ding, G.; Zhou, Y.; Yu, A. and Cai, B., (2001), "Characteristics and Fabrication of NiTi/Si Diaphragm Micropump," *Sensors and Actuators A: Physical*, Vol. 93 (1): 87–92.

Yamahata, C.; Lacharme, F. and Gijs, M.A.M., (2005), "Glass Valveless Micropump Using Electromagnetic Actuation," *Microelectronic Engineering*, Vol. 78-79: 6–6. doi:10.1016/j.mee.2004.12.018.

Yun, K.-S.; Cho, I.-J.; Bu, J.-U.; Kim, G.-H.; Jeon, Y.-S.; Kim, C.-J. and Yoon, E., (2001), "A Micropump Driven by Continuous Electrowetting Actuation for Low Voltage and Low Power Operations," *Proceedings of the IEEE International Conference on MicroElectroMechanical Systems*: 487–490. doi:10.1109/MEMSYS.2001.906585.

Zeng, S.; Chen, C.-H.; Mikkelsen, J.C., Jr and Santiago, J.G., (2001), "Fabrication and Characterization of Electroosmotic Micropumps," *Sensors and Actuators B: Chemical*, Vol. 79 (2-3): 107–114. doi:10.1016/S0925-4005(01)00855-3.

Zeng, S.; Chen, C.-H.; Santiago, J.G.; Chen, J.-R.; Zare, R.N.; Tripp, J.A.; Svec, F. and Frechet, J.M.J., (2002), "Electroosmotic Flow Pumps with Polymer Frits," *Sensors and Actuators B: Chemical*, Vol. 82: 209–212.

Zengerle, R.; Richter, A. and Sandmaier, H., (1992), "A Micro Membrane Pump with Electrostatic Actuation," *Proceedings of the IEEE MicroElectroMechanical Systems (MEMS '92), An Investigation of Micro Structures, Sensors, Actuators, Machines and Robot*: 19–24. doi:10.1109/MEMSYS.1992.187684.

Zengerle, R.; Ulrich, J.; Kluge, S.; Richter, M. and Richter, A., (1995), "A Bidirectional Silicon Micropump," *Sensors and Actuators A: Physical*, Vol. 50 (1): 81–86.

Zhang, P. and Wang, J., (2007), "Novel Signal Wave Pattern for Efficient Synthetic Jet Generation," *AIAA Journal*, Vol. 45 (5): 1058–1065. doi:10.2514/1.25445.

Zheng, S.; Chen, C.-H.; Mikkelsen, J.C., Jr and Santiago, J.G., (2000), "Fabrication and Characterization of Electrokinetic Micro Pumps," *The Seventh Intersociety Conference on Thermal and Thermomechanical Phenomena in Electronic Systems (ITHERM 2000)*: 31–36. doi:10.1109/ITHERM.2000.866167.

Ziada, S., (1995), "Feedback Control of Globally Unstable Flows: Impinging Shear Flows," *Journal of fluids and structures*, Vol. 9 (8): 907–923.

Ziada, S., (1999), "Feedback Control of Global Flow Oscillations," *Engineering Mechanics*, Vol. 6 (4/5): 337–354.

Appendix A

NUMERICAL GRID ANALYSIS

It is necessary to establish the independence of the numerical simulations results reported of the grid and time step size. This is achieved by running the simulations using different grid sizes and times steps and evaluating the change in the solution.

A.1 Grid Size Independence

In order to establish the independence of the solution from the grid size, four simulations were run with four different grid sizes using the same geometry and

operating parameters on a preliminary geometry with slight differences from the final geometry. The four simulations had uniform grid sizes of 100, 50, 25, and 12.5 µm. Since the main focus of the current study is investigating the flow rate generated from the micropump, the average flow rate through the pump was taken as a measure of the grid independence of the solution. The reported difference in flow rates for each of the grids as a percentage of the flow rate for the nonuniform grid used thereafter are +134%, +12%, -4%, and +0.5% for a grid size of 100, 50, 25, and 12.5 µm respectively. These results show that grid sizes of 25 and 12.5 µm showed variations of the flow rate below 5% from that of the used nonuniform 10 µm grid, indicating that for a mesh size below 25 µm the solution does not depend on the grid size.

A.2 Time Step Independence

In order to adequately resolve the excitation signal of the membrane, the time step was chosen for the simulations so that each actuation cycle was divided into 100 times step and thus the times step was different from one simulations case to the other depending on the frequency of actuation. The time step independence was performed on the base case having a frequency of excitation of 40 Hz. Three different simulations were performed with the actuation cycle being divided into 50, 100, and 200 time steps.

A.3 Simulation Time Independence

Since the numerical simulations start with zero flow velocity initial conditions along the domain, it takes a few actuation cycles to elapse before the solution reaches a steady state. Each simulation was run for 10 complete actuation cycles to ensure the solution has reached a steady state. The results utilized in the analysis are then recorded for the 11th cycle. The results show that after the third cycle the average flow rate reaches steady state. The simulations were allowed to continue for 7 more cycles to insure the full flow field has reached a steady state solution as well as accommodate for different cases run at different amplitudes and frequencies.

.

Appendix B

EXPERIMENTAL RESULTS

This appendix includes the calibration data used to calibrate the laser displacement sensor used to measure the membrane deflection as well as sample measurement signal obtained from the laser displacement sensor.

A Keyence LK-G82 CCD laser displacement sensor was used and statically calibrated using a micrometer attached to the bottom of the membrane to set a specific deflection and measure the corresponding response from the laser displacement sensor. FigureB.1 shows the calibration data for the laser displacement sensor. Each

measurement was repeated several times and the calibration curve was constructed by plotting the average value of the measurements at each input value and the error bars on the plot represent the standard deviation in the measurements at each input value. The data was then fitted with a linear trend line with a calibration coefficient of 0.7.

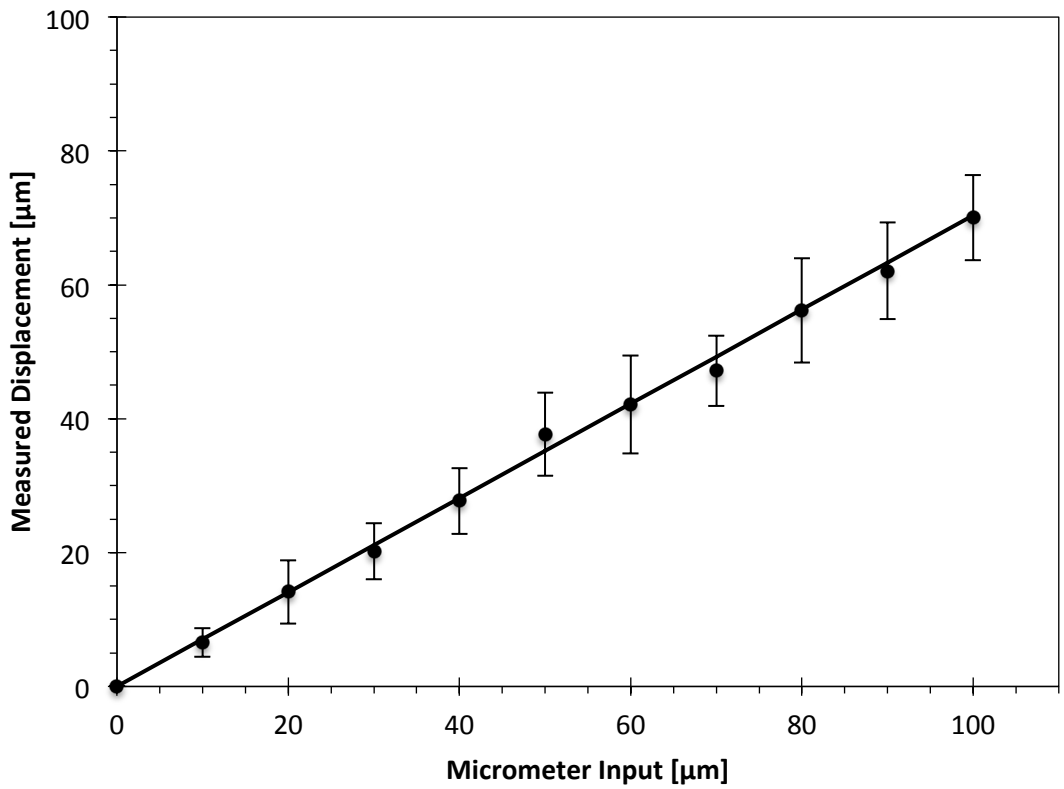

FigureB.1 Laser displacement sensor calibration curve.

A sample output signal from the laser displacement censor can be seen in Figure B.2. The amplitude values are the uncalibrated values reported by the sensor. The membrane amplitude is taken as the peak to peak value between the maximum and minimum values of the sensor output. In the shown case the uncalibrated amplitude is

90 µm, which after applying the calibration constant represents an actuation amplitude of 63 µm. For that specific reported case the frequency of excitation was 40 Hz

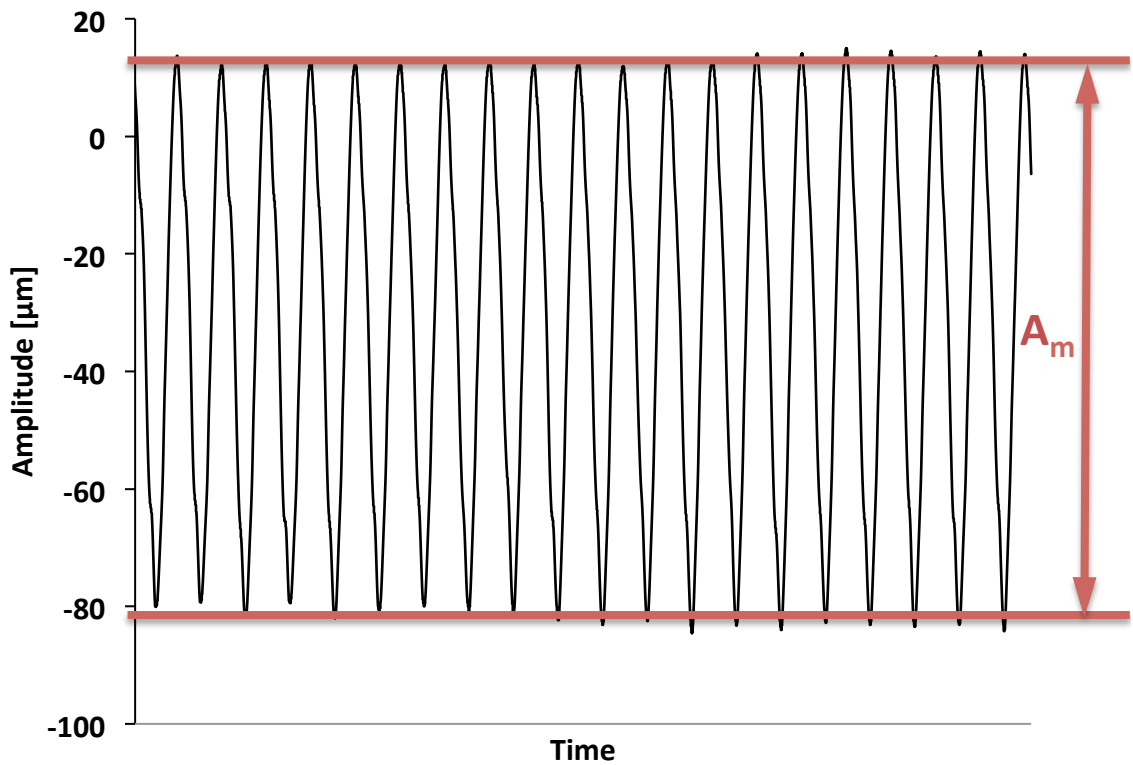

Figure B.2 Sample laser displacement sensor output signal.

Appendix C

UNCERTAINTY ANALYSIS

The uncertainty analysis for the measured parameters of the experimental measurements presented in this work will be outlined in this appendix. For a dependent variable, Y, given by the equation

$$Y = Y(X_1, X_2, X_3, ...X_i) \qquad [C.0]$$

where, X_i are the independent measured variables. The overall uncertainty in the quantity Y can be expressed as a function of the known uncertainties of each of the

independent variables X_i using the uncertainty propagation equation of Kline and McClintock (1953)

$$\delta Y = \sqrt{\sum_{i=1}^{N}\left(\frac{\partial Y}{\partial X_i}\delta X_i\right)^2} \qquad \text{[C.1]}$$

where δY is the uncertainty of the dependent variable Y and δX_i is the known uncertainty of the independent variable X_i. Each term in equation [C.1] represents the contribution made by the uncertainty of each independent variable to the overall uncertainty of the dependent variable.

Based on the above equation, the uncertainty in the flow rate measurement, Q, given by the equation

$$Q = \frac{V}{t} \qquad \text{[C.1]}$$

can be expressed as a function of the uncertainty of the accumulated fluid volume V and the time of accumulation t as:

$$\delta Q = \sqrt{\left(\frac{1}{t}\delta V\right)^2 + \left(\frac{-V}{t^2}\delta t\right)^2} \qquad \text{[C.1]}$$

therefore, the relative uncertainty of the flow rate can be obtained as

$$\frac{\delta Q}{Q} = \sqrt{\left(\frac{\delta V}{V}\right)^2 + \left(\frac{-\delta t}{t}\right)^2} \qquad \text{[C.2]}$$

The collected fluid volume was measured using a graduated container with a least count of 0.25 ml. Measurements of flow rate were based on collecting samples of fluid of a minimum volume of 1 ml and hence the maximum relative uncertainty in the volume measurement is ±12.5 %. Time was measured using a digital stopwatch with a least count of 0.01 second as well as. Assuming a human error of about 1 second in recording time. The minimum time recorded for a flow rate measurement was 40 sec resulting in a maximum relative uncertainty in the time measurement of ±2.5%. These values result in a maximum relative uncertainty in the flow rate measurement according to equation [C.2] of ±12.75%.

The amplitude of excitation was measured using a laser displacement sensor as discussed in Chapter 5. The device was calibrated against the static displacement of a micrometer and the measurements were repeated several times per measured displacement for several displacements in the range of 0 to 100 µm. The calibration data was fitted to a linear trend line to obtain a calibration constant and the standard deviation of all the measured values from the calibration equation was calculated leading to an uncertainty in the amplitude measurement of ±5 µm. The uncertainty in the measured frequency is very small due to the resolution of the signal generator, which was 0.1 Hz. Since the lowest measured frequency was 20 Hz, the relative uncertainty of the frequency was 0.5%.

Appendix D

NUMERICAL RESULTS

In Chapter 6 the base case was discussed in details and comparisons between different cases to investigate the effects of different geometrical dimensions and actuation parameters were based on sample instances throughout the actuation cycle. In this appendix details of all test cases presented in Chapter 6 will be shown. Each case will include a flow rate plot showing inlet, outlet, orifice flow rates and membrane displacement as well as average, maximum and minimum flow rates. The plots will also

include velocity contours, velocity vectors and velocity profiles for nine different instances throughout the excitation cycle.

D.1 Case W_i=200 µm, W_o= 400 µm, A_m= 40 µm, f= 40 Hz

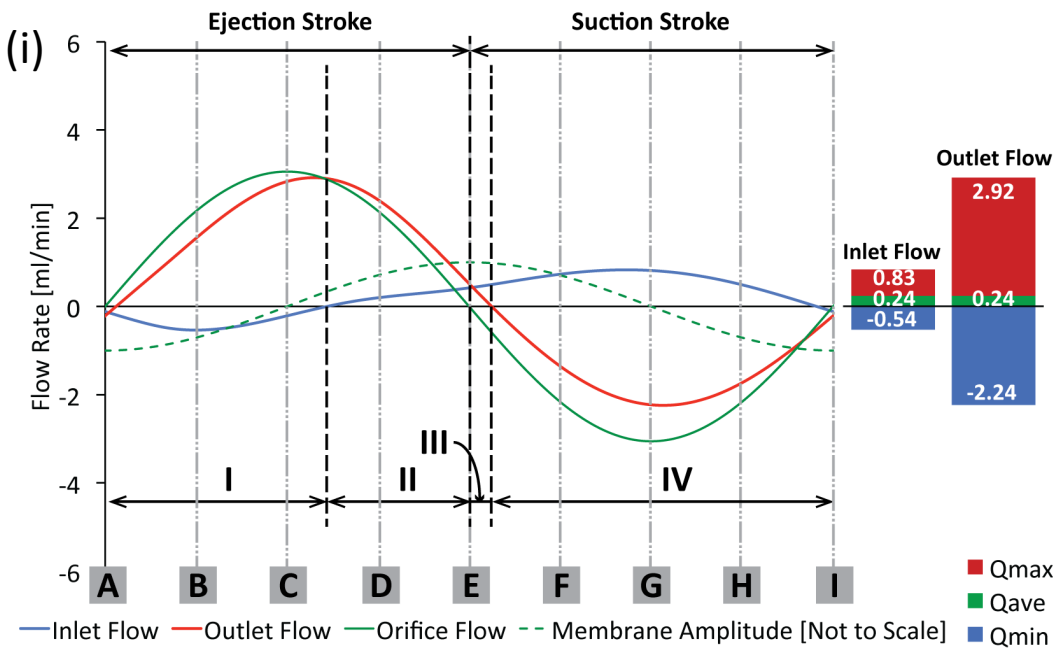

Figure D.1. Details of flow rates and field for the case
A_m = 40 µm, f = 40 Hz, W_i = 200 µm and W_o = 400 µm.
(i) [above] Cycle flow rates [A positive flow rate indicates flow in the forward direction (from inlet to outlet). For orifice flow, positive indicates flow out of the cavity].
Letters on the figure indicate instances along the actuation cycle where details of the flow field are shown in parts ii to v of the figure as follows:
[A] t/T=0.000, [B] t/T=0.125, [C] t/T=0.250,
[D] t/T=0.375, [E] t/T=0.500, [F] t/T=0.625,
[G] t/T=0.750, [H] t/T=0.875, [I] t/T=1.000.
(ii) [Page 211] Streamlines coloured by the velocity magnitude at the mid-height plane of the micropump.
(iii) [Page 212] Velocity vectors coloured by the velocity magnitude at the mid-height plane of the micropump.
(iv) [Page 213] Velocity profiles at three different locations along the length of the outlet channel at the mid-height plane of the micropump.
(v) [Page 214] Velocity profiles at three different locations along the length of the inlet channel at the mid-height plane of the micropump.

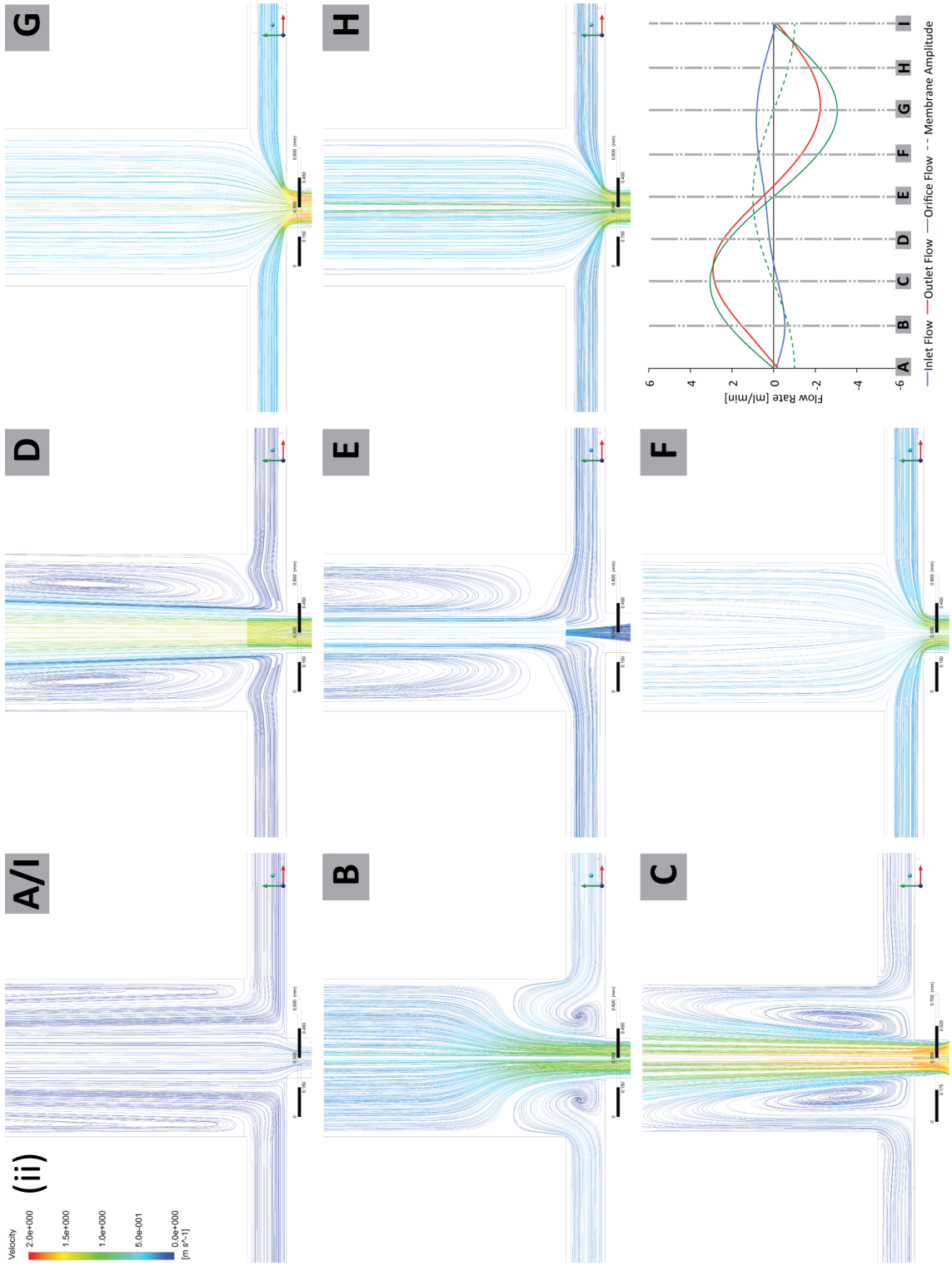

Figure D.1. Continued

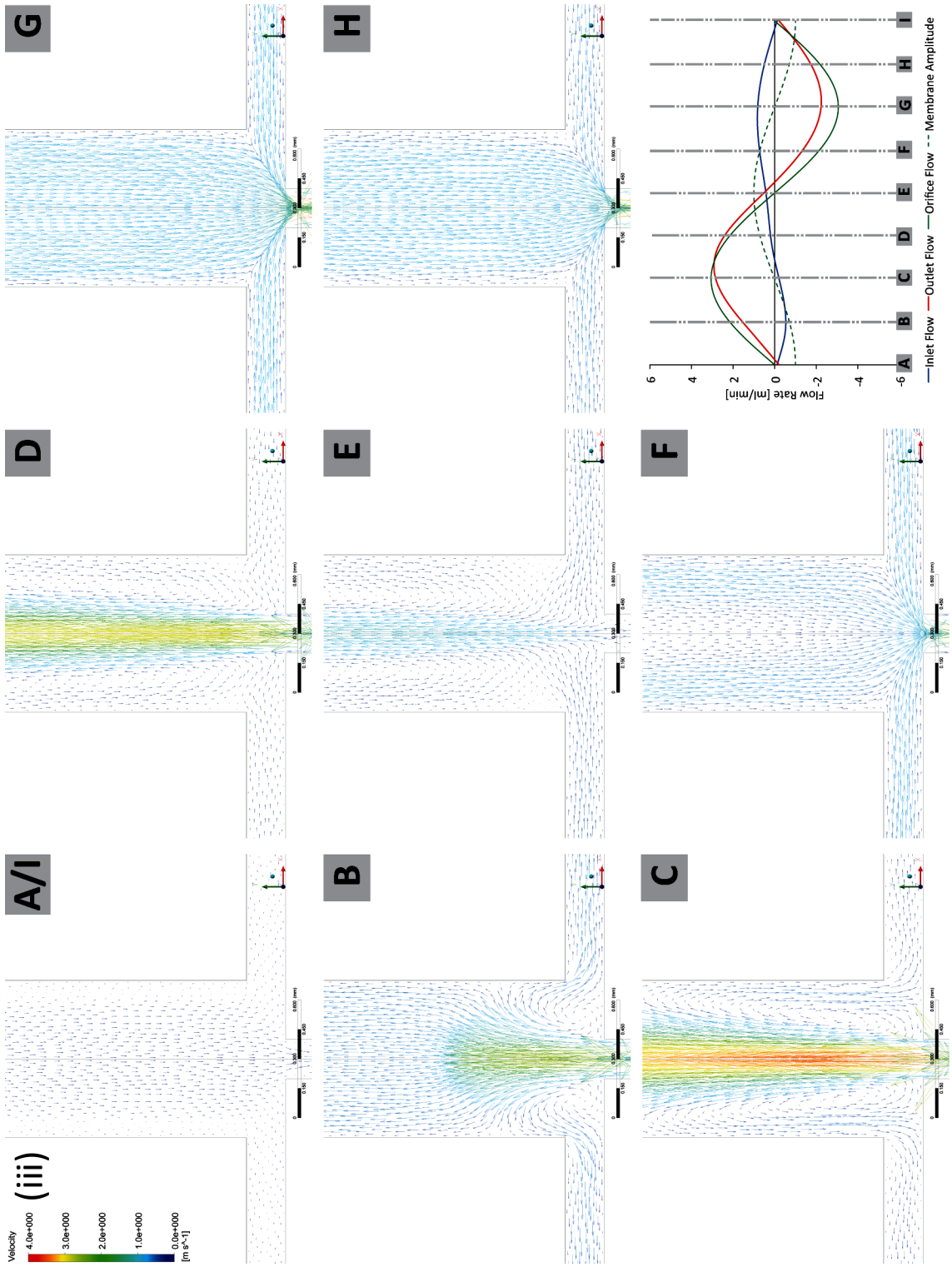

Figure D.1. Continued

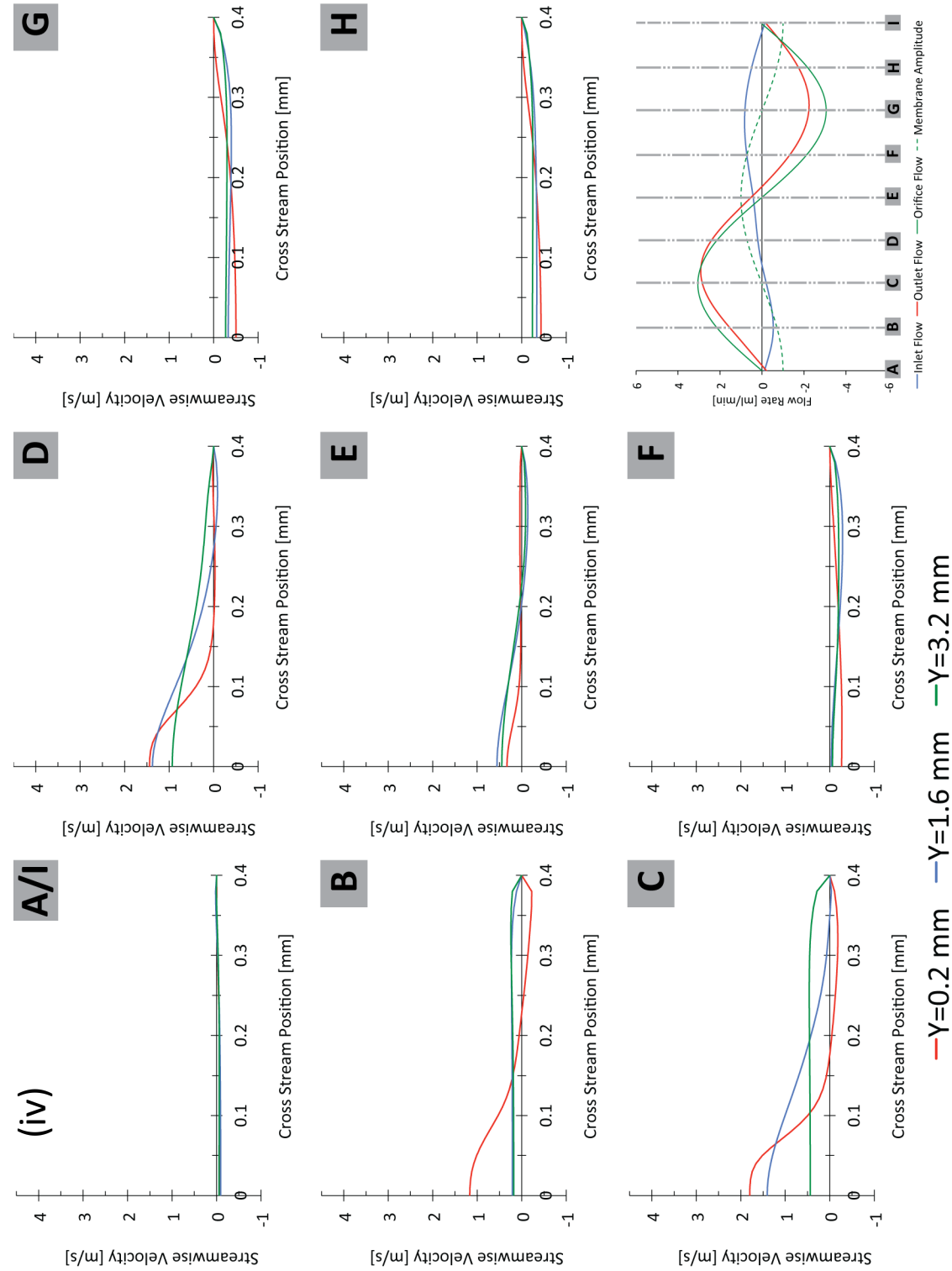

Figure D.1. Continued

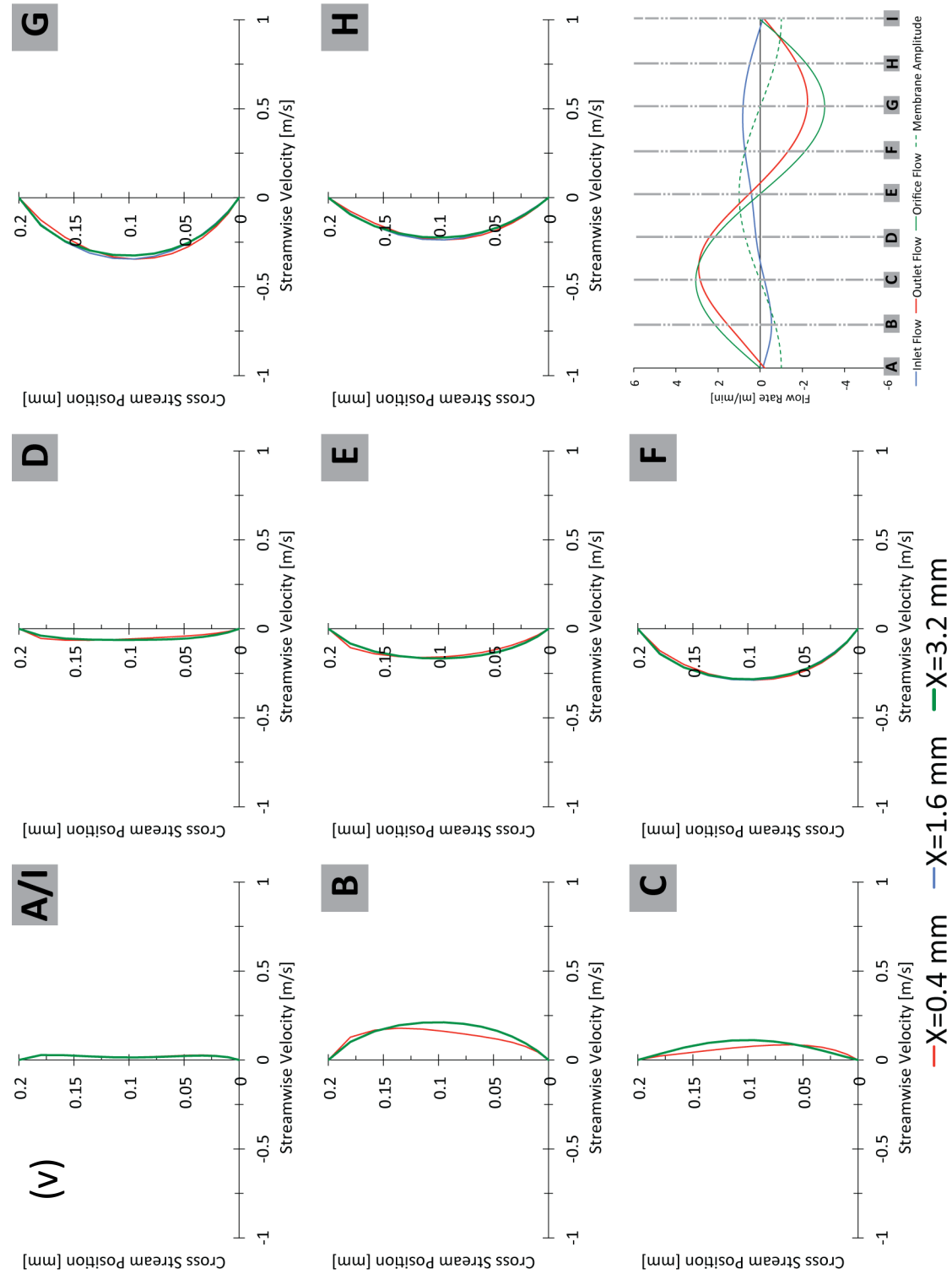

Figure D.1. Continued

D.2 Case W_i=400 µm, W_o= 200 µm, A_m= 40 µm, f= 40 Hz

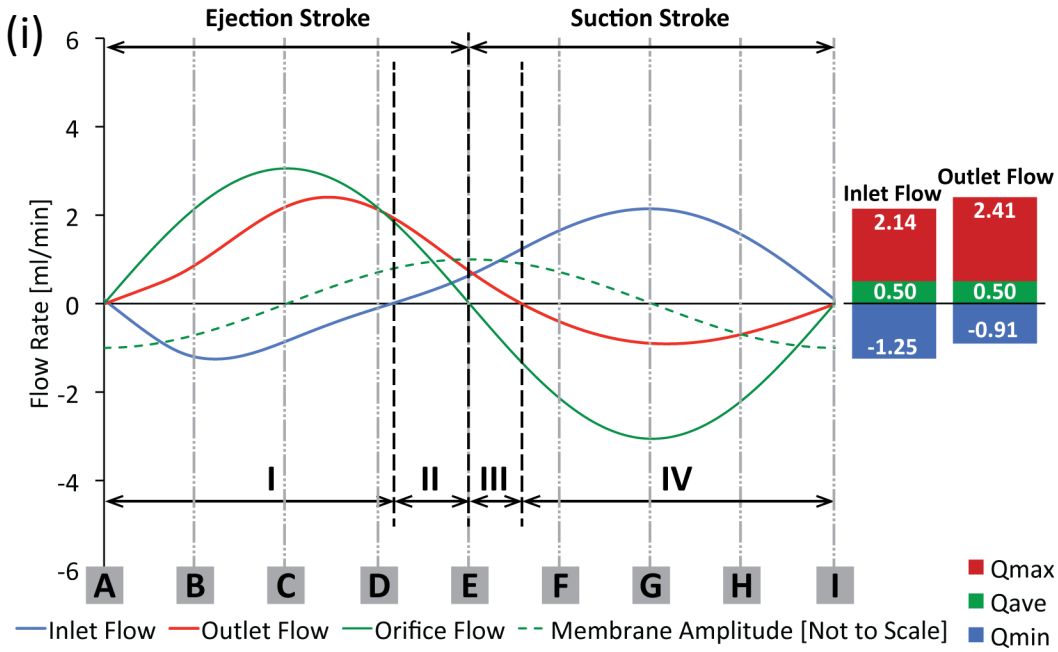

Figure D.2. Details of flow rates and field for the case
A_m = 40 µm, f = 40 Hz, W_i = 400 µm and W_o = 200 µm.
(i) [above] Cycle flow rates [A positive flow rate indicates flow in the forward direction (from inlet to outlet). For orifice flow, positive indicates flow out of the cavity].
Letters on the figure indicate instances along the actuation cycle where details of the flow field are shown in parts ii to v of the figure as follows:
[A] t/T=0.000, [B] t/T=0.125, [C] t/T=0.250,
[D] t/T=0.375, [E] t/T=0.500, [F] t/T=0.625,
[G] t/T=0.750, [H] t/T=0.875, [I] t/T=1.000.
(ii) [Page 216] Streamlines coloured by the velocity magnitude at the mid-height plane of the micropump.
(iii) [Page 217] Velocity vectors coloured by the velocity magnitude at the mid-height plane of the micropump.
(iv) [Page 218] Velocity profiles at three different locations along the length of the outlet channel at the mid-height plane of the micropump.
(v) [Page 219] Velocity profiles at three different locations along the length of the inlet channel at the mid-height plane of the micropump.

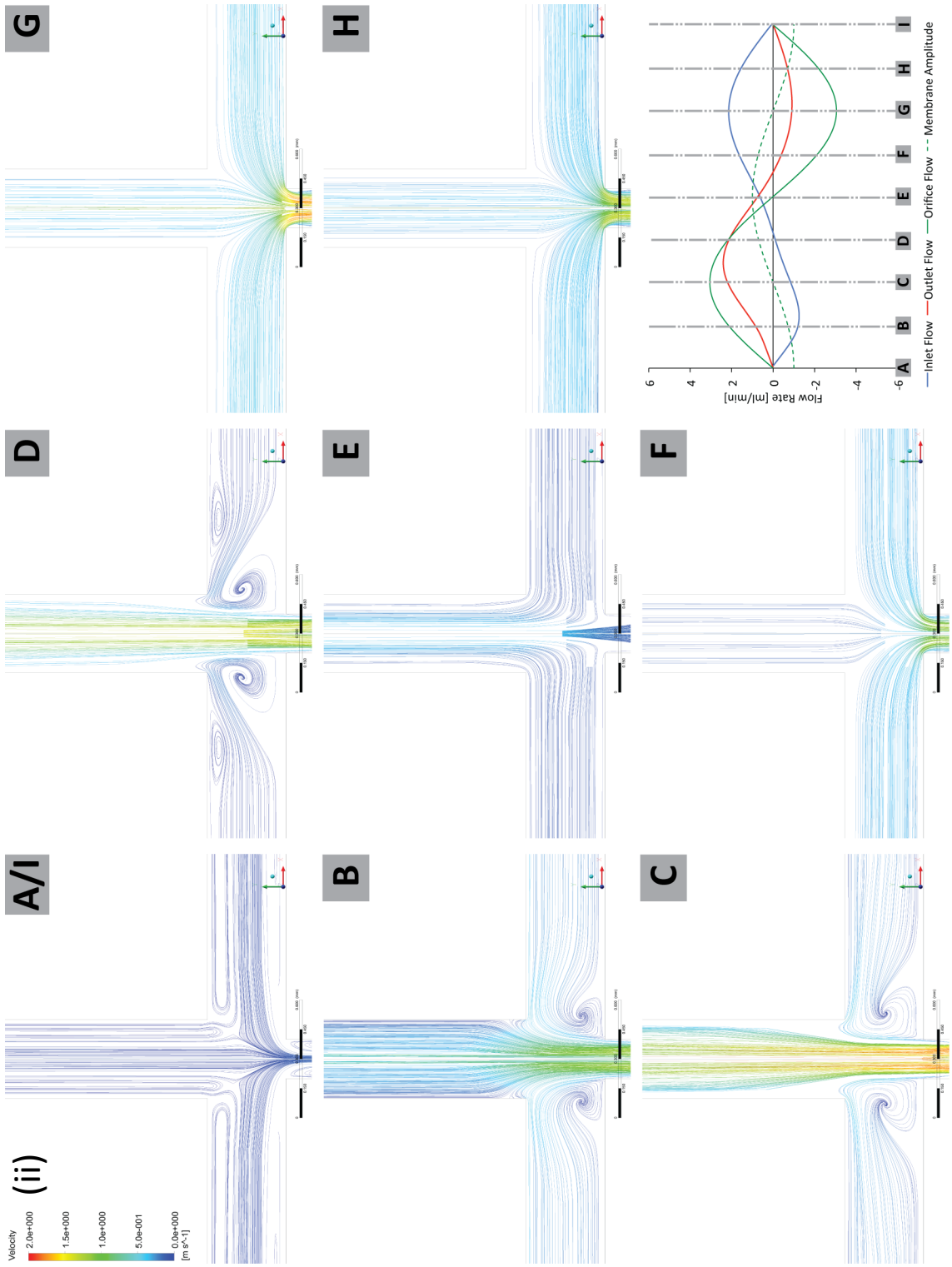

Figure D.2. Continued

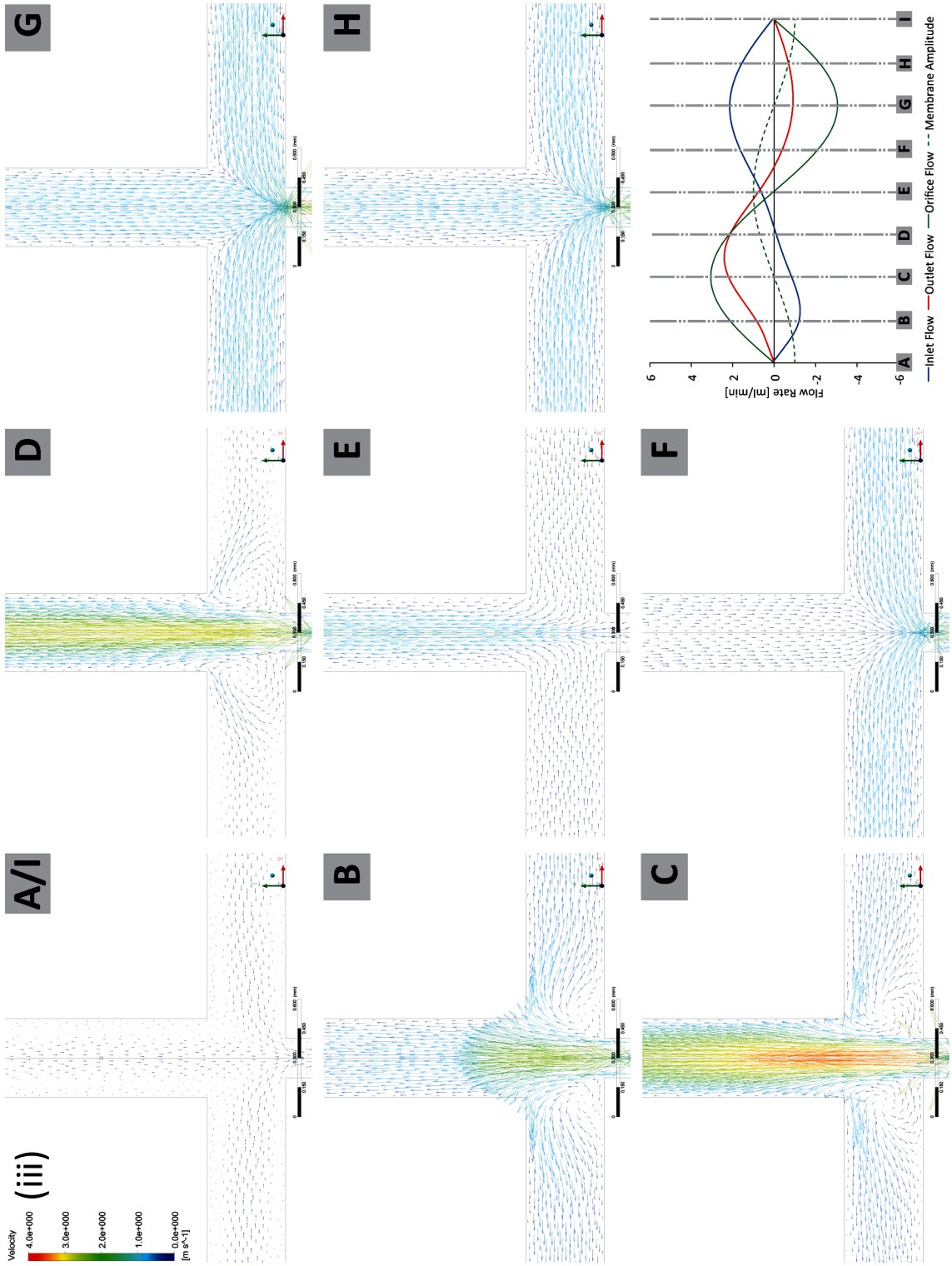

Figure D.2. Continued

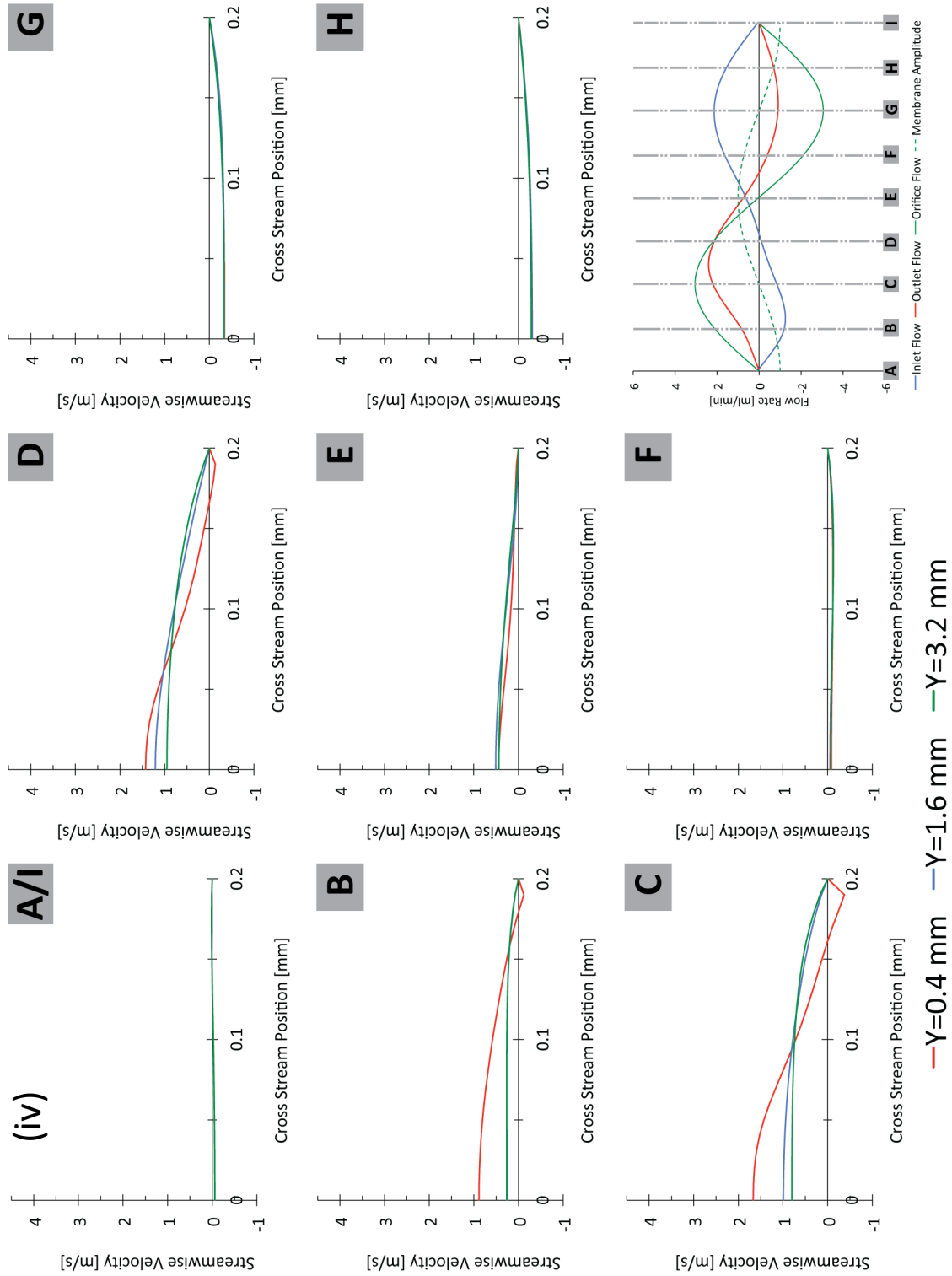

Figure D.2. Continued

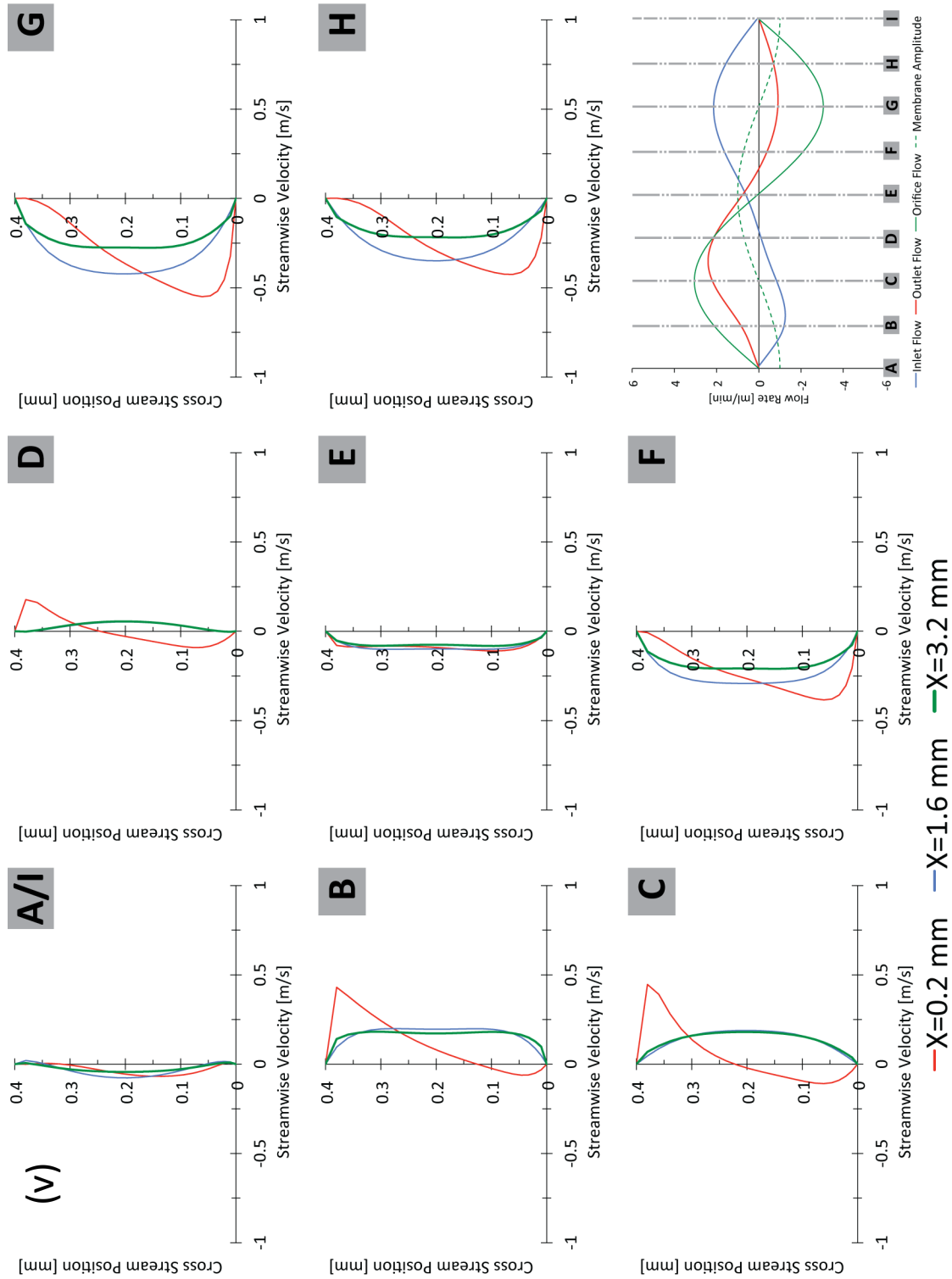

Figure D.2. Continued

D.3 Case W_i=400 µm, W_o= 400 µm, A_m= 20 µm, f= 40 Hz

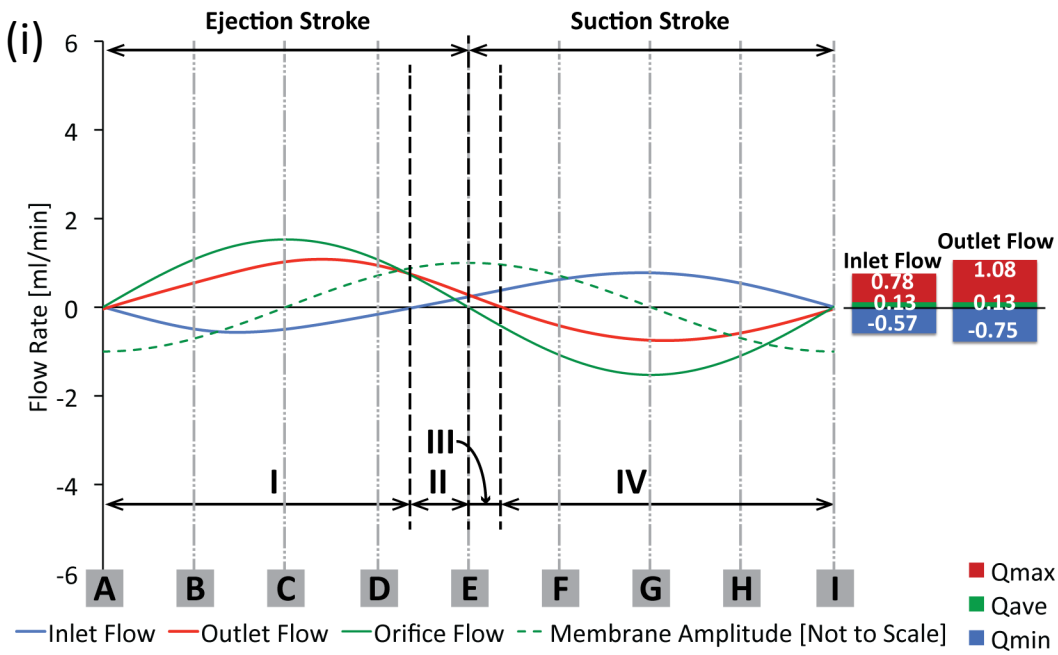

Figure D.3. Details of flow rates and field for the case
A_m = 20 µm, f = 40 Hz, W_i = 400 µm and W_o = 400 µm.
(i) [above] Cycle flow rates [A positive flow rate indicates flow in the forward direction (from inlet to outlet). For orifice flow, positive indicates flow out of the cavity].
Letters on the figure indicate instances along the actuation cycle where details of the flow field are shown in parts ii to v of the figure as follows:
[A] t/T=0.000, [B] t/T=0.125, [C] t/T=0.250,
[D] t/T=0.375, [E] t/T=0.500, [F] t/T=0.625,
[G] t/T=0.750, [H] t/T=0.875, [I] t/T=1.000.
(ii) [Page 221] Streamlines coloured by the velocity magnitude at the mid-height plane of the micropump.
(iii) [Page 222] Velocity vectors coloured by the velocity magnitude at the mid-height plane of the micropump.
(iv) [Page 223] Velocity profiles at three different locations along the length of the outlet channel at the mid-height plane of the micropump.
(v) [Page 224] Velocity profiles at three different locations along the length of the inlet channel at the mid-height plane of the micropump.

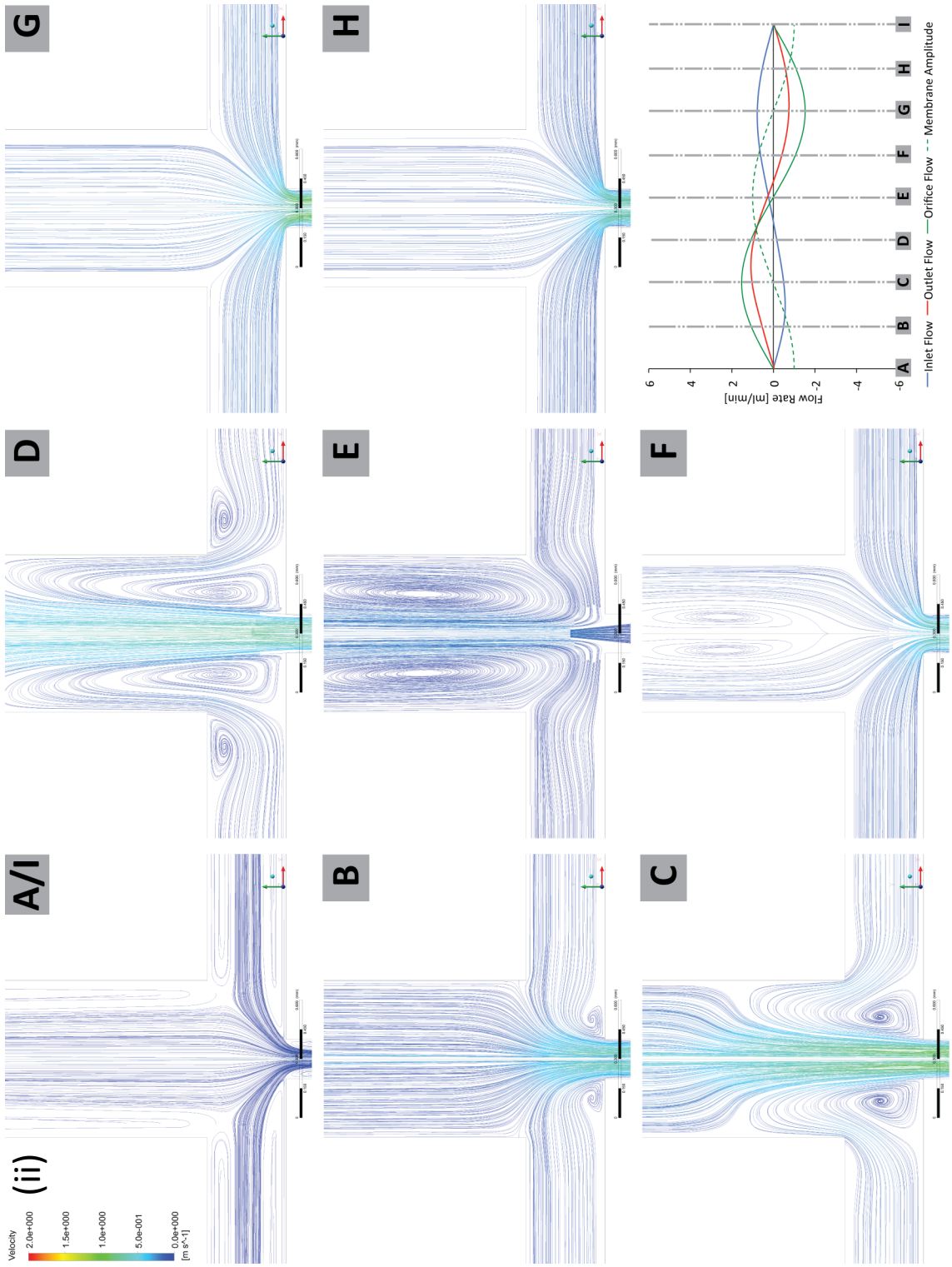

Figure D.3. Continued

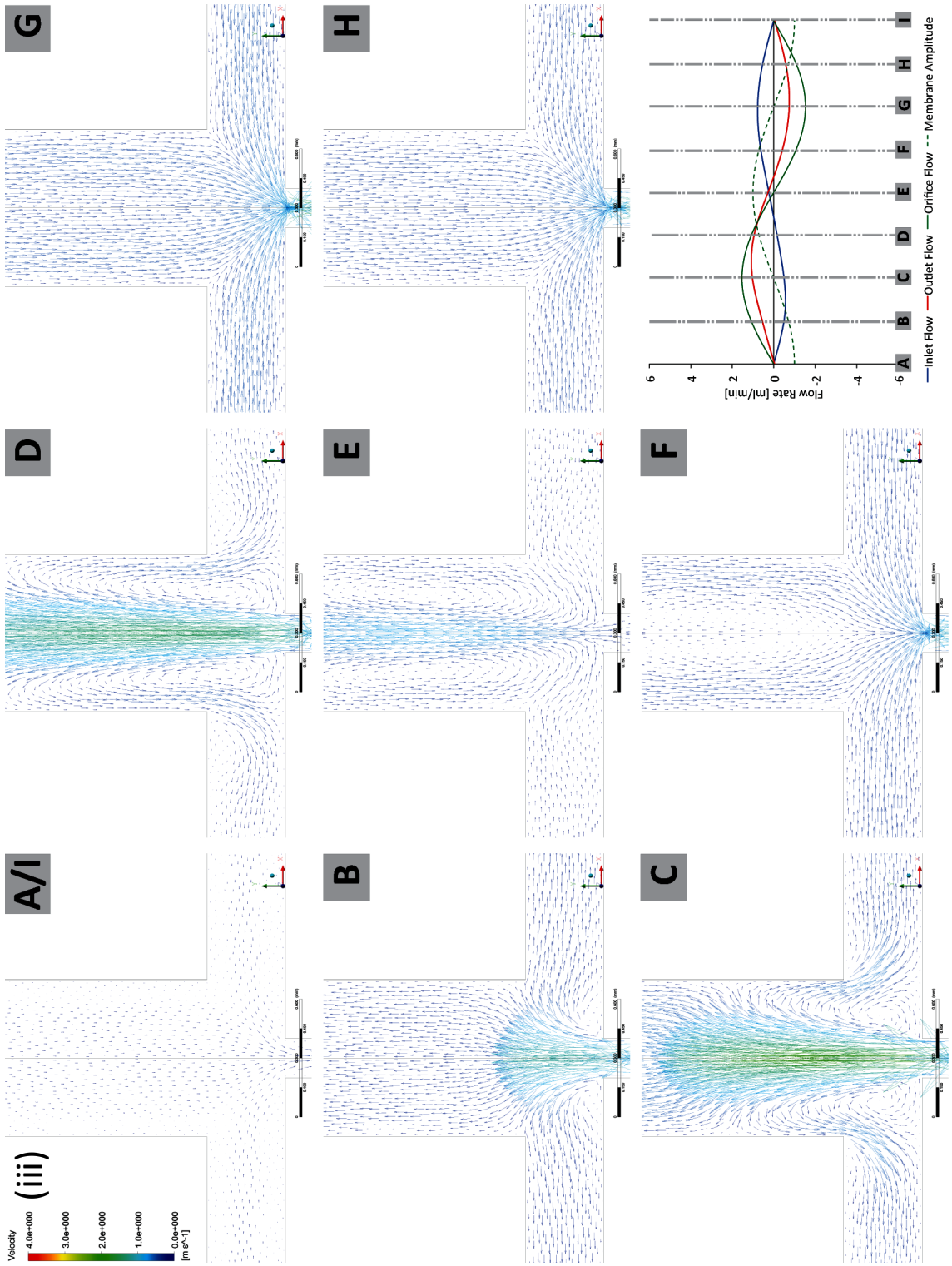

Figure D.3. Continued

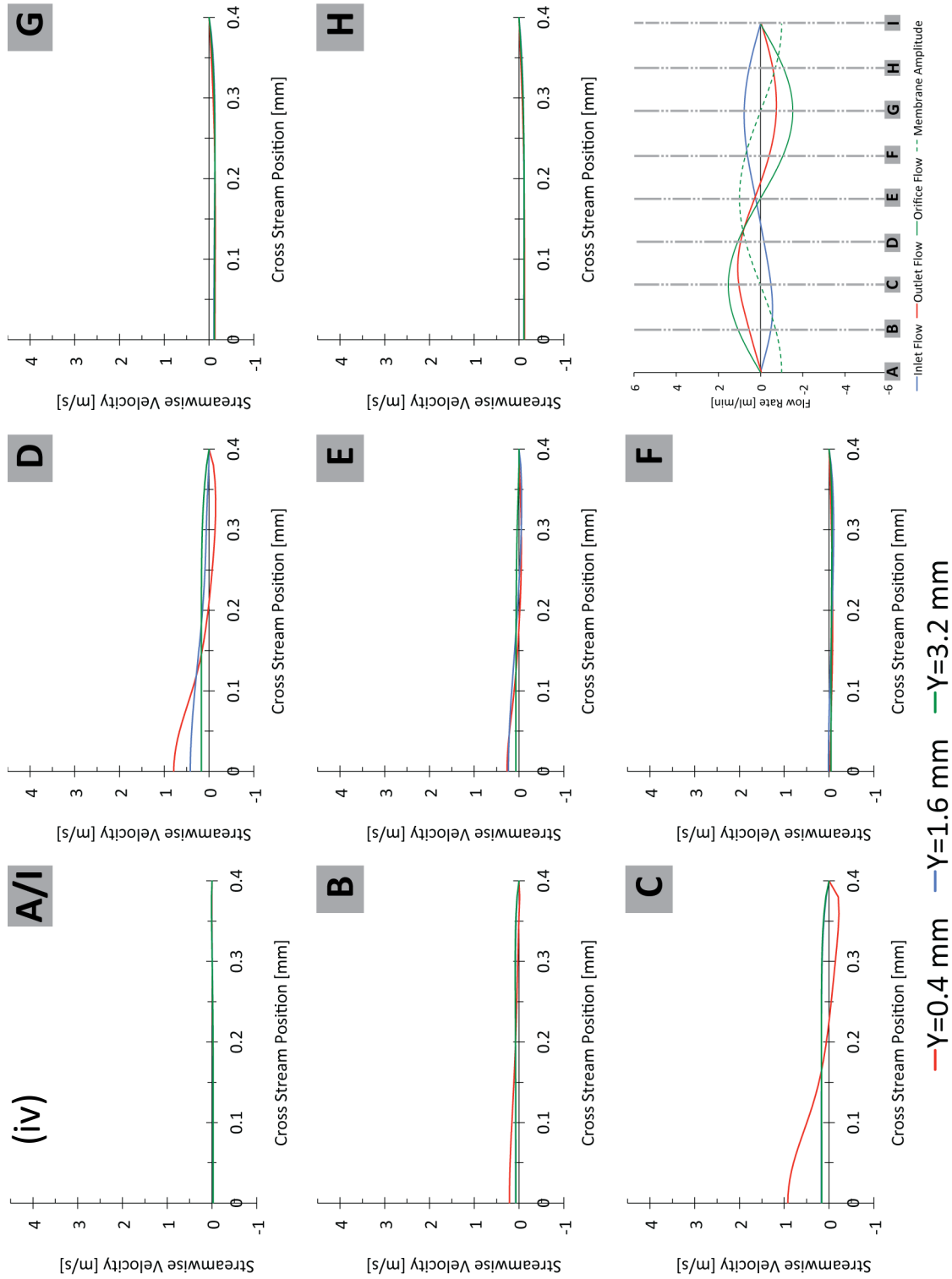

Figure D.3. Continued

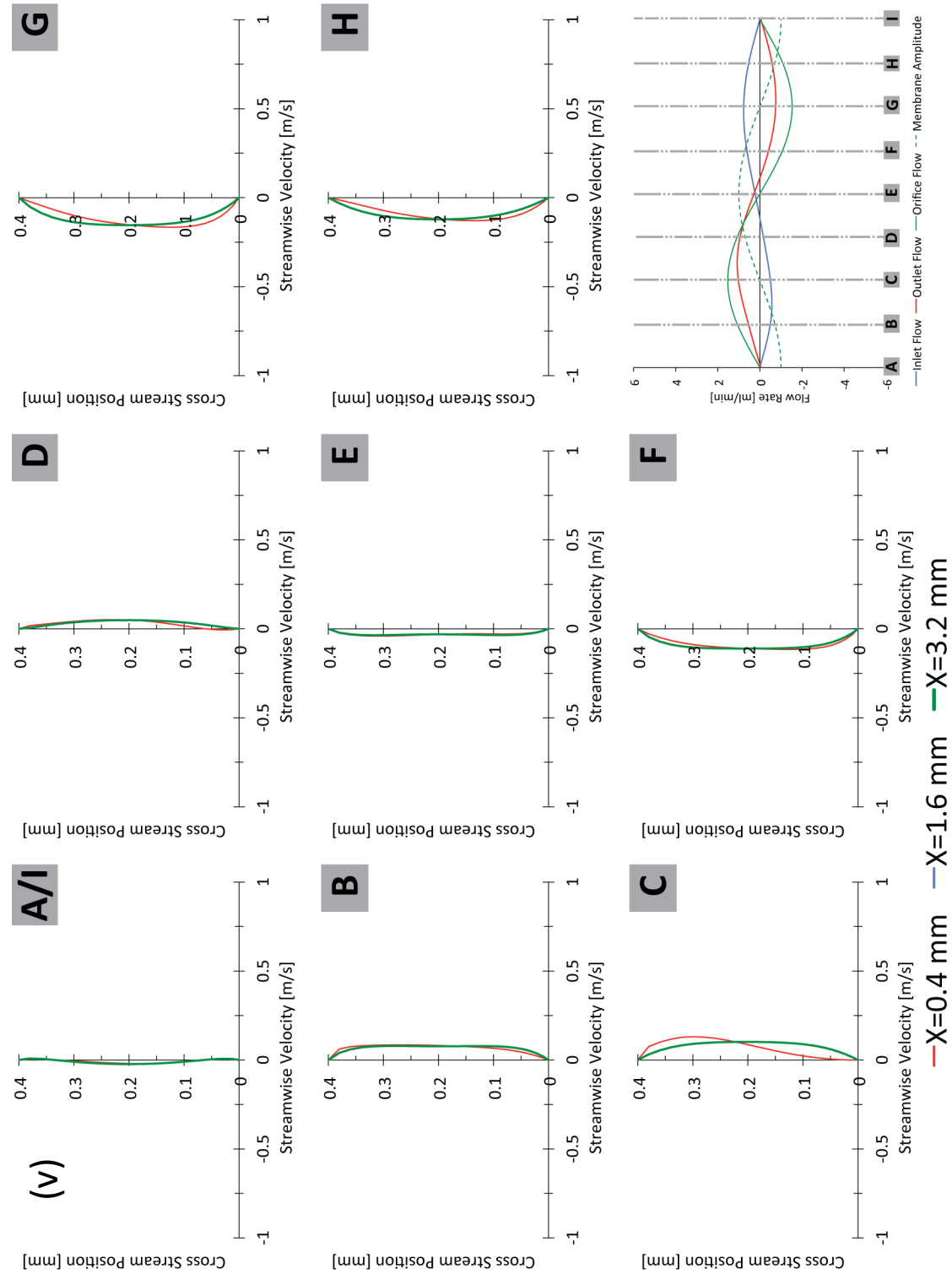

Figure D.3. Continued

D.4 Case W_i=400 µm, W_o= 400 µm, A_m= 40 µm, f= 20 Hz

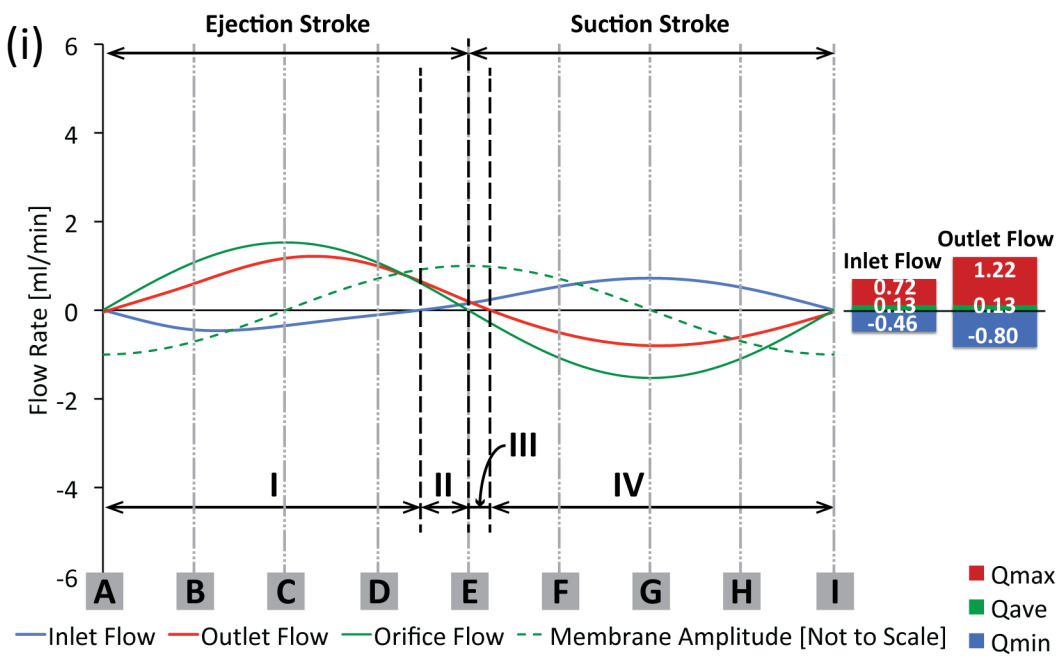

Figure D.4. Details of flow rates and field for the case
A_m = 40 µm, f = 20 Hz, W_i = 400 µm and W_o = 400 µm.
(i) [above] Cycle flow rates [A positive flow rate indicates flow in the forward direction (from inlet to outlet). For orifice flow, positive indicates flow out of the cavity].
Letters on the figure indicate instances along the actuation cycle where details of the flow field are shown in parts ii to v of the figure as follows:
[A] t/T=0.000, [B] t/T=0.125, [C] t/T=0.250,
[D] t/T=0.375, [E] t/T=0.500, [F] t/T=0.625,
[G] t/T=0.750, [H] t/T=0.875, [I] t/T=1.000.
(ii) [Page 226] Streamlines coloured by the velocity magnitude at the mid-height plane of the micropump.
(iii) [Page 227] Velocity vectors coloured by the velocity magnitude at the mid-height plane of the micropump.
(iv) [Page 228] Velocity profiles at three different locations along the length of the outlet channel at the mid-height plane of the micropump.
(v) [Page 229] Velocity profiles at three different locations along the length of the inlet channel at the mid-height plane of the micropump.

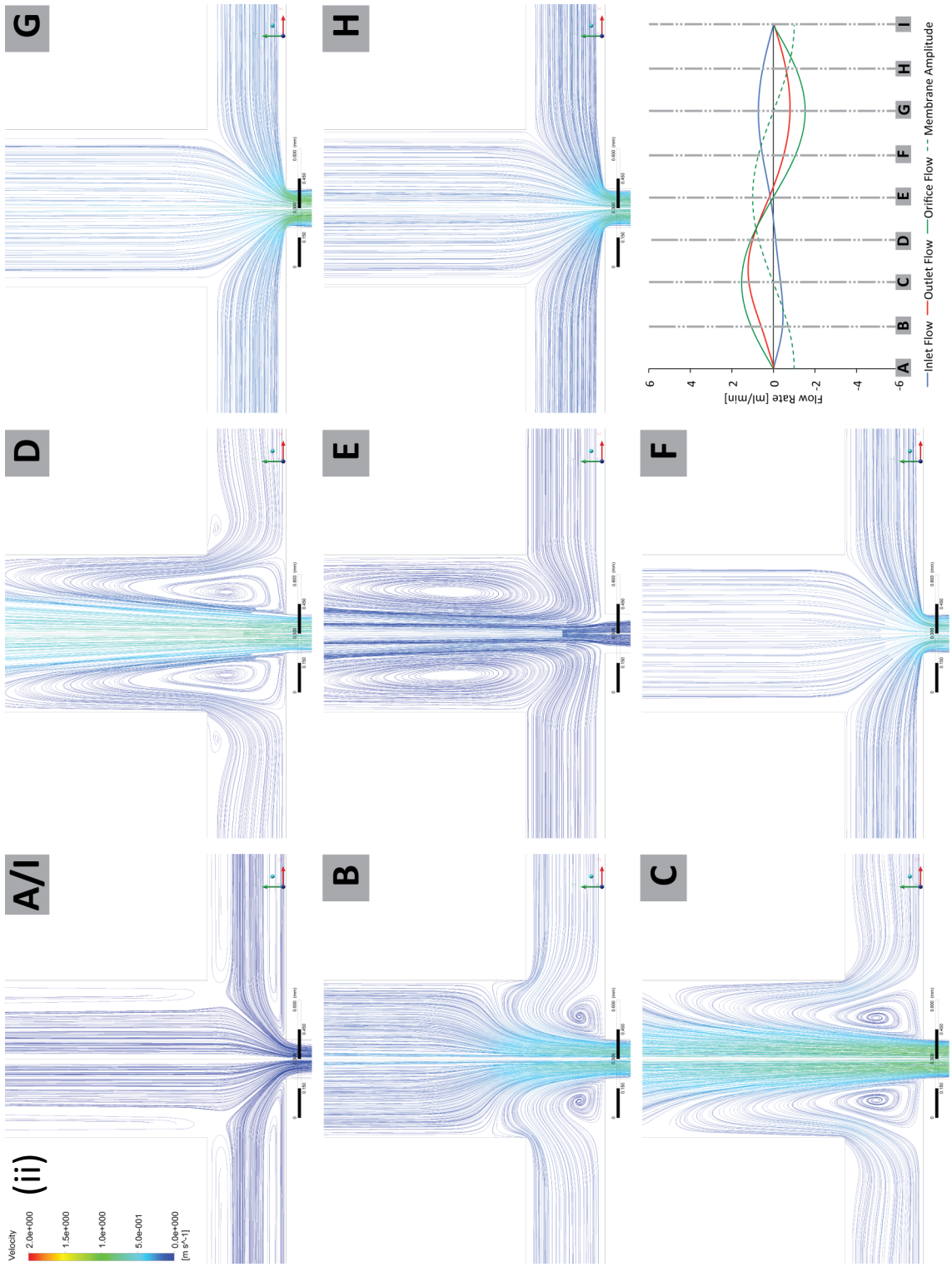

Figure D.4. Continued

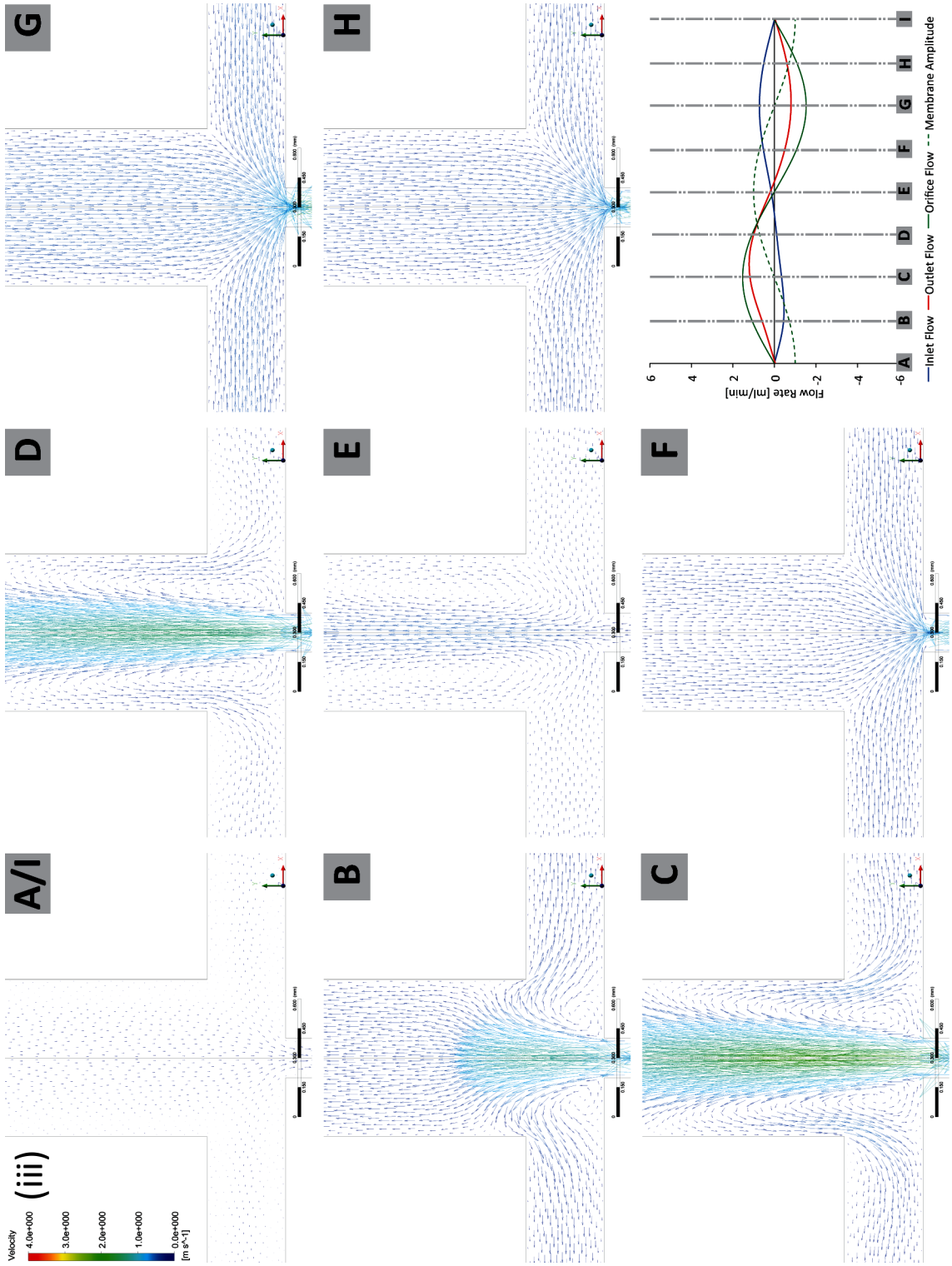

Figure D.4. Continued

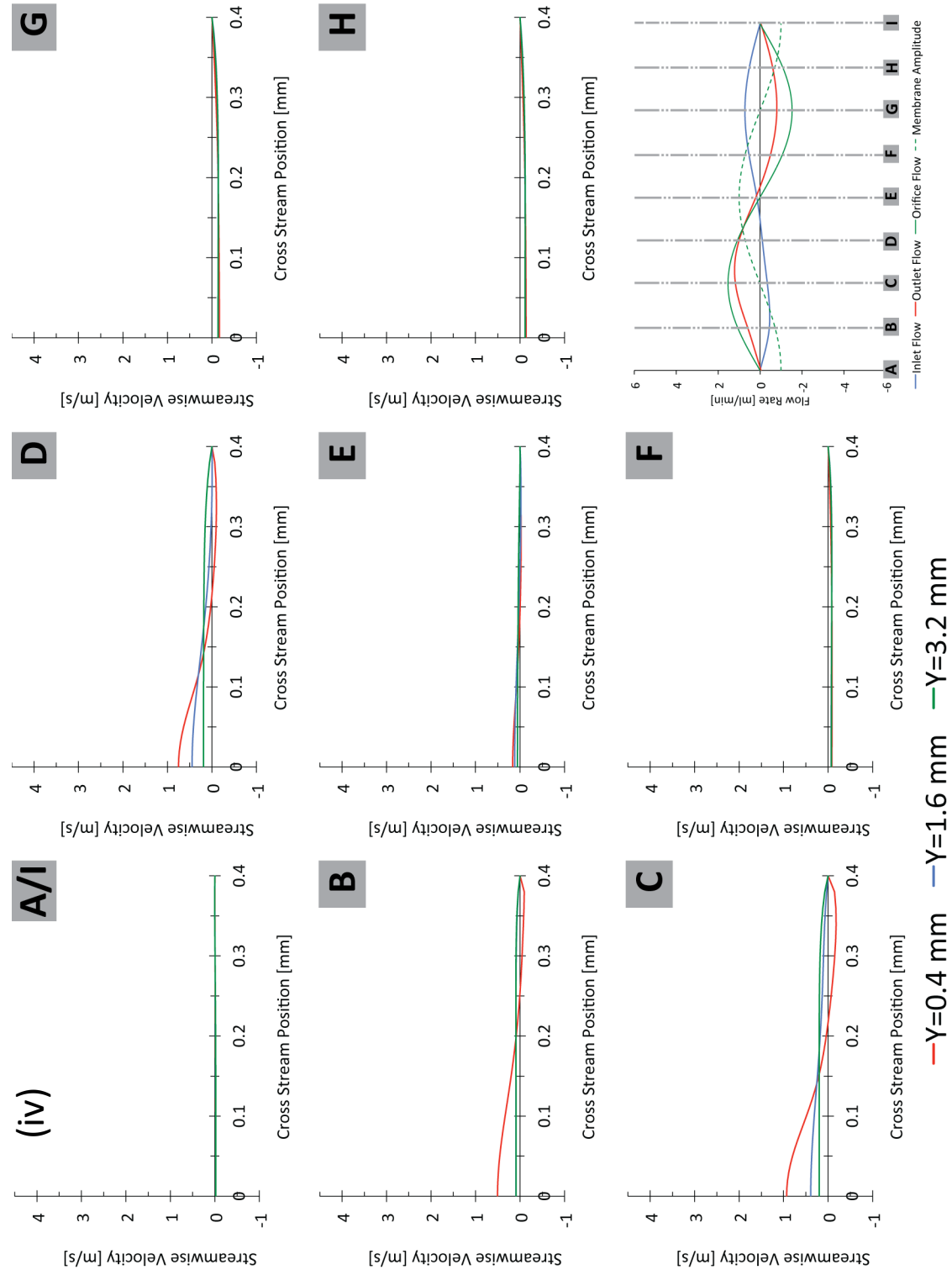

Figure D.4. Continued

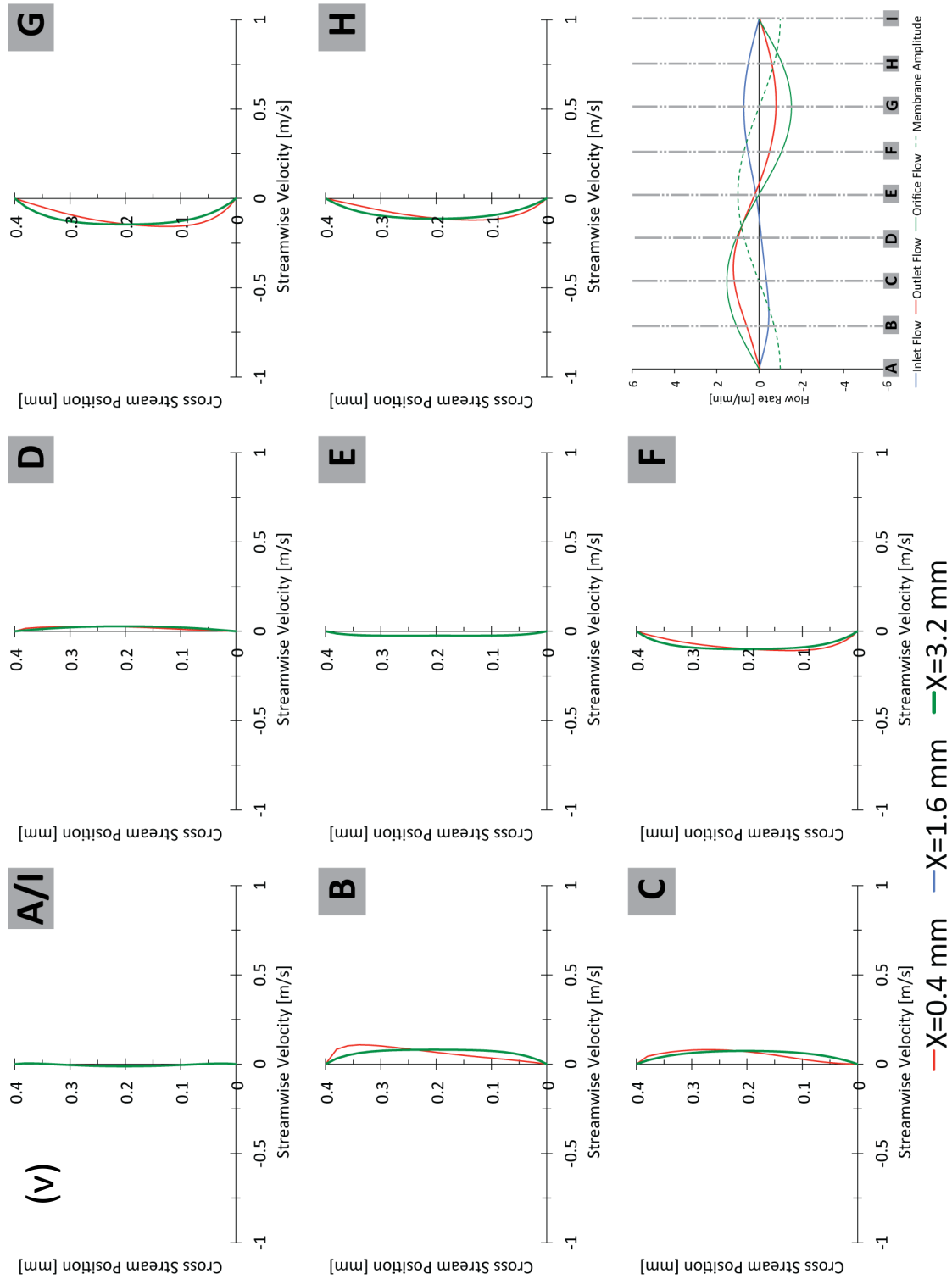

Figure D.4. Continued

D.5 Case W_i=400 µm, W_o= 400 µm, A_m= 40 µm, f= 40 Hz

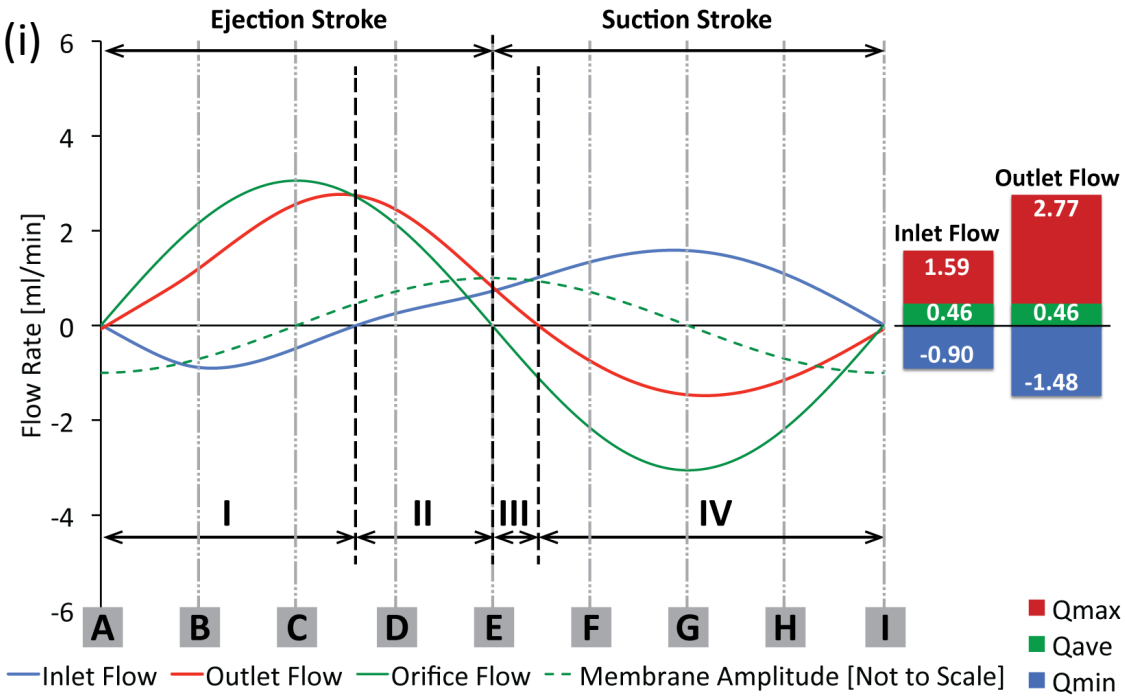

Figure D.5. Details of flow rates and field for the case
A_m = 40 µm, f = 40 Hz, W_i = 400 µm and W_o = 400 µm.
(i) [above] Cycle flow rates [A positive flow rate indicates flow in the forward direction (from inlet to outlet). For orifice flow, positive indicates flow out of the cavity].
Letters on the figure indicate instances along the actuation cycle where details of the flow field are shown in parts ii to v of the figure as follows:
[A] t/T=0.000, [B] t/T=0.125, [C] t/T=0.250,
[D] t/T=0.375, [E] t/T=0.500, [F] t/T=0.625,
[G] t/T=0.750, [H] t/T=0.875, [I] t/T=1.000.
(ii) [Page 231] Streamlines coloured by the velocity magnitude at the mid-height plane of the micropump.
(iii) [Page 232] Velocity vectors coloured by the velocity magnitude at the mid-height plane of the micropump.
(iv) [Page 233] Velocity profiles at three different locations along the length of the outlet channel at the mid-height plane of the micropump.
(v) [Page 234] Velocity profiles at three different locations along the length of the inlet channel at the mid-height plane of the micropump.

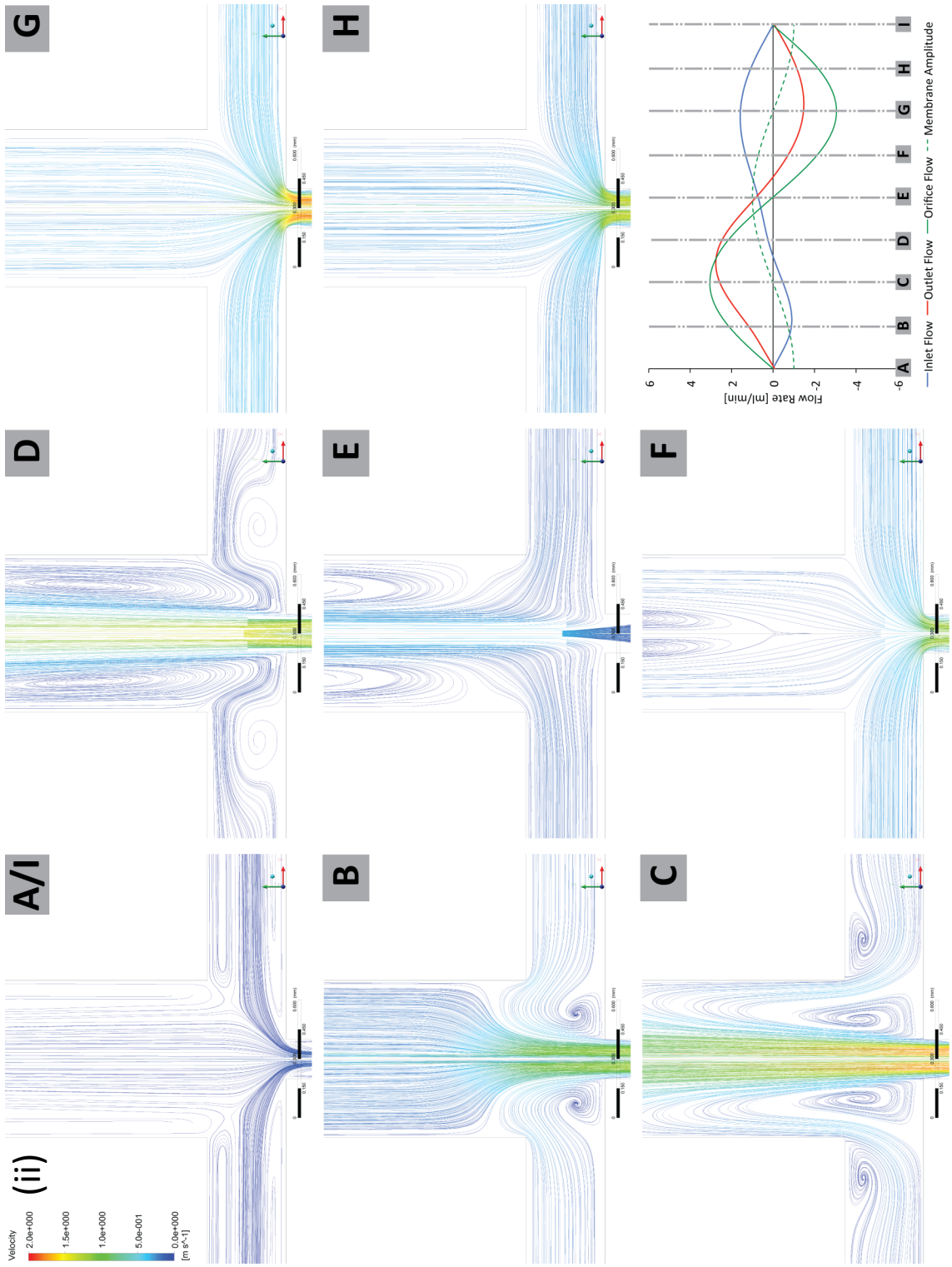

Figure D.5. Continued

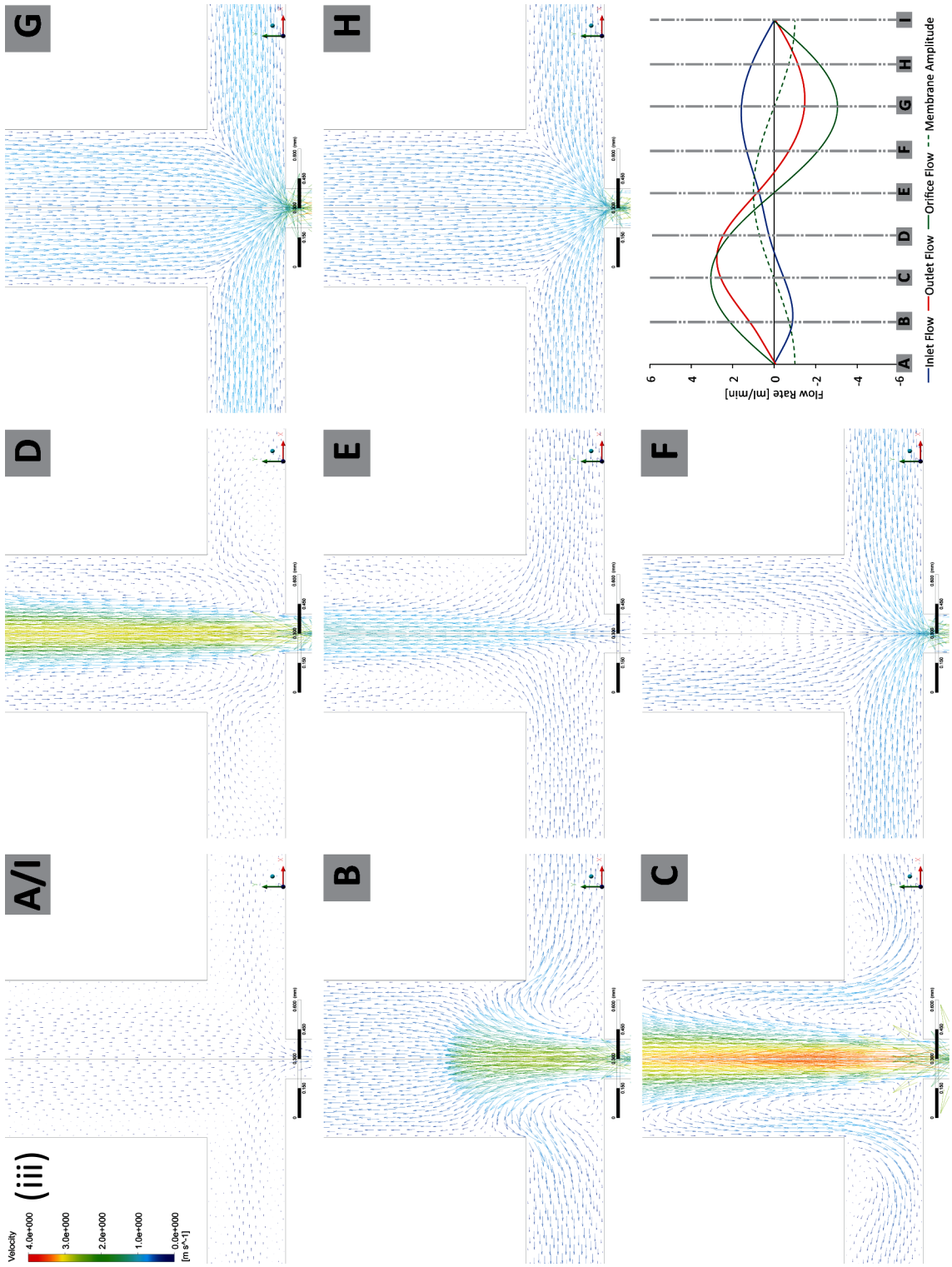

Figure D.5. Continued

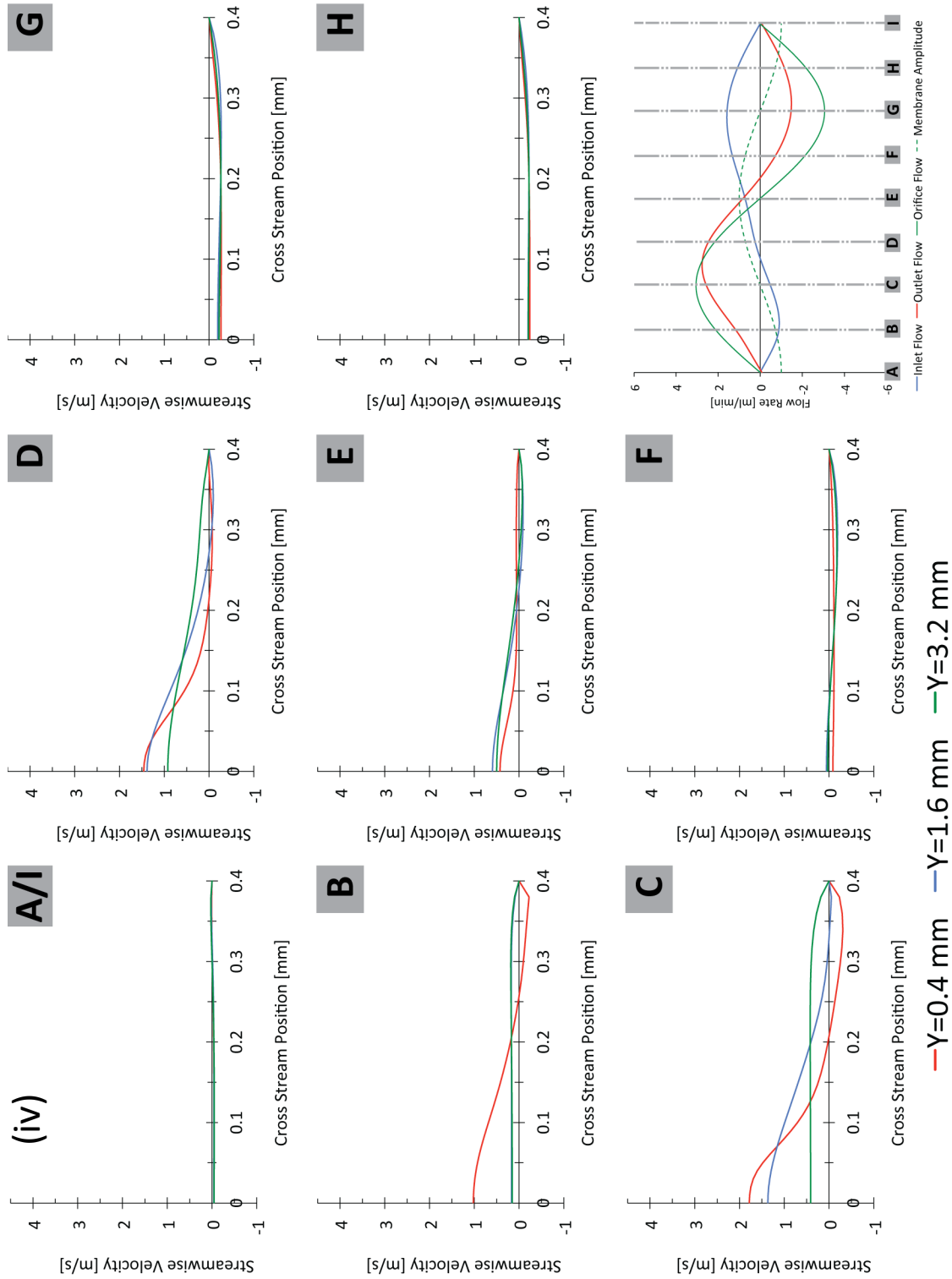

Figure D.5. Continued

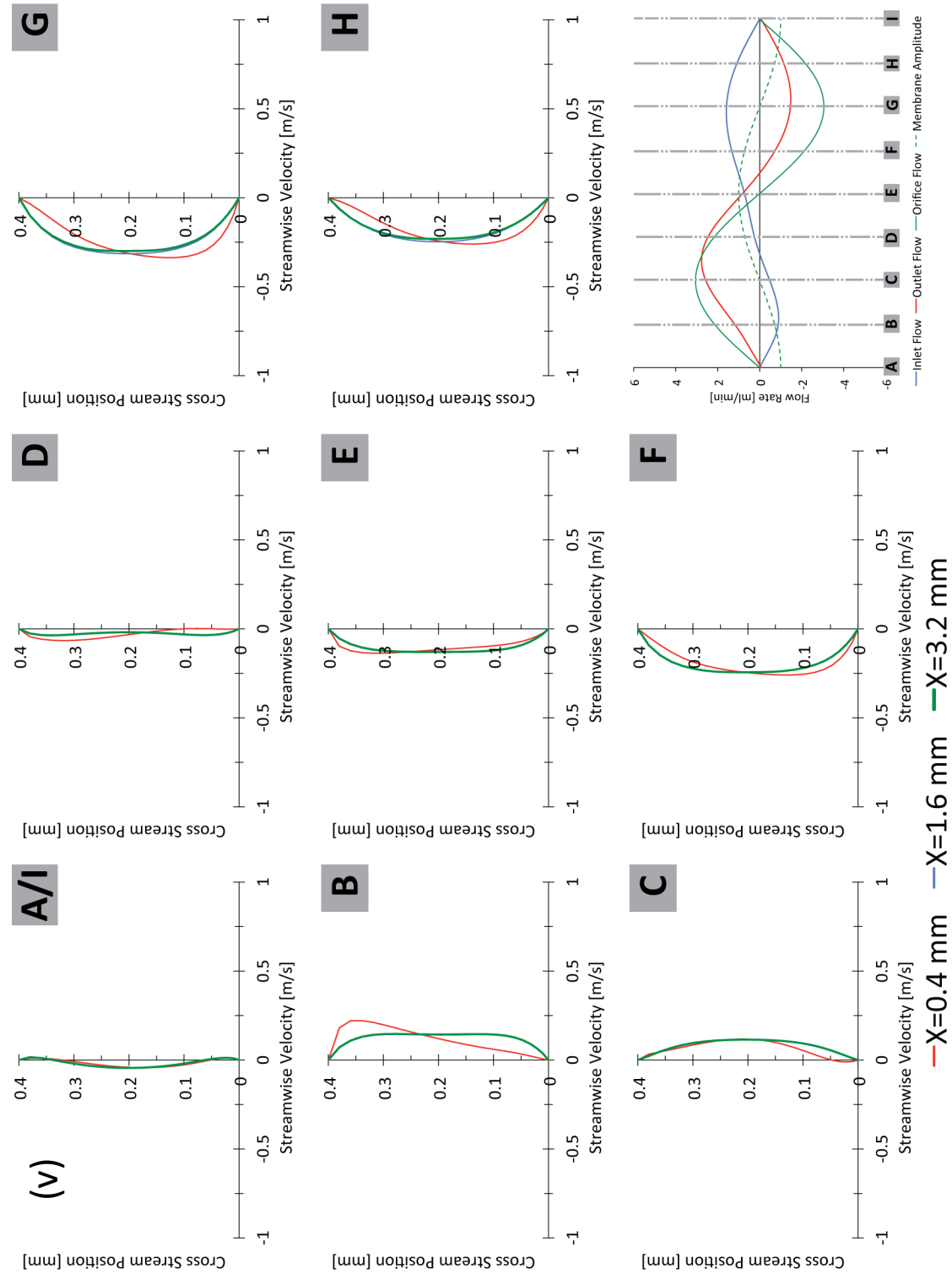

Figure D.5. Continued

D.6 Case W_i=400 µm, W_o= 400 µm, A_m= 40 µm, f= 60 Hz

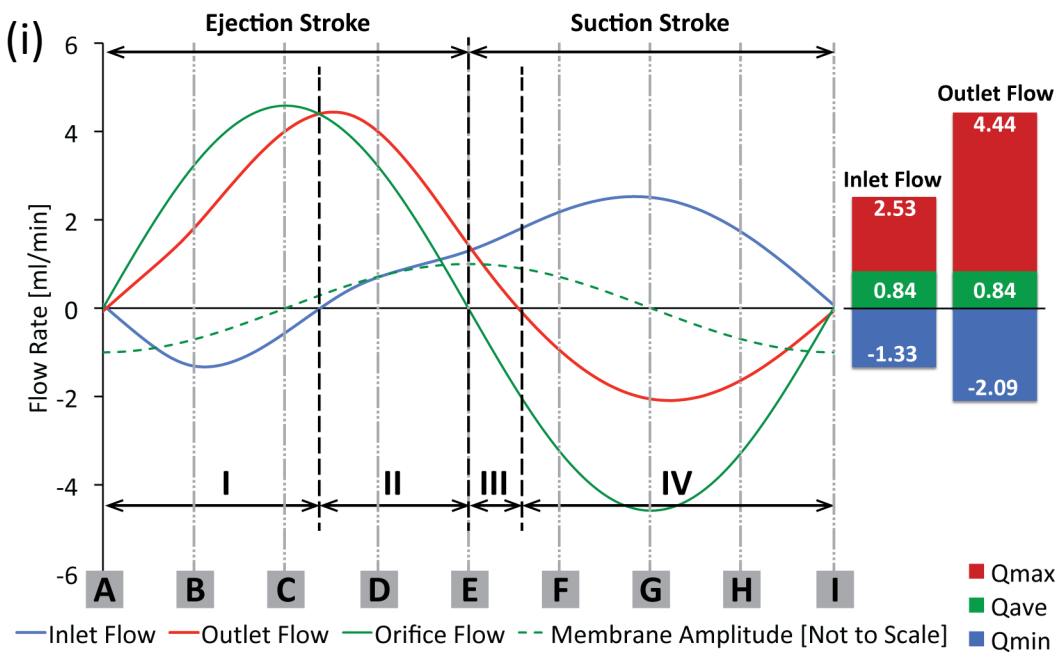

Figure D.6. Details of flow rates and field for the case
A_m = 40 µm, f = 60 Hz, W_i = 400 µm and W_o = 400 µm.
(i) [above] Cycle flow rates [A positive flow rate indicates flow in the forward direction (from inlet to outlet). For orifice flow, positive indicates flow out of the cavity].
Letters on the figure indicate instances along the actuation cycle where details of the flow field are shown in parts ii to v of the figure as follows:
[A] t/T=0.000, [B] t/T=0.125, [C] t/T=0.250,
[D] t/T=0.375, [E] t/T=0.500, [F] t/T=0.625,
[G] t/T=0.750, [H] t/T=0.875, [I] t/T=1.000.
(ii) [Page 236] Streamlines coloured by the velocity magnitude at the mid-height plane of the micropump.
(iii) [Page 237] Velocity vectors coloured by the velocity magnitude at the mid-height plane of the micropump.
(iv) [Page 238] Velocity profiles at three different locations along the length of the outlet channel at the mid-height plane of the micropump.
(v) [Page 239] Velocity profiles at three different locations along the length of the inlet channel at the mid-height plane of the micropump.

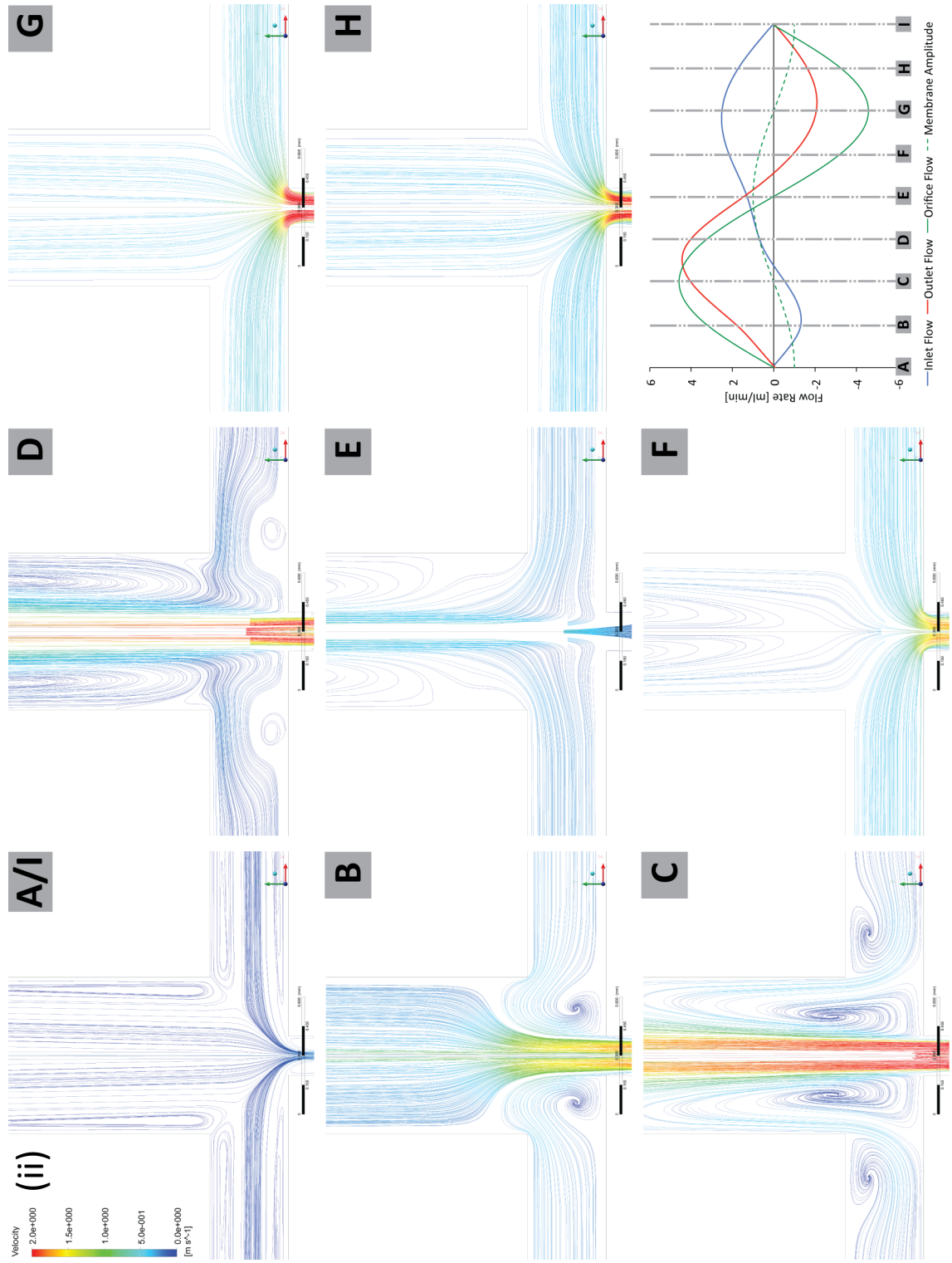

Figure D.6. Continued

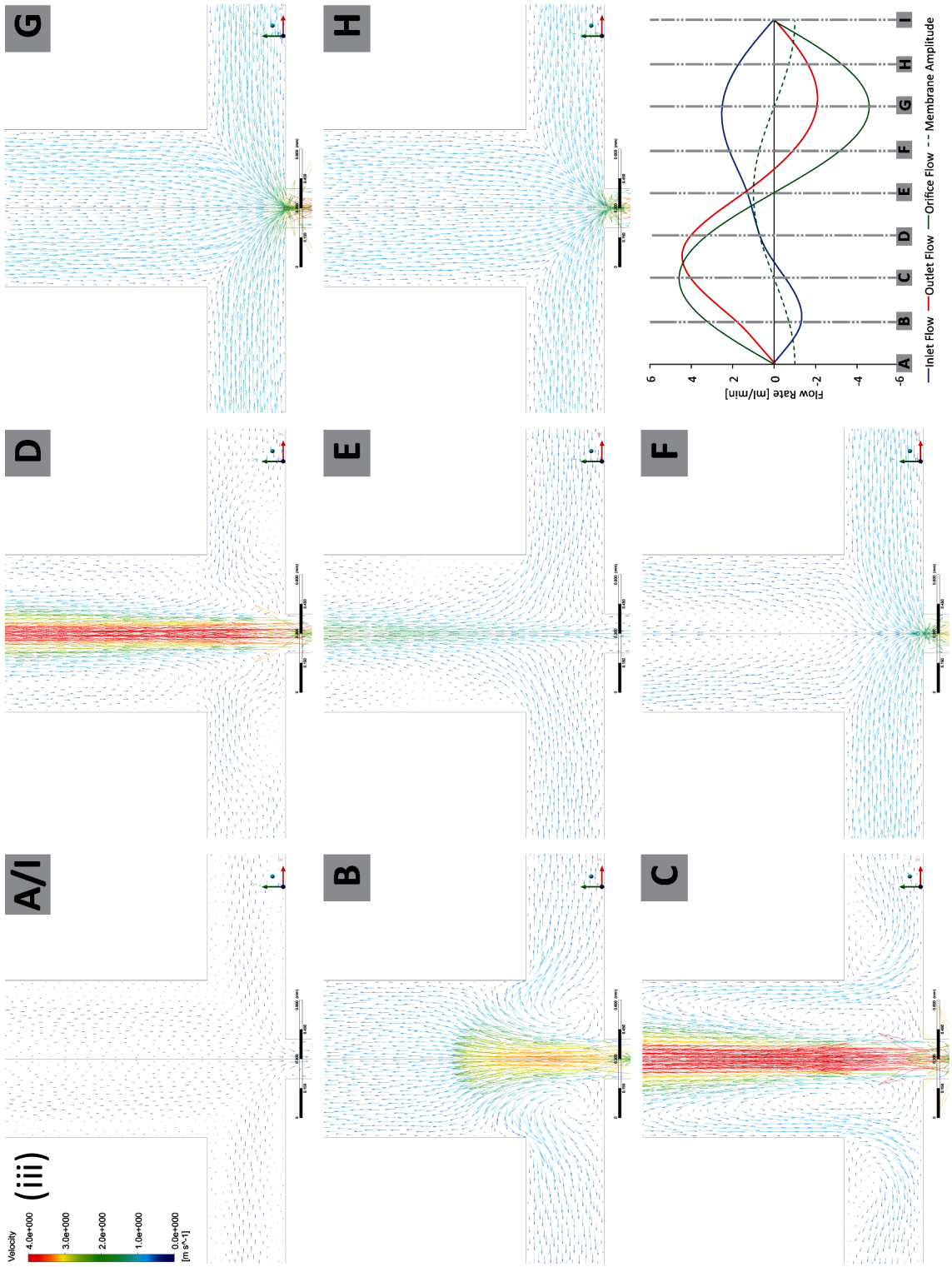

Figure D.6. Continued

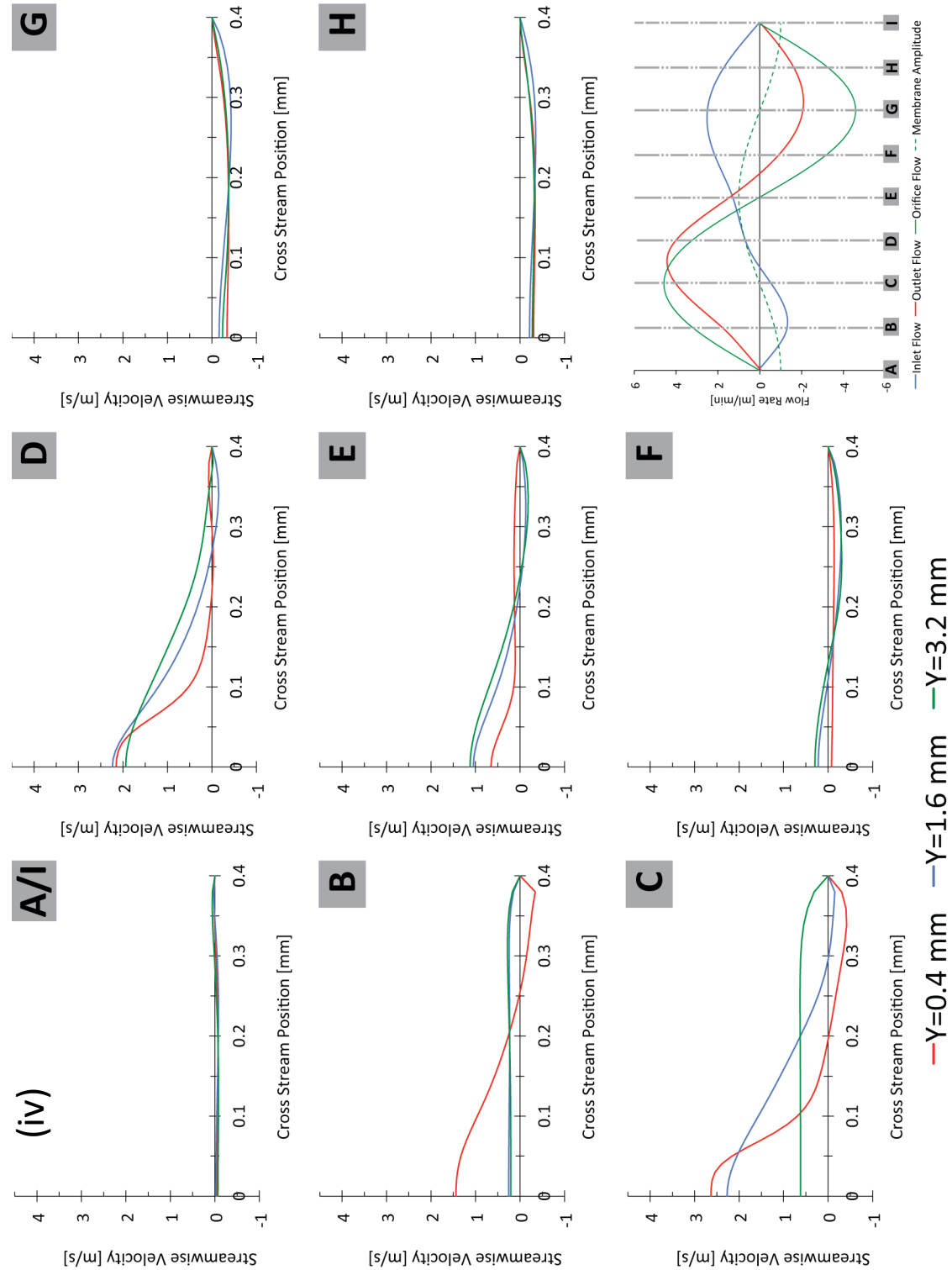

Figure D.6. Continued

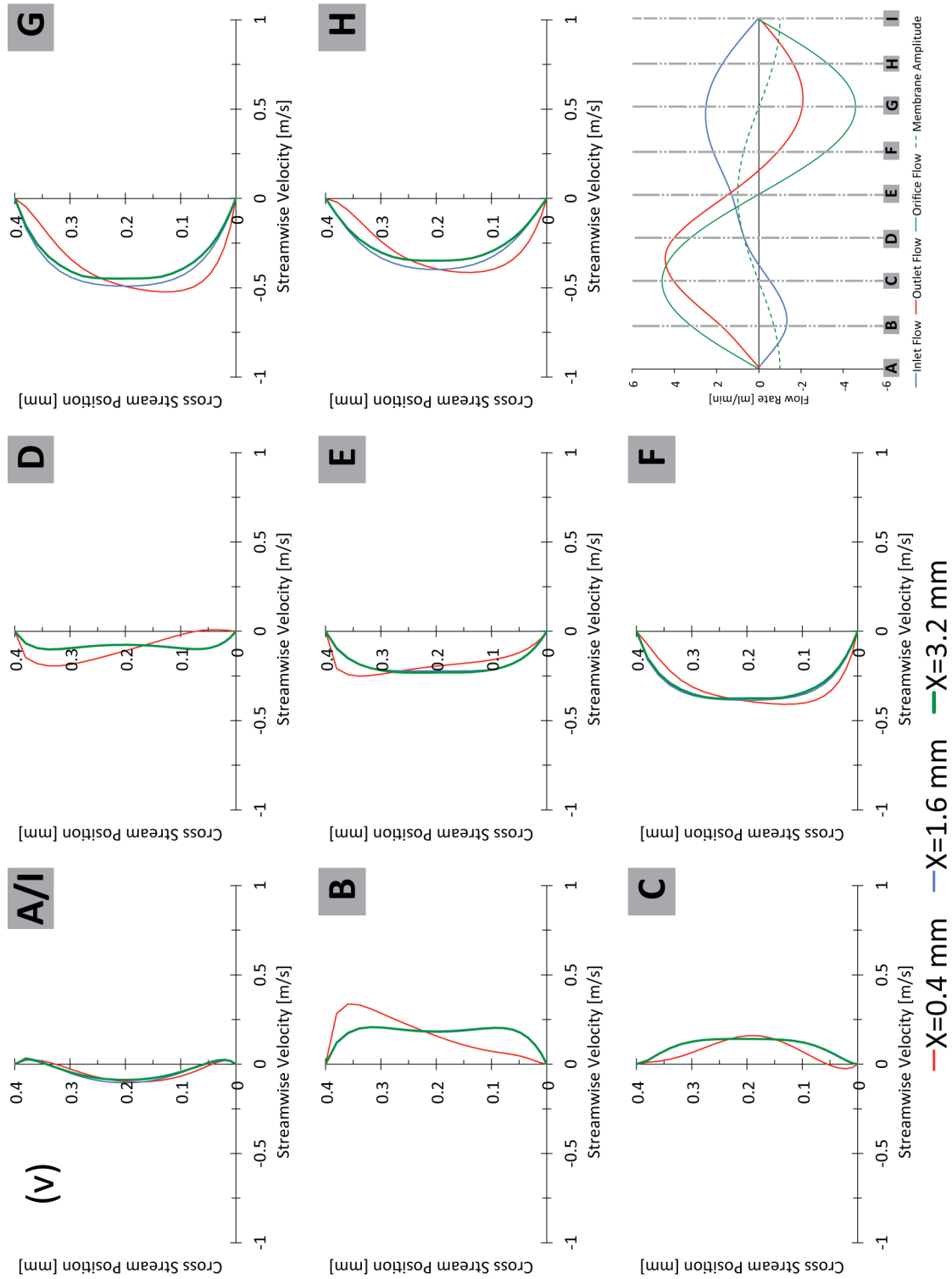

Figure D.6. Continued

D.7 Case W_i=400 µm, W_o= 400 µm, A_m= 60 µm, f= 40 Hz

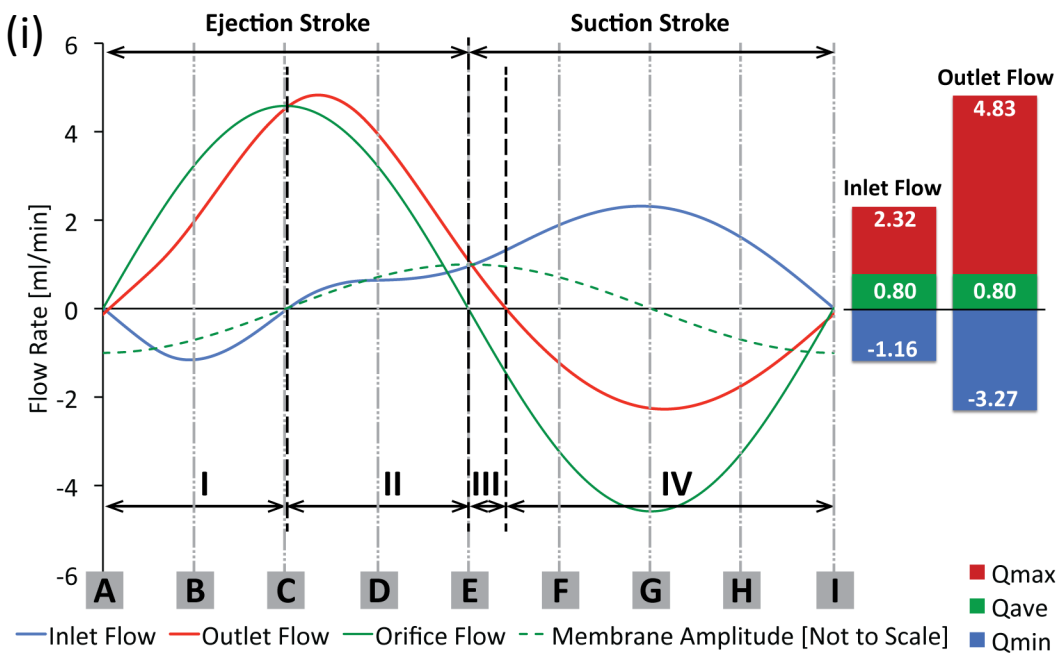

Figure D.7. Details of flow rates and field for the case
A_m = 60 µm, f = 40 Hz, W_i = 400 µm and W_o = 400 µm.
(i) [above] Cycle flow rates [A positive flow rate indicates flow in the forward direction (from inlet to outlet). For orifice flow, positive indicates flow out of the cavity].
Letters on the figure indicate instances along the actuation cycle where details of the flow field are shown in parts ii to v of the figure as follows:
[A] t/T=0.000, [B] t/T=0.125, [C] t/T=0.250,
[D] t/T=0.375, [E] t/T=0.500, [F] t/T=0.625,
[G] t/T=0.750, [H] t/T=0.875, [I] t/T=1.000.
(ii) [Page 241] Streamlines coloured by the velocity magnitude at the mid-height plane of the micropump.
(iii) [Page 242] Velocity vectors coloured by the velocity magnitude at the mid-height plane of the micropump.
(iv) [Page 243] Velocity profiles at three different locations along the length of the outlet channel at the mid-height plane of the micropump.
(v) [Page 244] Velocity profiles at three different locations along the length of the inlet channel at the mid-height plane of the micropump.

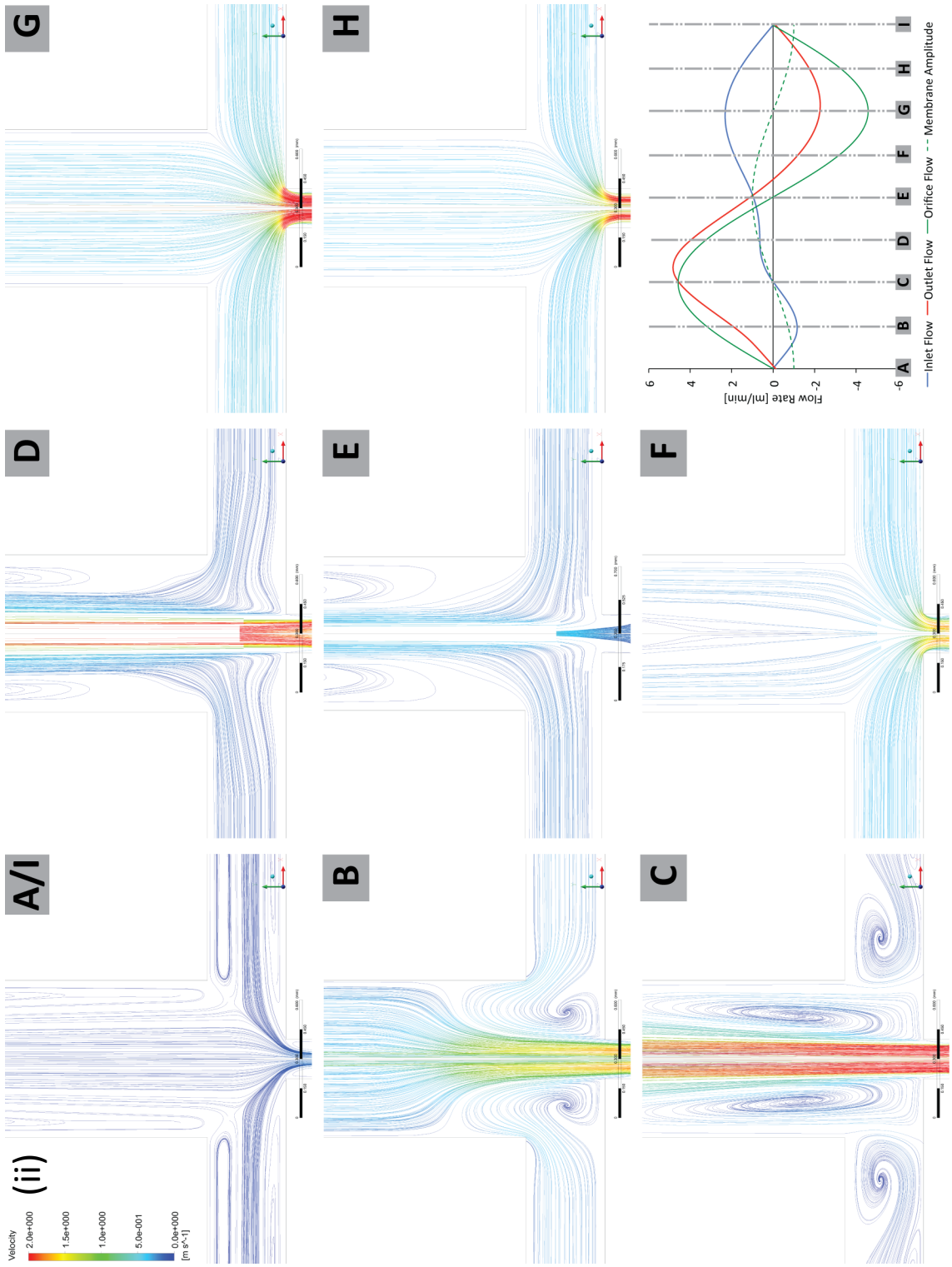

Figure D.7. Continued

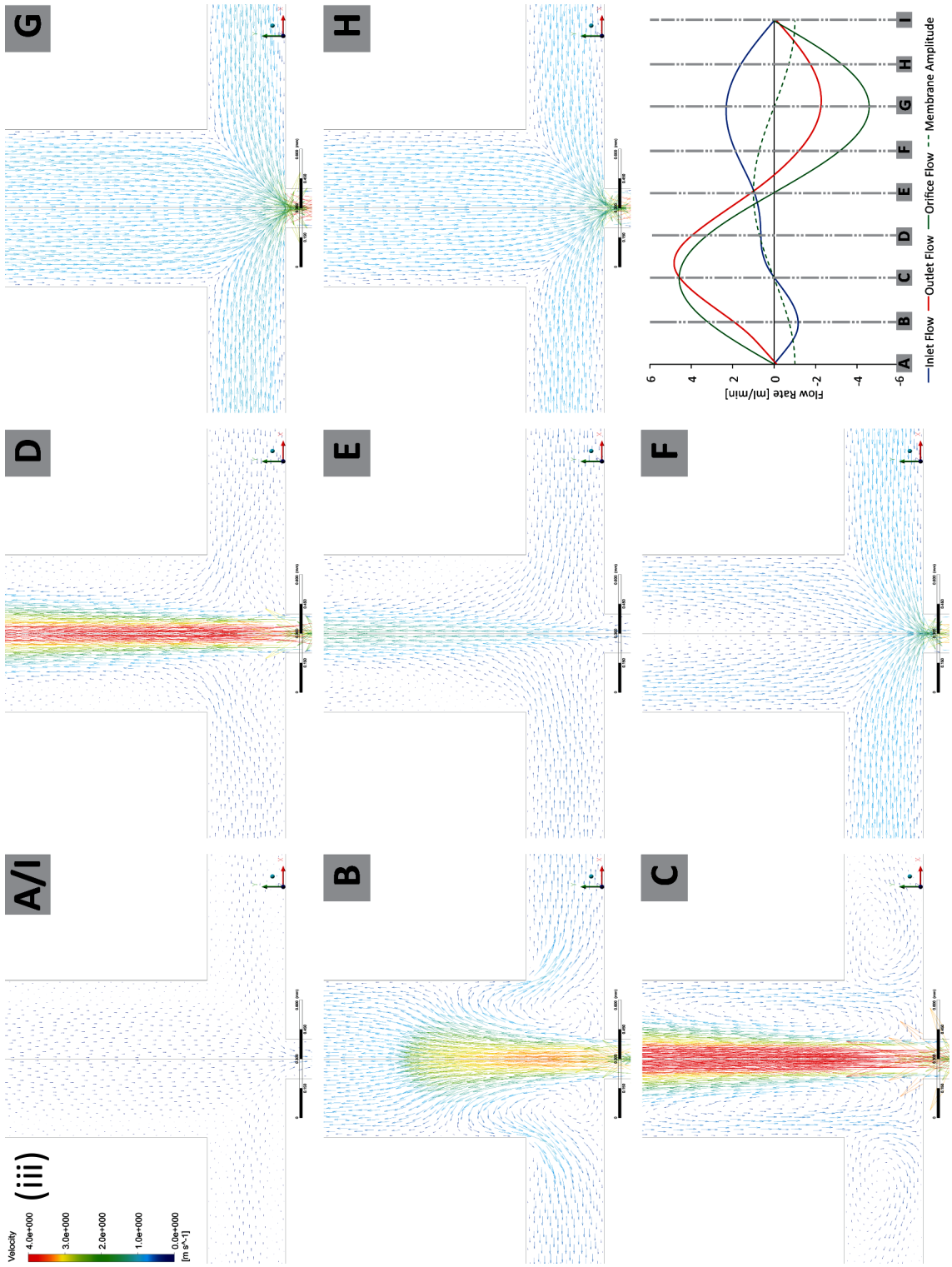

Figure D.7. Continued

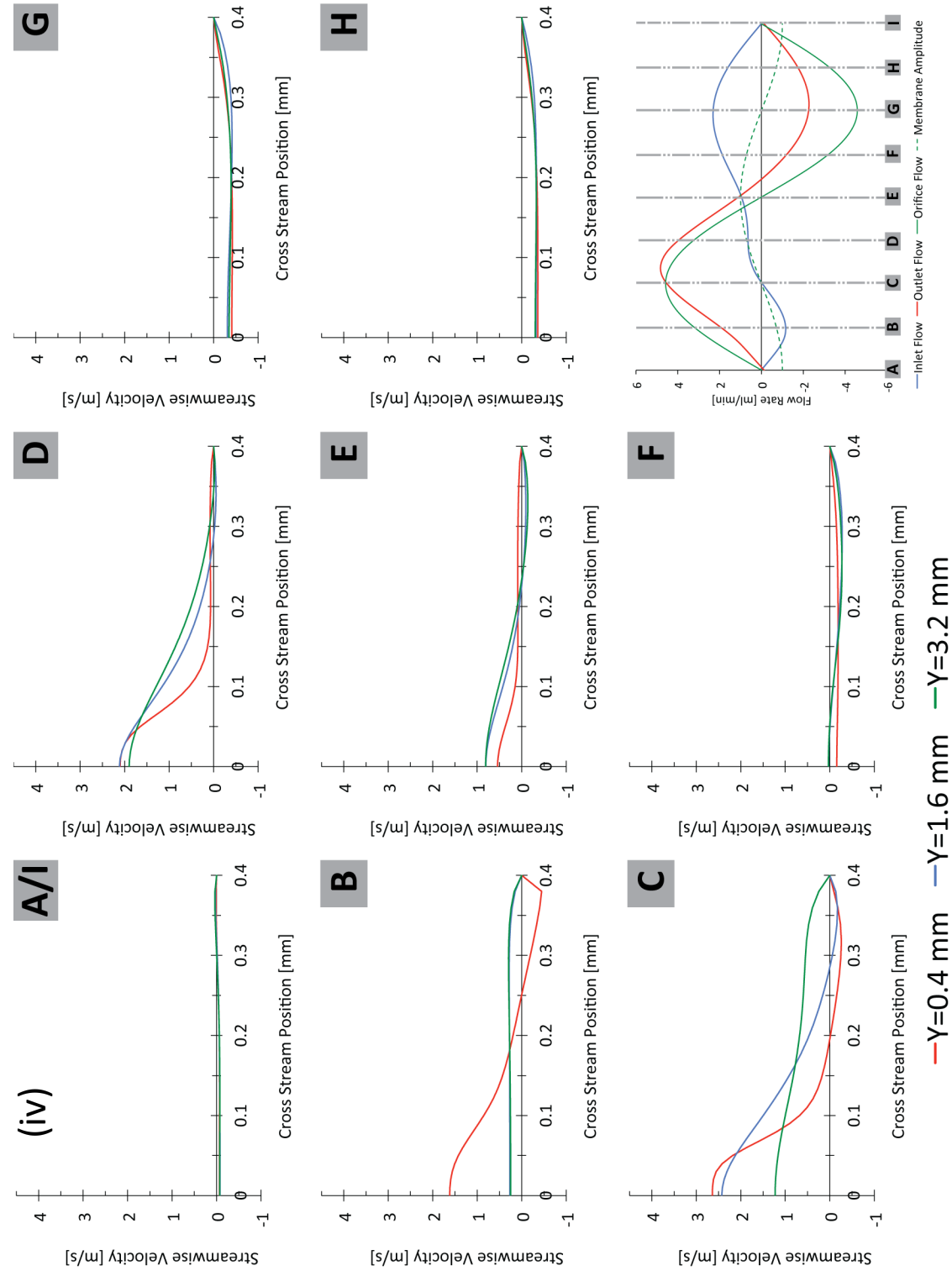

Figure D.7. Continued

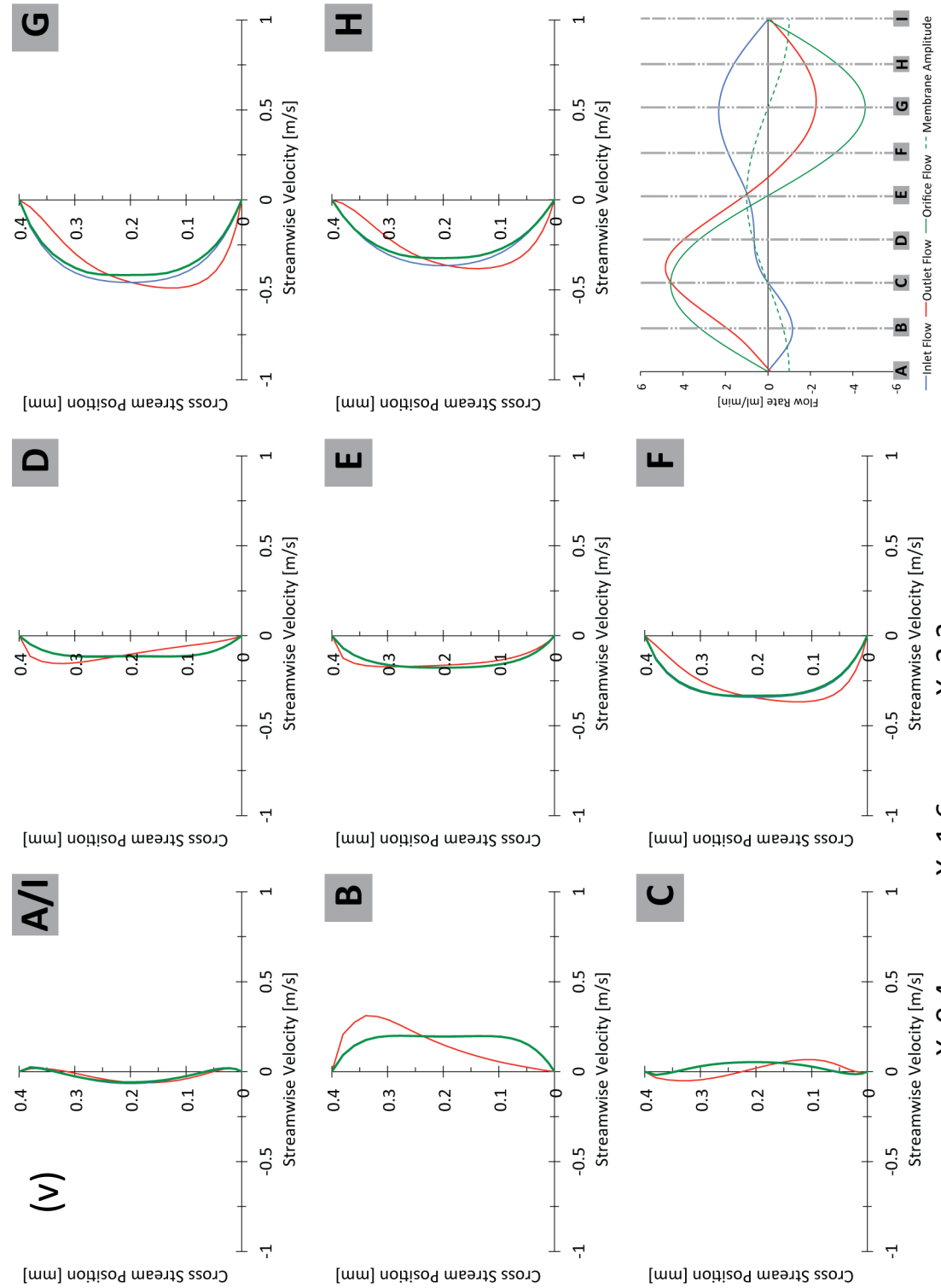

Figure D.7. Continued

D.8 Case W_i=400 µm, W_o= 800 µm, A_m= 40 µm, f= 40 Hz

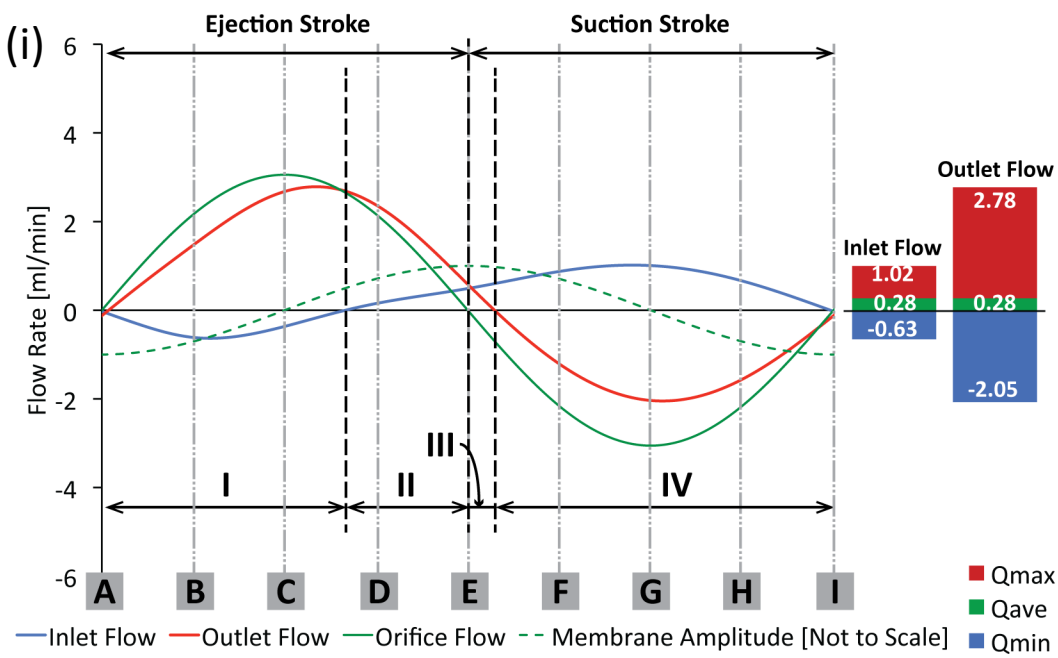

Figure D.8. Details of flow rates and field for the case
A_m = 40 µm, f = 40 Hz, W_i = 400 µm and W_o = 800 µm.
(i) [above] Cycle flow rates [A positive flow rate indicates flow in the forward direction (from inlet to outlet). For orifice flow, positive indicates flow out of the cavity].
Letters on the figure indicate instances along the actuation cycle where details of the flow field are shown in parts ii to v of the figure as follows:
[A] t/T=0.000, [B] t/T=0.125, [C] t/T=0.250,
[D] t/T=0.375, [E] t/T=0.500, [F] t/T=0.625,
[G] t/T=0.750, [H] t/T=0.875, [I] t/T=1.000.
(ii) [Page 246] Streamlines coloured by the velocity magnitude at the mid-height plane of the micropump.
(iii) [Page 247] Velocity vectors coloured by the velocity magnitude at the mid-height plane of the micropump.
(iv) [Page 248] Velocity profiles at three different locations along the length of the outlet channel at the mid-height plane of the micropump.
(v) [Page 249] Velocity profiles at three different locations along the length of the inlet channel at the mid-height plane of the micropump.

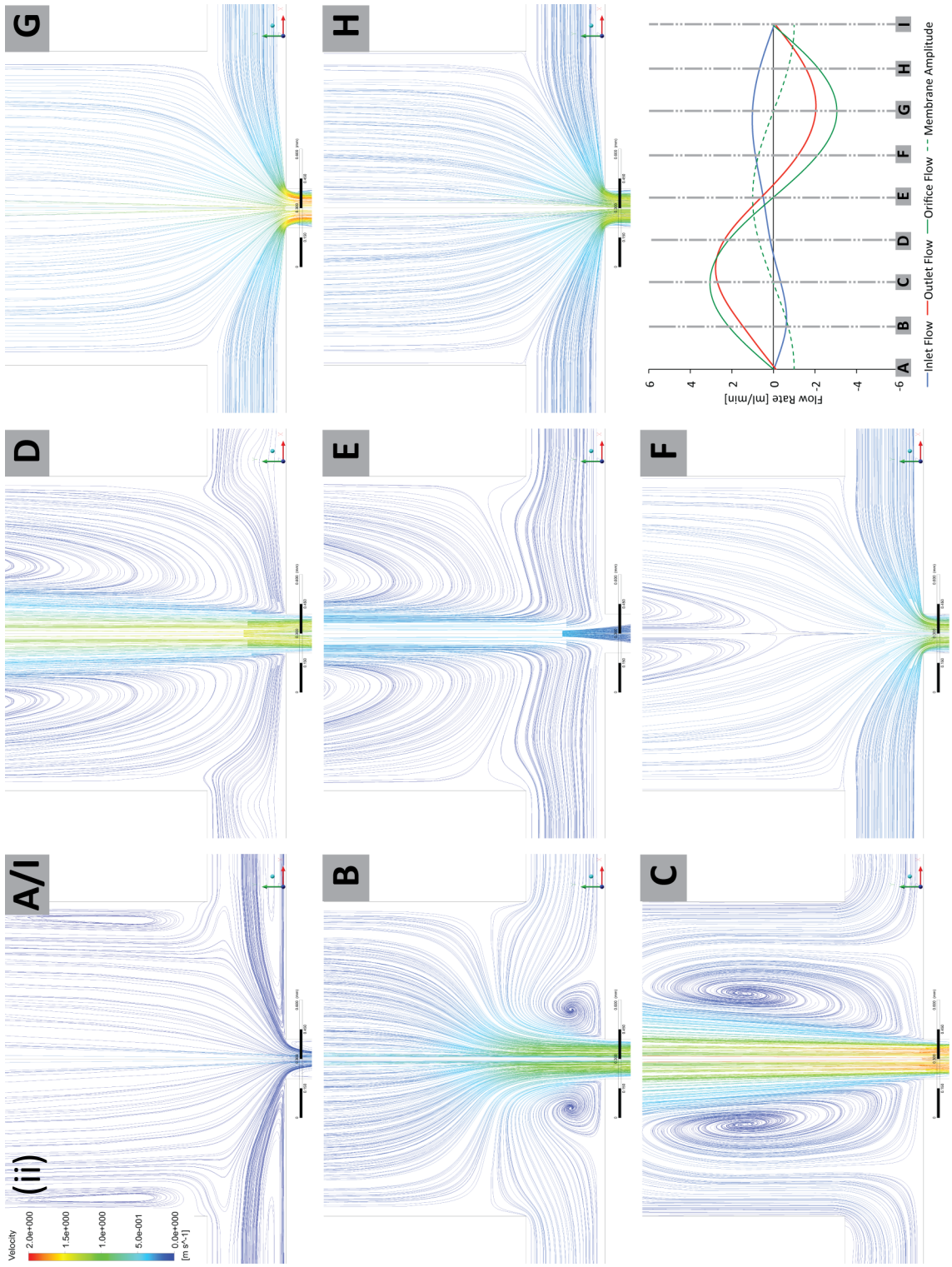

Figure D.8. Continued

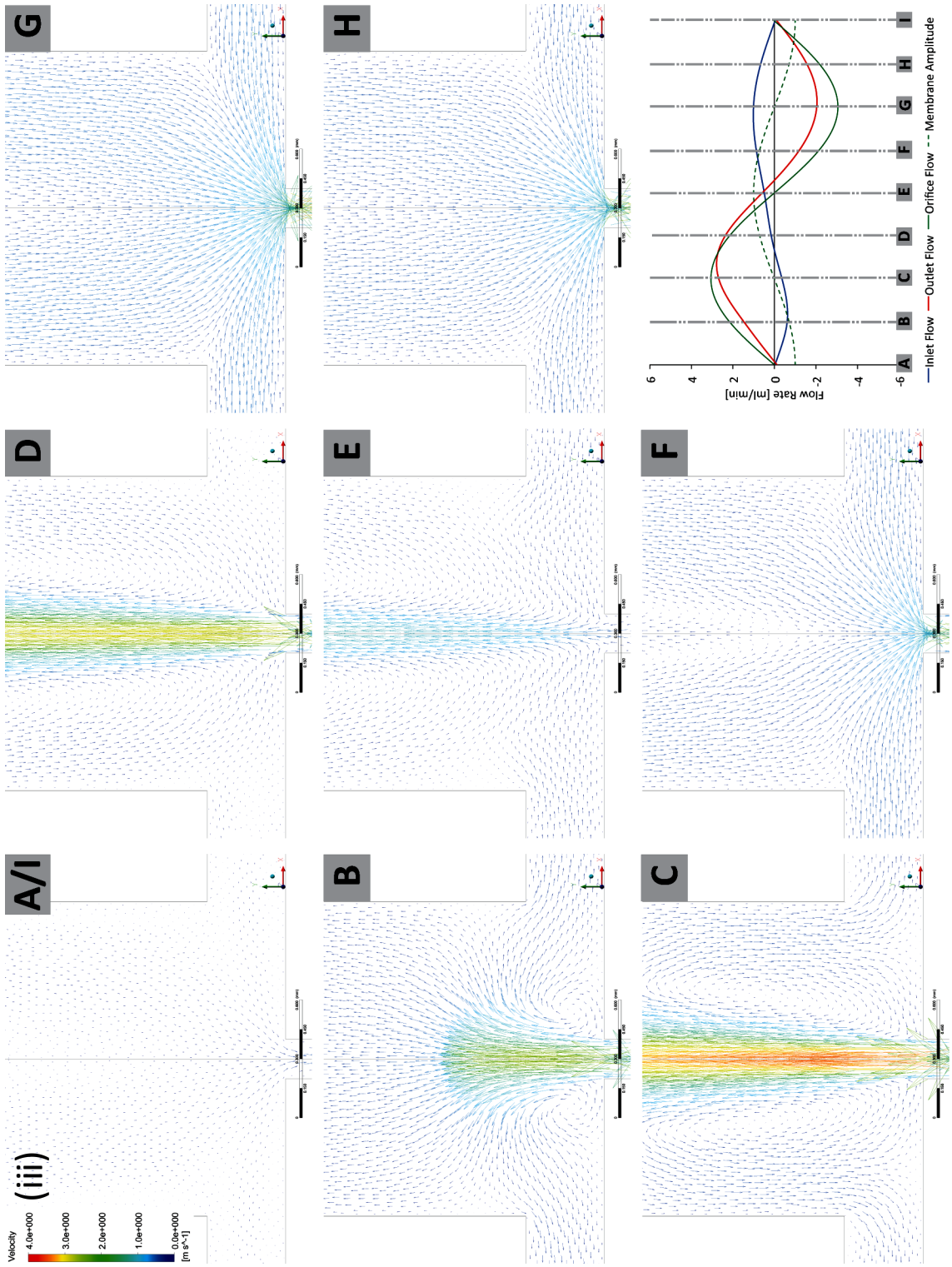

Figure D.8. Continued

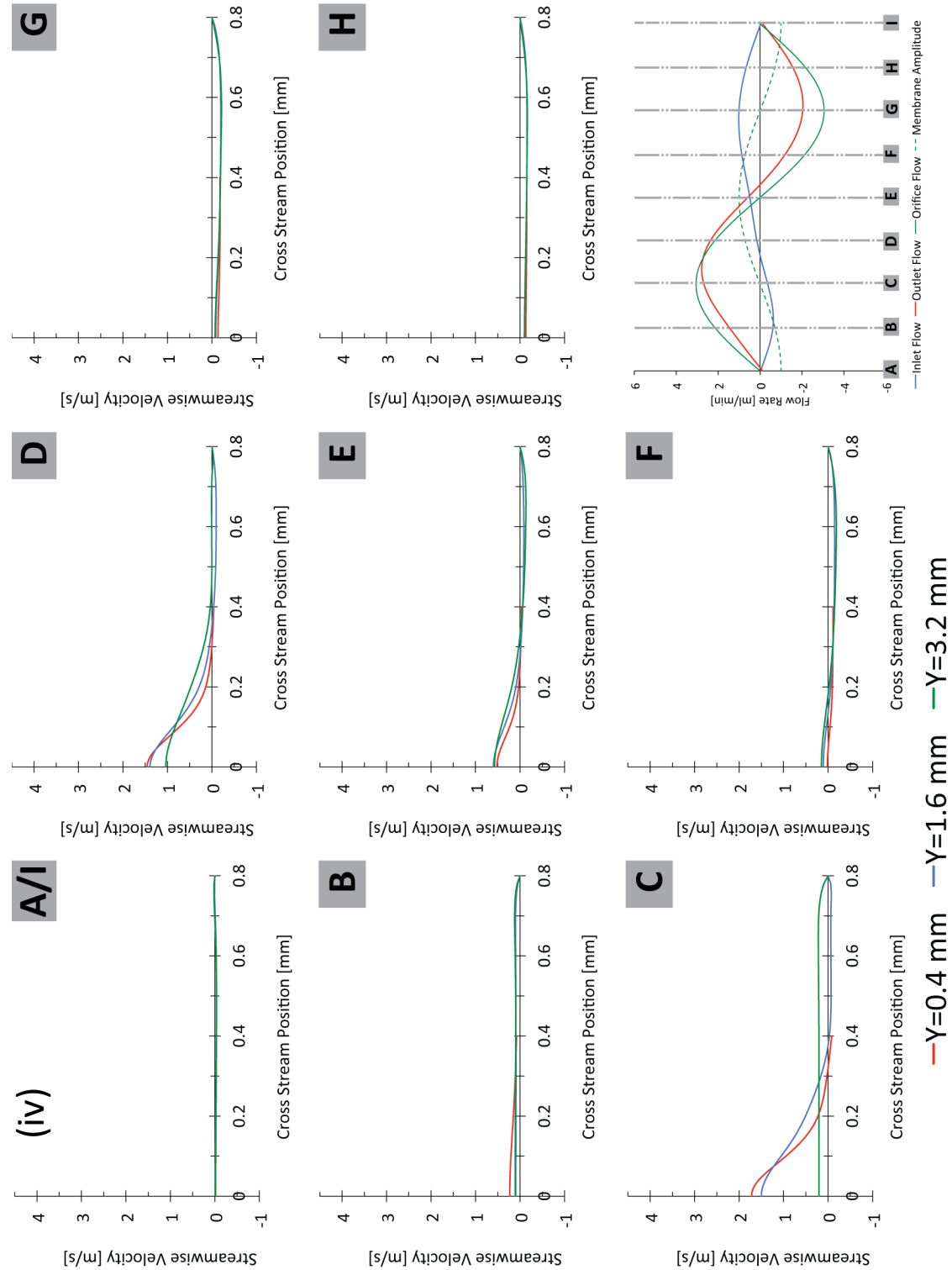

Figure D.8. Continued

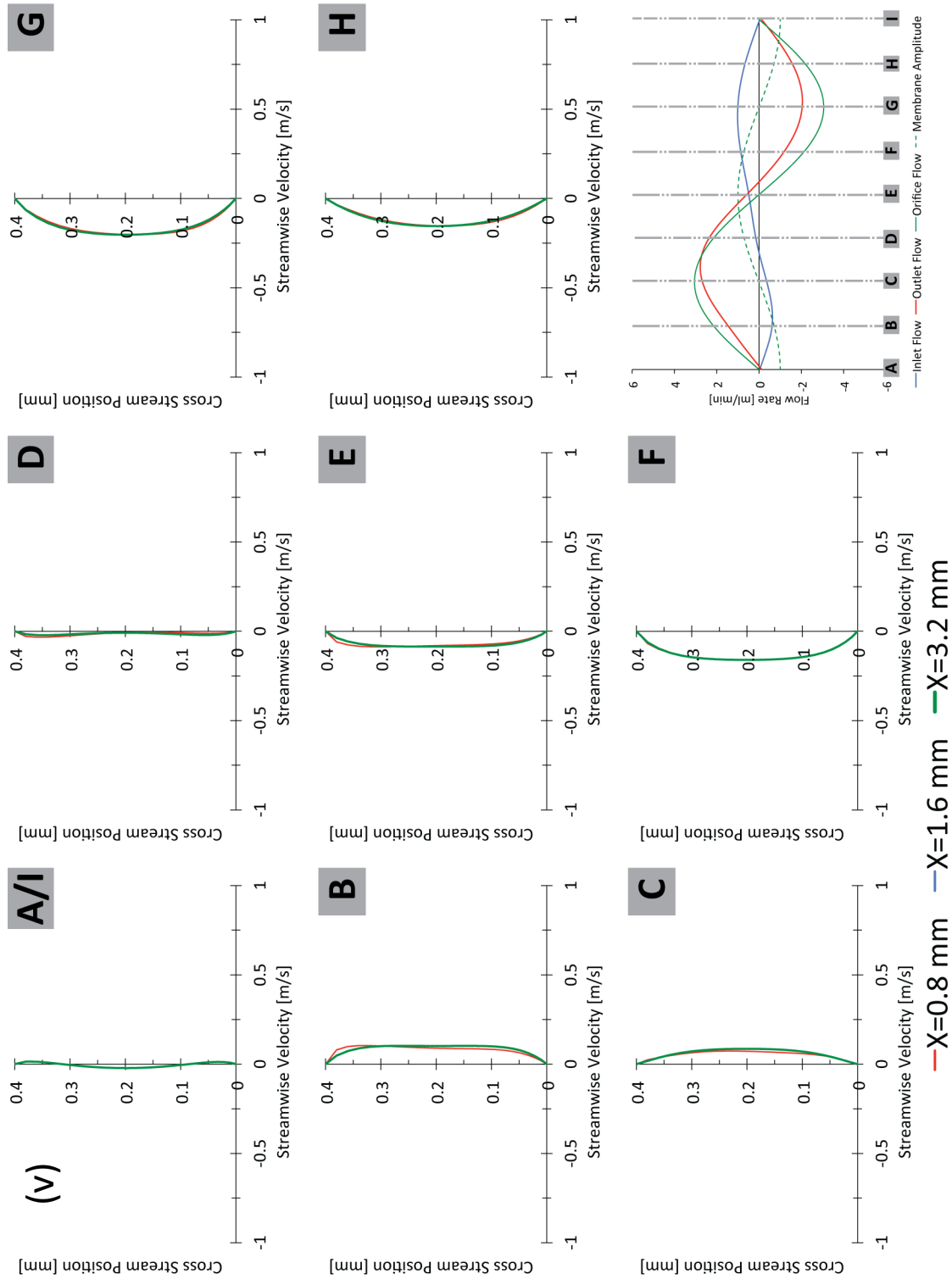

Figure D.8. Continued

D.9 Case W_i=800 µm, W_o= 400 µm, A_m= 40 µm, f= 40 Hz

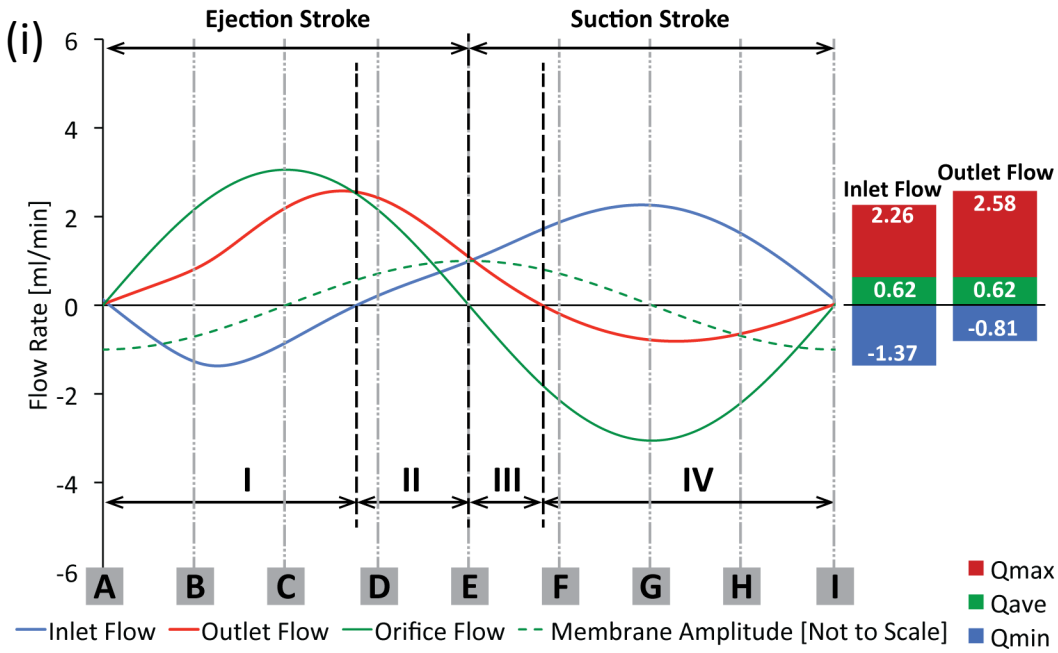

Figure D.9. Details of flow rates and field for the case
A_m = 40 µm, f = 40 Hz, W_i = 800 µm and W_o = 400 µm.
(i) [above] Cycle flow rates [A positive flow rate indicates flow in the forward direction (from inlet to outlet). For orifice flow, positive indicates flow out of the cavity].
Letters on the figure indicate instances along the actuation cycle where details of the flow field are shown in parts ii to v of the figure as follows:
[A] t/T=0.000, [B] t/T=0.125, [C] t/T=0.250,
[D] t/T=0.375, [E] t/T=0.500, [F] t/T=0.625,
[G] t/T=0.750, [H] t/T=0.875, [I] t/T=1.000.
(ii) [Page 251] Streamlines coloured by the velocity magnitude at the mid-height plane of the micropump.
(iii) [Page 252] Velocity vectors coloured by the velocity magnitude at the mid-height plane of the micropump.
(iv) [Page 253] Velocity profiles at three different locations along the length of the outlet channel at the mid-height plane of the micropump.
(v) [Page 254] Velocity profiles at three different locations along the length of the inlet channel at the mid-height plane of the micropump.

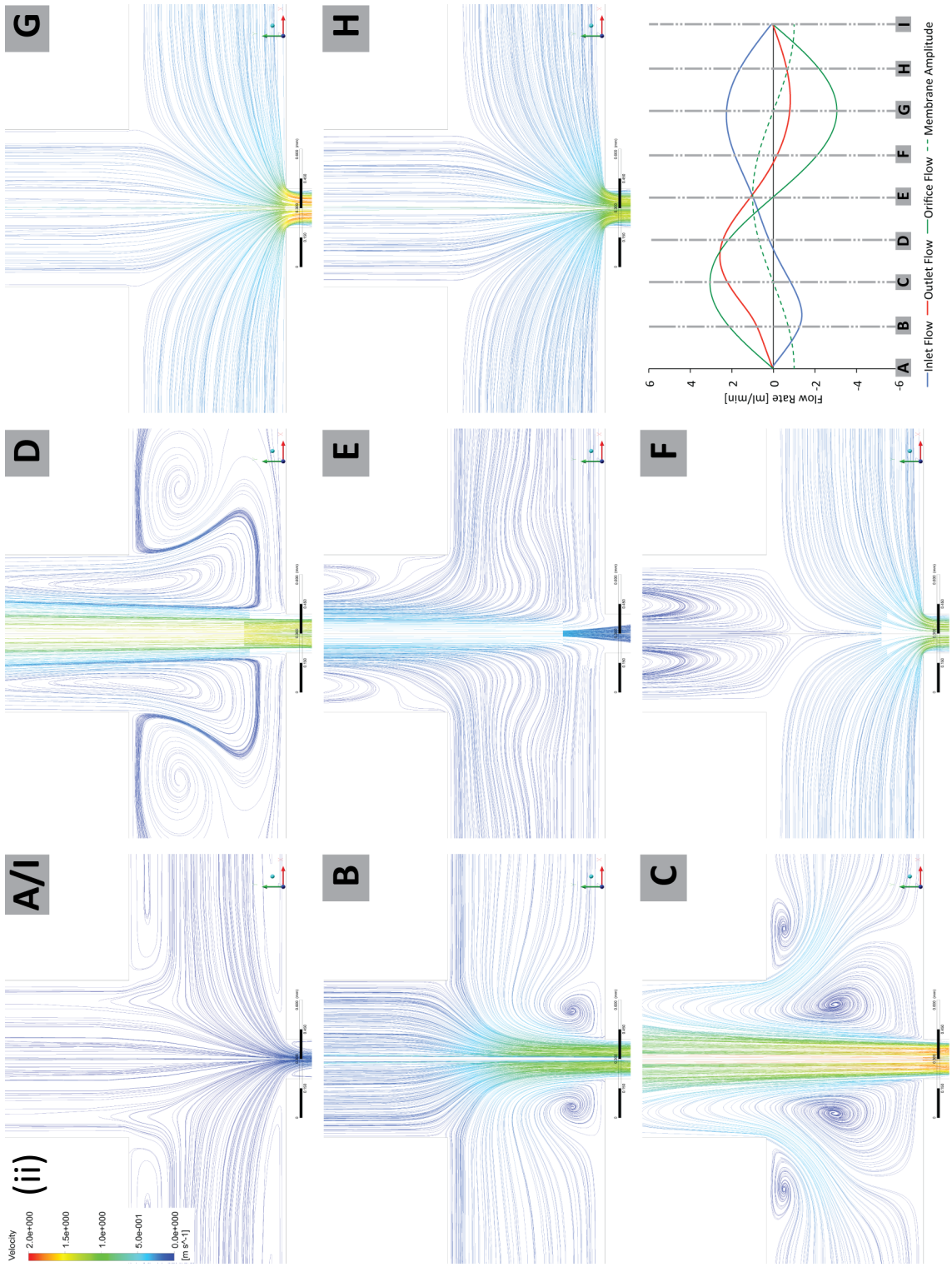

Figure D.9. Continued

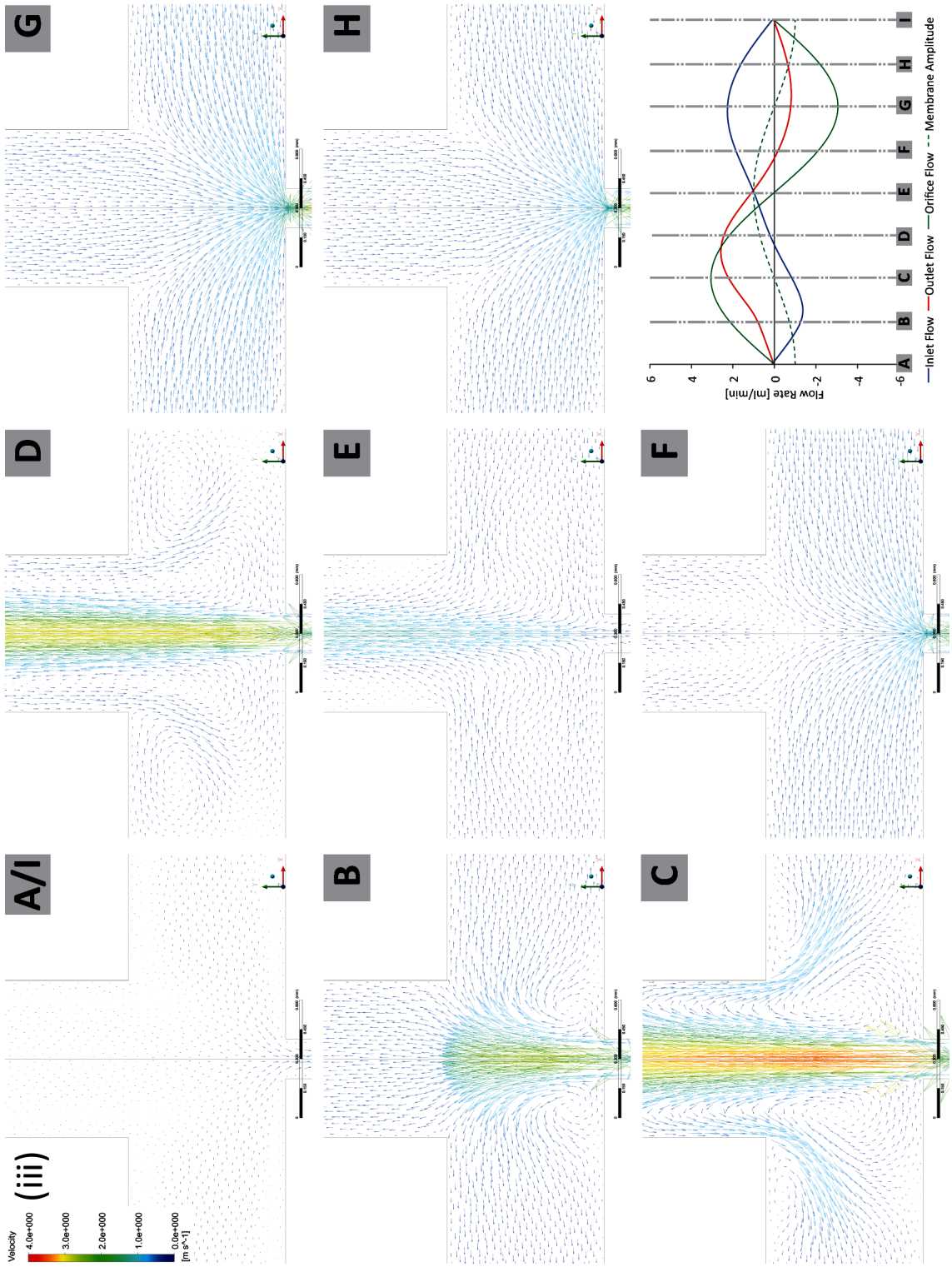

Figure D.9. Continued

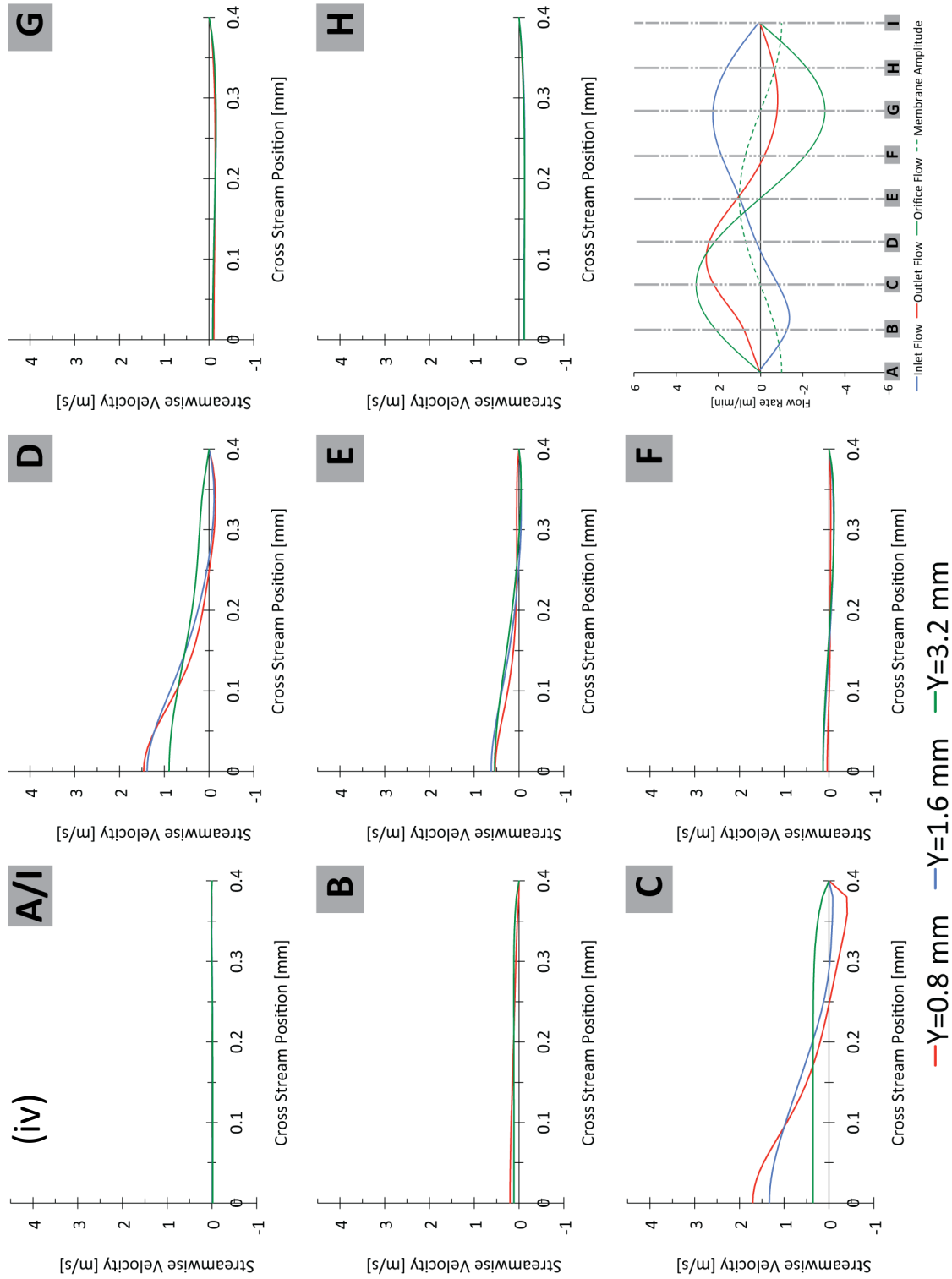

Figure D.9. Continued

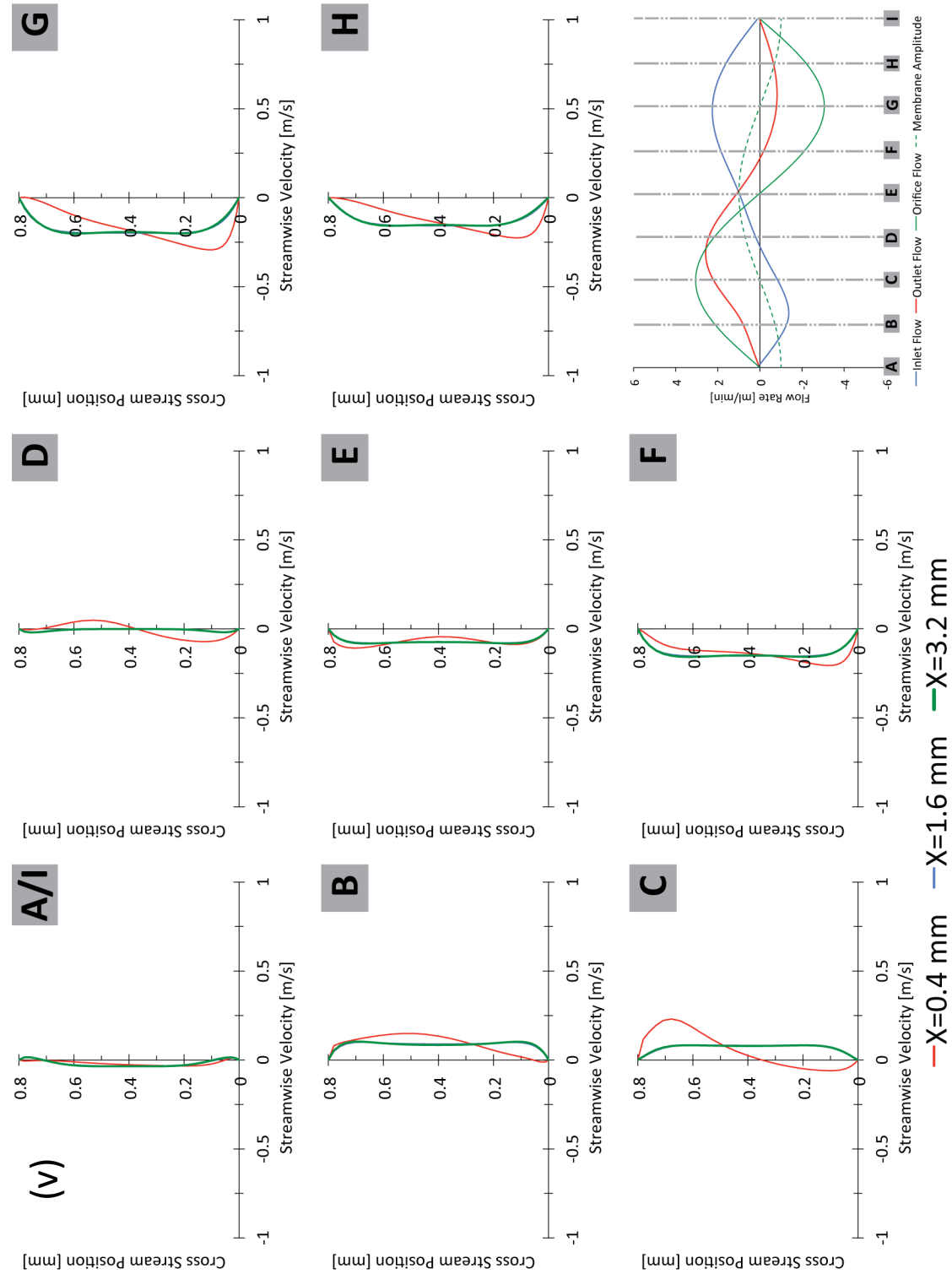

Figure D.9. Continued

D.10 Case W_i=400 µm, W_o= 400 µm, A_m= 40 µm, f= 40 Hz, k=0.25

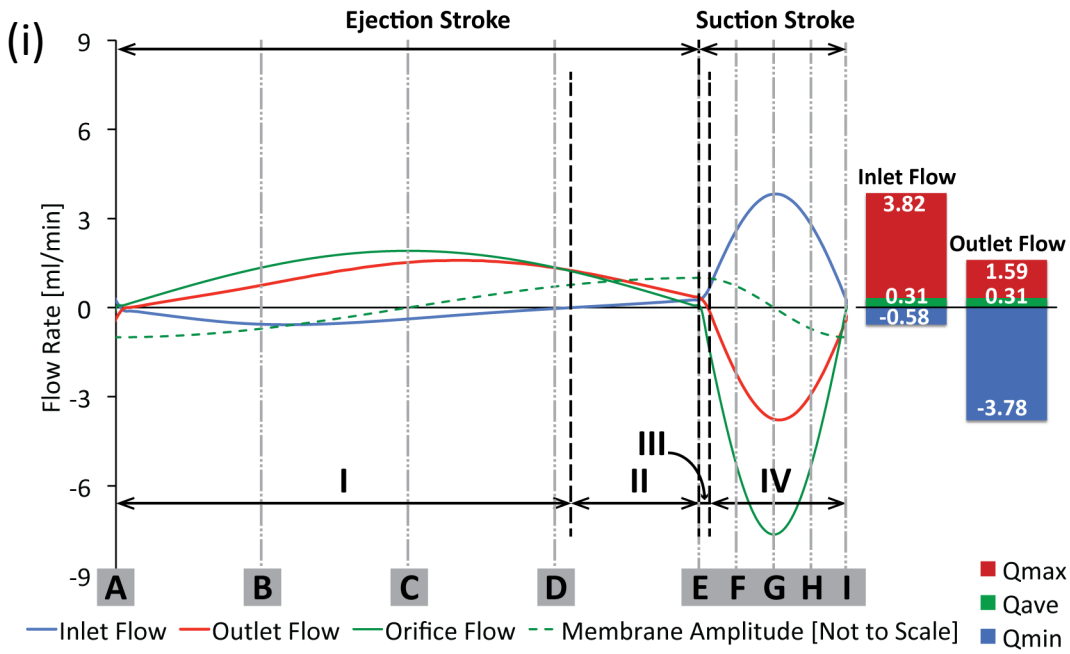

Figure D.10. Details of flow rates and field for the case
A_m = 40 µm, f = 40 Hz, k= 0.25, W_i = 400 µm and W_o = 200 µm.
(i) [above] Cycle flow rates [A positive flow rate indicates flow in the forward direction (from inlet to outlet). For orifice flow, positive indicates flow out of the cavity].
Letters on the figure indicate instances along the actuation cycle where details of the flow field are shown in parts ii to v of the figure as follows:
[A] t/T=0.000, [B] t/T=0.125, [C] t/T=0.250,
[D] t/T=0.375, [E] t/T=0.500, [F] t/T=0.625,
[G] t/T=0.750, [H] t/T=0.875, [I] t/T=1.000.
(ii) [Page 256] Streamlines coloured by the velocity magnitude at the mid-height plane of the micropump.
(iii) [Page 257] Velocity vectors coloured by the velocity magnitude at the mid-height plane of the micropump.
(iv) [Page 258] Velocity profiles at three different locations along the length of the outlet channel at the mid-height plane of the micropump.
(v) [Page 259] Velocity profiles at three different locations along the length of the inlet channel at the mid-height plane of the micropump.

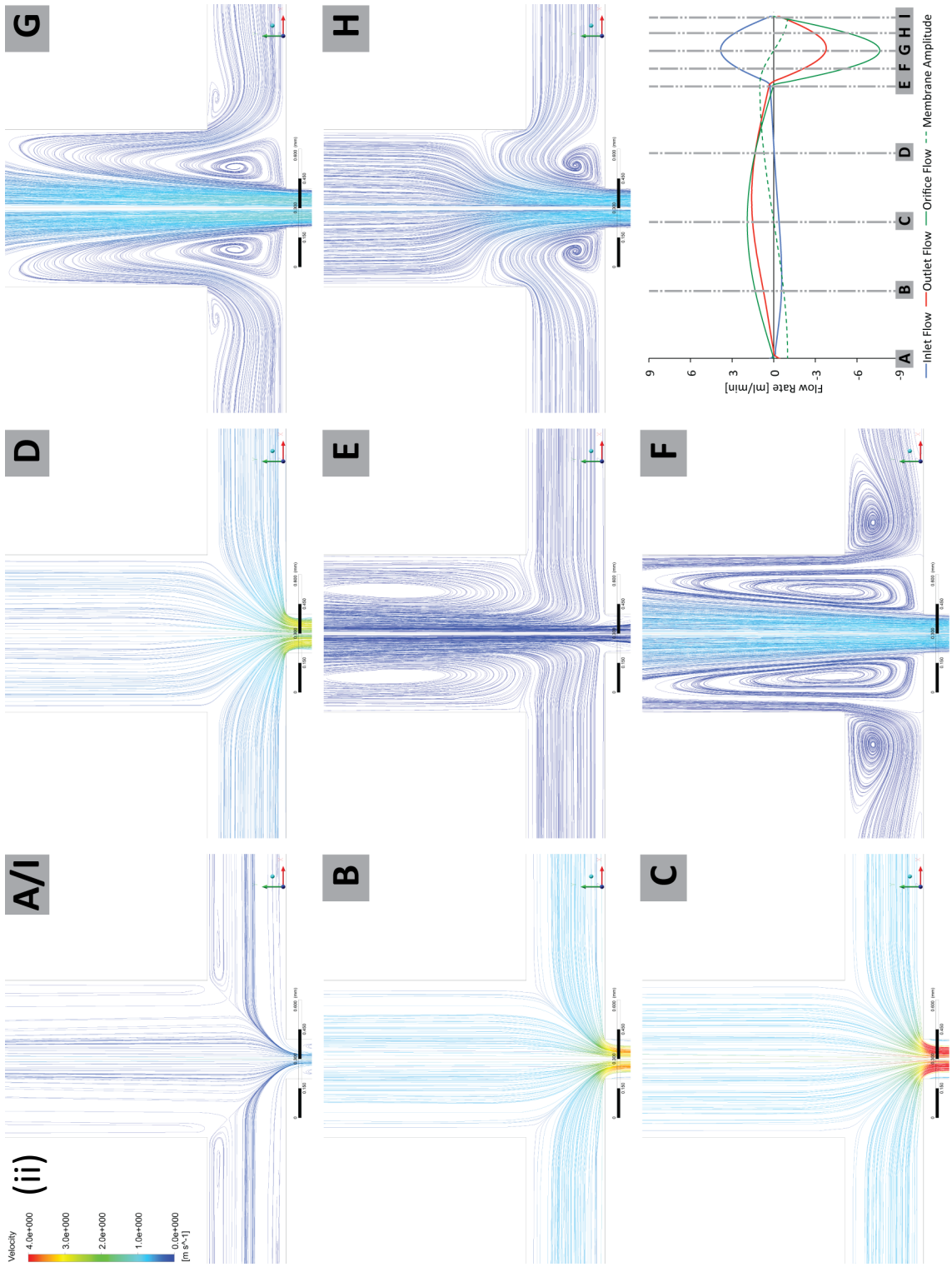

Figure D.10. Continued

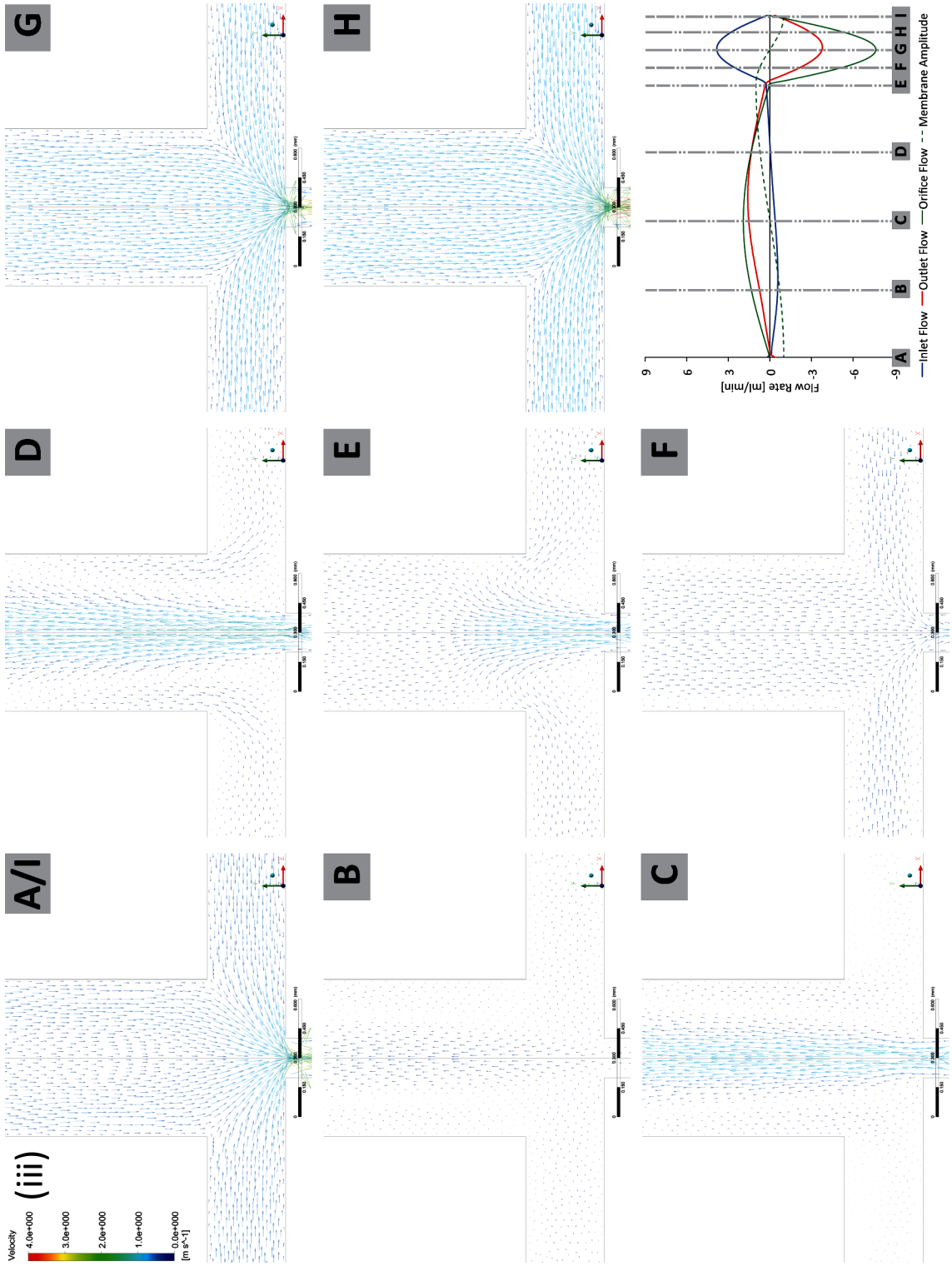

Figure D.10. Continued

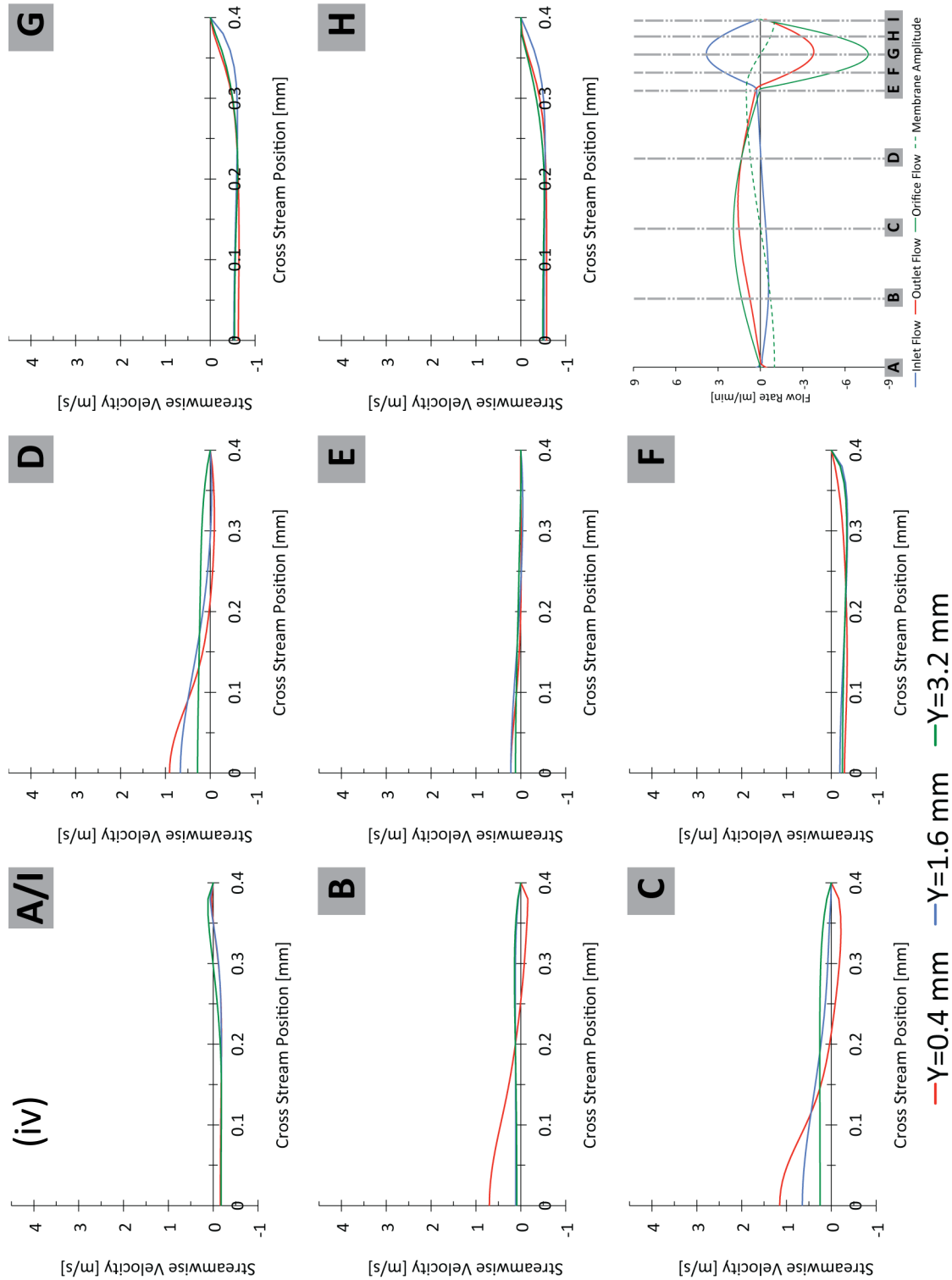

Figure D.10. Continued

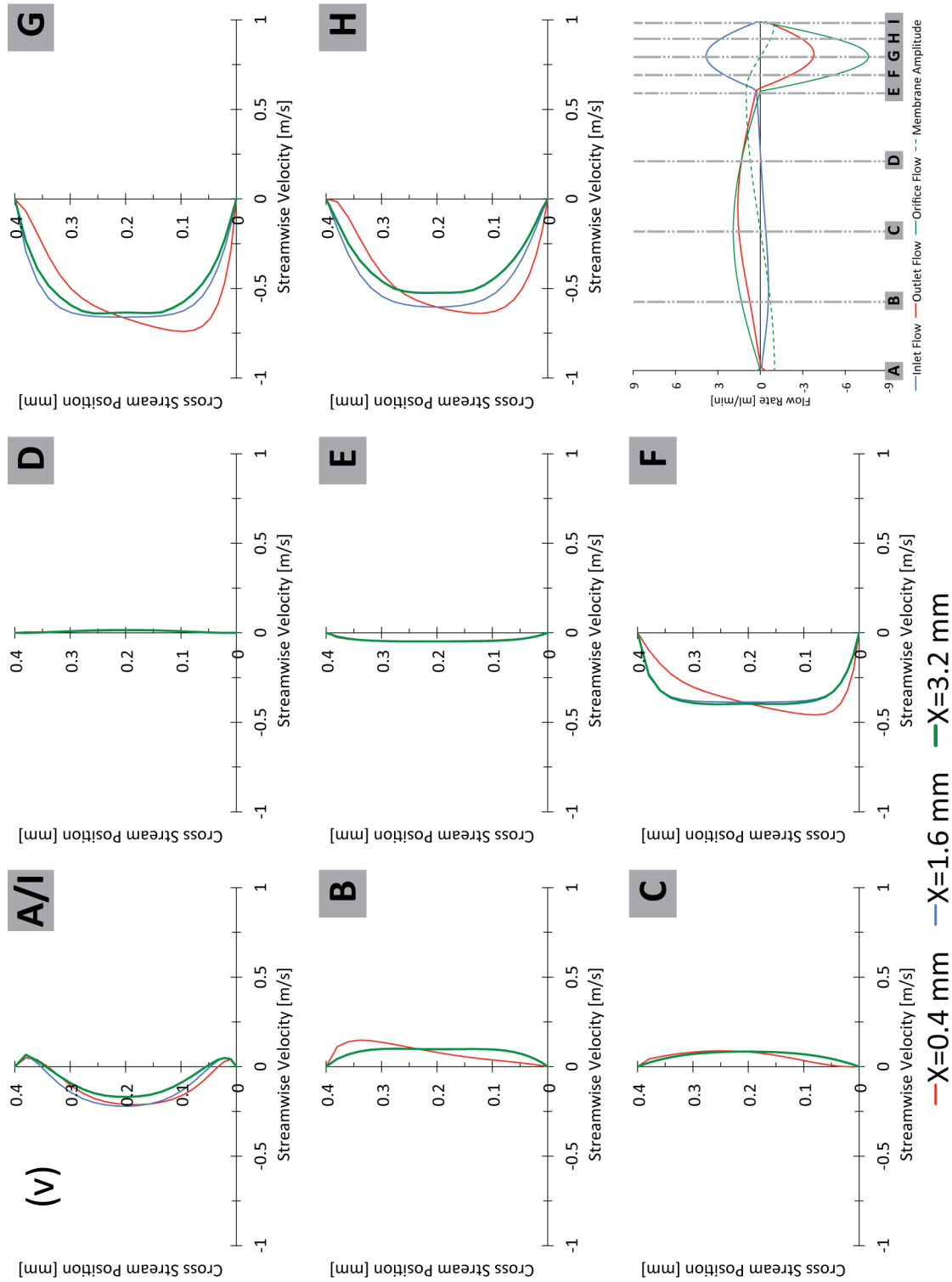

Figure D.10. Continued

D.11 Case W_i=400 µm, W_o= 400 µm, A_m= 40 µm, f= 40 Hz, k=4

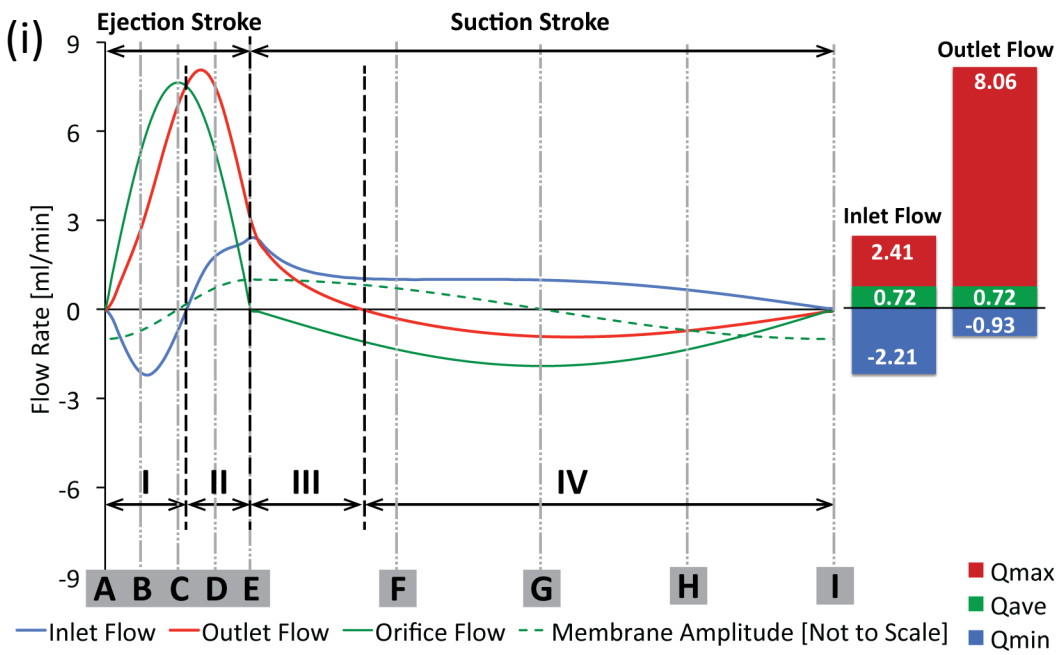

Figure D.11. Details of flow rates and field for the case
A_m = 40 µm, f = 40 Hz, k= 4, W_i = 400 µm and W_o = 400 µm.
(i) [above] Cycle flow rates [A positive flow rate indicates flow in the forward direction (from inlet to outlet). For orifice flow, positive indicates flow out of the cavity].
Letters on the figure indicate instances along the actuation cycle where details of the flow field are shown in parts ii to v of the figure as follows:
[A] t/T=0.000, [B] t/T=0.125, [C] t/T=0.250,
[D] t/T=0.375, [E] t/T=0.500, [F] t/T=0.625,
[G] t/T=0.750, [H] t/T=0.875, [I] t/T=1.000.
(ii) [Page 261] Streamlines coloured by the velocity magnitude at the mid-height plane of the micropump.
(iii) [Page 262] Velocity vectors coloured by the velocity magnitude at the mid-height plane of the micropump.
(iv) [Page 263] Velocity profiles at three different locations along the length of the outlet channel at the mid-height plane of the micropump.
(v) [Page 264] Velocity profiles at three different locations along the length of the inlet channel at the mid-height plane of the micropump.

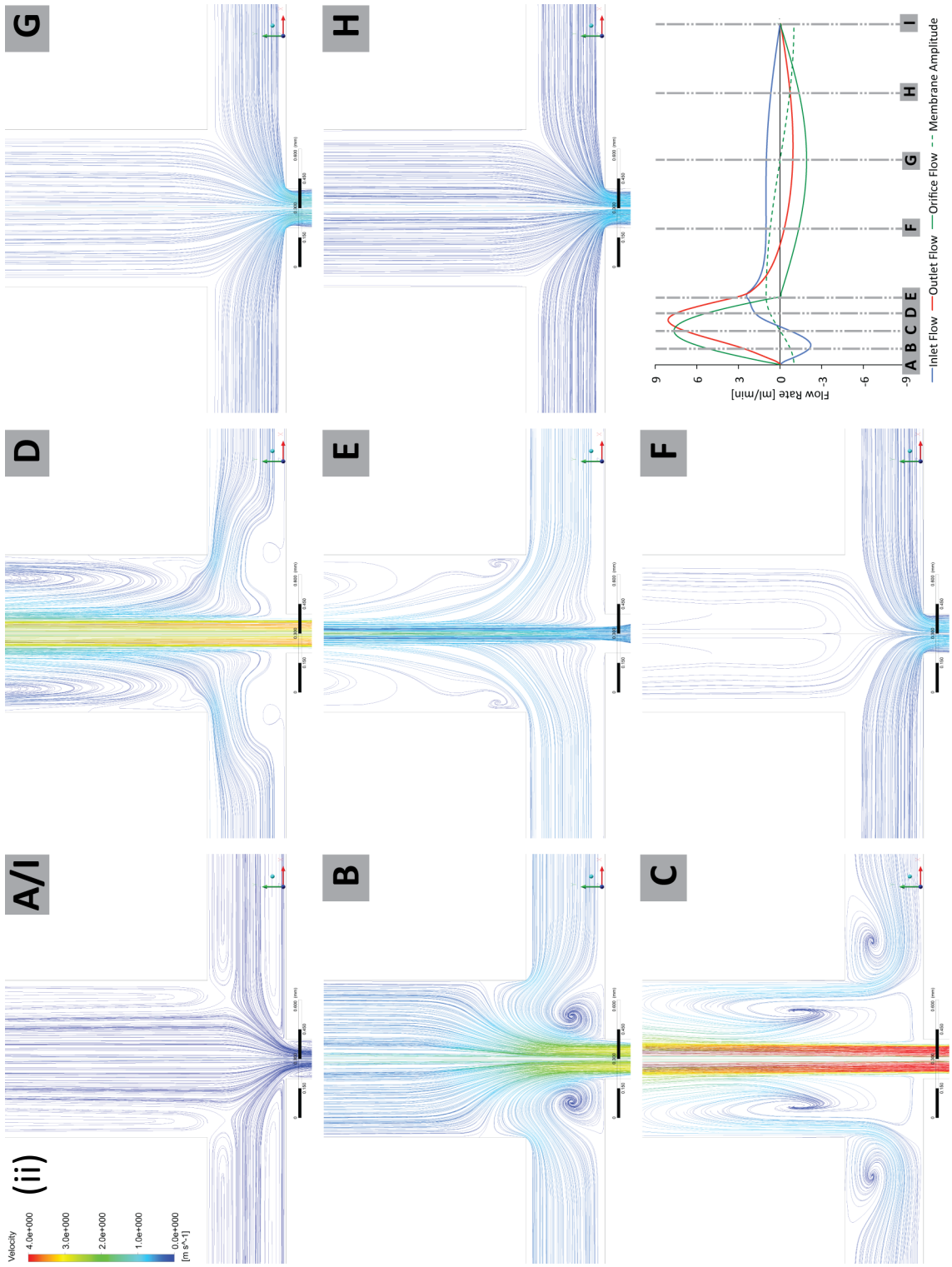

Figure D.11. Continued

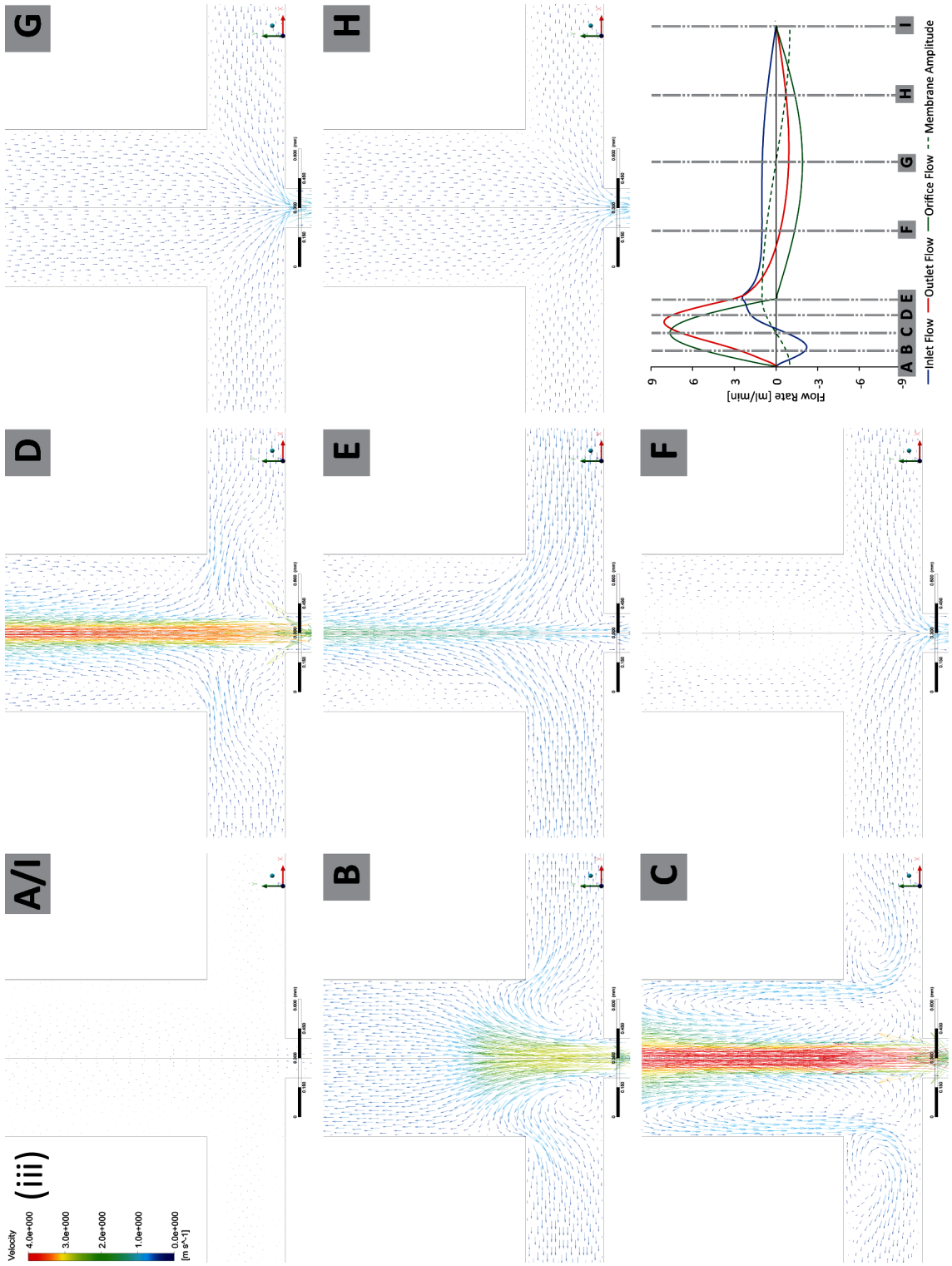

Figure D.11. Continued

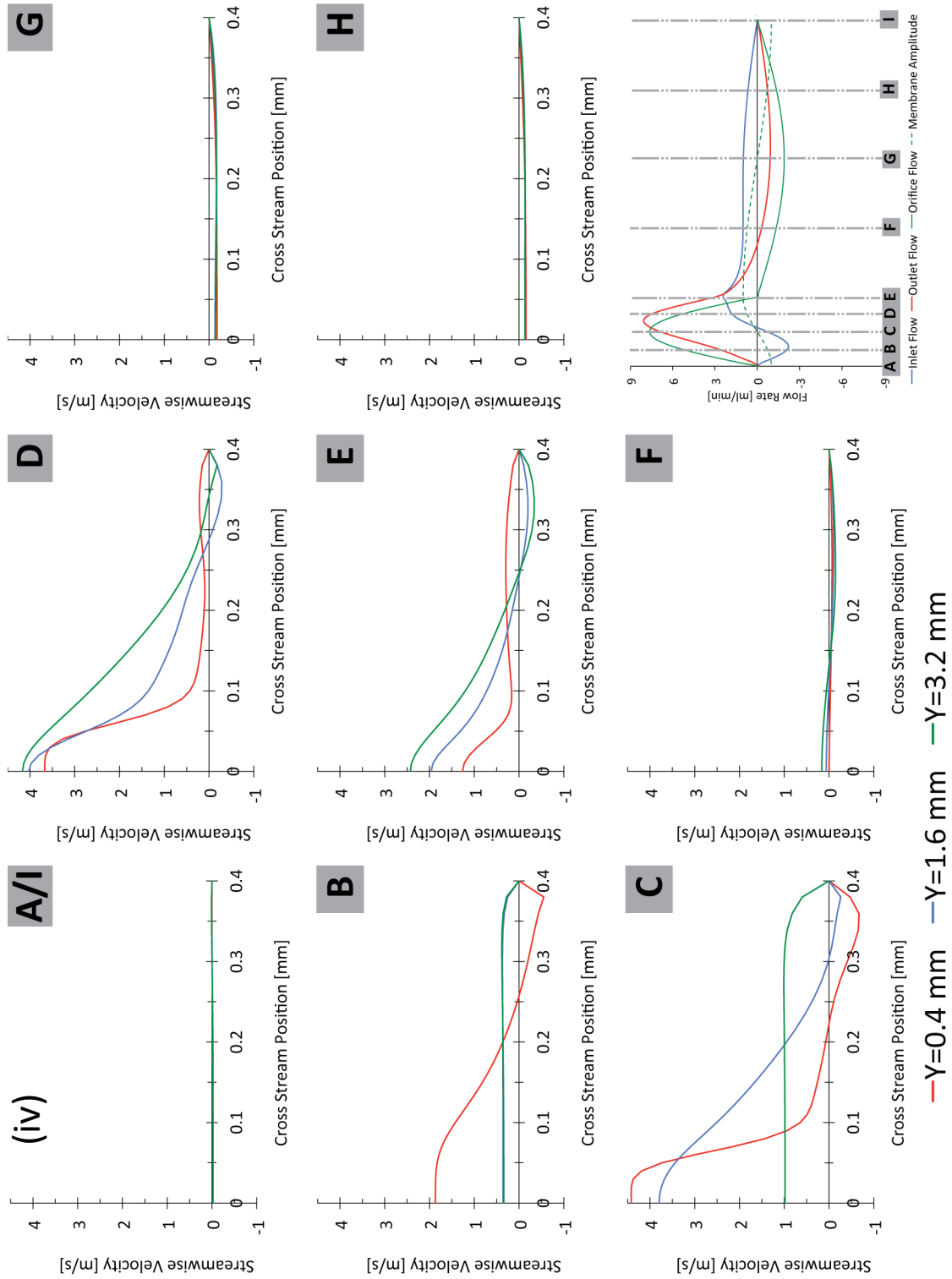

Figure D.11. Continued

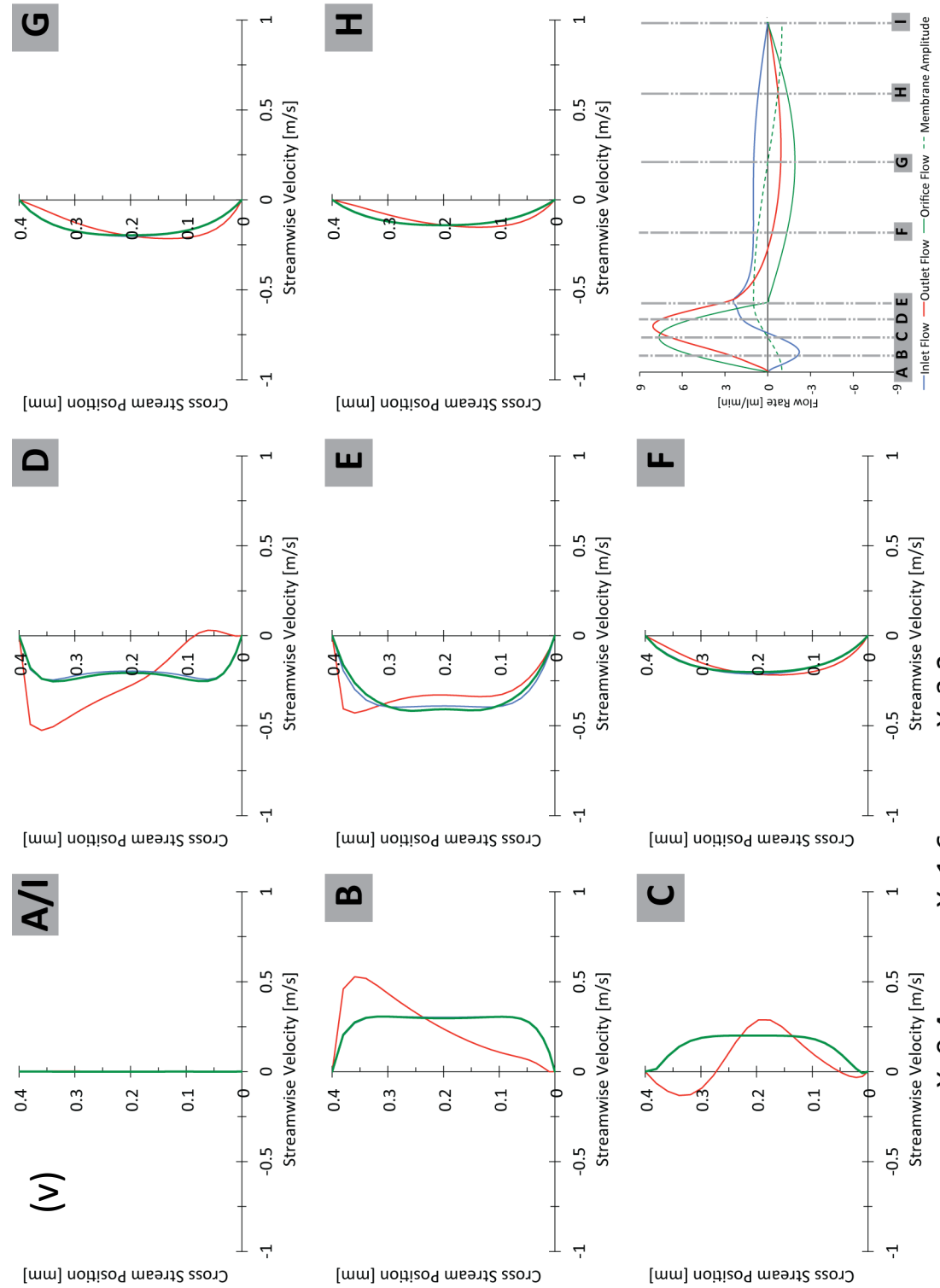

Figure D.11. Continued